

OBSERVATIONAL AND NUMERICAL STUDY OF DAYTIME
FLOWS IN AN ALPINE VALLEY

by

Magdalena Rucker

B.Math, University of Waterloo, 1992
M.Sc., The University of British Columbia, 1995

A THESIS SUBMITTED IN PARTIAL FULFILMENT OF
THE REQUIREMENTS FOR THE DEGREE OF

DOCTOR OF PHILOSOPHY

in

THE FACULTY OF GRADUATE STUDIES

(Atmospheric Science)

We accept this thesis as conforming
to the required standard

THE UNIVERSITY OF BRITISH COLUMBIA

September 22, 2003

© Magdalena Rucker, 2003

In presenting this thesis in partial fulfilment of the requirements for an advanced degree at the University of British Columbia, I agree that the Library shall make it freely available for reference and study. I further agree that permission for extensive copying of this thesis for scholarly purposes may be granted by the head of my department or by his or her representatives. It is understood that copying or publication of this thesis for financial gain shall not be allowed without my written permission.

Atmospheric Science

The University Of British Columbia
Vancouver, Canada

Date September 30, 2003

Abstract

Thermally-driven valley wind systems are an integral part of the meteorology in mountain valleys and hence play an important role in environmental issues of human habitation. While we have a basic understanding of the evolution and mechanisms of valley flows, very little is known about the spatial structures of these flows and how they relate to topography. This lack of understanding has been largely due to the lack of spatial resolution with conventional *in-situ* instrumentation.

This study utilizes high spatially-resolved Doppler lidar measurements to examine the spatial structure of daytime thermally-driven valley flows in the Wipptal, Austria. Results are presented for a number of days which provides insight into which flow aspects are influenced externally and which ones are induced locally. Numerical simulations are conducted to elucidate the flow dynamics in the Wipptal and to explore the role of topography.

Observations show that, regardless of external conditions, the wind speed increases with up-valley distance in the narrow section of the Wipptal. Analysis of the along-valley volume flux shows that the increase in wind speed cannot be explained as a Venturi effect due to the horizontal contraction of the valley sidewalls. Furthermore, significant subsidence must occur in this part of the valley in order to balance the along-valley volume flux divergence. Numerical modeling of the flow in the Wipptal supports the notion that the observed flow structure is linked to the valley geometry. Advection processes, however, are also found to play a significant role.

From these findings, it may be inferred that the along-valley kinematic structure is influenced by the geometry of the valley and that localized subsiding motion can occur over localized valley segments as a result of changes in the intra-valley pressure gradient. This calls into question the concept that heating in an entire catchment area is relayed back to the main valley through subsidence at the mouth of a tributary.

Contents

Abstract	ii
Contents	iii
List of Tables	v
List of Figures	vi
List of Acronyms and Abbreviations	ix
Acknowledgements	x
1 Introduction	1
1.1 Review of previous work	2
1.2 Research Objectives and Approach	9
2 The MAP (Wipptal) Field Study	11
2.1 Geographical Setting	11
2.2 Instrumentation	12
2.2.1 Doppler Lidar	13
2.2.2 Tethered Balloon	16
2.2.3 Surface Weather Stations	17
2.2.4 Hobo Temperature Loggers	18
2.2.5 Radiation Site	18
2.3 Synoptic and Local Conditions	18
3 Observations of Valley Flows in the Wipptal	23
3.1 Surface Observations	23
3.2 Doppler Lidar Observations	32
3.2.1 Along-valley Structure and Evolution	35
3.2.2 Cross-valley Flow Structure	46
3.2.3 Backscatter Intensity Analysis	49
3.3 Summary	60
4 Mass (Volume) Budget, Vertical Motion and the Role of Topography	62
4.1 Mass (Volume) Budget and Vertical Motion	62
4.1.1 Analysis	63
4.1.2 Results	68
4.2 The Role of Topography as Seen Through TAF	74

5	Numerical Study of Valley Flow in the Wipptal	78
5.1	Description of Numerical Model	78
5.2	Numerical Set-up and Experimental Design	79
5.3	Numerical Experiment REF: Reference Simulation	82
5.3.1	General Results	82
5.3.2	Comparison to Observations	91
5.3.3	Analysis of the Momentum and Heat Budgets	93
5.4	Numerical Experiments T1 through T4: Sensitivity to Terrain	102
5.5	Summary	111
6	Comparison to Other Studies	112
7	Summary and Recommendations for Future Research	118
7.1	Summary	118
7.2	Suggestions for Future Research	119
7.3	Thoughts on Scanning Strategies	120
	Bibliography	121
A	Determination of Surface Energy Fluxes	129
B	Calibration of Tethered Balloon Data	132
C	Hobo Temperature Measurements	135
D	Terrain Removal Algorithm	137
E	Pre-processing of RHI Scans	142
F	Composite Wind Profiles for 11 October	143
G	VAD Analysis	145
H	On Analysing Backscatter Intensity Fields	151

List of Tables

2.1	Description of Doppler lidar scans performed for this study.	16
2.2	Description of tethered balloon flights.	17
2.3	Description of surface weather stations.	18
2.4	Location of Hobo temperature loggers.	19
2.5	Summary of local ambient conditions during the study period.	21
3.1	Dreiseitl's valley wind criteria applied to various surface weather stations.	25
3.2	Surface up-valley flow characteristics at various weather stations.	28
3.3	Categorization of ambient wind conditions.	35
4.1	Values for the weighting factor F	67
4.2	Mean vertical velocities over the valley segment bounded by range gates RG5DV and RG5UV.	70
4.3	Volume flux and volume flux density at two range gates for all study days.	74
4.4	Wind speed and direction at mountain top height for Innsbruck Airport.	74
5.1	Summary of numerical experiments.	82
A.1	Site-specific surface parameters used in radiation scheme.	129
B.1	Regression coefficients for tether sondes.	133

List of Figures

1.1	Diurnal cycle of slope and valley flows in an idealized valley.	4
2.1	Topographic map of Northern Tirol with relevant geographical locations.	12
2.2	Along- and cross-valley profiles of the Wipptal.	13
2.3	Map of study area showing measurement sites.	14
2.4	Observation times for both Doppler lidar and tethered balloon.	15
2.5	Geopotential heights and temperature at 500 mbar over central Europe during the study period.	20
3.1	Surface measurements at station S105 for 13 October.	26
3.2	Sea-level pressure at Kufstein and Innsbruck during the study period.	27
3.3	Surface wind speed and direction at station S110 for 17 October.	29
3.4	Surface wind speed and direction for stations S106 and S107 on 17 October.	30
3.5	Difference in surface wind speed between stations S107 and S106.	31
3.6	Schematic diagram showing the effect of inclined flow on radial velocity measurements.	33
3.7	Topographic map of the Wipptal showing locations of the RHI scans.	34
3.8	Pseudo-RHI cross-sections for 11 October.	37
3.9	RHI cross-sections for 13 October.	39
3.10	VAD scans for 13 October.	41
3.11	RHI cross-sections for 14 October.	42
3.12	Lidar-derived wind profiles for 14 October.	42
3.13	RHI cross-sections for 16 October.	44
3.14	Lidar-derived wind profiles for 16 October.	45
3.15	RHI cross-sections for 17 October.	46
3.16	Lidar-derived wind profiles for 17 October.	47
3.17	VAD scans at 15° elevation for 16 and 17 October.	48
3.18	Example of radial velocities as a function of cross-valley distance.	49
3.19	Example of backscatter and radial wind profiles.	51
3.20	Radiosonde and tethered balloon potential temperature soundings for 17 October.	52
3.21	Fitted idealized curve for backscatter intensity calculated by detection algorithm.	53
3.22	Along-valley MAL height and transition zone thickness superimposed on RHI flow fields for 17 October.	53
3.23	Observed and fitted backscatter intensity profiles for 13 October.	54
3.24	Vertical profiles of specific humidity for 13 October.	55
3.25	Along-valley MAL height and transition zone thickness superimposed on RHI flow fields for 14 October.	56
3.26	Observed and fitted backscatter intensity profiles for 14 October.	57

3.27	Vertical profiles of potential temperature and specific humidity for 14 October. . .	57
3.28	Along-valley MAL height and transition zone thickness superimposed on RHI flow fields for 16 October.	58
3.29	Observed and fitted backscatter profiles for 16 October.	59
4.1	Schematic representation of the volume flux budget for a valley segment.	63
4.2	Examples of wind profile extrapolations to the surface.	64
4.3	Map of study area detailing orientation and width of cross-sections used in the volume flux analysis.	65
4.4	Cross-sectional area as a function of along-valley distance.	66
4.5	Normalized along-valley wind data as a function of cross-valley position.	68
4.6	Along-valley volume flux as a function of along-valley distance for 13 October. . .	70
4.7	Along-valley volume flux as a function of along-valley distance for 17 October. . .	71
4.8	Along-valley volume flux density as a function of along-valley distance for 13 October.	72
4.9	Along-valley volume flux density as a function of along-valley distance for 17 October.	73
4.10	Topographic map of the Wipptal catchment area showing valley segments used in TAF analysis.	76
4.11	Geometric ratios as a function of N-S distance.	77
5.1	Prospective view of computational domain.	80
5.2	Initial potential temperature profile for the reference simulation REF and rawin- sonde sounding for 11 October 1999.	82
5.3	Modeled net radiation and surface sensible heat flux for simulation REF.	83
5.4	Spatial variation of the modeled surface sensible heat flux for simulation REF. . .	84
5.5	Simulated near-surface winds in the Wipptal for numerical experiment REF. . . .	85
5.6	Location of observed and modeled RHI scans.	86
5.7	Modeled RHI cross-sections of the along-valley wind component for REF.	87
5.8	Vertical profiles of the modeled along-valley wind component at two locations (REF).	88
5.9	Cross-sections of potential temperature contours and wind vectors along the cen- ter of the Wipptal for simulation REF.	90
5.10	Modeled and observed RHI cross-sections of the along-valley wind component. . .	92
5.11	Vertical wind profiles at two locations in the Wipptal from numerical experiment REF and from observations obtained on 16 and 17 October.	93
5.12	Grid points used in momentum and heat budget analysis.	94
5.13	Heat and momentum budgets for 0900-1000 UTC as a function of along-valley distance for simulation REF.	97
5.14	Heat and momentum budgets for 1100-1200 UTC as a function of along-valley distance for simulation REF.	98
5.15	Heat and momentum budgets for 1300-1400 UTC as a function of along-valley distance for simulation REF.	99
5.16	Heat and momentum budgets for 1500-1600 UTC as a function of along-valley distance for simulation REF.	100

5.17	Volume-averaged along-valley potential temperature and wind speed as a function of along-valley distance for simulation REF.	101
5.18	Modified topographies for simulations T1, T2, T3 and T4.	103
5.19	Modeled near-surface winds at 1200 UTC for simulations REF, T1, T2, T3 and T4.	104
5.20	Modeled RHI images of the along-valley wind component at 1200 UTC for simulations REF, T1, T2, T3 and T4.	105
5.21	Along-valley momentum budget for 1100-1200 UTC as a function of along-valley distance for simulation T1.	106
5.22	Along-valley momentum budget for 1100-1200 UTC as a function of along-valley distance for simulation T1.	107
5.23	Along-valley momentum budget for 1100-1200 UTC as a function of along-valley distance for simulation T3.	108
5.24	Along-valley momentum budget for 1100-1200 UTC as a function of along-valley distance for simulation T4.	109
5.25	Valley geometric ratio A/V as a function of along-valley distance for topographies used in numerical experiments.	110
6.1	Schematic representation of the effects of side valleys on the mass budget of segments of the main valley.	113
6.2	Car traverse along the Inntal.	114
6.3	Map of the Kali Gandaki Valley.	116
6.4	Modelled isentropes and wind in a section along the Kali Gandaki Valley.	117
A.1	Surface energy budget for station S999.	131
B.1	Linear regression plots for tether sondes.	133
C.1	Pseudo-vertical Hobo temperature profiles for 14, 16 and 17 October.	136
D.1	Two individual Doppler lidar beams showing backscatter intensity.	138
D.2	Schematic of backscatter intensity return signal for different terrain hits.	139
D.3	Lidar scan showing backscatter intensity before and after terrain removal.	141
F.1	Composite profiles of the along-valley wind component for 11 October.	144
G.1	Wind speed and direction for 11 October.	146
G.2	Wind speed and direction for 13 October.	147
G.3	Wind speed and direction for 14 October.	148
G.4	Wind speed and direction for 16 October.	149
G.5	Wind speed and direction for 17 October.	150

List of Acronyms and Abbreviations

AGL	above ground level
ASL	above sea level
LIDAR	Light Detection and Ranging
NOAA	National Oceanic and Atmospheric Administration
MAL	mixed aerosol layer
MAP	Mesoscale Alpine Programme
MAP-SOP	Mesoscale Alpine Programme - Special Observation Period
PGF	pressure-gradient force
PPI	plan position indicator
PRF	pulse repetition frequency
RAMS	Regional Atmospheric Modeling System
RANS	Reynolds-Averaged Navier-Stokes
RG	range gate
RGxxDV	range gate xx down-valley from lidar
RGxxUV	range gate xx up-valley from lidar
RHI	range height indicator
TAF	topographic amplification factor
VAD	velocity azimuth display

Acknowledgements

This study would not have been possible without the support and contributions of many people and institutions.

First of all, I would like to express my deepest gratitude to my family and friends, who over the years - and especially in the final months - have rallied behind me and given me the moral support and encouragement to bring this project to its completion. It is to them that I dedicate this work.

I would like to express my sincerest thanks to my research supervisor Douw Steyn who provided financial and intellectual support of my research, and gave me with the opportunity to participate in the MAP field study in Austria. I also thank my research committee Ian McKendry, Tim Oke and Roland Stull, the university examiners Greg Lawrence and Rich Pawlowicz, and the external examiner Bill Neff for providing useful suggestions to improve this document.

Many individuals contributed to the success of this field study. I am indebted to Bob Banta and Michael Hardesty at the NOAA Environmental Technology Laboratory who consented to the dual use of the lidar during MAP, and to Richard Marchbanks, Janet Intrieri and Lisa Darby for operating the lidar when everyone else was sightseeing. Lisa Darby also assisted greatly in my initial forays with Doppler lidar data. Peter and Chris Jackson helped immensely with the tethered balloon logistics. Ekkehart Dreiseitl kindly provided the power generator. I thank Georg Mayr for his organizational efforts of the MAP field campaign in the Brenner Pass area, and Roland Mayr for his assistance in locating a spot for the tethered balloon. The following people provided MAP data: Dave Whiteman kindly made available the Hobo temperature measurements; Stephen Mobbs provided surface weather station data; and Roland Mayr provided the radiation measurements. Land Tirol provided the high resolution digital terrain data used throughout this study.

All numerical simulations were performed on the linux cluster in the Department of Physics and on the Monster Super Cluster at the Geophysical Disaster Computational Fluid Dynamics Centre in the Faculty of Science, both at the University of British Columbia. I am very grateful to Matt Choptuik and Henryk Modzelewski for their computing expertise and support in using these clusters.

Many thanks go to Alberto Martilli who was extremely generous with his time and knowledge in helping me with the numerical modeling. He endured many questions and often provided a sounding board for my ideas. I am also grateful for the helpful discussions - research related and otherwise - I have had with Dave Whiteman, Mathias Rotach, Peter Jackson, Craig Clements, Ian Okabe, Bruce Ainslie, Pascal Haegeli, Bob Wilson, Ali Mountz and Nora Sleumer. I thank Rolf Hertenstein and Greg Poulus for providing the tendency extraction code. Stephan DeWekker graciously provided a compiled version of RAMS.

I wish to thank the following organizations who funded this work: The Natural Science and Engineering Research Council of Canada (NSERC) provided two years of support through a postgraduate scholarship. The University of British Columbia (UBC) offered one year of

support via its University Graduate Fellowship. The UBC Geography Department provided personal funding through several teaching assistantships. NSERC grants to Douw Steyn supported several research assistantships, covered partial costs of involvement in the MAP-Wipptal field study, covered computing and day-to-day research costs and funded several conference visits and workshops. The author also received partial travelling funds from NOAA/ETL.

Lastly, but most importantly, I thank Gord Betenia for his love and encouragement, and for keeping laughter in my life.

We shall not cease from exploration
And the end of all our exploring
Will be to arrive where we started
And know the place for the first time.

Little Gidding V,
Four Quartets.
T.S. Eliot (1943)

Chapter 1

Introduction

The earth's orography is responsible for a myriad of meteorological flows which we typically categorize as either mechanical or thermal in nature. While mechanically induced flows - such as gap winds or down-slope wind storms - are famous for their dramatic effects, it is the gentler thermally-driven flows which are prevalent over much of the year (Blumen, 1990) and hence regularly influence near-surface airflow characteristics in mountainous terrain. These flows play an important role in environmental issues of human habitation and activity in mountainous terrain, such as forest fire control, thunderstorm and precipitation initiation, wind energy potential, agriculture and anthropogenic pollutant transport (Furger et al., 2000).

Thermally-driven wind systems in mountain valleys have been studied for many years, giving us a basic understanding of the evolution and mechanisms of valley flows. And while some efforts have been directed towards understanding the role of topography (e.g. Steinacker, 1984; McKee and O'Neal, 1989), a direct link between topographical relief and valley flow characteristics still eludes us. This is no doubt due to the overwhelming complexity of mountainous terrain and interactions of thermally-driven flows at different scales, points emphasized by Vergeiner and Dreiseitl (1987) and Whiteman (1990). In addition, however, very few observations have been available to examine the spatial structure of valley flows, a necessary step if one wants to make assertions about topographical influences. The lack of observations have been largely due to the difficulty of capturing spatial flow characteristics in complex terrain with conventional *in-situ* instrumentation. This is particularly true for daytime flows which tend to be much deeper than their nighttime counterparts (Whiteman, 1995). Lastly, no attempts have been made to integrate observations from different valleys in order to elucidate the effects of topography. It seems that the flow in each valley - although assumed to be governed by the same processes - is considered unique.

This dissertation is an investigation of daytime thermally-driven flows in an alpine valley. Specifically, it investigates the along-valley structure of the flow, and how it relates to the topographical relief of the valley. The premise of this work is that topographical relief forms, no matter how seemingly unique, share common characteristics or effects on valley flows. This dissertation is a small step towards understanding the link between topography and valley flow characteristics.

The remainder of this introductory chapter reviews previous work on thermally-driven wind systems in mountainous terrain (section 1.1), and concludes with the research approach and

objectives of this dissertation (section 1.2).

1.1 Review of previous work

Although scientific research on thermally-driven wind systems in valleys first emerged in the early nineteenth century, this review begins with work published by A. Wagner and E. Ekhart in the 1930's and 1940's (e.g. Wagner, 1932a, 1932b, 1932c, 1938; Ekhart, 1944, 1948). By integrating theoretical concepts from the past with vast observational results by their contemporary co-workers - such as Jelinek, Moll, Everdingen and Riedel, just to mention a few - as well as their own aerological investigations, Wagner and Ekhart developed a conceptual model of valley flow systems which for the most part is still considered valid today. It was also in this period that the distinction between valley and slope winds¹ was first made. Generally speaking, valley winds flow along the axis of a valley while slope winds blow parallel to the incline of a mountain slope or valley sidewall. The prefixes 'up' or 'down' denote the direction of the flow. Historically-minded readers are referred to Hawkes (1947) who provides an insightful account of developments and disputes of valley wind theory prior to the 1930's.

Following the 1940's, interest and research on thermally-driven valley wind systems waned (Vergeiner and Dreiseitl, 1987), but resurged in the late 1970's and 1980's. A substantial number of field experiments were conducted during that period. Some of the major ones include the HAngWindExperiment Innsbruck (HAWEI) in 1978 which focused on the slope wind system and its role on the thermal structure of the valley's atmosphere; the DISchmatal KlimaUnter-Suchungen (DISKUS) in 1980 which took place in a medium-sized, idealized end valley (Freytag and Hennemuth, 1981); the 1982 Mesoskaliges Experiment im Raum Kufstein/Rosenheim (MERKUR) in which measurements along a major, deep Alpine valley were obtained (Freytag, 1983); and the Atmospheric Studies in Complex Terrain (ASCOT) programme which, over a period of several years (1979-1984, 1988), examined drainage flows in a number of valleys in California and Colorado (e.g. Clements et al., 1989). More recently, field studies such as VOTALP (Vertical Ozone Transport in the ALPs) (Wotawa and Gromp-Kolb, 2000) have concentrated on pollutant transport over mountainous terrain. Finally, boundary-layer processes in an alpine valley were investigated as part of the MAP (Mesoscale Alpine Programme) field campaign in 1999 (Rotach, 2000). The field studies mentioned above are just a small subset of the studies that have been conducted. A more comprehensive list of field experiments as well as an excellent summary of observational findings is provided by Whiteman (1990). Other comprehensive reviews of field studies and concepts on thermally-driven wind systems over mountainous terrain can be found in Atkinson (1981), Sturman (1987), Vergeiner and Dreiseitl (1987), Barry (1992) and Whiteman (2000).

¹In this study, the terms valley and slope winds are used. Alternative terminologies which have been used in the literature for local wind systems in mountainous terrain are listed in Whiteman (1990).

The valley wind theory developed by Wagner and Ekhart was schematically summarized by Defant (1949) (shown in Figure 1.1) and is briefly described here. The diurnal cycle begins at sunrise (a). As air adjacent to the sunlit valley sidewalls begins to warm, up-slope flows form over the slopes. The valley air, however, is still colder than the atmosphere over the plain, and thus a valley wind continues to blow down-valley. Air removed from the valley by up-slope flows is replaced with warmer air from above. This effect, together with direct heating of the valley air itself, causes the valley atmosphere to warm and therefore the pressure to decrease. At some point, pressure in the valley is equal to pressure over the plain and down-valley flow ceases to exist (b). As the valley air is further warmed, a pressure drop from the plain to the valley develops and an up-valley flow forms (c), increasing in intensity as the pressure difference increases. In the late afternoon, the slopes become shaded and up-slope flows cease to blow (d). The up-valley flow persists as the valley air is still warmer than the air over the plain. As the slopes cool radiatively, they eventually become colder than the valley atmosphere and down-slope winds develop (e). Upward motion in the valley center and radiative emission as a whole work together to continually cool the valley air until the pressure in the valley is again equalized with the pressure over the plain. At this point, up-valley flows cease (f). As cooling continues, the pressure gradient as well as the valley flow reverses (g). This situation continues until the morning, when the rising sun causes the slopes to warm and the down-slope flows to cease (g) and the cycle begins anew (a).

Defant's scheme, of course, is only an idealized representation of valley flows. It does not take into account synoptic or topographic influences. For example, asymmetrical heating of valley sidewalls due to valley orientation and slope exposure can cause lags between the onset of slope winds on both sides and produce cross-valley winds (Urfer-Henneberger, 1970). The scheme also emphasizes the preceding development of slope flows to valley flows, while some investigations (particularly in smaller valleys) demonstrate almost concurrent development of slope and valley winds (e.g. Urfer-Henneberger, 1970; Buettner and Thyer, 1966). The time lag of the valley wind system depends on the size of the valley (Vergeiner, 1983).

Whiteman (1982) extended the valley wind theory by elucidating the close relationship between the evolution of winds and the thermal structure of the atmosphere in a valley. In his studies, Whiteman (1982) often found a convective boundary layer (CBL) throughout the whole valley atmosphere. In other studies, however, the valley CBL is either very shallow (e.g. Brehm and Freytag, 1982; Kuwagata and Kimura, 1995; Furger et al., 2000; De Wekker, 2002) or nonexistent (Freytag, 1985). The conceptual model by Whiteman (1982) emphasizes the role of slope flows in distributing heating at the sidewalls to the rest of the valley atmosphere through compensating subsidence motion. It should be noted, however, that this concept is based on local compensation (i.e. when the valley wind has not yet developed), and it is unclear what role slope flows serve (if in fact they are developed) when the valley flow is in full swing.

Theoretically, the valley wind system represents the lower branch of a circulation that exists

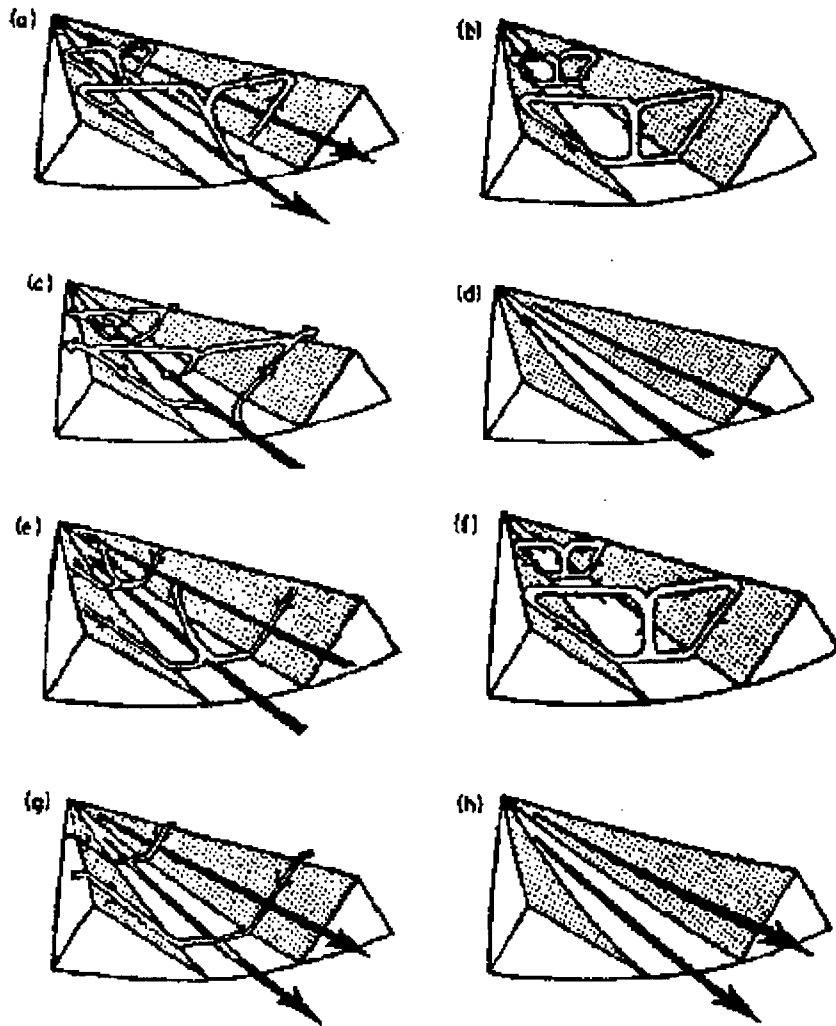


Figure 1.1: Diurnal cycle of slope and valley flows in an idealized valley. Explanation is given in the text.
(Adopted from Defant (1949).)

between mountain and plain while the anti-wind represents the upper or return branch of the circulation (Whiteman, 1990). Anti-winds, however, are very difficult to observe and interpret since compensatory currents above ridgelines are not restricted to the valley atmosphere, and may therefore be quite weak or easily masked by larger synoptic-type flows. Some studies have observed anti-winds (Buettner and Thyer, 1966; Vergeiner, 1983; Reiter et al., 1984) while others have not or are cautious about their interpretations (Egger et al., 2000; Hennemuth and Schmidt, 1985; Kuwagata and Kimura, 1995; Reiter et al., 1983; Freytag, 1988).

Both the slope and valley wind systems are baroclinic flow phenomena. Slope winds form when a layer of air adjacent to the slope is warmed or cooled relative to the ambient air at the same level away from the slope. Similarly, valley winds form as a result of horizontal temperature gradients. The valley atmosphere experiences larger diurnal temperature amplitudes than the atmosphere over the plain (e.g. Nickus and Vergeiner, 1984; Freytag, 1985). The differing diurnal temperature ranges produce a diurnally varying horizontal pressure gradient that causes the wind to blow up-valley during daytime and down-valley during nighttime. Typical values of the horizontal pressure gradients in valleys are 1.4-2.1 mb/100 km (Vergeiner and Dreiseitl, 1987; Hennemuth and Schmidt, 1985; Freytag, 1988), although Freytag (1988) observed a pressure gradient of 5 mb/100 km during nighttime near the mouth of the Inntal.

Wagner (1932a) first tried to attribute the diurnal temperature variation between valley and plain to the volume effect. The volume effect can be formally expressed by combining the first and second laws of thermodynamics, which provides the following equation

$$d\theta = \frac{dq}{\rho c_p V (T/\theta)}. \quad (1.1)$$

where $d\theta$ [K] is the potential temperature change in a volume of air V [m^3] with density ρ [$kg\ m^{-3}$], c_p [$J\ kg^{-1}\ K^{-1}$] is the specific heat, and dq [J] is a given heat input. The ratio of actual temperature to potential temperature, (T/θ) , is approximately unity. Equation 1.1 states that for a given heat input, the potential temperature change is inversely proportional to the volume of air being heated or cooled. Without loss of generality, the heat input dq may be written as $dq = Q_s A dt$ where Q_s is the sensible heat flux [Wm^2], A is the surface area [m^2] and dt is some time interval [s]. The surface area, A , is generally approximated by the horizontal area A_{xy} at the top of the volume (e.g. Steinacker, 1984; Vergeiner and Dreiseitl, 1987; McKee and O'Neal, 1989). The ratio of diurnal temperature range between valley and plain for some time interval can then be written as

$$\frac{d\theta_{valley}}{d\theta_{plain}} = \frac{\left[\frac{A_{xy_{valley}}(h)}{V_{valley}} \right]}{\left[\frac{A_{xy_{plain}}(h)}{V_{plain}} \right]} \quad (1.2)$$

where $A_{xy}(h)$ is the horizontal area through which energy enters the tops of the volumes at height $z = h$ and V is the volume of air to be heated. By using cross-sections with unit

thickness, the ratio can also be expressed as

$$\frac{d\theta_{valley}}{d\theta_{plain}} = \frac{\left[\frac{W_{valley}}{A_{yz_{valley}}} \right]}{\left[\frac{W_{plain}}{A_{yz_{plain}}} \right]} \quad (1.3)$$

where W is the width at the top of the respective cross-sections, and A_{yz} is the area of the vertical cross-section. The term topographic amplification factor or TAF was later coined by Müller and Whiteman (1988) for the ratios given in Equations 1.2 and 1.3.

By choosing equal reference areas or widths over the valley and plain, the ratios given in Equation 1.2 or 1.3 further simplify as

$$\frac{d\theta_{valley}}{d\theta_{plain}} = \frac{V_{plain}}{V_{valley}} = \frac{A_{yz_{plain}}}{A_{yz_{valley}}}. \quad (1.4)$$

This is what Wagner (1932a) had in mind. However, his calculations based on an idealized U-shaped valley cross-section could not account for the observed magnitude of the temperature ratio between valley and plain using topographical arguments alone (2.2 vs 1.4), never mind that dynamic effects were not yet included. This discrepancy was again echoed by Brehm and Freytag (1982).

To rectify this problem, Steinacker (1984) proposed that it was not the geometric valley cross-section but rather the area-height distribution that was the determining factor. His concept rested on the notion that sidevalleys and higher lying plateaus provide much heating area with little volume to be heated, and that this heating is imparted to the main valley through thermally-direct circulations much in the same way that slope flows heat the valley atmosphere. By considering a portion of the Inntal around Innsbruck along with the entire catchment area of the Wipptal, Steinacker was able to obtain a volume ratio of 2.1, in much better agreement with the observed 2.2. Steinacker (1984) also considered the effects of temperature stratification on the geometrically induced horizontal pressure gradient, but this concept remains to be explored further (Whiteman, 1990).

There are several weaknesses with the area-height relationship proposed by Steinacker (1984). Although it circumvents the difficulty of quantifying valley cross-sections where tributaries intersect the main valley, it is not clear which portion of the main valley would be affected by a sidevalley. And while there is some evidence to suggest that flow into tributaries causes subsidence and therefore warming in the main valley (Brehm, 1986), the effect of tributary flow on the thermodynamics and dynamics in the main valley still needs to be investigated. Tributary flows were studied during ASCOT (Coulter et al., 1989; Porch et al., 1989), but only for the nocturnal case. The concept that heating from the terrain as a whole makes its way from small-scale flows (slope flows) to progressively larger-scale flows (i.e. from slopes to valley cross section and from side valleys and alpine meadows to the main valley and large basins) seems a logical explanation for a mountain range as a whole, but the idea that heating takes place as

part of a closed circulation in a catchment area is rather optimistic. Observations presented in this study do not support this concept.

Up to this point, it has been assumed that valley flows are driven by a pressure gradient that develops between valley and plain. Work by McKee and O'Neal (1989) showed that variations in valley geometry along the valley's length could also produce intra-valley pressure gradients that drive valley winds, and that calculations of TAF ratios along a valley could be used to determine whether the valley was draining or pooling. This initial success by McKee and O'Neal (1989) suggested that the TAF concept could be used as a simple framework for evaluating relative strengths of valley wind systems (Whiteman, 1990). TAF, however, is only a geometric measure of the valley's topography. It does not take into account atmospheric dynamics (such as advection, thermal structure, ambient winds) or changes in surface properties (orientation and inclination of surfaces, soil moisture, albedo, etc) which in turn can alter the sensible heat input into the valley atmosphere.

The along-valley structure of valley wind systems and how it relates to topography has not received much research attention. For the daytime case, thus far, invariant wind speeds with along-valley distance (which indicates along-valley mass/volume flux convergence) have been observed in mid-sized tributary or end-valleys (Buettner and Thyer, 1966; Hennemuth, 1987; Prévôt et al., 1998) while observations in the Inntal - a major Alpine valley - show an increase in wind speed with up-valley distance (or along-valley volume flux divergence) (Freytag, 1987). Along-valley volume flux divergence has also been observed for nocturnal flows (e.g. Rao, 1968; Post and Neff, 1986; Freytag, 1987). As pointed out by Freytag (1988), however, the valley mass budget for the nighttime case is fundamentally different from that of the daytime case. For the nighttime situation, slope and tributary flows into the main valley contribute to the along-valley volume flux divergence, while for the daytime case, slope and tributary flows contribute to along-valley volume flux convergence. It is with this picture in mind that the along-valley volume flux divergence in the Inntal appears as an unusual result (Freytag, 1987; Whiteman, 1990).

Although valley wind systems are thermally-induced, external influences are almost always present. Vergeiner and Dreiseitl (1987) note that

“... during the four years of our valley wind project (1978-1982) we were unable to find a case as ‘nice’ and undisturbed as our ‘ideal’ one during preliminary testing in 1977 ...”

Climatological studies by Dreiseitl et al. (1980) and Vergeiner (1983) show that valley wind days and weak-gradient days are not necessarily the same. The level of influence of ambient flows on thermally-driven wind systems depends on the topography, the temperature structure aloft and the strength of ambient winds. Several observations have shown that once the protecting stable nocturnal region is eroded by convective mixing, upper level flows are able to mix down-

ward², erasing the local wind system (e.g. Banta, 1984; King, 1997; Clements, 1999). Shallow valleys appear more susceptible to influences of ambient flows than deep valleys (Whiteman, 1990) although observations made during ASCOT indicate that nocturnal drainage flows in deep valleys can be affected by ambient flows as well. Forced channeling occurs when winds blow either up or down the valley's axis, depending on the direction of the geostrophic flow aloft. Pressure-driven channeling occurs when the pressure gradient aloft is stronger than the thermally produced pressure gradient. Winds in the valley are thus driven by the component of the geostrophic pressure gradient along the valley's length (Whiteman and Doran, 1993). Possible effects of pressure-driven channeling along a bent valley were recently examined by Koßmann and Sturman (2003).

In more recent years, studies have investigated the temporal and spatial distributions of atmospheric aerosols over mountainous terrain using lidar (light detection and ranging) data (Carnuth and Trickl, 2000; Nyeki et al., 2000; Savov et al., 2002). It is not yet clear how the aerosol structure relates to the boundary layer structure over mountainous terrain. Lidar backscatter data have been used over flat terrain to infer the convective boundary layer height (Marsik et al., 1995; Hayden et al., 1997; Högeli et al., 2000). Over flat terrain surrounded by mountains (such as the Lower Fraser Valley or the Los Angeles Basin), lidar observations frequently show elevated layer structures (e.g. McElroy and Smith, 1991; McKendry et al., 1997; McKendry and Lundgren, 2000), which are produced by advective processes such as thermally-driven slope flows or mountain venting. It seems reasonable to assume that the same processes are also at work over alpine terrain, but that with the more complex nature of the orography, individual elevated layer structures are no longer distinguishable, but instead merge into step-like aerosol layer structures. Work by De Wekker (2002) confirms this.

Numerous studies of thermally-driven valley wind systems using numerical models can be found in the literature (e.g. Bader and McKee, 1985; Ulrich, 1987; Atkinson and Shahub, 1994; Ramanathan and Srinivasan, 1998; Zängl et al., 2001; De Wekker, 2002; Colette and Street, 2002), although only two studies have examined the effects of different valley geometries on the flow. Li and Atkinson (1999) investigated the dynamical flow characteristics for four differently shaped idealized valley topographies, but concentrated solely on the morning and evening transition periods. Somieski (1987) studied the effects of idealized valley geometries on the strength of day- and night-time valley flow circulations. His results suggest that only in valleys (with level bottoms) for which the mean crest height increases with up-valley distance, can valley flows be found along the length of the valley. Otherwise, the valley flow is limited to the entrance of the valley. Also, the inclusion of tributaries increases the intensity of the wind in the main valley. Comparison of heat budgets for various segments show that heating through cross and vertical advection is larger further up-valley than it is near the valley mouth. In contrast, the effects of cold air advection decreases further up-valley. The cold air advection near

²Whiteman and Doran (1993) refers to this process as downward transport of horizontal momentum.

the entrance of the valley is so large that it causes a pre-mature cooling of the valley atmosphere near the valley mouth. Somieski also conducted a large series of sensitivity experiments which showed that different surface characteristics have significant influence on the wind intensities.

Conceptual models, which deal with valley wind circulations at a more elementary level, have been developed as well (Egger, 1987a, 1987b; Vergeiner and Dreiseitl, 1987; Egger, 1990a). Using such a model, Egger (1990b) studied the linkage of flow in a main valley and the circulation in sidevalleys for the daytime situation. His results suggest that the mass flow into a tributary is balanced mainly by downward motion on top of the main valley. The heating in the main valley associated with this downward motion can induce valley flow in the main valley before the thermal circulation in the main valley penetrates to the mouth of the tributary. Vigorous flow into tributaries occur only if their topographic amplification factors are larger than that of the main valley.

1.2 Research Objectives and Approach

This dissertation is a study of the spatial structure of daytime thermally-driven wind systems in a deep alpine valley, and how this structure is linked to the valley topography. To this end, high spatially- and temporally-resolved observations from a Doppler lidar system are presented of flows in the Wipptal (Wipp Valley), Austria. The Doppler lidar has been used successfully in numerous studies of flow over complex terrain, including sea breezes (Banta et al., 1993), severe surface winds (Clark et al., 1989), nocturnal canyon flows (Banta et al., 1995), wind-flow patterns in the Grand Canyon (Banta et al., 1999), Föhn flow (Darby et al., 2000). The Doppler lidar has also been used to study nocturnal valley flows (Post and Neff, 1986; Banta et al., 1997), but the present study of daytime valley flows using Doppler lidar technology is the first of its kind³.

Measurements for this study were obtained for several days. Instead of concentrating on one 'ideal' case study, all days are included in the analysis. The utilization of all study days provides insight into the day-to-day similarities and differences in the flow characteristics and hence provides information on what characteristics may be induced locally, and which ones are influenced externally. Numerical modeling is then applied to investigate the underlying physical mechanisms and to explore the role of topography.

This research addresses the following research questions:

- What are the spatial and temporal structures of daytime thermally-driven flows in a narrow, deep alpine valley?

³Doppler lidar measurements of up-valley flow during the morning transition period were obtained in the Brush Creek Valley during the ASCOT study (Post and Neff, 1986). However, very little has been published of these observations.

-
- What is the along-valley mass budget and what implications does it have for vertical motion in the valley?
 - What can be learned from lidar backscatter intensity data regarding the aerosol layer structure in alpine valleys?
 - Can the TAF concept be used to predict the along-valley kinematic behaviour of the valley flow?
 - What is the role of topography in the observed structure of the along-valley wind?
 - What role do dynamic processes play in the structure of valley flows?
 - What scanning strategies should be employed for studies of daytime, thermally-driven flows?

The dissertation is organized as follows: In Chapter 2, a description of the field study is given. Chapter 3 then presents observations from various *in-situ* instruments as well as the Doppler lidar measurements. In Chapter 4, an analysis of the along-valley volume budget and its implications for vertical motion is presented, and the role of topography is discussed in terms of TAF. In Chapter 5, the results from numerical modeling are described, and sensitivity analysis pertaining the effects of topographical features are presented. Chapter 6 discusses studies of flows in other valleys in relation to the results presented in this study. Finally, Chapter 7 summarizes the results of this research and provides recommendations for future work.

Chapter 2

The MAP (Wipptal) Field Study

In the fall of 1999, a small field study was carried out in the Wipptal¹ (Wipp Valley), Austria, to investigate daytime thermally-driven wind systems. This study was embedded in the larger scale Mesoscale Alpine Programme (MAP) field campaign - an international research effort aimed to improve knowledge of meteorological and hydrological processes over the Alps. Although the focus of MAP in the Wipptal area was to examine foehn and gap flows, a sequence of fine weather days provided the opportunity to study thermally-driven days while taking advantage of existing instrumentation. A general description of MAP is found in Bougeault et al. (2001).

This chapter describes the geographical setting of the study area, the instrumentation as well as the synoptic and local conditions during the study period.

2.1 Geographical Setting

The Wipptal is a predominantly NNW-SSE oriented valley located in Northern Tirol, Austria (Figure 2.1). It is a major tributary valley of the Inntal, and runs from the city of Innsbruck south to the Brenner Pass (1373 m ASL). The valley is roughly 35 km long, and has an average slope angle of 1.3° . The valley floor consists of agricultural lands interspersed with villages and small patches of forest. A railway and major transportation highway run along the valley. Valley sidewalls are covered with forests (mainly conifers) up to the tree line at about 1800 m ASL. Alpine meadows and bare rock are found above tree line. The Wipptal itself has several tributaries, the largest one being the Stubaital near its entrance.

The portion of valley under study lies roughly within a 6 km radius of the Doppler lidar (Figure 2.1). The topographical features of this valley section are now described in more detail. At the northern terminus of the study domain, approximately 5 km south of the mouth of the Wipptal, the Stubaital branches southwest from the Wipptal. A sharply rising ridgeline that separates the Wipptal from the Stubaital forms a narrow and deep, V-shaped valley. The slopes of the sidewalls in this section are roughly 20° . Further up-valley from the lidar, the Wipptal broadens somewhat before narrowing again at the southern terminus of the study domain (Figure 2.2). The mountain tops surrounding the Wipptal generally reach heights of 2600 to 2800 m ASL. Due to the bends in the Wipptal and the numerous tributaries, it is difficult to objectively determine the effective ridgeline. In the study domain, the lower ridgeline to the

¹'Tal' means 'valley' in German.

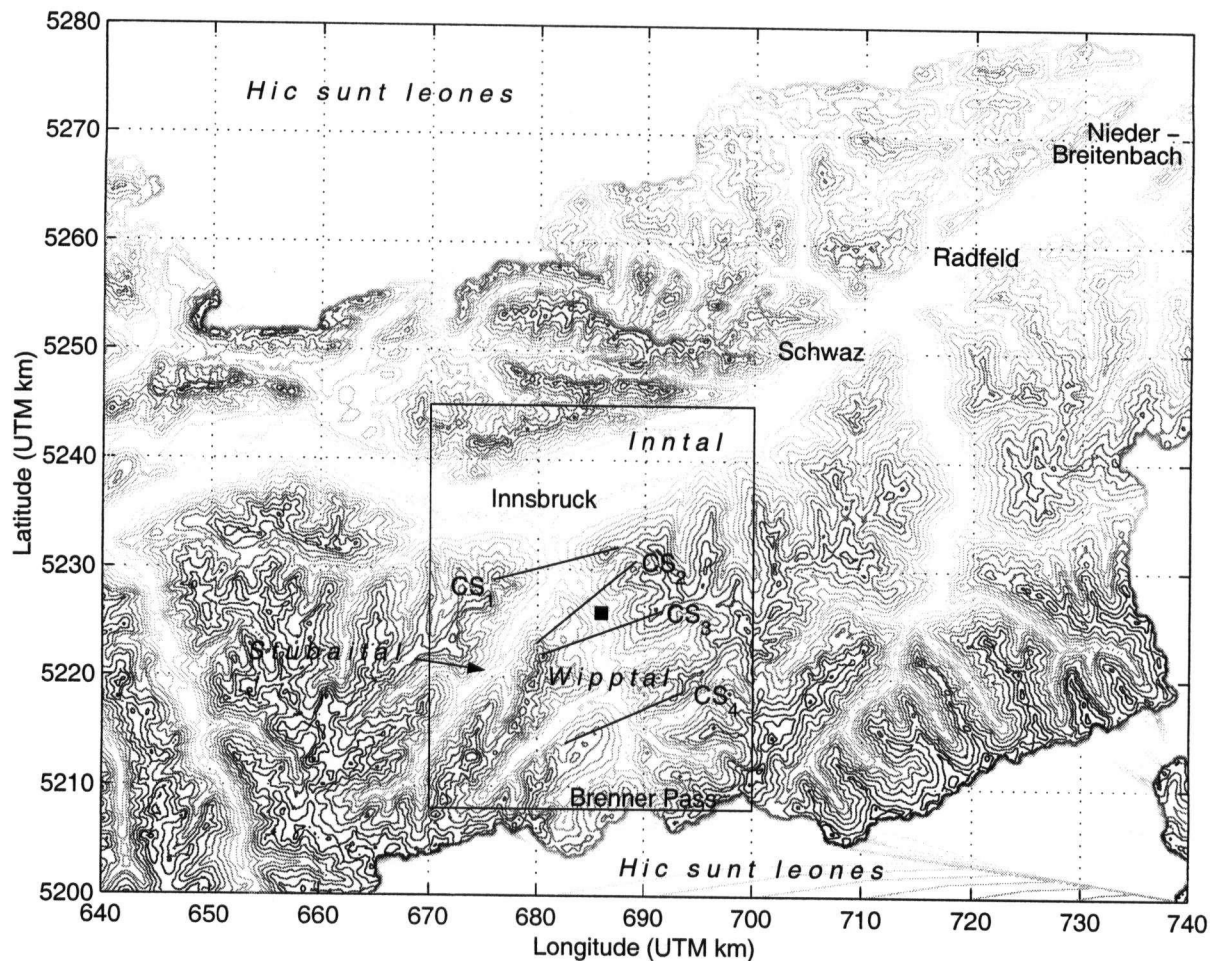


Figure 2.1: Topographic map of Northern Tirol with relevant geographical locations referred to in the main text. The rectangle encompasses the Wipptal area, and is shown in more detail in Figure 2.3. Cross-sectional profiles of the Wipptal indicated by black lines are shown in Figure 2.2. For reference, the location of the Doppler lidar is marked by a solid square. Contour interval is 200 m.

west of the valley is assumed as the effective ridge height.

2.2 Instrumentation

As part of the MAP field study, a number of remote sensing and *in-situ* instruments were deployed in the Wipptal area. Only a subset of the instrumentation, which is relevant to the study at hand, is described in this section. For a complete list and description, the reader is referred to Mayr et al. (2003). Measurement sites are shown in Figure 2.3 and are described in the text that follows. The measuring periods for the lidar and tethered balloon are shown in

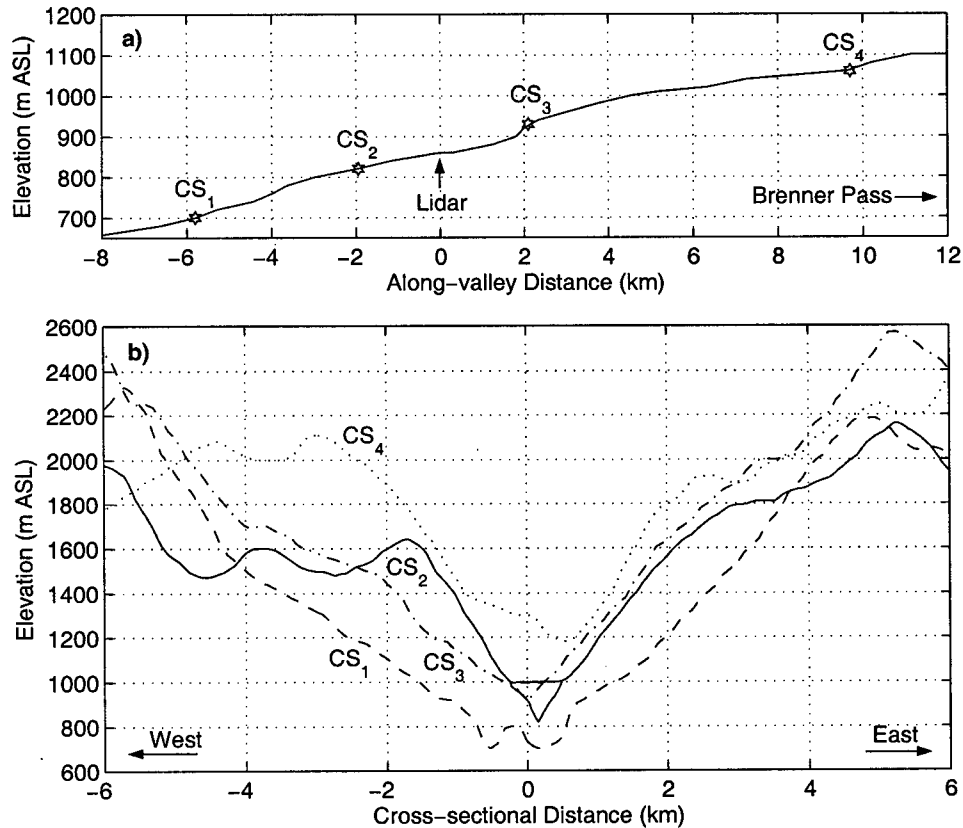


Figure 2.2: a) Along-valley profile of valley bottom showing locations of cross-valley profiles; b) Cross-valley profiles at four different locations indicated in Figure 2.1.

Figure 2.4. It should be noted that lidar measurements on the morning of 14 October were lost due to faulty data recording. Furthermore, tethered balloon measurements are not available for 16 October as flight permissions could not be obtained for that day.

2.2.1 Doppler Lidar

Doppler lidar is an active remote-sensing instrument which transmits short pulses of radiation into the atmosphere and then measures the backscattered energy. While incoherent or backscatter lidars measure only the intensity of returned energy, coherent or Doppler lidars also observe the frequency (or Doppler) shift between the transmitted and received energy pulse. In contrast to radars and sodars, lidar beams are tightly collimated with beam width typically between 10^{-4} to 10^{-3} radians (Stephens, 1993). Because of its narrow beam and absence of sidelobe radiation, a lidar can scan close to the surface without the returned pulse of energy being contaminated by terrain. This particular feature makes the lidar ideally suited for studies of wind over complex terrain.

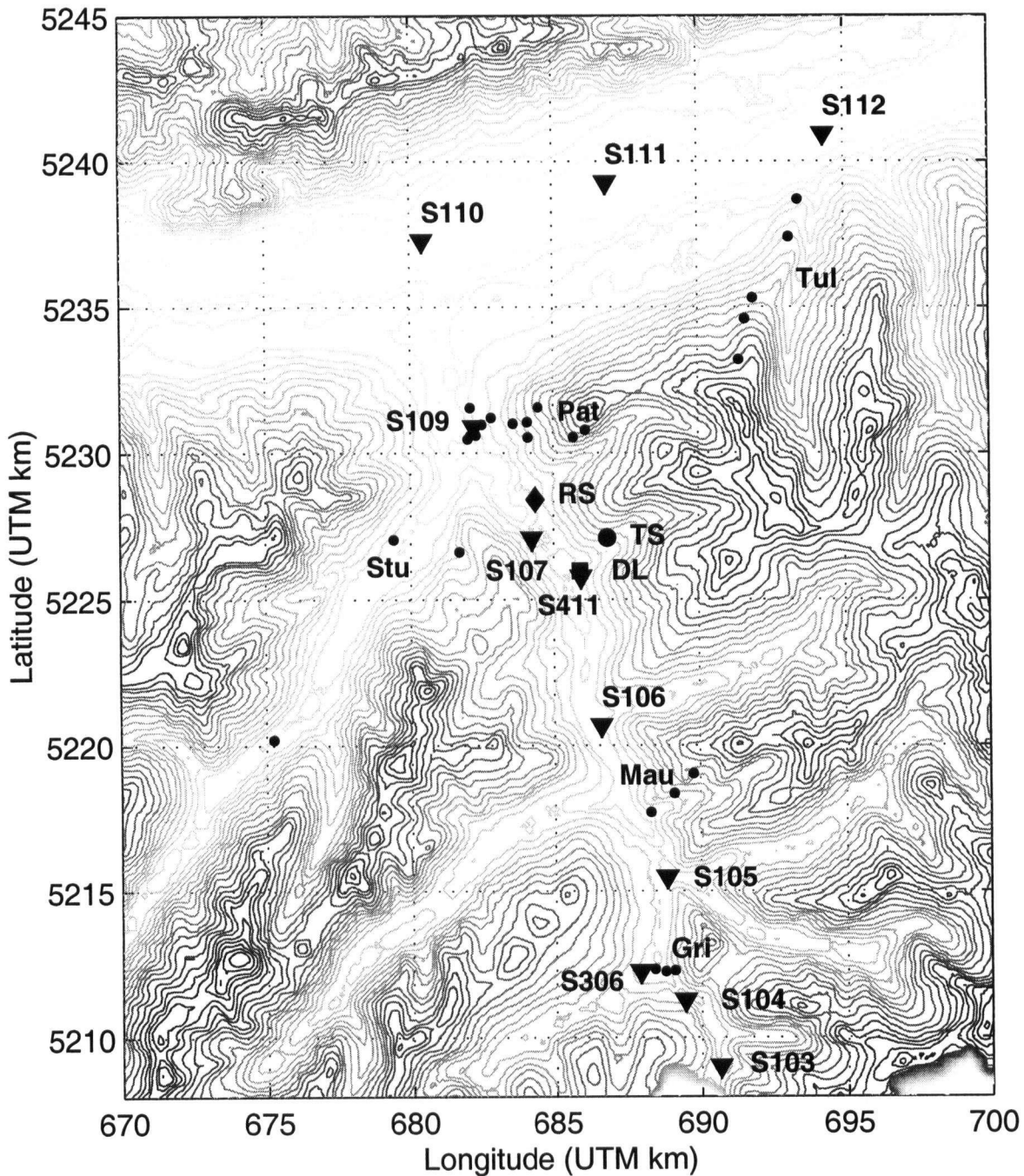


Figure 2.3: Map of study area showing measurement sites reported in the study. Shown are the locations of Doppler lidar (solid square, denoted 'DL'), tethered balloon (solid circle, denoted 'TS') and radiation site (solid diamond, denoted 'RS'). Surface weather stations are marked with solid triangle (listed as 'S***'). Hobo temperature loggers are indicated by solid dots, and their profiling lines are labelled (Tul, Pat, Stu, Mau and Gri). Contour interval is 100 m.

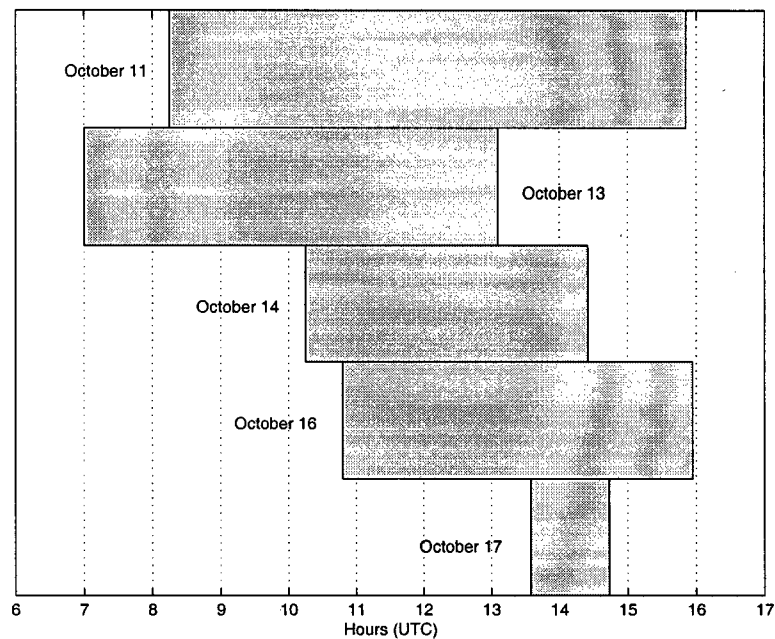


Figure 2.4: Observation times for both Doppler lidar and tethered balloon during the study period.

During the MAP field study, the NOAA/ETL TEACO2 Doppler lidar was deployed in the Wipptal area. Technical details for this Doppler lidar can be found in Post and Cupp (1990). This lidar transmits pulses of eye-safe, coherent infrared light at a wavelength of $10.59 \mu\text{m}$. At this wavelength, attenuation is dominated by water vapour and carbon dioxide absorption while scattering is primarily due to aerosol particles. For typical atmospheric aerosol size distributions, most of the backscattered energy comes from particles about $1 \mu\text{m}$ in diameter (Banta et al., 1992). Particles of this size are excellent tracers of atmospheric motion (Banta et al., 1992), and therefore the radial velocity component (i.e. the component of motion along the axis of the transmitted beam) determined from the Doppler-shifted frequency can be assumed to be that of the wind (Banta et al., 1992). The TEACO2 Doppler lidar has a velocity accuracy of 0.6 m s^{-1} .

The Doppler lidar was located in the Wipptal near the SE entrance of a small tributary valley, Arzthal (5225986 m UTM N, 685910 m UTM E) at an elevation of 1065 m ASL (Figure 2.3). Data from this lidar are generally processed in range gates at 300 m intervals. The minimum range of the lidar is dictated by hardware while the maximum range depends on the strength of the signal which is a function of lidar system parameters and atmospheric conditions. For this study, the minimum range varied between 1.2 and 1.5 km while the maximum range was generally around 7-8 km. A pulse repetition frequency (PRF) of 10 Hz was used during this study. To reduce noise and improve the reliability of the velocity estimates, five pulses were averaged for each velocity estimate, giving an effective PRF of 2 Hz . For a stationary scan, the

Name	Type	θ_{min}	θ_{max}	$\delta\theta$	ϕ_{min}	ϕ_{max}	$\delta\phi$	angular resolution	δt
RHI178	RHI	178.0°	180.0°	0.0°	0.0°	180.0°	@2.0°s ⁻¹	1°	1.5 min
RHI320	RHI	320.0°	322.0°	0.0°	0.0°	180.0°	@2.0°s ⁻¹	1°	1.5 min
VAD1025	Stepped PPI	0.0°	360.0°	@2.0°s ⁻¹	10.0°	25.0°	5.0°	1°	12 min
TPPI13	Stepped PPI	300.0°	75.0°	@4.0°s ⁻¹	0.0°	30.0°	5.0°	2°	5 min
HRVS19	Stepped RHI	19.0°	40.0°	1.0°	13.0°	30.0°	@0.6°s ⁻¹	0.3°	10 min
HRVS29	Stepped RHI	29.0°	40.0°	1.0°	13.0°	25.0°	@1.0°s ⁻¹	0.5°	10 min
HRVS51	Stepped RHI	40.0°	51.0°	1.0°	13.0°	25.0°	@1.0°s ⁻¹	0.5°	10 min
TRHI39	RHI	39.0°	39.0°	0.0°	13.0°	41.0°	@0.4°s ⁻¹	0.2°	variable
STRTB	Stare scan	-	-	-	-	-	-	-	variable

Table 2.1: Description of Doppler lidar scans performed for this study. θ refers to the azimuth angle from north, and ϕ is the elevation angle from horizontal. $\delta\theta$ and $\delta\phi$ indicate either the step increment or the scanning rate (when preceded by '@'). The column labeled 'angular resolution' refers to the angle covered by each beam. δt is the time required in minutes to complete one scanning sequence.

sampling volume of a range gate is pencil-like (ie long and narrow). For moving scans, however, the sampling volume is larger and depends on the effective PRF and the scanning rate.

A number of different scans were performed in rotation during the study. Details of the scans are provided in Table 2.1. RHI178 and RHI320 refer to vertical (RHI) scans along the valley axis in the up- and down-valley direction, respectively. The conical VAD1025 scans provide general flow information while the TPPI13 (partial VAD scans) and HRVS** (high resolution volume scans) scans provide detailed information of the flow structure in the vicinity of the valley sidewall. TRHI39 scans were coordinated with tethersonde ascents, while stare scans (STRTB) were performed while the tethered balloon was stationary at certain heights.

Post-processing of Doppler lidar data includes the flagging and extraction of terrain contaminated range gates (Appendix D), as well as the removal of range gates with weak return signal. The return signal cut-off varied from day-to-day, and was determined subjectively.

2.2.2 Tethered Balloon

A tethered balloon was operated from a grassy field on the slopes of a small tributary valley (Arztal) (Figure 2.3) at an elevation of 1400 m ASL. The location of the tethered balloon (686860 m UTM E, 5227111 m UTM N) was approximately 1.5 km from the lidar and therefore within the volume scanned by the lidar. Vertical profiles of wind speed and direction, temperature and relative humidity were obtained with an Atmospheric Instrumentation Research Inc. (AIR) Tethersonde (Model TS-3A-SPH). Measurements were recorded as 10 second averages. Tethersonde flights were made approximately every hour and were coordinated with lidar scans. Ascents occurred in one of two ways: continuously at an ascent rate of about $1 m s^{-1}$ ('CONT'), or in steps whereby the tethered balloon remained at a constant height for several minutes ('STEP'). The time required for an ascent ranged between 15 and 20 minutes for continuous ascents, and between 30 and 40 minutes for step ascents. For all flights, with the exception of 'MINI' flights which were performed while waiting for the lidar to finish its scanning sequence,

Date	Flight Number	Flight Type	Start	Start Ascent	Top	Finish Ascent	Finish
11 Oct	1	CONT	0816	0822	0839	0837	0857
	2	STEP	0916	0918	0948	1007	1017
	3	CONT	1018	1020	1037	1058	1109
	4	STEP	1121	1123	1158	1217	1218
	5	CONT	1219	1230	1245	1302	1305
	6	MINI	1306	1308	1312	1316	1317
	7	STEP	1324	1325	1350	1406	1408
	8	CONT	1421	1422	1438	1503	1509
	9	CONT	1510	1511	1530	1550	1551
13 Oct	1	CONT	0704	0707	0724	0745	0746
	2	CONT	0747	0751	0807	0826	0827
	3	MINI	0833	0834	0837	0840	0841
	4	CONT	0841	0846	0903	0922	0924
	5	CONT	0936	0938	1002	1015	1020
	6	STEP	1034	1042	1123	1137	1139
	7	CONT	1159	1200	1217	1232	1244
14 Oct	1	CONT	1012	1017	1037	1054	1055
	2	MINI	1113	1122	1137	1138	1139
	3	STEP	1140	1150	1227	1243	1243
	4	CONT	1249	1256	1322	1339	1340
	5	CONT	1341	1346	1405	1424	1425
17 Oct	1	CONT	1335	1340	1354	1411	1412
	2	CONT	1413	1414	1428	1442	1444

Table 2.2: Times and types of tethered balloon flights during the slope flow study. Times are in UTC. Types of ascent are described in the text.

the full length of the tether line (approx. 950 m) was used. Table 2.2 lists the times and types of the tether sonde flights. Data calibration and post-processing of the tether sonde data is described in Appendix B.

2.2.3 Surface Weather Stations

During the Special Observing Period (SOP) of MAP, a total of 36 surface weather stations were positioned throughout the study area, measuring pressure, humidity, temperature, wind speed and direction. For this study, only stations located near the valley bottoms of the Inntal and Wipptal are considered. Stations which did not provide full information of the wind direction (all S2**) or did not show any significant changes in wind signal at any point in time (due to poor location) were furthermore excluded from the analysis. Details of the final eleven stations are given in (Table 2.3).

Several research institutes contributed to this research effort, and hence a number of different types of weather stations were employed. Stations S1** installed by the University of Leeds were microbarographs combined with surface weather stations. University of Innsbruck operated Davis surface stations (S3**) while the University of Munich employed Friedrich weather stations (S4**).

Station ID	Latitude (m UTM)	Longitude (m UTM)	Elevation (m ASL)	Measurement height (m AGL)	Temporal resolution
S103	690651	5209021	1373	9.6	10 min
S104	689446	5211271	1228	10.3	10 min
S105	688852	5215482	1098	14.5	10 min
S106	686626	5220675	1121	10.8	10 min
S107	684228	5227081	938	9.1	10 min
S109	682206	5230890	912	9.6	10 min
S110	680435	5237289	612	3.0	10 min
S111	686865	5239266	565	10.6	10 min
S112	694312	5240941	554	9.6	10 min
S306	687922	5212239	1278	10.4	1 hr
S411	685941	5225786	1084	2.0	1 hr

Table 2.3: Site identification, location, measurement height (for wind), and available temporal resolution for surface weather stations reported in this study.

2.2.4 Hobo Temperature Loggers

Twenty-three (out of a total of thirty-five) Hobo temperature loggers were positioned in the Inntal and Wipptal to form five different pseudo-vertical profiles along valley sidewalls (Figure 2.3). A detailed description of the Hobo temperature logger is given by Whiteman et al. (2000). The temperature loggers were positioned roughly 2 m AGL. An effort was made to place the temperature loggers at fixed altitude intervals along the slopes. This, however, resulted in large differences in exposure and surface characteristics of the Hobo temperature loggers. Temperatures were recorded as 5 minute averages.

2.2.5 Radiation Site

Radiation measurements were obtained at one site (684355 m UTM E, 5228406 m UTM N, 1100 m ASL) in the Wipptal (Figure 2.3). The site was located in the middle of a slightly sloped, grassy field. Radiometers were pointed perpendicular to the horizontal datum (that is, not perpendicular to the slope). In addition to in- and out-going longwave and shortwave radiation, temperature, humidity and wind speed were measured at a height of 2 m AGL. Measurements were recorded as 5 min averages.

2.3 Synoptic and Local Conditions

During 11-17 October 1999, an upper level blocking ridge situated over central Europe provided generally fair weather conditions over the study area. Geopotential heights at 500 mbar reached values of 5800 m or higher, indicating a warm, dry, and therefore stable airmass. No precipitation was reported in the Wipptal during this period.

The evolution and break-down of the omega ridge is documented in Figure 2.5 which shows geopotential height and temperature at 500 mbar. On 11 October, an upper level ridge was located over central Europe, with the axis extending from Algeria to southern Scandinavia. A

Profile ID	Station ID	Latitude (m UTM)	Longitude (m UTM)	Elevation (m ASL)
Pat	501	682001	5230469	708
	502	682096	5230594	821
	503	682286	5230600	901
	504	682820	5231206	995
	505	682090	5231551	1142
	506	683584	5231007	1243
	507	684099	5230534	1349
	508	684083	5231056	1436
	509	684469	5231569	1565
	510	682486	5230973	1725
	511	685699	5230539	1920
	512	686116	5230786	2105
Gri	516	688407	5212316	1182
	517	688767	5212239	1281
	518	689086	5212271	1437
Mau	519	688299	5217719	1319
	520	689104	5218367	1646
	521	689759	5219033	1951
Stu	525	681695	5226633	1220
	526	679407	5227053	1001
	527	675249	5220188	975
Tul	528	693437	5238686	855
	529	693123	5237407	1160
	530	691889	5235320	1468
	531	691617	5234600	1702
	532	691404	5233202	2001

Table 2.4: Location of Hobo temperature loggers.

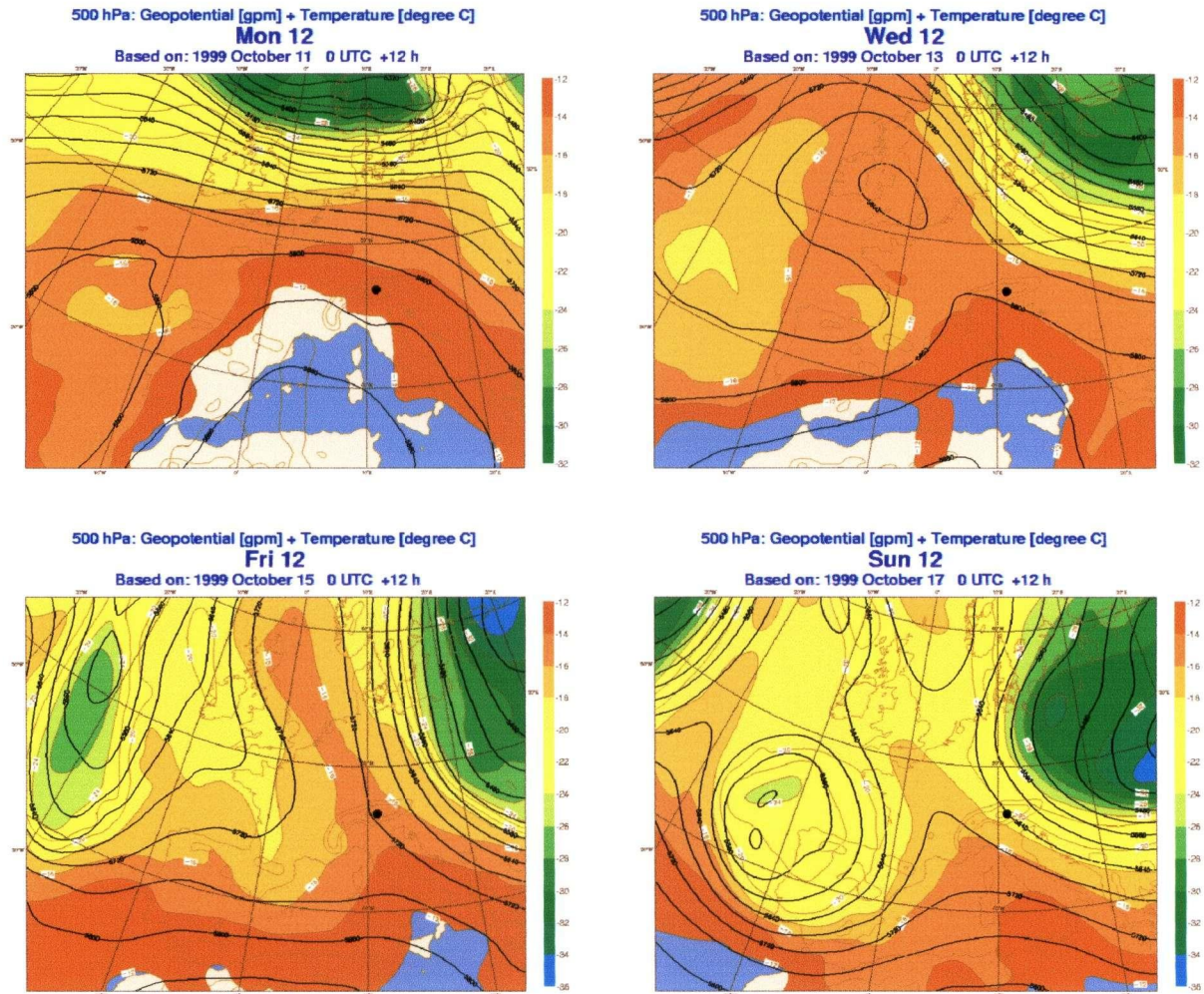


Figure 2.5: Geopotential heights and temperature at 500 mbar over central Europe for 1200 UTC on a) 11 October; b) 13 October; c) 15 October; and d) 17 October. The black dot marks the approximate location of the study area. Taken from ECMWF forecasts initialized at 0000 UTC. (Available at http://www.map.ethz.ch/sop-doc/sop_info/sop_info.htm.)

surface high off the coast of the British Isles extended south-east over central Europe. The flow over the alpine area was predominantly north-westerly, with generally weak pressure gradients at all levels. By 13 October, the upper level ridge had amplified, forming a classic blocking omega ridge, oriented from the North Sea south to the Alps. On this day, the flow over the alpine area was predominately westerly flows, with low pressure gradients at all levels. On 14 October, the upper level blocking ridge weakened slightly and moved eastward. While the western parts of the Alps remained under weak pressure gradients, the eastern portion of the Alps was influenced by the outer parts of a trough to the east of the blocking ridge, producing predominantly northerly flows aloft. By 16 October, the blocking ridge had weakened somewhat

Day	Innsbruck Airport (2800-3000 m ASL)	Wipptal-Lidar (2400-2800 m ASL)	Cloud/Fog Formation
11 Oct	4 ms^{-1} WNW - 4 ms^{-1} W	4 ms^{-1} S	clear in morning, afternoon convective clouds
13 Oct	4 ms^{-1} W - 7 ms^{-1} WNW	3-4 ms^{-1} SSE	clear in morning, increasing cirrus, cirro-stratus
14 Oct	7 ms^{-1} WNW - 9 ms^{-1} N	8 ms^{-1} NW	morning valley fog, afternoon cirrus
16 Oct	2 ms^{-1} N - 6 ms^{-1} WNW	2-4 ms^{-1} NW - N	morning valley fog, afternoon convective clouds
17 Oct	6 ms^{-1} WNW - 9 ms^{-1} NW	8 ms^{-1} WNW	morning valley fog, afternoon convective clouds

Table 2.5: Summary of local ambient conditions during the study period.

but was still situated over Europe with its axis from the North Sea down to Balears. Cut-off lows were situated on either side of the blocking ridge, one centered over Eastern Europe, the other west of the Iberian peninsula. Again the western alpine region remained under weak gradients, but the eastern part was under the weak influence of the low situated to the east of the blocking ridge, producing north-westerly flows aloft. On 17 October, the blocking ridge still remained, but the cut-off low over Eastern Europe had moved further westward. The alpine region remained under predominantly north-westerly flow aloft.

Local ambient wind and cloud conditions are summarized in Table 2.5. Wind conditions at Innsbruck Airport are based on 00 UTC radiosonde soundings and represent averaged values for a 200 m layer above the mountain tops (2800-3000 m ASL). Ambient wind conditions in the Wipptal are based on vertical wind profiles derived from Doppler lidar VAD scans (see Appendix G). While the local ambient winds observed at Innsbruck and in the Wipptal are in agreement with synoptic conditions on 14, 16 and 17 October, southerly flows are observed in the Wipptal above the valley wind layer on 11 and 13 October. On 11 October, the weak southerly flows are attributed to pressure channelling (Whiteman and Doran, 1993). On 13 October, a very localized downslope wind storm was observed near Gries (station S105 in Figure 2.3). It is assumed that the southerly wind aloft is partially caused by channeling of the windstorm down the Wipptal.

In terms of local cloud or fog formation, the nights of 11 and 13 October were clear while valley fog developed during the nights of 14, 16 and 17 October. The valley fog during the latter half of measuring period is attributed to low level moisture brought inland from the Baltic Sea and trapped by subsidence. The fog generally dissipated by 1000 UTC. During the day of 11 October, skies were generally clear with some convective clouds. Fog tendrils could occasionally be observed over forested stands. The morning of 13 October saw clear skies, but as the day progressed, high cirrus clouds moved in which thickened into cirro stratus clouds. At 12 UTC, cirro cumulus and convective/orographically induced cloud puffs were observed to the west. A local down-slope windstorm with clouds hugging the mountain top could be observed further up-valley at Gries. On 14 October, cirrus clouds started to move into the area at approximately

1230 UTC. October 16 and 17 were clear in the afternoon with occasional convective clouds.

Sunrise and sunset occurred at approximately 0530 and 1630 UTC, respectively. Due to shading effects, the upper slopes of the Arzthal were sunlit between 0650 and 0700 UTC while the tethersonde site received direct sunlight roughly 20 minutes later. The valley bottom was sunlit at roughly 0745 UTC. In the late afternoon, the valley bottom became shaded at roughly 1430 UTC while the tethersonde site was in the shade at approximately 1600 UTC. Solar noon corresponds 1100 UTC.

Chapter 3

Observations of Valley Flows in the Wipptal

“... poorly observed systems tend to be imagined as simply structured.”

Neff (1995)

In this chapter, *in-situ* and Doppler lidar observations of valley flows in the Wipptal are presented. The chapter is organized as follows. The first section summarizes observations from a number of surface weather stations. In addition to providing flow information near the ground, the continuous surface measurements confirm the thermal nature of the flows observed during the study period and thus provide an important context for interpreting the lidar observations. The second section describes the along- and cross-valley kinematic structure of daytime valley flow as observed by the Doppler lidar. In addition, backscatter intensity profiles are examined for clues of transport and distribution of aerosols by the valley flow. The chapter concludes with a summary of the observations.

3.1 Surface Observations

Before examining *in-situ* and lidar observations for valley flow characteristics, it is of interest to show that the study days are representative of valley wind days. The term ‘valley wind day’ refers to days on which the valley flow is primarily driven by horizontal pressure gradients that develop as a result of differential heating along the valley axis or between air in the valley and air at the same level over the adjacent plain. The proper criterion to identify valley wind days is therefore the twice-daily reversal of the pressure gradient. Historically, however, the criterion has been based on the twice-daily reversal of the surface wind (e.g. Dreiseitl et al., 1980; Vergeiner, 1983) since measurements of surface winds are easily obtained (Vergeiner and Dreiseitl, 1987). In this analysis, both criteria (based on pressure and surface winds) are examined.

The reader is reminded here of the implicit assumption that the surface winds are part of the valley wind system; that is, they are driven by the same thermal driving force that affects the entire valley atmosphere. While this assumption is reasonable for valleys with horizontal bottoms, it may not be entirely appropriate for valleys with sloping floors. In the latter case, perceived up-valley winds at the surface may be described more accurately as slope flows along the valley axis (also called up-floor winds (e.g. Whiteman, 1990)). The difference is a subtle

distinction in the way the horizontal pressure gradient forms. In the case of valley flows, the driving force is differential heating of the entire valley atmosphere, while slope flows form a result of a slanted/heated surface. Wagner (1938) and Ekhart (1944) already pointed to observations (in valleys with steeply sloping valley floors) of 'shallow slope winds along the valley floor' which appeared to be offset from the onset and cessation of valley flows at higher elevations. In this study, surface observations from stations in the relatively horizontal Inntal as well as the sloping Wipptal (inclination of valley bottom is approximately 1.3 degrees between Innsbruck and the Brenner Pass) are examined. Due to no or sparse lidar observations near the surface or during transition periods, it is not possible to determine unequivocally the nature of the surface flows. It does appear that in the Wipptal, flow in the up-valley direction ceases earlier at the surface than at higher elevations in the valley (i.e. compare stations S106 with S107 in Table 3.2), but on the other hand, the onset of the flow in the up-valley direction is slower, and the surface winds stronger than one would expect with typical slope winds (say, $2 - 3 \text{ m s}^{-1}$).

In this study, the valley wind criteria defined by Dreiseitl et al. (1980) were applied to hourly-averaged surface observations of wind speed and direction at eleven weather stations in the Wipptal and Inntal. Dreiseitl's criteria specify that valley wind days must have

- Three hours of down-valley winds in the morning, with the reversal of wind direction from down-valley flow to up-valley flow occurring between 0300-1300 UTC and 0200-1200 UTC for stations in the Inntal and Wipptal, respectively.
- Three hours of up-valley wind in the afternoon.
- Three hours of down-valley winds in the evening, with the reversal of wind direction from up-valley flow to down-valley flow occurring between 1400-2300 UTC and 1300-2200 UTC for stations in the Inntal and Wipptal, respectively.

The restrictions on the times of flow reversals are intended to remove from the data set conditions which mimic valley winds but which are not thermal in nature (i.e. passages of fronts, foehn, etc.).

The valley wind criteria are applied to all eleven surface stations. For practical purposes, a $\pm 45^\circ$ variation is allowed around the valley flow orientation. Observations in this study as well as other studies (e.g. Dreiseitl et al., 1980; Reiter et al., 1983) show that nocturnal valley flows are often weak and variable. Calms, defined as winds with speeds less than 1 m s^{-1} , are therefore counted as down-valley winds.

The results are listed in Table 3.1. The valley wind criteria is satisfied on all days for most, but not all locations. A valley wind pattern at the Brenner Pass station (S103) is not observed, which may be attributed to the relatively unprotected and exposed terrain at the Brenner Pass. Interestingly, observations from a surface station near the town of Terzing to the south of the pass (not shown here) suggest a diurnal wind pattern which is in agreement with the valley

Day	Wipptal								Inntal		
	S103	S104	S306	S105	S106	S411	S107	S109	S110	S111	S112
11 Oct	no	yes	yes	yes	yes	yes	yes	-	-	yes	yes
13 Oct	no	no	no	no	yes	yes	yes	-	-	yes	yes
14 Oct	no	yes	yes	no	yes	yes	yes	-	-	no	yes
16 Oct	no	yes	yes	no	yes	yes	yes	-	-	yes	no
17 Oct	no	yes	yes	no	yes	yes	yes	yes	yes	no	no

Table 3.1: Dreiseitl's valley wind criteria applied to surface weather stations in the Wipp- and Inntal. The criteria are described in the text. Failure of the criteria is indicated by 'no', and success by 'yes'. Dashed symbol indicates missing data.

wind pattern in the Wipptal, but in contradiction to the theoretical wind pattern in its own valley. Similar observations have been made in other valleys, the best-known example of which is the Maloja wind in the upper Engadine Valley near the Maloja Pass (Whiteman, 1990).

Failure of the valley wind criteria at station S105 in the Wipptal (with the exception of 13 October) and stations S111 and S112 in the Inntal is primarily due to the lack of wind reversal in the morning hours, although a marked increase in up-valley wind speeds during the daytime followed by calms in the evenings is generally observed at these stations. The absence of wind reversal at these stations in the latter half of the study period is attributed to low clouds and fog which filled the valleys in the mornings and did not dissipate until approximately 1000 UTC on those days. The cloud cover compensates nighttime radiative cooling through downward longwave radiation as well as enhances radiative interactions between the valley floor, sidewalls and cloud base which in turn reduces or eliminates the thermal gradient which drives the valley flow. This effect is clearly seen in pseudo-vertical temperature profiles obtained by Hobo temperature loggers in the early morning hours (Appendix C). Although obtained at different locations in the Inntal, Wipptal, and Stubaital, the profiles show no discernable differences in temperature.

On 13 October, no surface stations up-valley from and including station S105 satisfy the valley wind criteria. A closer inspection of measurements at station S105 (Figure 3.1) shows strong winds from the ESE direction, with peak winds exceeding 7 m s^{-1} between 0900 and 1200 UTC. Sudden jumps in temperature and dips in relative humidity recordings match those which accompany downslope windstorms, and suggest that a windstorm commenced at approximately 0130 UTC and ceased at 1500 UTC. An hydraulic jump was observed near station S105 (Roland Mayr, personal communication; personal photographs). Measurements at other stations, however, suggest that this downslope windstorm is very localized. Station S306 records relatively weak winds from the SW to SE direction, while station S104, seemingly cut off by the disturbance from the valley flow system further down the valley, records calms for most of the day. Station S106, located down-valley from S105, shows the development of up-valley flows, albeit with a slight delay. Further down-valley, no effects of the windstorm are apparent in the surface measurements.

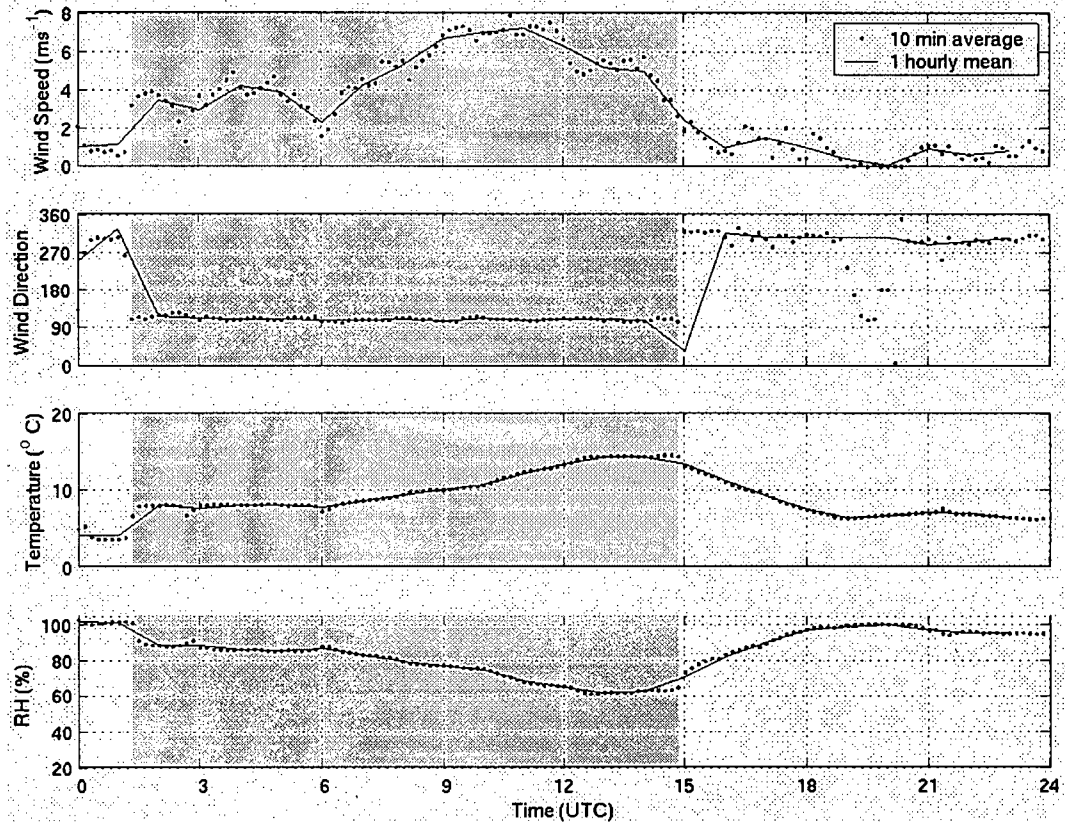


Figure 3.1: Surface wind speed, direction, temperature and relative humidity at station S105 for 13 October. Dots represent 10-minute averaged recorded data while black line represents hourly averages. The period of downslope windstorm is shaded in gray.

One final feature of interest in Table 3.1 is that the valley flow criteria are consistently fulfilled on every day at stations S106, S411 and S107. These stations are located in a section of the Wipptal where the valley is particularly well defined through deep and narrow sidewalls. It is this portion of the valley for which lidar observations were obtained.

Another way of identifying a valley wind day is to look for a twice-daily reversal in the horizontal pressure gradient. Pressure analysis, however, is much more limited than surface wind analysis. For one, sensors have to be placed sufficiently far apart so that actual pressure variations exceed the accuracy of the pressure sensors (compare a typical pressure gradient of 0.2 mb per 10 km to an accuracy of ± 0.3 mb). Another problem - especially when dealing with sloping valley bottoms - is the hydrostatic effect introduced by reducing pressure measurements to the same reference height. These errors are much larger than any horizontal pressure differences, and can obscure any observational differences.

Figure 3.2 illustrates the diurnal change in mean sea-level pressure in the Inntal between

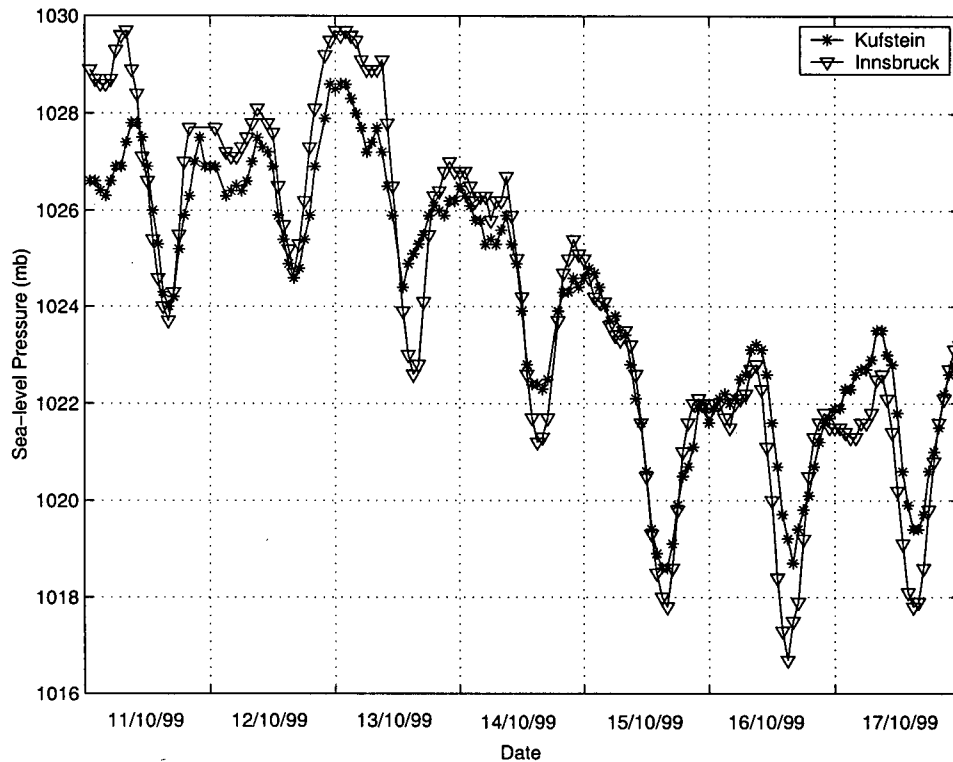


Figure 3.2: Sea-level pressure at Kufstein (495 m ASL) and Innsbruck (579 m ASL) during the study period. Data points represent hourly averages.

Kufstein (near the exit of the valley) and Innsbruck, approximately 70 km apart. The graph shows the diurnal heating and cooling effects of the valley superimposed on a general decreasing trend of the mean sea-level pressure. The diurnal reversal of the pressure gradient is best seen on 11 and 13 October while for the rest of the study period, the expected pressure gradient is well developed during daytime, but not so well defined for those nights during which valley fog developed in the Inn- and Wipptal. The concept that a larger pressure gradient induces stronger winds is qualitatively supported by Table 3.2 and Figure 3.2. Larger velocities observed in the Inntal (stations S111 and S112) on 13, 16 and 17 October correlate well with larger pressure differences observed between Kufstein and Innsbruck on those days.

Characteristics of up-valley flows such as onset, cessation, duration, peak wind speed and time of peak wind speed are listed in Table 3.2. These values were obtained from hourly-averaged data, but interpolated to the closest half hour. Information was also included for stations which only partly satisfied the valley wind criteria.

No consistent pattern in terms of times and duration of up-valley flow at various stations emerges from Table 3.2. A number of factors contribute to this seemingly unclear picture. For one, transition periods were often observed at stations with wind blowing across-valley and

Date		Wipptal							Inntal		
		S104	S306	S105	S106	S411	S107	S109	S110	S111	S112
11 Oct	Onset	1000	1030	0900	0900	0930	0900	-	-	0930	0930
	Cessation	1530	1430	1400	1500	1630	1530	-	-	1700	1700
	Duration	5.5	4.0	5.0	6.0	7.0	6.5	-	-	7.5	7.5
	Peak Wind	2.4	3.5	3.6	4.1	4.9	3.6	-	-	4.6	3.3
	Time	1200	1200	1200	1100	1200	1100	-	-	1500	1500
13 Oct	Onset	NA	NA	NA	1100	0900	0800	-	-	1230	1230
	Cessation	NA	NA	NA	1700	1730	1800	-	-	2030	2030
	Duration	NA	NA	NA	6.0	8.5	10.0	-	-	8.0	8.0
	Peak Wind	NA	NA	NA	3.6	3.9	3.0	-	-	6.4	4.2
	Time	NA	NA	NA	1300	1600	1600	-	-	1500	1500
14 Oct	Onset	1300	1130	NA	1100	1100	1000	-	-	NA	1200
	Cessation	1600	1530	1730	1600	1700	1700	-	-	1800	1730
	Duration	3.0	4.0	NA	5.0	6.0	7.0	-	-	NA	5.5
	Peak Wind	2.4	2.9	3.2	2.9	3.4	2.4	-	-	4.9	3.4
	Time	1500	1400	1300	1300	1430	1300	-	-	1500	1530
16 Oct	Onset	1200	0930	NA	0900	0900	0700	-	-	1230	NA
	Cessation	1530	1530	1500	1500	1730	1700	-	-	1830	1730
	Duration	3.5	6.0	NA	6.0	8.5	10.0	-	-	6.0	NA
	Peak Wind	2.2	3.2	3.9	4.8	4.3	2.4	-	-	6.3	4.3
	Time	1500	1400	1400	1200	1400	1200	-	-	1500	1600
17 Oct	Onset	1200	1100	NA	1000	1030	1000	1100	1000	NA	NA
	Cessation	1530	1530	1630	1430	1530	1600	1800	1830	1900	1900
	Duration	3.5	4.5	NA	4.5	5.0	6.0	7.0	8.5	NA	NA
	Peak Wind	3.2	2.3	4.2	5.0	5.1	3.4	2.2	5.1	6.0	4.0
	Time	1400	1400	1500	1200	1300	1200	1300	1500	1500	1500

Table 3.2: Surface up-valley flow characteristics at weather stations in the Wipptal and Inntal, showing onset, cessation, duration, peak wind speed (in ms^{-1}) and time of peak wind speed. Dashed symbols indicate missing data, while 'NA' indicates non-identifiable flow characteristics.

small time differences may well be due to the practical difficulty of what to consider as up-valley flow. Another contributing factor is temporal differences in the thermal forcing from day to day (clear skies vs low clouds in the morning vs cirrus clouds in the afternoon). One picture that does emerge from the surface analysis and which agrees with other studies (e.g. Wagner, 1938; Freytag, 1988) is that in the spectrum of valley wind systems, flow response in smaller volume valleys is quicker and more variable than in their larger counterparts. So while, for example, the wind speed maximum in the Inntal consistently occurs around 1500 UTC, this time varies considerably in the Wipptal. From Table 3.2 it also appears that the duration of valley flow decreases with up-valley distance. Keeping in mind the limitations of surface measurements as pointed out earlier in this section, this suggests that much of the volume of air carried through the lower portion of the Wipptal does not arrive at the end of the valley (i.e. Brenner Pass) but rather that the flow is diverted into tributaries of the Wipptal.

Not all stations listed in Table 3.2 show daytime up-valley flows along their respective valleys. In particular, stations S306 and S105 in the Wipptal and station S110 in the Inntal record up-valley flows into nearby tributary valleys. Although data from station S110 (located at the

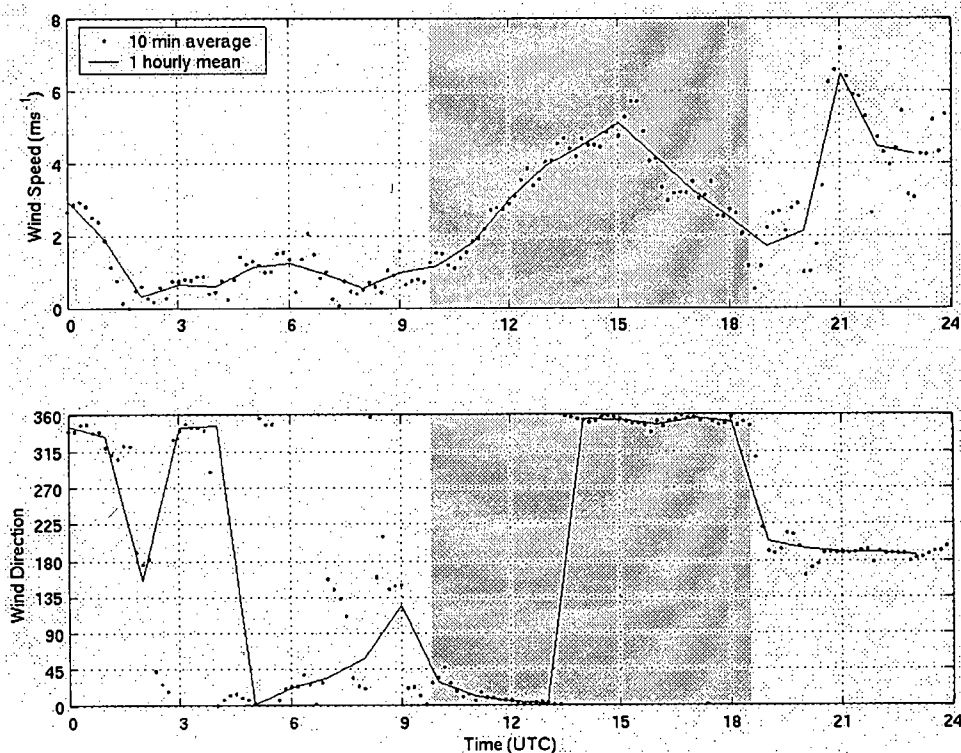


Figure 3.3: Surface wind speed and direction at station S110 for 17 October. Dots represent 10-minute averaged recorded data while black line represents hourly averages. The gray shaded area indicates daytime flow into the Wipptal.

Institute of Meteorology at the University of Innsbruck) is available for only one day during this study period, wind observations from this particular station were examined in detail by Dreiseitl et al. (1980). Figure 8 of that paper indicates that during weak gradient conditions in the summer (23 days in total), flow from the ENE to ESE direction accounted for 70% of hourly measurements between 1500 and 1800 UTC, while 7% of the measurements showed northerly flow. This result strongly suggests that the predominant direction at Station S110 during valley wind days should be easterly, not northerly. Measurements at station S110 on 17 October (Figure 3.3) show the typical development of up-valley flow, but which is directed into the Wipptal - *not* the Inntal - at all times during the up-valley flow period. It is uncertain at this point what causes station S110 in the middle of the Inntal to be influenced by tributary flow into the Wipptal on some days and not others. As will be shown later, however, lidar observations on 17 October show distinctly different radial velocity patterns which were not observed on other study days. One possible explanation is that stronger stability aloft limits the vertical movement of air, and air drawn into the Wipptal is directly removed from the Inntal.

Since stations S106 and S107 lie within the scanning range of the lidar, a few more comments

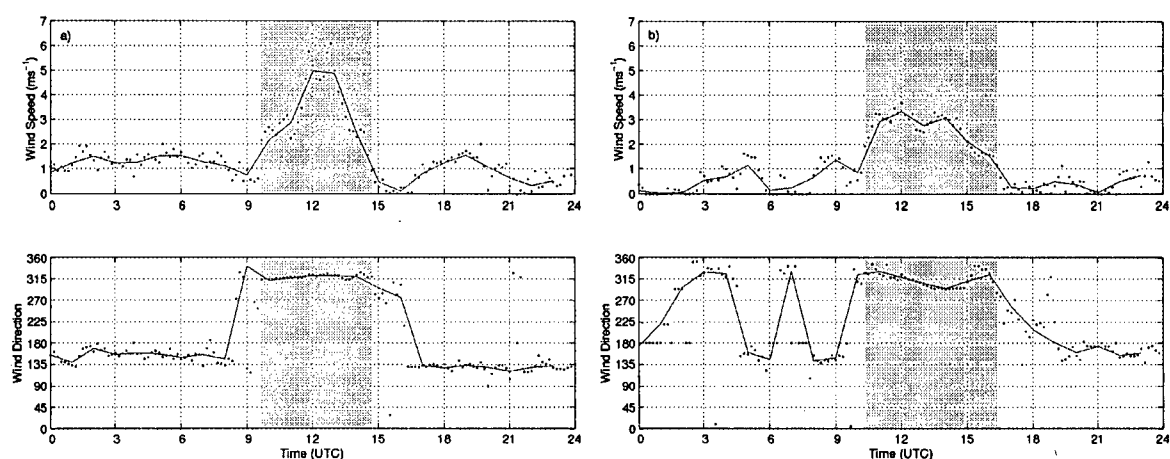


Figure 3.4: Surface wind speed and direction at stations a) S106 and b) S107 on 17 October. Dots represent 10-minute averaged recorded data while black line represents hourly averages. Periods of up-valley winds are shaded in gray.

on the flow characteristics at these two stations are warranted¹. Figure 3.4 shows wind speed and direction at these two stations for 17 October. The up-valley period is shaded in gray. Station S106 shows the classic reversal of the surface wind from down-valley (SSE) to up-valley (NW) and a return to down-valley, with the up-valley wind being much stronger than its nocturnal counterpart. Station S107 shows a similar pattern, although the nocturnal flow at this station is weaker and more sporadic in wind direction.

The wind direction at station S106 is fairly constant throughout the up-valley wind phase, while at station S107, the wind rotates during the course of the up-valley wind period from 335° to 295° and back to 335° . Similar rotations of the valley flow at station S107 were observed on all study days, except for 13 October. On this day, high cirrus clouds reduced incoming solar radiation, and it is therefore assumed that the differential heating of valley sidewalls was not as large as on other days. Similar rotations of the surface valley flow were observed in the Dischmatal, Switzerland (Hennemuth and Schmidt, 1985). At station S411, the valley flow routinely rotates from 320 degrees to 340 to 360 degrees, although the change in direction occurs primarily between 1400-1500 UTC.

Figure 3.4 also indicates that during peak flow times, the flow at station S106 is much stronger than at station S107. This characteristic was consistently observed on all study days (Figure 3.5). Near the onset and cessation of the valley flow period, however, this trend generally reverses, with the valley wind building faster and decreasing slower further down-valley than up-valley. The trend of increasing wind speeds with distance in the up-valley direction is

¹Station S411 also lies within the scanning range of the lidar, but is excluded here since it is positioned somewhat above the valley bottom.

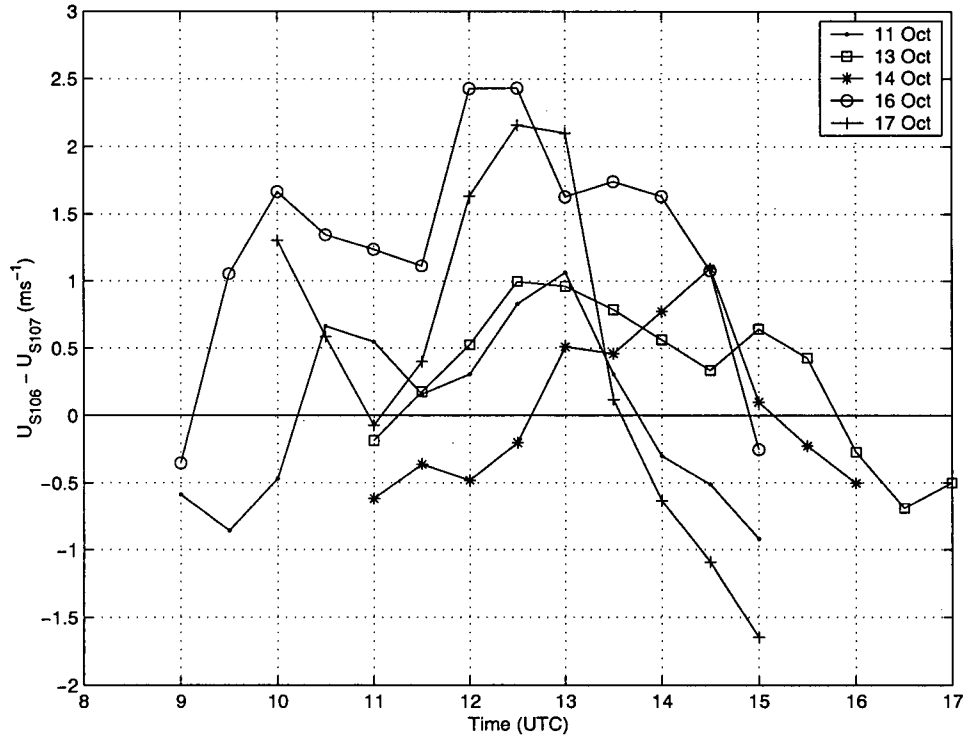


Figure 3.5: Difference in half-hour averaged surface wind speeds between stations S107 and S106 for periods of up-valley wind only. Positive values indicate stronger surface winds at the up-valley location (S106).

also observed in the lidar data, although the difference in wind speeds increases towards the afternoon, whereas the difference in surface wind speeds is already decreasing. This will be discussed in more detail in the following section.

In summary, the analysis of surface data suggests that the forcing of the surface winds in the Inntal and Wipptal is thermal in nature. The majority of failures of the valley flow criteria appear to be associated with the nocturnal development of valley fog in the latter part of the study period which prohibits the formation of down-valley winds during nighttime. A clear delay in the onset of up-valley flow on mornings with valley fog is not apparent. A likely explanation for this is that on clear mornings, the early morning insolation helps to reverse the pressure gradient as well as break down the nocturnal temperature inversion in the valley, while on cloudy mornings, the weaker insolation is balanced by smaller horizontal temperature gradients or atmospheric inversions which have to be reversed or destroyed. On 13 October, a localized downslope windstorm disrupts the up-valley flow in the upper portion of the Wipptal. The ideal valley flow criteria on this day, however, are still fulfilled at surface stations in the lower Wipptal as well as the Inntal. Lastly, observations suggest that near-surface up-valley

winds in the upper valley are generally stronger than those in the lower valley.

3.2 Doppler Lidar Observations

The following lidar analysis is based on VAD1025, PPI13 and RHI178/320 scans. Details of these scans are provided in Chapter 2. VAD and PPI scans provide information on the horizontal structure of the flow while RHI scans resolve the vertical structure. VAD and PPI images show radial velocities with the sign convention of negative values denoting flow away from the lidar (yellow/red shades), and positive values showing flow towards the lidar (blue shades). RHI images show the horizontal projection of the radial velocity component along the 178° and 320° azimuths. These components may be interpreted as the horizontal, along-valley wind. The basis for this interpretation as well as its limitations are discussed in more detail below. To provide a quasi-continuous visualization of the flow along the valley, the sign convention for RHI images is positive in the up-valley direction and negative in the down-valley direction. Each RHI image represents an average of two consecutive RHI scans obtained over a 6-minute period. Details of the pre-processing of RHI data are found in Appendix E. It should be noted that the RHI images offer a two-dimensional view of a complex three-dimensional flow phenomenon, and therefore do not capture all aspects of the flow such as Coriolis effects on the valley flow.

Lidar data are presented relative to the position of the lidar. To avoid confusion between the location of range gates and the direction of flow (particularly in this chapter), the phrases 'upper valley' or 'above the lidar' are used to denote measurements up-valley (or south) from the lidar, and 'lower valley' or 'below the lidar' describe measurements down-valley (or north) from the lidar.

Several comments are necessary about the interpretation of Doppler lidar data. Instrument biases aside, errors in the analysis of Doppler lidar derived wind fields generally arise from the assumptions made in interpreting lidar observations. For the lidar analysis in the Wipptal, two assumptions were made. These assumptions as well as their consequences are described below.

Assumption of Horizontal Flow: To remove the effect of changing elevation angles, radial velocity components were projected horizontally. The assumption of horizontal flow is less appropriate near the surface where the flow is terrain-following, but accurate at higher elevations where the flow gradually levels out (neglecting gravity waves). The valley floor of the Wipptal has an average inclination of 1.3° , and thus the horizontal projection differs from the terrain-following projection by 0.03%.

Although negligible for this analysis (due to the small inclination angle of the valley floor), another measuring bias should be kept in mind when lidar scans of terrain-following flow are performed in opposing directions (i.e. up-valley vs down-valley). For an inclined but homogeneous flow, the measured radial component is $v \cos(EL + \theta)$ in the down-valley direction, but $v \cos(EL - \theta)$ in the up-valley direction (Figure 3.6). Symbol v represents the actual wind speed,

θ the angle of the wind with respect to the horizontal (or the inclination of the terrain), and EL the elevation angle of the lidar beam, also taken from the horizontal. The lidar thus measures a smaller radial velocity component in the down-valley direction than in the up-valley direction. For small inclination angles, this measuring bias is negligible (for the values, $v = 5 \text{ m s}^{-1}$, $\theta = 2^\circ$, and $EL = 20^\circ$, the difference in radial velocities is less than 3%), but larger errors could occur in steeper terrain.

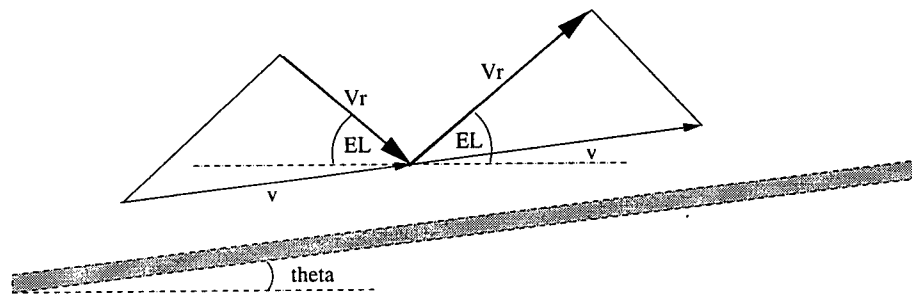


Figure 3.6: Schematic diagram showing the effect of inclined flow on radial velocity measurements. See main text for explanation of variables.

Assumption of Along-valley Flow: The assumption is made that the RHI scans capture the along-valley component of the valley flow. Because the azimuth angles used for the RHI scans approximate fairly well the along-valley axis of the Wipptal (Figure 3.7), the radial velocity component along those scans actually represents the along-valley wind component. Geometrical errors due to differences between lidar beam direction and orientation of the valley axis are assumed negligible. Below the lidar, the azimuth angle of the RHI scan and the valley orientation differs by 5° , while above the lidar, the difference in azimuth angle for the first few range gates is closer to 11° .

Above the ridgeline, the flow is no longer confined by valley sidewalls and the along-valley flow assumption therefore no longer holds. For continuity reasons, radial velocities of the flow

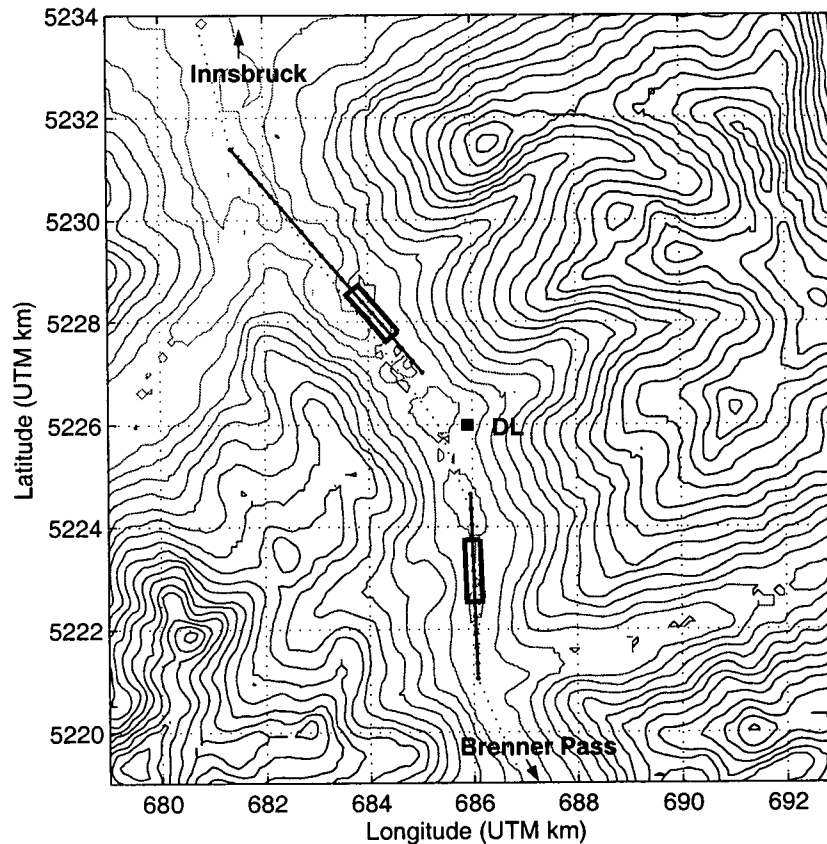


Figure 3.7: Topographic map of the Wipptal showing the RHI scans at 178 and 320 degrees (heavy solid line) in relation to the centerline of the valley (dotted line). The center of range gates are indicated by dots. The boxes mark range gates for which vertical wind profiles are shown.

above the ridgelines are included in the RHI images, although the radial velocity component may not represent the true wind speed. VAD scans were therefore analyzed for the flow structure aloft. Vertical wind profiles derived from linear VAD analysis of range gates above the valley atmosphere show reasonable agreement with tethered sonde soundings. These profiles are shown in Appendix G.

VAD and PPI scans were also examined for the horizontal flow structure within the valley atmosphere. Due to the elevation angles of the available scans and the width of the valley at higher elevations, a large range in azimuth angle was required to scan the entire cross-section of the valley. If there are cross-valley winds present in the valley (as was indicated by surface observations at S107), this may influence the interpretation of the cross-valley structure of the along-valley wind component.

Lastly, it should be mentioned that for this study period, wind measurements from other instruments were not available to verify the Doppler lidar observations. Such a comparison,

Day	Categorization
11 Oct	light winds, opposing direction
13 Oct	winds, opposing direction (disturbance by downslope wind storm)
14 Oct	moderate winds, same direction (coupled)
16 Oct	light winds, same direction
17 Oct	moderate winds, same direction (decoupled)

Table 3.3: Categorization of ambient wind conditions.

however, was carried out by Durran et al. (2002) who compared winds retrieved by the Doppler lidar with airborne wind observations collected by the NOAA WP-3D aircraft during conditions of gap flows (also during the MAP field study). Their results show good agreement between the Doppler lidar and the aircraft measurements north of the lidar, but significant differences in wind speed south of the lidar. Although the source of this difference has not been established definitely, the authors suspect that it may be due to the tendency of the aircraft to bank more steeply and more rapidly in the narrow upper portion of the Wipptal, thereby degrading the accuracy of the airborne observations.

The Doppler lidar analysis is divided into three parts. The first part discusses the evolution and along-valley structure of the valley flow, whereby the study days are presented in context with ambient wind conditions. The second part briefly examines the cross-valley structure. Lastly, the third section looks at structures in the backscatter intensity fields.

3.2.1 Along-valley Structure and Evolution

This section highlights the along-valley spatial structure and evolution of winds in the Wipptal. Although the analysis presented in Section 3.1 establishes the thermal nature of the flow during the study period, ambient conditions have a large influence on the structure and evolution of valley winds. Ambient wind conditions for all study days are summarized in Table 3.3.

11 October

RHI 178/320 scans were unfortunately not performed on 11 October. To facilitate comparison to the other study days, pseudo-RHI cross-sections (shown in Figure 3.8) were composed from VAD1025 and PPI13 scans for the upper and lower valley sections, respectively. On this day, these two scans were performed consecutively within a time span of 15 minutes. Horizontally projected radial velocities were averaged at each range gate over a 40° sector centered around the 178° and 320° azimuths. Corrections for azimuth angles were thereby not applied. The vertical resolution varies from 117 m at 1.35 km from the lidar (range gate 5 or RG5) to 510 m at 5.85 km from the lidar (RG20). Also indicated in Figure 3.8 are the exact heights of individual layers. These were obtained from interpolation between consecutive range gates with opposing wind directions. In some instances, the colour coding in Figure 3.8 does not reflect

the true flow direction. This problem is an artifact of the graphing package and is caused by a combination of weak wind speeds and sparse data coverage. Arrows were therefore added to the figures to indicate the correct flow directions.

As Figure 3.8 shows, the valley flow system in the Wipptal is well developed on this day. The vertical extent of the up-valley wind is defined by southerly flow aloft which remains relatively weak (less than 4 m s^{-1}) throughout the day (Figure G.1).

The first pseudo-RHI composition at approximately 0900 UTC shows a layer of weak up-valley flow below the effective ridgeline (Figure 3.8). Another layer of up-valley flow is visible aloft but is separated by a layer of flow in the down-valley direction. At 1015 UTC, the up-valley wind has intensified and extends well above the ridgeline. The sandwiched layer of down-valley flow is almost completely eroded, although remnants of it are still visible below the lidar. The up-valley flow layer aloft is weakening as well. Above the lidar, there is no evidence of down-valley flow. By 1100 UTC, the valley flow is fully developed in both directions and extends almost 1400 m above the valley floor - well above the effective ridgeline. The maximum intensity of the flow is observed at approximately 1230 UTC. Although the spatial coverage differs below and above the lidar, the lidar observations strongly suggest that the wind speed gradually increases with distance in the up-valley direction. At 1230 UTC, for example, maximum wind speeds of 7 m s^{-1} are observed at about 250 m AGL in the lower valley portion while wind speeds of 8 m s^{-1} are observed 500 m above the valley floor in the upper valley. Bearing in mind a Prandtl-type profile, it is possible that wind speeds above the lidar exceed 10 m s^{-1} closer to the valley bottom. At 1300 UTC, flow below the lidar has weakened somewhat but remains at the same intensity in the upper valley. At 1500 UTC, the valley flow above and below the lidar has weakened. The flow above the lidar, however, still retains speeds of $4 - 5 \text{ m s}^{-1}$ at 500 m above valley floor while the flow at the same height in the lower valley has decreased to about 1 m s^{-1} .

The depth of the up-valley flow changes with time and along-valley distance. At 0900 UTC the upper extent of the valley flow reaches to heights of roughly 2500 m ASL and appears constant along the valley axis. As the day progresses, the height of the valley flow drops approximately 300 m in the lower valley, but only 100 m in the upper valley. Between 1300 and 1500 UTC, a further decrease in the depth of the valley flow is observed approximately 2 km below lidar. Subsidence in the valley atmosphere as compensation for air being removed by slope flows has been suggested by Whiteman (1982), but the inhomogeneous decrease in the flow depth along the valley axis suggests that subsidence below the lidar may be larger to compensate for the observed along-valley velocity divergence. This is emphasized by the additional decrease in depth at 1300 UTC whereby the flow has decreased in intensity much more in the lower valley portion than in the upper section of the valley.

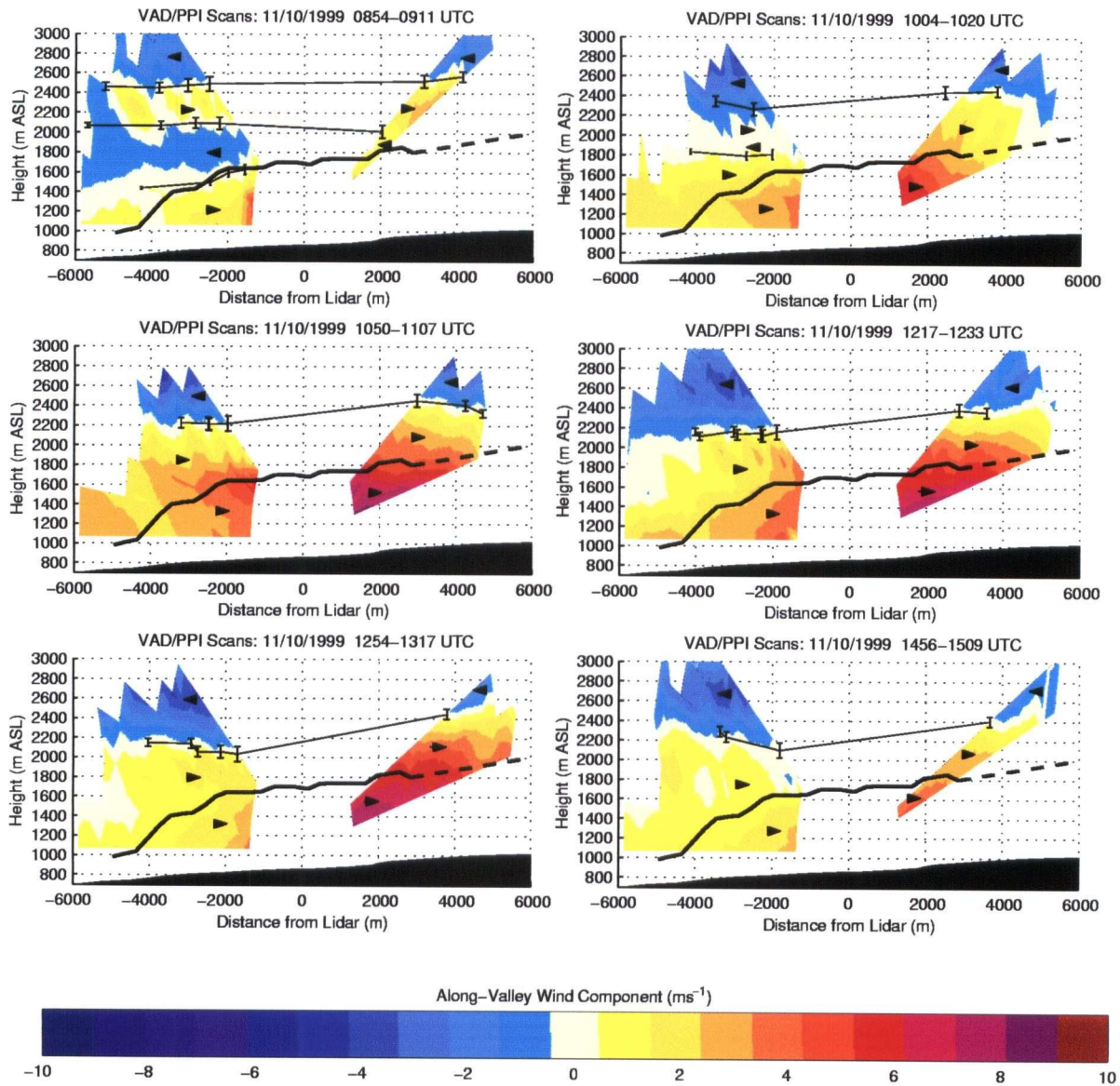


Figure 3.8: *Pseudo-RHI cross-sections showing horizontally projected radial velocities along the valley centerline for 11 October. Data below the lidar are based on TPPI13 scans covering elevation angles 0° to 30° , while data above the lidar are based on VAD1025 scans with elevation angles ranging from 10° to 25° . Some faulty VAD scans (particularly for the images at 0854, 1254 and 1456 UTC) were excluded from the analysis. Positive values indicate up-valley flow while negative velocities denote down-valley flow. Arrows are superimposed to clarify flow direction. The thin lines mark the heights of individual layers with opposing flow whereby the error bars indicate the vertical resolution (proportional to the cosine of the elevation angle). The solid black area marks the valley floor. The effective ridge line is shown with a heavy solid/dashed line.*

13 October

On 13 October, up-valley winds are observed by the lidar despite a localized down-slope wind storm which occurs roughly 10 km above the lidar site (see Section 3.1). The up-valley flow layer remains relatively shallow for most of the day. Several factors may have contributed to this. In the late morning hours, incoming solar radiation was greatly reduced by thickening cirrus clouds, thus decreasing the sensible heating of the valley atmosphere. In addition, channeling of the downslope windstorm to the lower section of the Wipptal may have influenced the onset as well as limited the spatial extent of the up-valley flow layer.

Figure 3.9 displays the RHI images for 13 October. Throughout the day, a layer of opposing (down-valley) flow is visible aloft. This layer decreases in strength and depth during the day as a layer with weak positive radial velocities descends. The 0000 UTC radiosonde sounding at Innsbruck shows weak (less than 3 m s^{-1}) winds aloft from the WNW direction. The flow aloft (with positive radial velocities) may therefore correspond to the light westerly flow aloft.

Up-valley flow is first visible in the upper section of the valley at 0845 UTC. Surface station S106 located roughly 5 km above from the lidar, however, only records up-valley flows at 1100 UTC while stations S107, located 3 km below the lidar, shows up-valley winds commencing at 0800 UTC. Station S411 located near the lidar shows up-valley flows at 0900 UTC. These observations suggests that an up-valley flow layer was present below the lidar by the time the second RHI scan was obtained, but that the layer was too shallow to be captured by the RHI scan. Above the lidar, however, surface and lidar observations suggest that a shallow layer of up-valley flow developed aloft while surface winds remained in the down-valley direction.

The flow structure and strength on this day are quite different than on the previous one. Maximum wind speeds do not exceed 6 m s^{-1} , and the height of the valley flow remains below 1500 m ASL. Again, velocity divergence appears to occur in the up-valley direction. The upper extent of the up-valley flow layer is either constant or decreases slightly with respect to mean sea level. This translates into an overall decrease in the depth of the up-valley flow with up-valley distance. At 1216 UTC, for example, the depth of the flow 4 km below the lidar is roughly 600 m while 6 km above the lidar, the depth has halved. Although this decrease in depth could be due to the mechanical disturbance in the upper part of the Wipptal, a similar feature was observed on 16 October when the flow aloft was in the same direction as the valley flow.

From the RHI scans, the nature of the flow aloft is not clear. In particular, it is not obvious if the flow aloft is thermally-driven (particularly in the morning hours) or if it is due to the downslope windstorm which was observed in the upper valley. A more complete explanation may be given with the help of VAD scans. Figure 3.10 shows a sequence of VAD scans taken at 10° elevation. The first VAD image at 0830 UTC shows flow in the down-valley direction, reaching speeds of $7 - 8 \text{ m s}^{-1}$ and banking heavily to the right (eastern) side of the valley below the lidar. Above the lidar, the flow is in the down-valley direction in the center of the valley, but an up-valley flow layer is observed on the eastern side which extends to almost

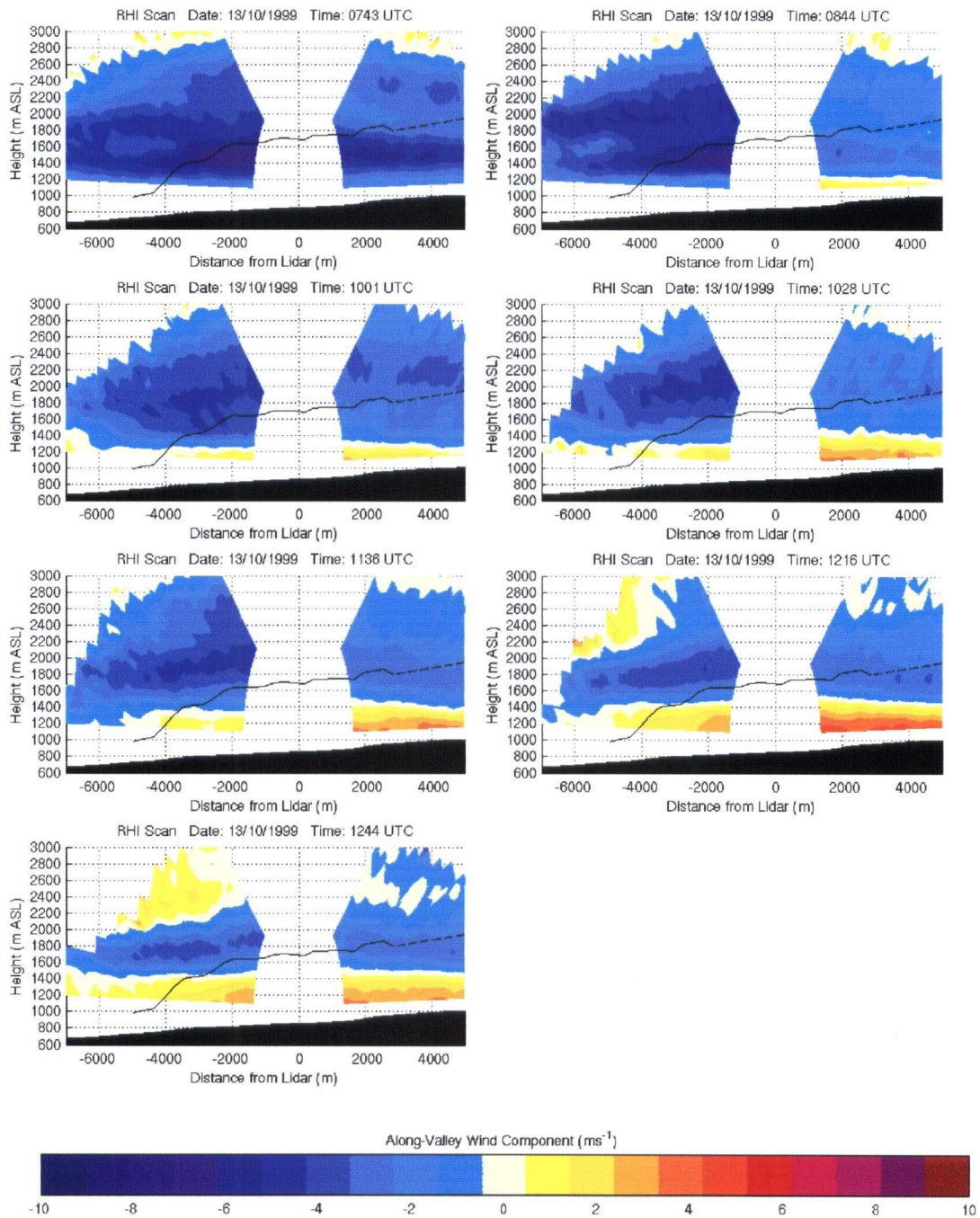


Figure 3.9: RHI cross-sections for 13 October, showing the horizontally projected radial velocity component along the valley axis. Positive values indicate flow in the up-valley direction, while negative velocities denote flow in the down-valley direction. The valley floor is shown in black at the bottom of each figure. The heavy black solid/dashed line indicates the effective ridgeline.

ridge-height. Similar flow asymmetries have been observed in other valleys (e.g. Reiter et al., 1983). Although an exact explanation for this phenomenon is still lacking, Reiter et al. (1983) proposed that differential heating of valley sidewalls (due to shading effects) could play a role. This explanation, however, seems unlikely for this situation as the up-valley flow occurs towards the shaded (eastern) side of the valley. By 0920 UTC, the down-valley flow above the lidar has weakened significantly, while the up-valley flow appears to be expanding in the lower layers towards the valley center. Up-valley flow also appears to be developing on the western side of the valley (possibly flow into the small basin). At 1015 UTC, the down-valley flow above the lidar has re-intensified aloft, while the layer of up-valley flow has decreased in depth. At 1140 UTC, the layer of up-valley flows which earlier in the morning extended throughout the depth of the valley has disappeared, but a shallow layer of up-valley flow is now visible across the scan. As the up-valley flow deepens, it also becomes visible below the lidar. These observations suggest that the down-valley flow is thermal in nature earlier in the morning, but is later induced by the downslope windstorm.

14 October

Figure 3.11 shows the available RHI images for 14 October. The upper level flow is moderate ($\approx 8 \text{ m s}^{-1}$) and from the NNW. The first RHI image at 1145 UTC shows slightly stronger up-valley wind speeds near the valley bottom, separated from the flow aloft by a layer of weaker winds. The upper-level flow displays a wave-like structure with an amplitude of roughly 200 m and a wavelength of 12 km. Extrapolation of the wave to the NNW (in line with the flow at that level) suggests that it formed over the mountain chain just north of Innsbruck (see Figure 2.1). Unfortunately, there is not enough information available to determine if this is a mountain wave. The following RHI scans, taken within a time span of one hour, all show similar flow features. There is no distinct wind speed minimum which separates the valley flow from the upper level flow and no organized vertical structure is apparent in the valley flow. Backscatter analysis presented in Section 3.2.3 suggests that the lack of vertical structure in the valley flow is due to coupling of the valley flow with the flow aloft. Due to the reduced coverage in the latter three lidar scans, the wave structure of the flow aloft is not recognizable although a strong wind shear layer is still visible.

Figure 3.12 shows vertical profiles of the horizontal along-valley wind component taken at several range gates (8 through 12) above and below the lidar. While there is very little change in the vertical flow structure below the lidar, the lower portion of the flow above the lidar increases by roughly 2 m s^{-1} , thus increasing the flow divergence. The large difference in wind speed above a 1000 m AGL appear to be due to the wave-like structure.

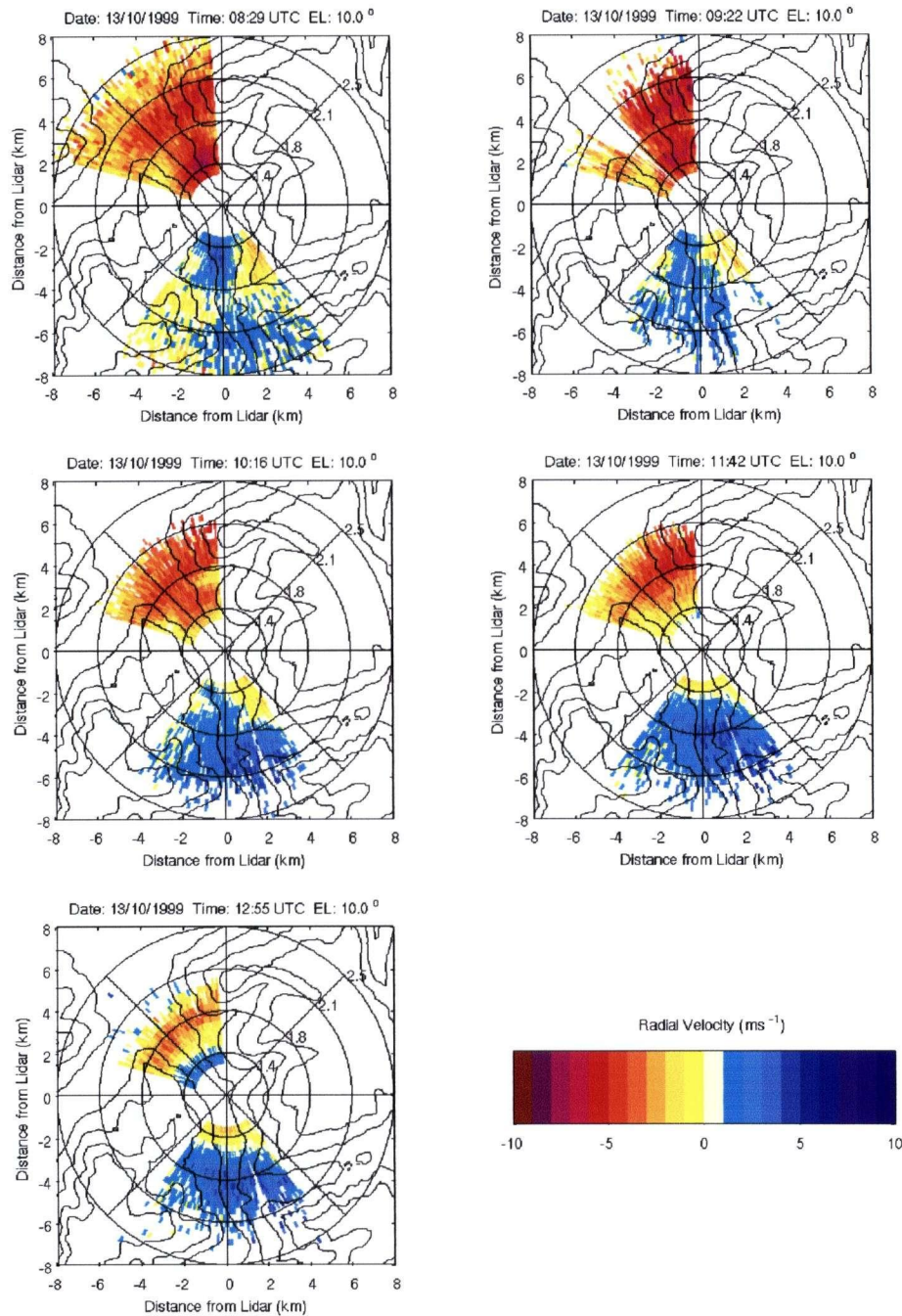


Figure 3.10: Plan view of VAD scans at 10 degree elevation taken on 13 October. The images show the radial velocity component, with positive values indicating flow towards the lidar and negative velocities denoting flow away from lidar. Superimposed are topographic contour lines at 1100, 1400, 1700 and 2000 m ASL. The range rings mark the horizontal distance in km from the lidar (as indicated on the left and bottom axes). The corresponding height (in km) of each range ring is given in the first quadrant.

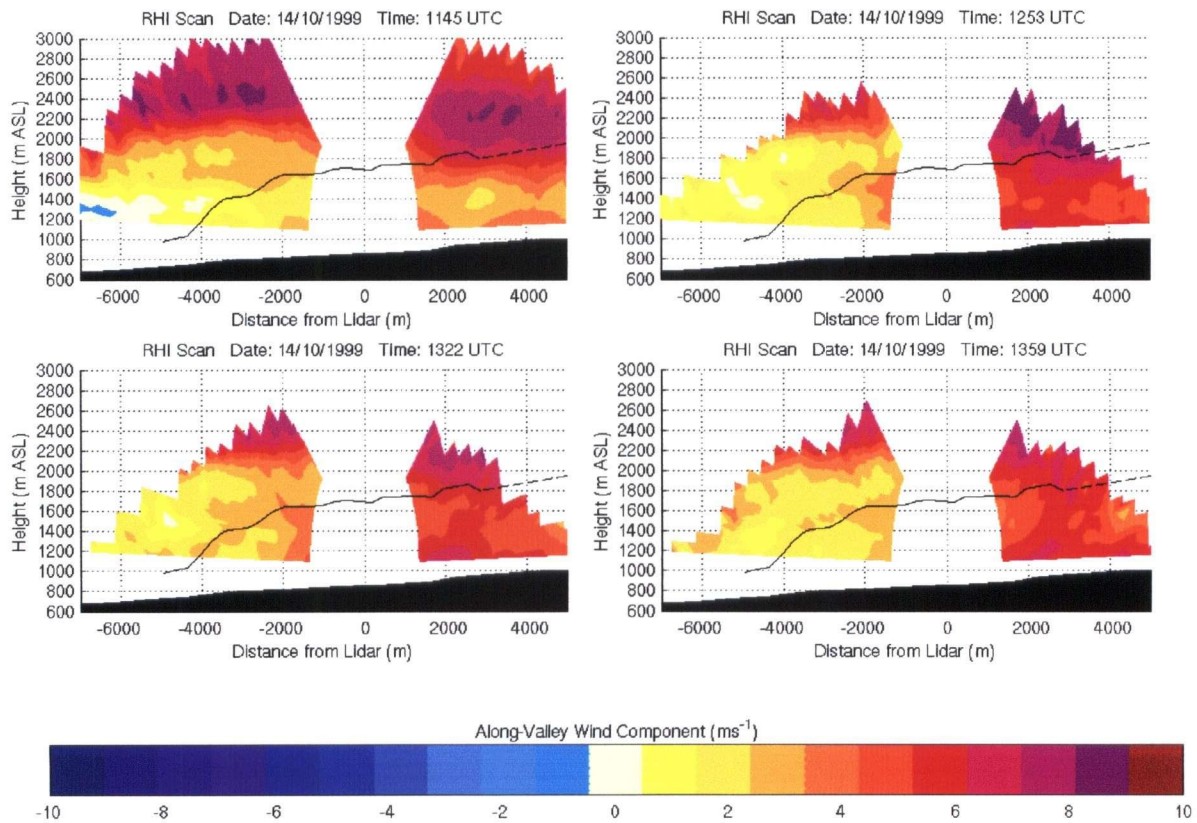


Figure 3.11: RHI cross-sections for 14 October. For further explanation, see Figure 3.9.

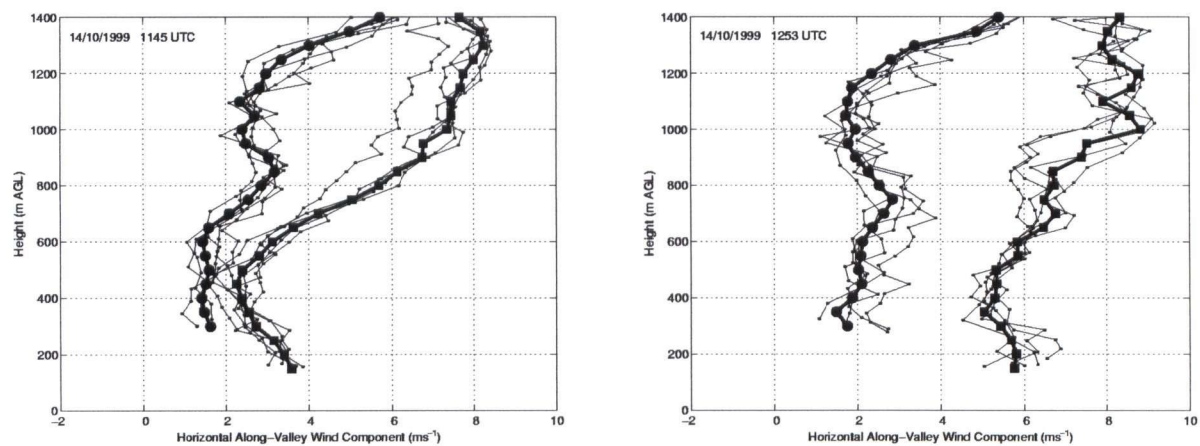


Figure 3.12: Vertical profiles of the horizontal along valley wind component for range gates 8-12 (2.25-3.45 km from lidar) up-valley (solid squares) and down-valley (solid circles) from the lidar site for 14 October. Thin lines with dots show individual profiles while heavy lines with solid circles/squares indicate averaged profiles.

16 October

Figure 3.13 shows the RHI scans for 16 October. The ambient wind on this day is weak and from the northwesterly direction. The first RHI image at 1100 UTC shows up-valley flow below the lidar which is still weak but extends to the ridgeline. Above the lidar, the valley flow is more strongly developed. A layer of down-valley flow is visible below the lidar between roughly 1600 and 2000 m ASL. A VAD scan taken 10 minutes earlier shows that this layer exists across the entire valley cross-section, but is slightly deeper towards the center of the valley than near the sidewalls. Although not visible in the RHI scan, a small remnant of down-valley flow aloft above the lidar can be seen in the VAD scans (the down-valley flow appears towards the eastern sidewall and is therefore not visible in the RHI scan along the center of the valley). By 1145 UTC, the down-valley flow has completely disappeared in the upper valley while weak down-valley flow still persists in the lower valley. By 1200 UTC, the remnant of down-valley flow below the lidar has disappeared as well, and the up-valley flow now appears to be fully developed. A distinct vertical structure in the valley flow is not discernable below the lidar, except for a slight increase in wind speed with distance in the up-valley direction. The flow obtains a minimum at roughly 2400 m ASL. The flow above the lidar has a more layered structure, which - until 1230 UTC - appears not to be terrain-following, but decreasing in depth with distance in the up-valley direction. By 1300 UTC, the layered flow structure is more terrain-following but this eventually dissipates. By 1450 UTC, a layer of almost uniform wind speed extends to a height of 2100 m ASL, with a slight minimum in the wind visible at approximately 2400 m ASL.

At this point it is unclear why the flow structure above the lidar is not terrain-following, but this observation is supported by the backscatter intensity analysis which is presented in the following section. A similar flow development was also observed on 13 October.

Vertical wind profiles from below and above the lidar are shown in more detail in Figure 3.14. The lower and upper valley profiles show little similarity in structure or temporal evolution. Between the first and last RHI scan taken on this day, there is very little change in the wind profiles below the lidar, which are almost constant with height. Above the lidar, the up-valley wind speed increases throughout the day, most notably, however, at higher elevations. A distinct flow maximum occurs at 300 m AGL. At this height, the difference in wind speed between the lower and upper valley at times reaches 5 m s^{-1} .

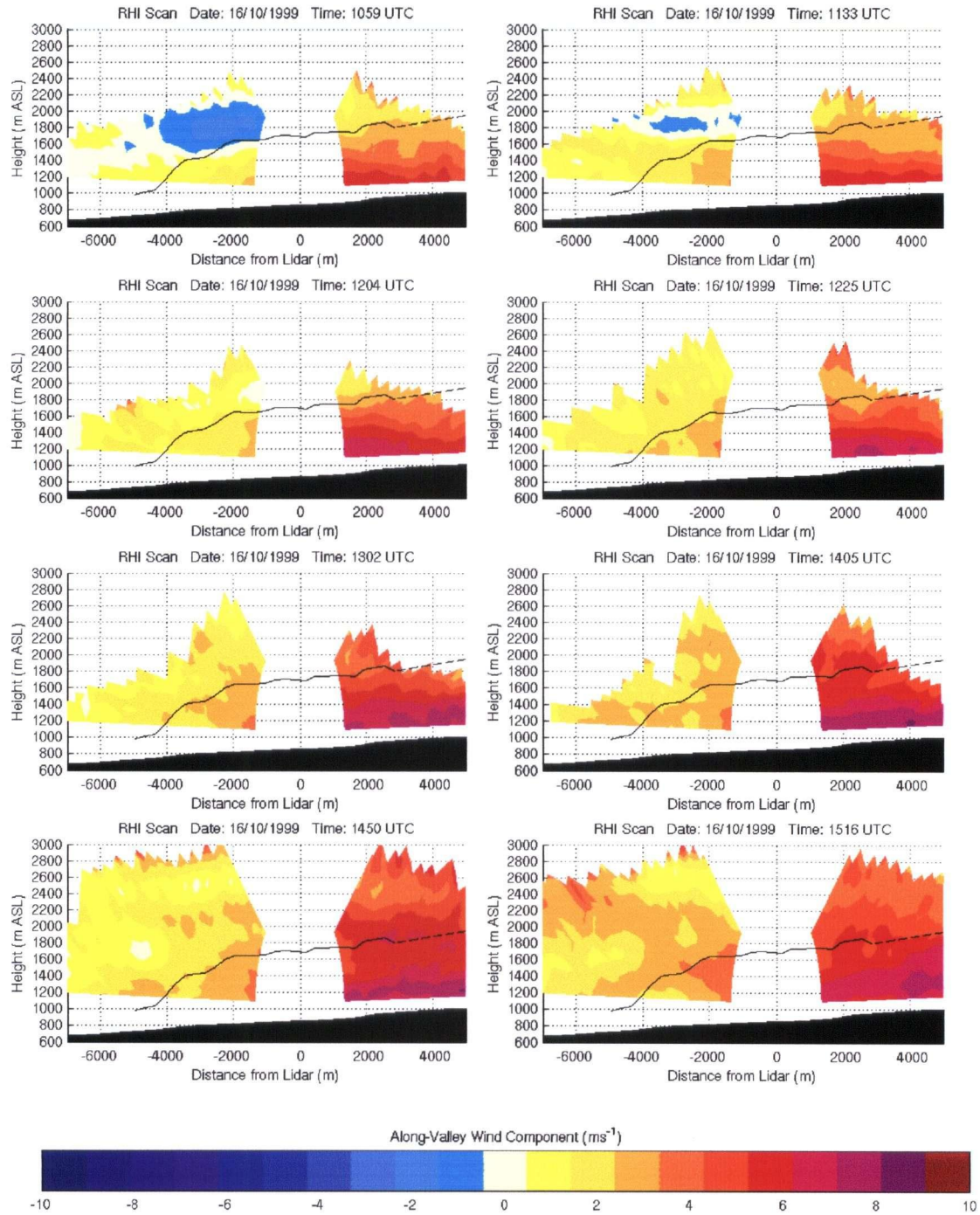


Figure 3.13: RHI cross-sections for 16 October. For further explanation, see Figure 3.11.

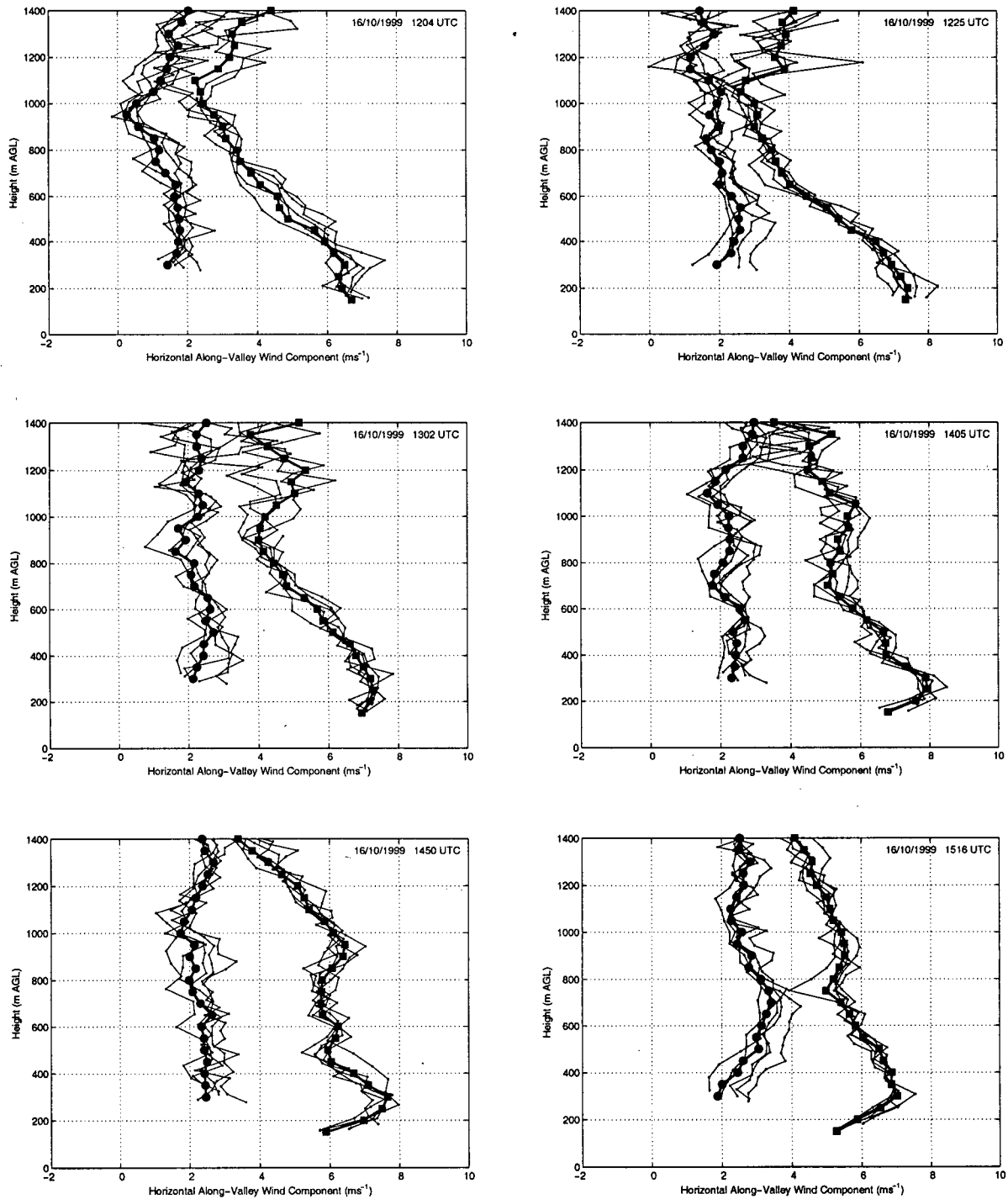


Figure 3.14: Vertical profiles of the horizontal along valley wind component for range gates 8-12 (2.25-3.45 km from lidar) up-valley (solid squares) and down-valley (solid circles) from the lidar site for 16 October. Thin lines with dots show individual profiles while heavy lines with solid circles/squares indicate averaged profiles.

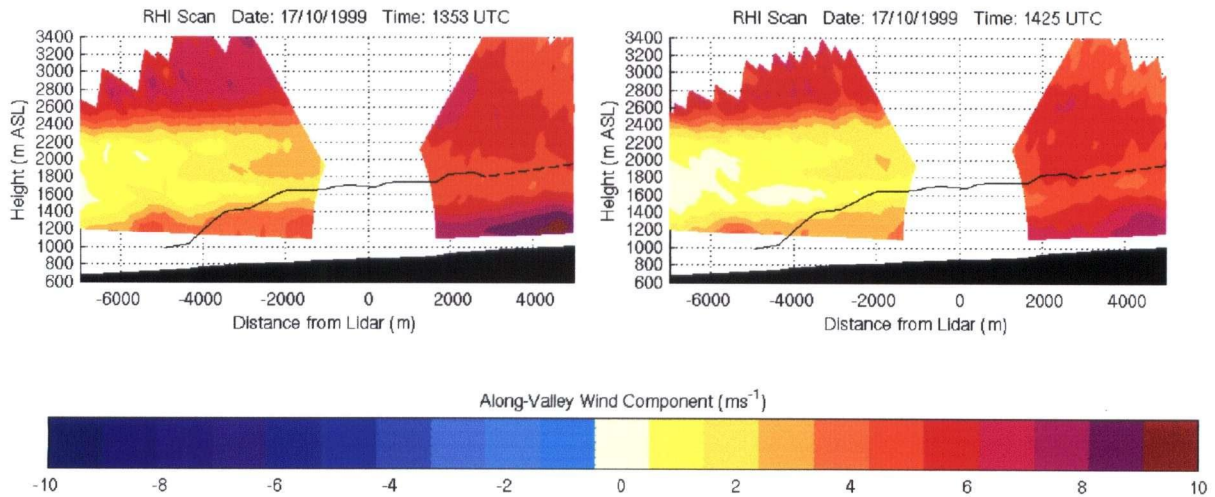


Figure 3.15: RHI cross-sections for 17 October. For further explanation, see Figure 3.13.

17 October

The RHI cross-sections obtained on 17 October (Figure 3.15) show a well developed up-valley flow regime which is clearly separated from the upper level flow through a wind minimum. The upper level flow on this day is moderate ($7 - 8 \text{ m s}^{-1}$ at 2800 m ASL) and from the north-west. The depth of the valley flow is roughly 800 m and remains constant along the valley axis. As on the previous study days, the valley flow gradually increases with distance in the up-valley direction. This flow divergence is not just limited to the valley atmosphere proper, but also occurs above the effective ridgeline. At 2600 m ASL, however, the wind is constant and from the NW. Apparent differences in the along-valley wind component in the RHI images at this height and above are due to the different azimuth angles with which the up- and down-valley scans were obtained.

Figure 3.16 shows the vertical flow structure in more detail. The velocity profile below the lidar appears parabolic in shape, while above the lidar the velocity profile shows a closer correspondence to the Prandtl profile (Atkinson, 1981), with a distinct peak at 200 m AGL.

3.2.2 Cross-valley Flow Structure

Until now, only lidar data along the center axis of the valley have been presented. For those scans, no *a priori* assumption about the flow is necessary as the RHI scan along the valley axis measures the along-valley wind component. Interpretation of the cross-valley structure of the along-valley flow is more complicated as it is not possible to distinguish with a single (radial) wind component between cross-valley flow components and cross-valley structures in the along-valley flow component.

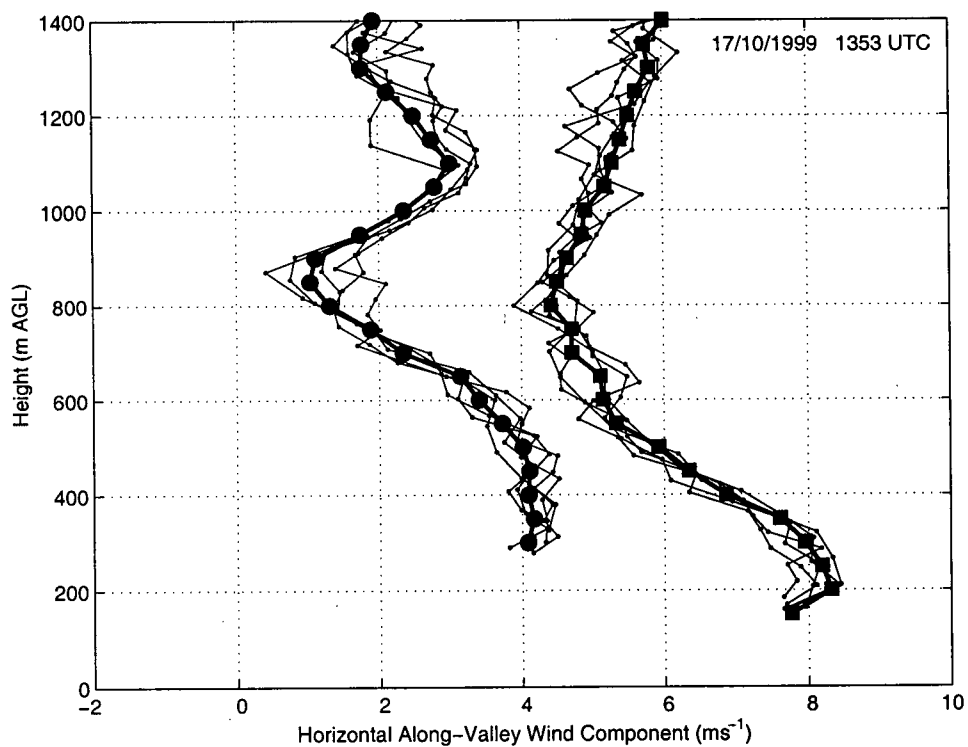


Figure 3.16: Vertical profiles of the horizontal along valley wind component for range gates 8-12 (2.25-3.45 km from lidar) up-valley (solid squares) and down-valley (solid circles) from the lidar site for 17 October. Thin lines with dots show individual profiles while heavy lines with solid circles/squares indicate averaged profiles.

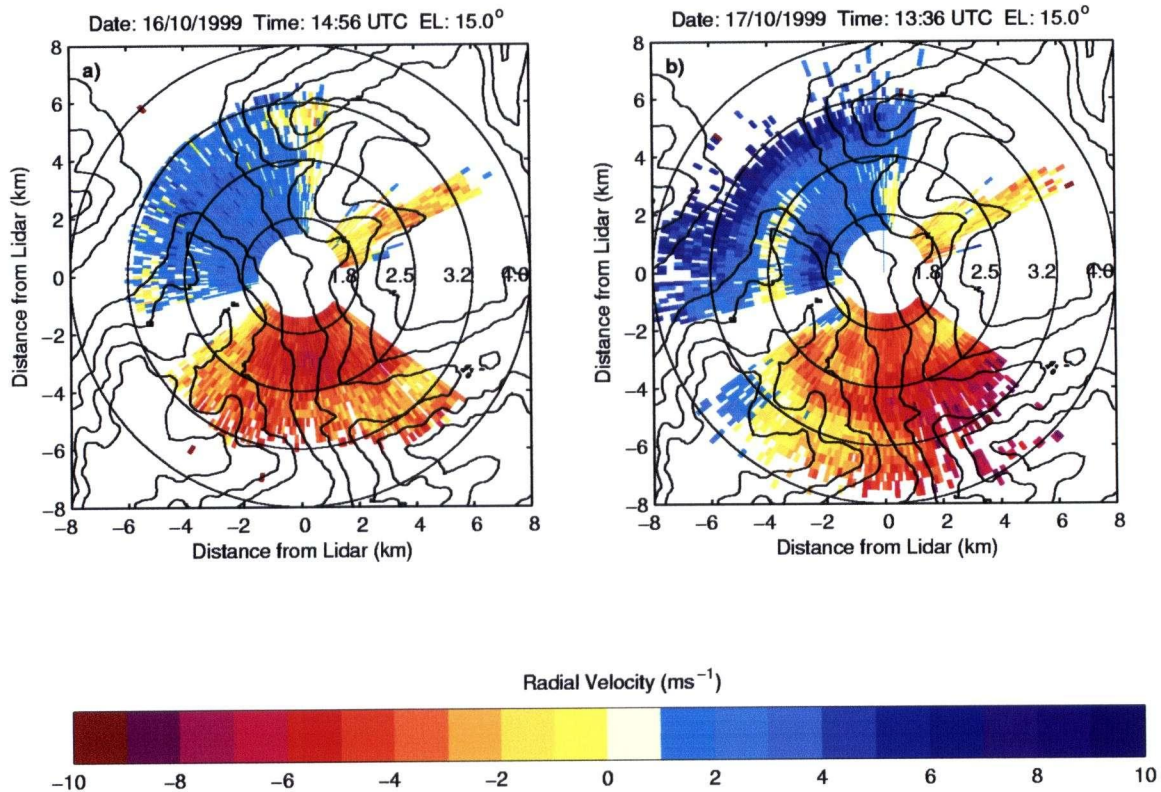


Figure 3.17: VAD scans at 15° elevation for a) 16 October and b) 17 October. The images show the radial velocity component, with positive values indicating flow towards the lidar and negative velocities denoting flow away from lidar. Superimposed are topographic contour lines at 1100, 1400, 1700 and 2000 m ASL. The range rings mark the horizontal distance in km from the lidar (as indicated on the left and bottom axes). The corresponding height (in km) of each range ring is given in the first quadrant.

Figure 3.17 shows VAD scans at 15° elevation for 16 and 17 October. The radial velocities are fairly evenly distributed, and there is no evidence of flow asymmetries, particularly on 16 October. On 17 October, the VAD scan shows strong radial velocities towards the lidar near the western ridgeline between 1600 and 1800 m ASL, but radial velocities away from the lidar at about 2100 m ASL. One possible interpretation is that a strong stable layer at 1800 m ASL (see Figure 3.20) limits the vertical movement of air and forces the flow around the ridge.

In some VAD scans, it appears that the up-valley flow does not entirely fill the widened valley segment to the south of the lidar. Figure 3.18 shows the location of a VAD10 scan in relation to the topography, and the corresponding radial velocities. There is a distinct jump in radial velocity around the 204° azimuth which may indicate a change in the nature of the flow; that is from flow along the Wipptal to flow perpendicular to the valley sidewalls.

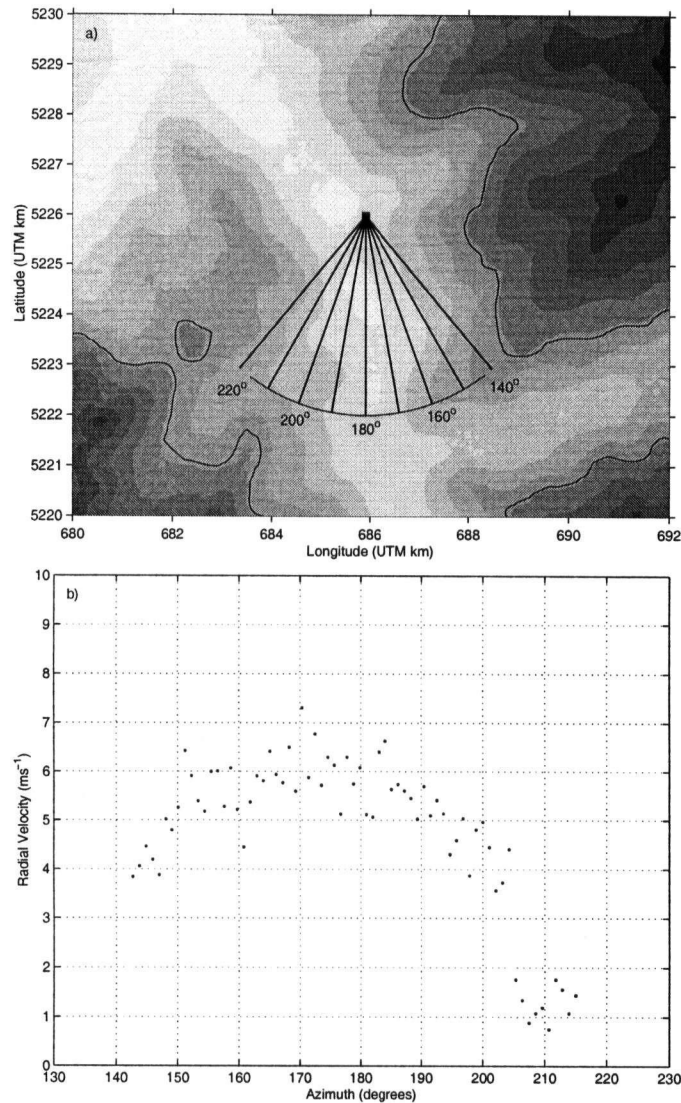


Figure 3.18: a) Location of lidar data obtained for range gate 14 of a VAD scan at 10° elevation (circular arc). The Doppler lidar site is marked with a solid square. Also shown are the azimuth angles in increments of 10° . The contour shading is in intervals of 200 m. The black line indicates the 1770 m ASL contour line (same height as the lidar data for that range gate); b) Radial velocities for RG14 corresponding to circular arc in a). Data is from VAD10 scan at 1453 UTC on 16 October.

3.2.3 Backscatter Intensity Analysis

In this section, an analysis of the backscatter intensity fields is presented in order to examine the distribution of aerosols in the Wipptal in relation to the kinematic structure of the valley flow. The analysis uses the following approach: single pseudo-vertical backscatter intensity profiles at constant range gates are objectively examined for specific structures. This process is then repeated for all profiles and the results are plotted along the valley axis. This methodology

follows very closely the approach taken by Hägeli et al. (2000), but is new for this type of lidar data. Backscatter intensity data from CO₂ lidars cannot be spatially mapped (for a more detailed explanation, see Appendix H) and therefore spatial maps of the raw intensity data are not presented, but rather the structure in the intensity data. It should be noted that this analysis does not consider absolute or temporal trends in backscatter intensity values.

Preliminary examination of pseudo-vertical (created by vertical projecting lidar data from a RHI scan at a constant range gate) backscatter intensity profiles showed the existence of several layer structures. In Figure 3.19, for example, a bottom layer (up to 1700 m ASL) coincides with the valley flow layer as defined by the flow minimum. Another layer extends from 1900 to 2600 m ASL, the top of which corresponds to the height of surrounding mountain tops. Another layer occurs between 2800 and 3300 m ASL before the backscatter intensity levels off. Analogous to De Wekker (2002), the bottom layer may be defined as the valley boundary layer (BL), while the total layer (up to the height of 3300 m ASL) could be considered the mountain BL. The structures of these layers depend on stability structure, local topography, and advective processes.

The overall aerosol structure is influenced by the valley flow system (transport of polluted air into mountain interior), vertical mixing and advection processes (such as mountain venting) which are in turn strongly influenced by the stability structure and the terrain configuration. Although the well-mixed backscatter profile in the lower portion of the valley is reminiscent of backscatter profiles one would expect to see in a convective boundary layer (CBL), one cannot necessarily expect the potential temperature structure to show a well mixed profile. However, the stability structure strongly influences the aerosol layering. So, for example, the rawinsounding at Innsbruck and tethered profiles in the Arzthal confirm an inversion layer at roughly 1800 m ASL (Figure 3.20).

The following analysis concentrates on the along-valley behaviour of the lowest layer which exhibits a well-mixed backscatter profile. This layer will be referred to as the mixed aerosol layer (MAL) to distinguish it from the mixed layer (ML) which infers a well-mixed potential temperature structure. To determine the vertical extent of the MAL, the detection scheme by Steyn et al. (1999) was applied to unsmoothed pseudo-vertical backscatter intensity profiles obtained at constant range gates. This detection scheme identifies the MAL depth by minimizing some measure of disagreement between the observed backscatter profile and an idealized backscatter profile $B(z)$ which is mathematically formulated using

$$B(z) = \frac{(b_m + b_u)}{2} - \frac{(b_m - b_u)}{2} \operatorname{erf} \left(\frac{z - z_m}{s} \right). \quad (3.1)$$

Symbol b_m denotes the mean backscatter in the aerosol layer, b_u is the mean backscatter in the free atmosphere, z_m is the altitude of the aerosol layer top, and s is related to the thickness of the entrainment zone. The idealized backscatter profile in Equation 3.1 represents the profile one would expect under well-mixed convective conditions. In this application, the scheme is

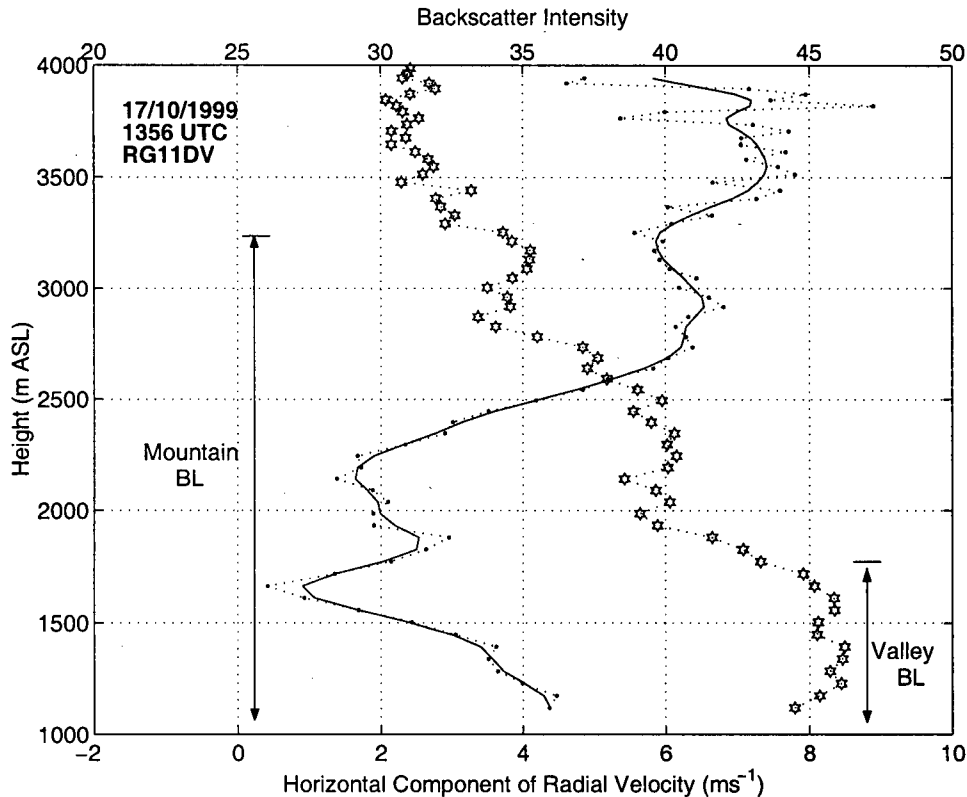


Figure 3.19: Example of pseudo-vertical profiles of backscatter intensity (stars) and horizontal projection of radial wind component (solid dots) at 1356 UTC on 17 October for range gate 11 below the lidar (RG11DV). The solid line shows the smoothed wind profile (using a Gaussian filter with $\sigma = 50\text{m}$).

used to objectively identify the height of the aerosol layer which is clearly distinguishable from the air above. Inferences about the stability of the layer are thereby not made. One of the advantages of this scheme is that it uses the whole profile to determine the MAL height and is therefore fairly robust with respect to elevated backscatter structures (Steyn et al., 1999). It should be emphasized that the chosen fitting profile is highly idealized and only corresponds to the most simplified structure of the PBL - it fails when the backscatter profile exhibits multiple step-like features which do not at all conform with the simple profile that the scheme assumes for backscatter.

Figure 3.19 shows multiple structures in the backscatter profile. To ensure the proper working of the scheme, an upper limit z_b was imposed on each profile to remove the higher layer structures. Values of z_b (determined by trial and error) were 2265, 2165, 2465 and 2365 m for 13, 14, 16 and 17 October, respectively. Physically unrealistic results (such as negative MAL heights, entrainment zones larger than the MAL height) were discarded. In addition, all fits were visually inspected to ensure that the fit was proper.

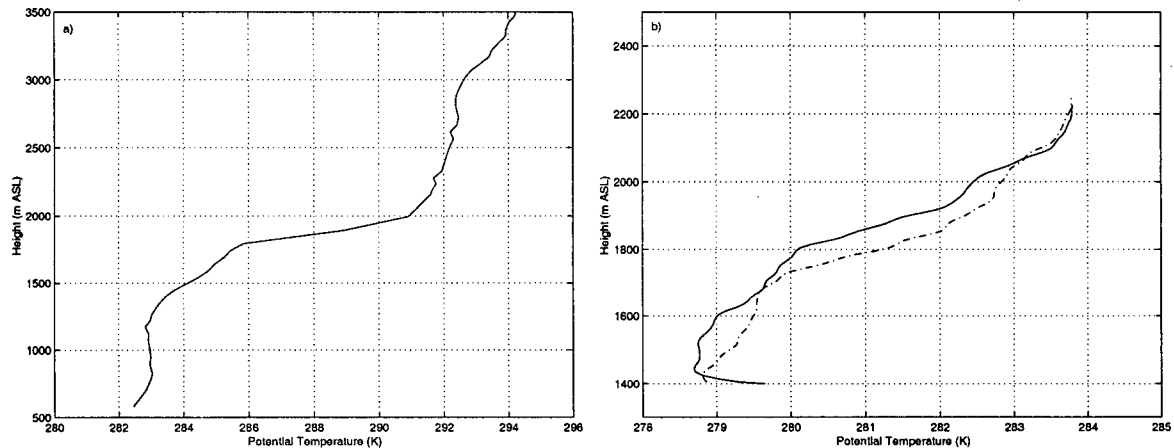


Figure 3.20: Vertical potential temperature soundings for 17 October a) at Innsbruck Airport at 1105 UTC and b) near Doppler lidar at 1335 UTC (solid line) and 1413 UTC (dashed line). Please note use of the different scales.

An example of a single backscatter profile and the corresponding fitted profile is shown in Figure 3.21. The horizontal lines represent the detected instantaneous MAL height and thickness of the transition zone.

By applying the detection scheme to all range gates, the trend of the MAL height along the valley is obtained. Figure 3.22 shows the along-valley MAL depth and the transition zone thickness superimposed on the kinematic field (same as Figure 3.15) for 17 October. The gap in the lines of the first image indicates range gates for which the detection scheme failed. In both images, the MAL depth down-valley from the lidar is slightly deeper than the valley flow (as defined by the height of the wind minimum), but generally follows the inclination of the valley floor. Above the lidar, the MAL height decreases with respect to the mean sea level. This interesting feature, which appears in both RHI cross-sections, may be due to several reasons. Sinking motion over the main valley which compensates flow into the nearby tributary valley may cause the observed decrease in the MAL height. Another explanation, however, may be that this decrease in MAL depth is associated with subsiding motion which is induced by the along-valley volume flux divergence. Analysis of the along-valley volume flux is presented in the following chapter.

Results from 17 October suggest that there is a link between the kinematic flow field and the vertical extent of aerosol mixing. Discussion of the other study days is presented next.

For 13 October, the detection scheme fails for almost all backscatter profiles. Figure 3.23 shows backscatter intensity and radial velocity profiles at 0743 and 1216 UTC for range gate RG10UV. The first profile, taken during conditions of down-valley flow, shows slightly decreasing backscatter intensity values with a sharp drop occurring at roughly 2300 m ASL. At 1216 UTC

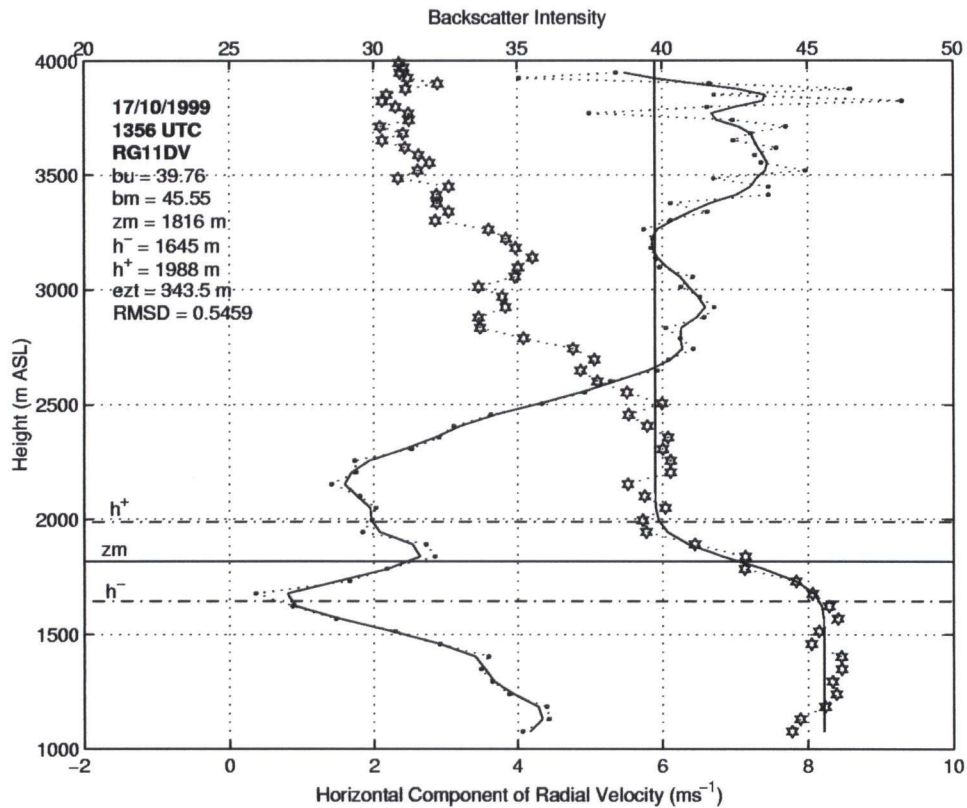


Figure 3.21: Fitted idealized curve calculated by the detection algorithm superimposed on the observed backscatter intensity and radial velocity profiles shown in Figure 3.19.

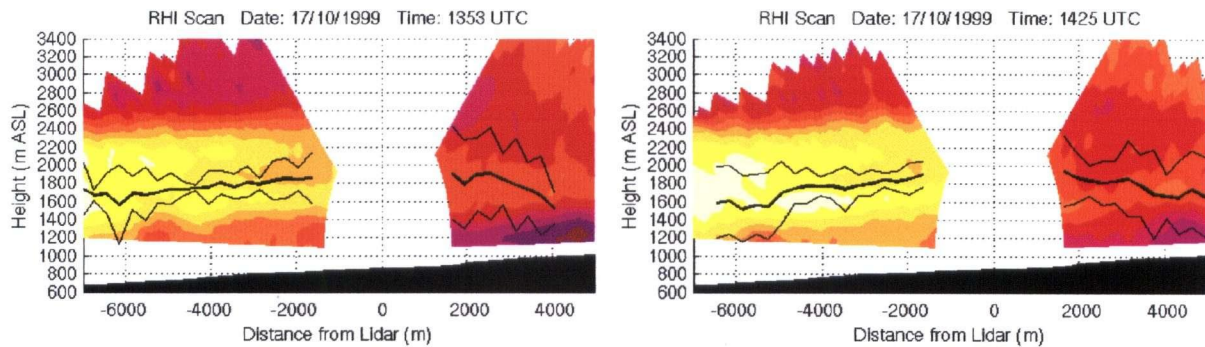


Figure 3.22: Along-valley MAL height and transition zone thickness superimposed on RHI flow fields for 17 October (same as Figure 3.15).

the backscatter intensity decreases almost linearly with height. An MAL cannot be identified even though the up-valley flow is almost 500 m in depth. Structures in the backscatter intensity profiles are qualitatively mirrored by profiles of specific humidity obtained with the tethered

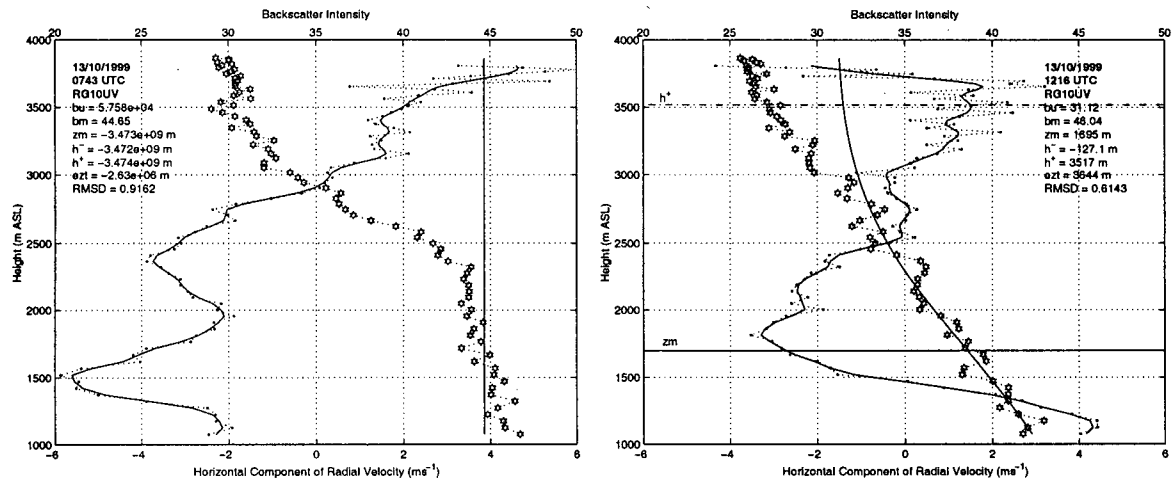


Figure 3.23: Observed (stars) and fitted (solid line) backscatter intensity profiles at range gate 10 above the lidar (RG10UV) on 13 October at a) 0743 UTC and b) 1216 UTC. The horizontal projection of radial wind component (solid dots) is shown for reference.

balloon (Figure 3.24). The first profile at 0700 UTC shows almost no variation in specific humidity with height while later profiles show the specific humidity decreasing with height. Layers in the specific humidity profiles which would indicate a well-mixed convective boundary layer cannot be identified on this day. This suggests that the smaller net radiation due to high-lying cirrus clouds (see Appendix A) allowed less vigorous mixing and slope flow transport in the valley atmosphere. The weak slope flows are also supported by tethered balloon measurements (not shown).

Figure 3.25 shows the along-valley MAL height and transition layer thickness superimposed on wind fields for 14 October. Although the wind field shows little or no vertical structure (except for the wind shear layer at 2000 m ASL), the MAL is well defined for most range gates (see Figure 3.26). In all four RHI images, the MAL height does not follow the inclination of the valley floor, but remains nearly invariant at 1500 m ASL. Another aerosol layer appears to be associated with the wind shear layer at 2000 m ASL. Although no temperature soundings are available for the Wipptal proper, soundings from the tributary Arzthal (Figure 3.27) offer a clue for the non-terrain-following behaviour of the MAL. The first potential temperature profile obtained at roughly 1030 UTC shows a well defined ML capped by a sharp temperature inversion layer of 4 K. The following soundings taken between 1140 and 1400 UTC, however, show a much more complicated boundary layer structure: the ML extends to a height of approximately 1500 m ASL, but the sharp inversion layer has been replaced with several layers of varying stability. The multi-layer structure is also apparent in the specific humidity profiles. These profiles suggest that strong winds aloft eroded the capping temperature inversion and mixed warmer, drier air down towards the surface. Heating at the surface, however, was still vigorous enough to

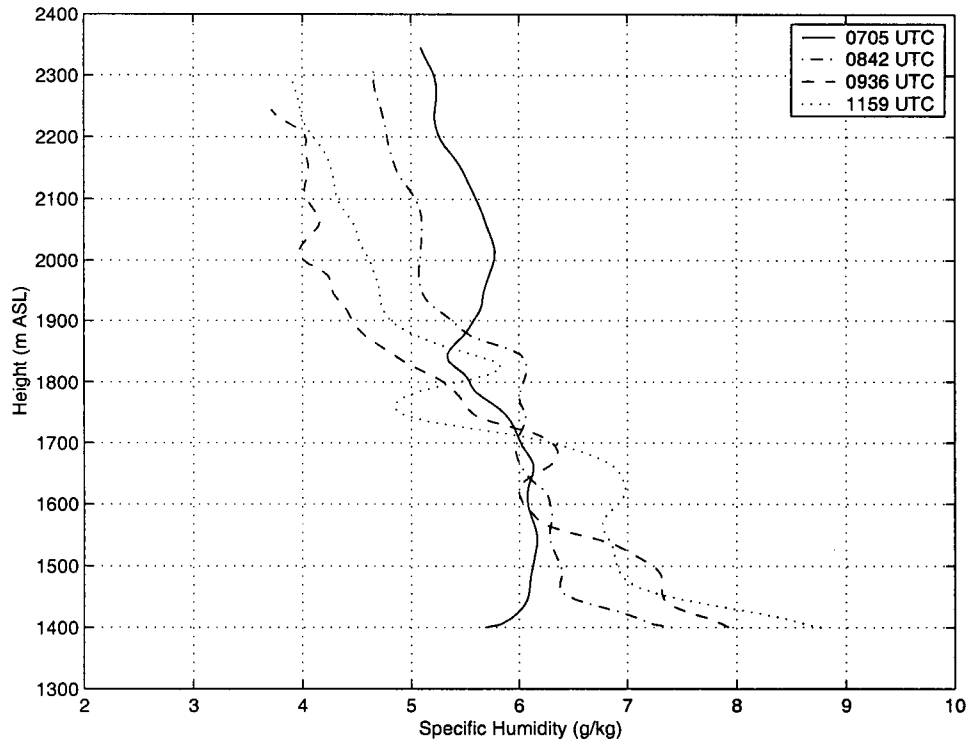


Figure 3.24: Vertical profiles of specific humidity profiles for 13 October.

maintain well-mixed condition for a shallow layer. The down-mixing of strong winds aloft offers an explanation for the lack of a clear minimum (as well as the overall lack of structure) in the lidar observed wind field and the non-terrain-following behaviour of the MAL height. The observations on this day suggest that the top of the MAL is not determined by the strength of surface heating, but rather by the eroding effects of large-scale winds aloft.

Finally, Figure 3.28 shows the temporal behaviour of the MAL for 16 October. Above the lidar where the valley flow is fully developed, the MAL is relatively deep, reaching heights of roughly 2000 m ASL. The MAL structure mirrors the behaviour of the isodop lines (lines of equal radial wind speeds); that is, the depth of the MAL *decreases* with distance in the up-valley direction. After 1300 UTC, the detection scheme fails for almost all range gates above the lidar. Figure 3.29 shows vertical backscatter profiles for the same range gate at 1225 and 1405 UTC. A well defined MAL can be seen in the profile at 1225 UTC, but not at 1405 UTC. It is interesting to note that the almost total failure of the detection scheme corresponds with the observed 'up'-mixing of wind speed and the disappearance of the layered structure in the flow field.

The decrease in MAL depth above the lidar is also observed on 17 October (see Figure 3.22), but a similar descent of the isodop lines is not apparent on that day. Of interest on 16 October is also the large jump in MAL depth across the minimum range of the lidar at 1225 UTC

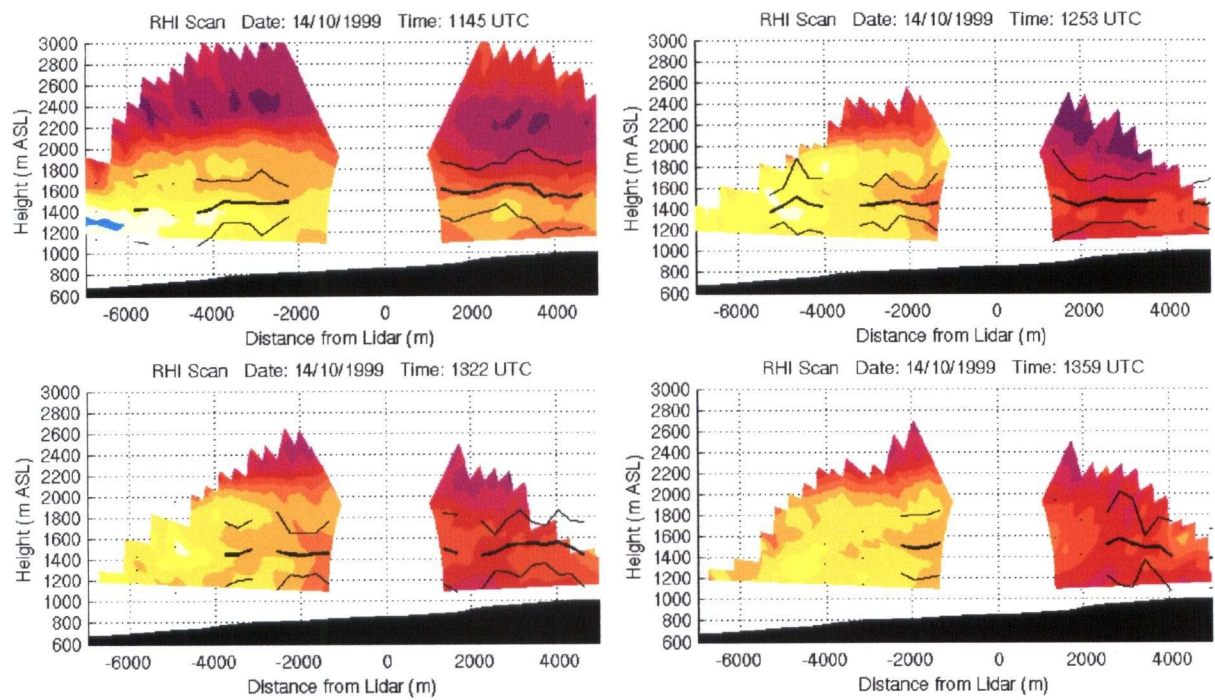


Figure 3.25: Along-valley MAL height and transition zone thickness superimposed on RHI flow fields for 14 October (same as Figure 3.11).

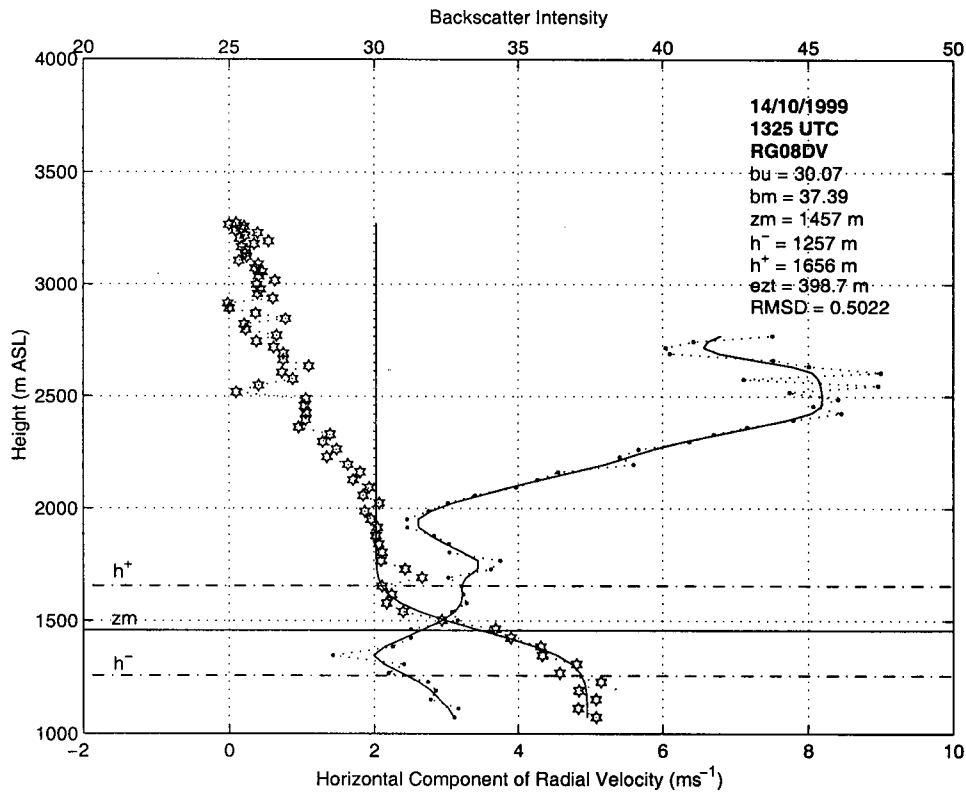


Figure 3.26: Observed (stars) and fitted (solid line) backscatter intensity profiles at range gate 8 below the lidar (RG08DV) on 14 October at 1325 UTC. The horizontal projection of the radial wind component (solid dots) is shown for reference.

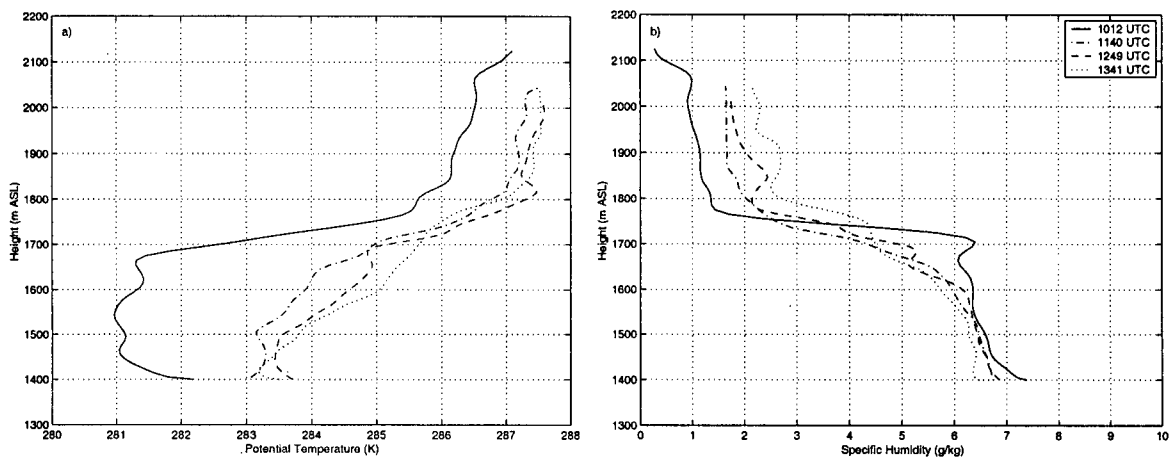


Figure 3.27: Soundings of a) potential temperature and b) specific humidity near the Doppler lidar for 14 October.

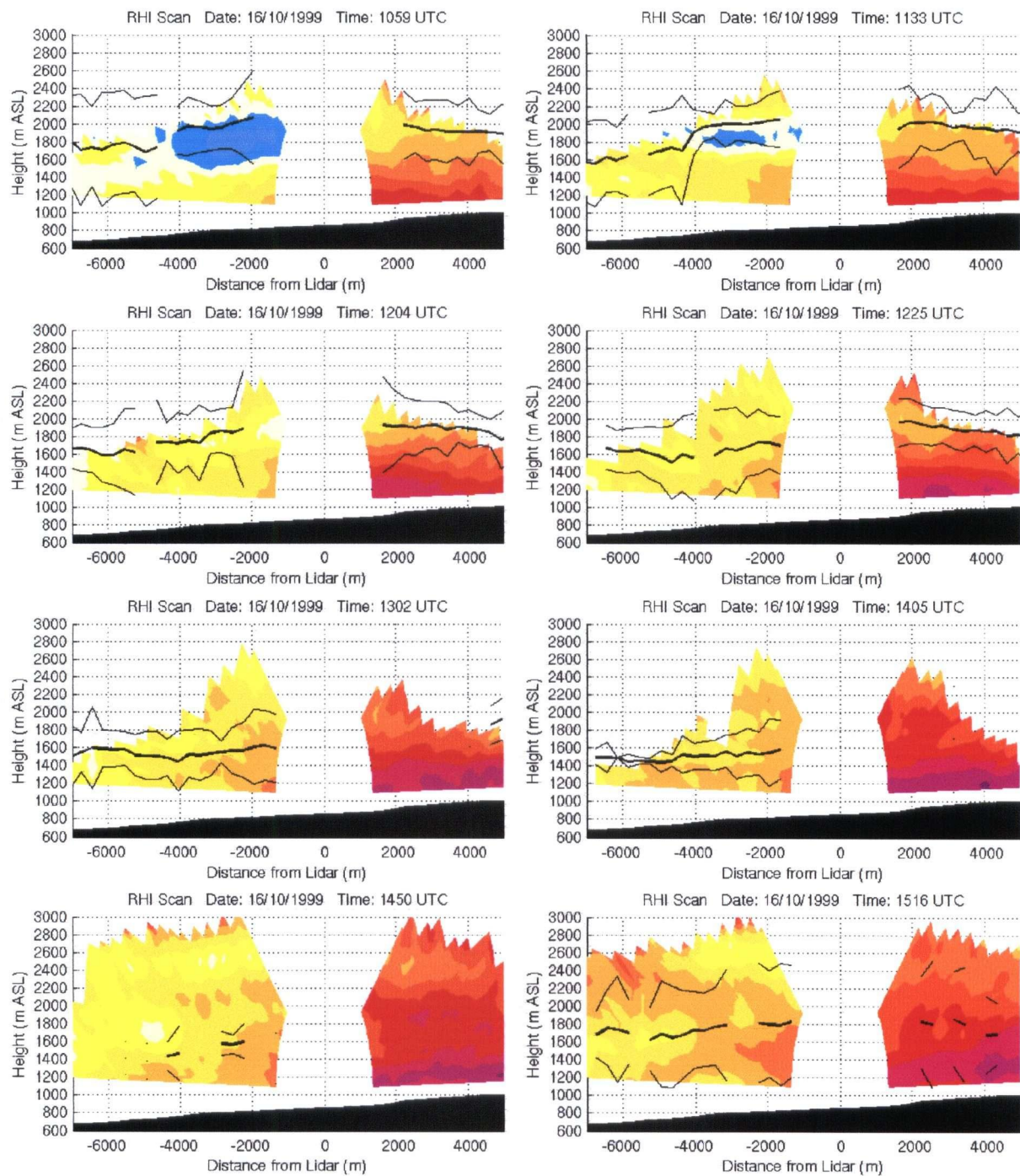


Figure 3.28: *Along-valley MAL height and transition zone thickness superimposed on RHI flow fields for 16 October (same as Figure 3.13).*

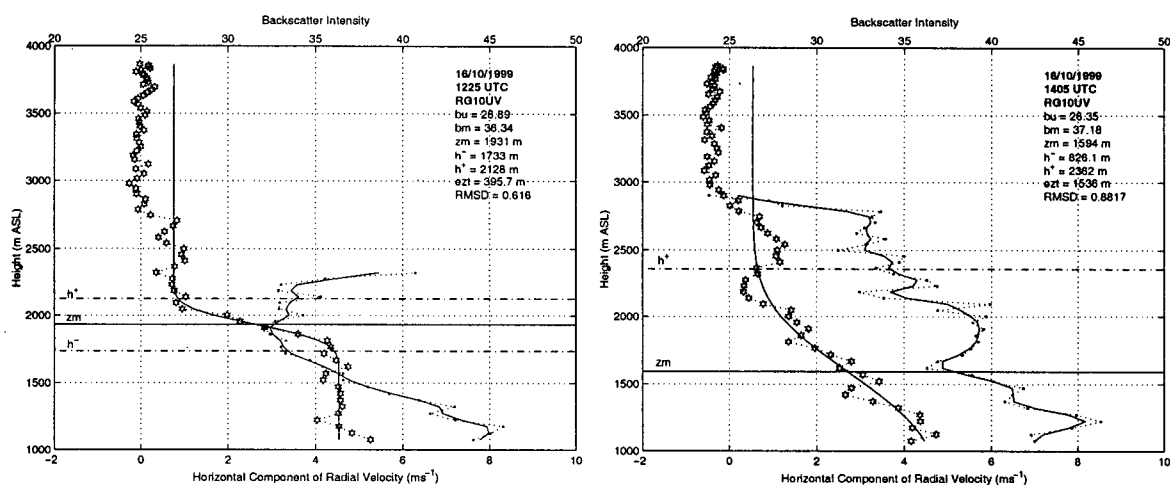


Figure 3.29: Observed (stars) and fitted (solid line) backscatter intensity profiles at range gate 10 above the lidar (RG10UV) on 16 October at a) 1225 UTC and b) 1405 UTC. The horizontal projection of the radial wind component (solid dots) is shown for reference.

(Figure 3.28). One possible explanation for this is that much greater heating and turbulent mixing of the valley atmosphere occurs in the narrow section of the valley (i.e. within a 2 km radius of the lidar).

Down-valley from the lidar, the MAL height matches the top of the return flow layer at about 2000 m ASL. Between 1100 and 1130 UTC, a drop in MAL height occurs at roughly 4 km down-valley from the lidar where the return flow ceases. As the return flow layer dissipates, the MAL decreases gradually to a height between 1400 - 1600 m ASL. In contrast to the MAL south of the lidar, the MAL north of the lidar remains relatively well defined as indicated by the success of the detection scheme. It is difficult to say what causes the top of the MAL to correspond with the top of the down-valley wind. While it is possible that the MAL is a nocturnal residual layer, the close correspondence between the return flow layer and the MAL suggests that as the upper level flow bifurcates from up-valley to down-valley, aerosols at higher elevations of the valley flow south of the lidar are transported in the down-valley flow at the same height.

The distinct difference in performance of the backscatter scheme between up-valley and down-valley profiles may be used to infer differences in convective activity between the up-valley and down-valley portion of the valley. One possible explanation for this pattern is that in the down-valley portion, subsidence occurs to provide mass continuity for the flow divergence in the valley, while in the up-valley portion, vertical mixing due to greater heating is blurring the boundary between the mixed layer and mountain atmosphere. It is believed that on this day, shear-driven entrainment plays little or no role as the winds aloft are weaker than the valley flow.

3.3 Summary

The *in-situ* and lidar observations presented in this chapter show thermally driven valley flows under varying external conditions. On 11 October, a well defined valley flow system develops under weak, opposing ambient winds. The valley flow is roughly 1400 m deep, and quite strong. On this day, wind speeds of about 8 m s^{-1} are observed in the middle of the valley atmosphere. On 13 October, a localized windstorm occurs roughly 10 km up-valley from the lidar and cirrus clouds greatly reduce the surface warming, but a valley flow - albeit shallow and weak - still develops on this day. On 14 October, moderate winds aloft in the same direction as the valley flow disrupts the valley flow, mixing down into the valley atmosphere, and destroying much of the vertical structure seen on other days. On 16 October, the upper level winds are weak and in the same direction as the valley flow. The valley flow system that develops on this day is approximately 1100-1400 m in depth. The wind structure as well as the backscatter intensity analysis suggests that the capping inversion is eroded in the afternoon and the valley flow recouples with the flow aloft. Because the wind aloft is weak, the valley flow system is not disrupted. On 17 October, a well defined valley flow system develops under moderate upper level flows in the same direction as the valley flow, whereby a strong inversion keeps the valley flow decoupled from the upper level flow. On this day, near surface wind speeds of 10 m s^{-1} are observed.

Despite differences in the ambient wind conditions and the spatial structures of the valley winds, several similarities are also observed. These are summarized as follows:

- On all days, an increase of the along-valley wind component with distance in the up-valley direction is observed in the section surrounding the lidar site.
- As the valley flow increases in the up-valley direction, the flow structure changes as well. In particular, the vertical wind profile changes from flat (almost parabolic) to Prandtl-shaped. The wind speed maximum thereby shifts closer to the ground.
- The morning transition period from down-valley to up-valley flow occurs more quickly south of the lidar than north from the lidar (11 and 16 October).
- Above the ridgeline, the flow intensity also appears to increase with up-valley distance (11, 16 and 17 October).
- During the evolution of the valley wind, the flow structure up-valley from the lidar initially is constant or decreases in height relative to mean sea level. Only later in the afternoon does the flow become terrain following (13 and 16 October).
- There are no particular asymmetries in the cross-valley structure visible in the lidar data.

- Backscatter intensity profiles show the existence of several aerosol layer structures. Generally, the lowest layer is associated with the valley flow, while the upper layer often coincides with the mountain tops.
- On 16 and 17 October, the MAL depth up-valley from the lidar tends to decrease with along-valley distance.
- There is evidence that suggests that the intensity of vertical (convective) mixing may vary between valley segments.
- On one day, the MAL is - in addition to the convective mixing - influenced by large-scale flows aloft. In particular, the MAL height is not determined by a capping inversion layer, but is rather determined by a layer of wind shear aloft (14 October).

Chapter 4

Mass (Volume) Budget, Vertical Motion and the Role of Topography

In this chapter, the mass (volume) budget for the Wipptal is examined in order to understand the underlying physical process of the observed wind field, particularly the along-valley flow divergence. Lastly, the possible role of topography is examined by analyzing the along-valley variation of the topographic amplification factor (TAF).

4.1 Mass (Volume) Budget and Vertical Motion

In the following analysis, the flow is assumed to be steady and incompressible. The incompressibility assumption allows the air density to be treated as a constant and mass fluxes to be expressed as volume fluxes. The steady-state volume flux budget for an idealized valley segment shown in Figure 4.1 is given by

$$V_{x_{out}} - V_{x_{in}} + V_{tributary} + V_{slope} + V_w = 0 \quad (4.1)$$

where $V_{x_{out}}$ is the along-valley volume flux leaving the valley segment, $V_{x_{in}}$ is the along-valley volume flux entering the valley segment, $V_{tributary}$ is the volume flux leaving through tributaries, V_{slope} is the volume flux leaving via slope flows, and V_w is the volume flux leaving the segment through the top (the arrows in Figure 4.1 indicate the direction of flow for which the fluxes are positive). From Equation 4.1, one can infer that for the daytime situation mass leaving the valley segment through tributary and slope flows is balanced either through flow convergence along the valley axis ($V_{x_{out}} - V_{x_{in}} < 0$) or through subsidence ($V_w < 0$) at the top of the valley segment. However, if there is volume flux divergence along the valley axis ($V_{x_{out}} - V_{x_{in}} > 0$), then subsidence *must* occur to balance both the along-valley flow divergence and the air leaving through slope and tributary flows. This analysis concerns itself primarily with the along-valley volume flux, and the vertical motion implied by the along-valley volume flux divergence/convergence.

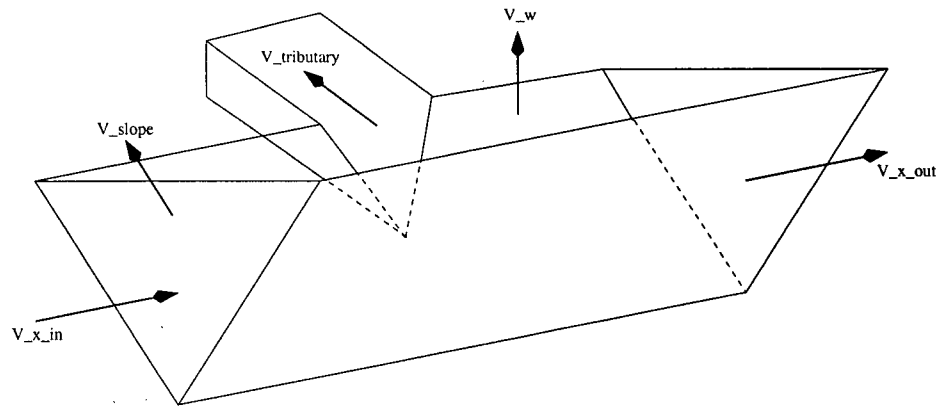


Figure 4.1: Schematic representation of the volume flux budget for a valley segment (drawn for the daytime situation).

4.1.1 Analysis

The along-valley volume flux is calculated for each range gate using the formula

$$V(\zeta) = \int_0^{h(\zeta)} F u(\zeta, z) w(\zeta, z) dz \quad (4.2)$$

where $V(\zeta)$ denotes the total volume flux [$m^3 s^{-1}$] as a function of along-valley distance ζ [m], $w(\zeta, z)$ [m] is the width of the valley as a function of height and distance, and $u(\zeta, z)$ [$m s^{-1}$] is the lidar-measured, along-valley wind component as a function of height and distance. The weighting factor F represents the ratio of the mean cross-sectional, along-valley wind speed and the wind speed measured by the RHÍ scan. This weighting factor, which is very similar to the flux ratio used by King (1989), takes into account that the cross-valley profile of the along-valley

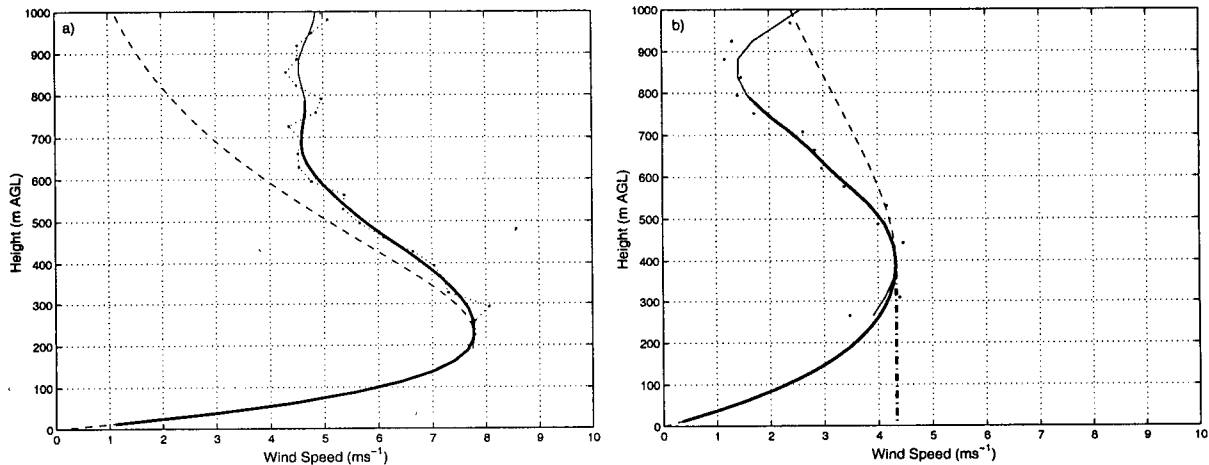


Figure 4.2: Examples of wind profile extrapolations to the surface for a) above the lidar and b) below the lidar. The observed profiles are shown with solid dots/dotted lines while the solid lines indicate the smoothed wind profile using a Gaussian filter. The dashed lines represent the Prandtl profiles which match the magnitude and height of the flow maximum in the observed profiles. The heavy lines show the final wind profiles used in the analysis. In (b), the heavy dashed/dotted line marks the 'straight line' extrapolation.

flow component is not homogeneous across the valley.

The analysis is limited to range gates 5-16 in the up-valley direction, and range gates 5-14 in the down-valley direction. Vertical profiles of horizontally projected radial velocities are smoothed using a Gaussian filter with $\sigma = 50\text{ m}$. The numerical integration of Equation 4.2 uses layers that are 25 m in depth. Small azimuth corrections (4%) are applied to radial velocity components for range gates 5 to 7 up-valley from the lidar to account for the local valley orientation but are considered negligible elsewhere.

Since the lidar observations do not extend to the valley bottom, the wind profiles are extrapolated to the surface using a generalized Prandtl formulation of the form of $u(z) = Az e^{-Bz}$ (Figure 4.2) whereby constants A and B are determined separately for each range gate to match the magnitude and height of the flow maximum for that particular profile. This type of extrapolation implicitly assumes that the wind maximum is contained within the observed profile. It is uncertain if this is indeed the case for profiles measured down-valley from the lidar where the data void spans the lowest 300 m of the valley flow. For 17 October, the volume flux based on the extrapolated portion of the flow is roughly 1-7% of the total volume flux in the up-valley direction, and 6-16% in the down-valley direction. On 13 October, the percentages are 4-15% in the up-valley direction, and 11-35% in the down-valley direction. The large percentages for this day are due to the shallow depth of the valley flow.

Cross-sectional widths as a function of height and distance are determined from topograph-

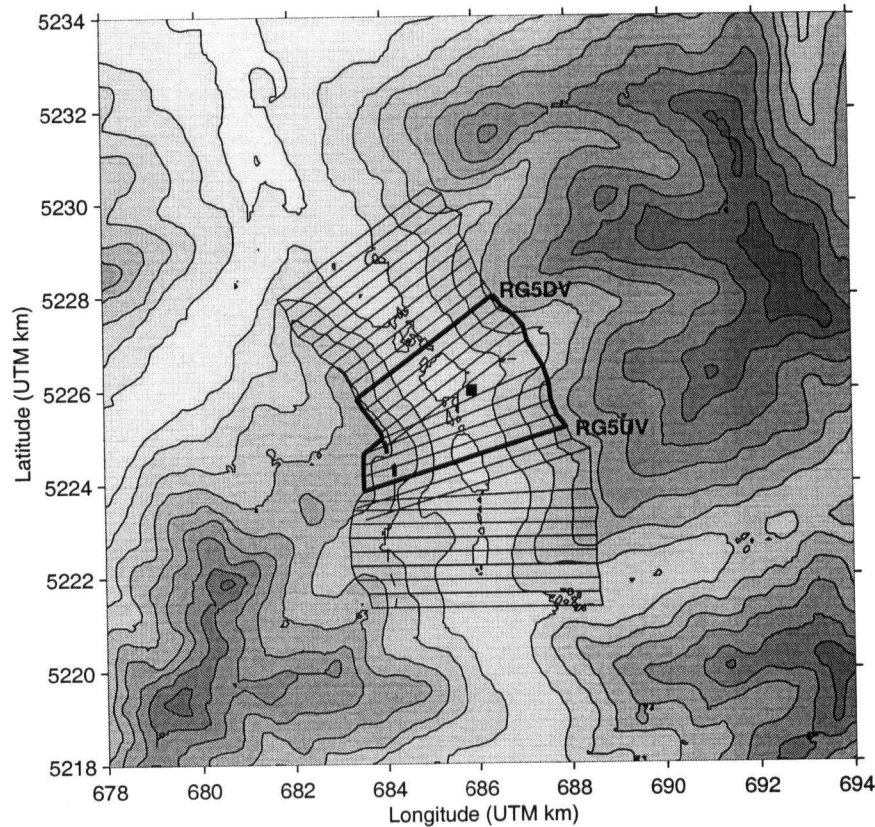


Figure 4.3: Map of study area detailing orientation and width of cross-sections used in the volume flux analysis (range gates RG14DV through RG16UV). The cross-sectional widths are based on a height of 800 m AGL (used for 17 October). The thin/heavy solid lines indicate the outer edges of the budget volumes. The thin/heavy dashed lines shows the cross-section widths by excluding the widening of the valley.

ical cross sections obtained from a 100 m resolution digital terrain model of Tirol. It should be noted that inaccuracies with regard to the height of the valley floor exist in the digital terrain model (shown in Figure 4.3). Cross-sectional profiles were therefore corrected with hand-digitized profiles from a 1:25000 topographical map. The valley is divided into piece-wise straight segments, and cross-sections at each range gate are drawn perpendicular to the local valley orientation (Figure 4.3). Since the analysis concerns itself with the volume flux along the Wipptal and not in its tributaries, some cross-sectional profiles are modified to exclude terrain features associated with sidevalleys. Reductions in cross-sectional areas due to slope flows are considered negligible. Several cross-sectional profiles below the lidar (RG8DV to RG14DV) are extrapolated vertically since the valley flow slightly exceeds the height of the western ridge.

Figure 4.4 shows the cross-sectional area at each range gate for a constant depth of 800 m

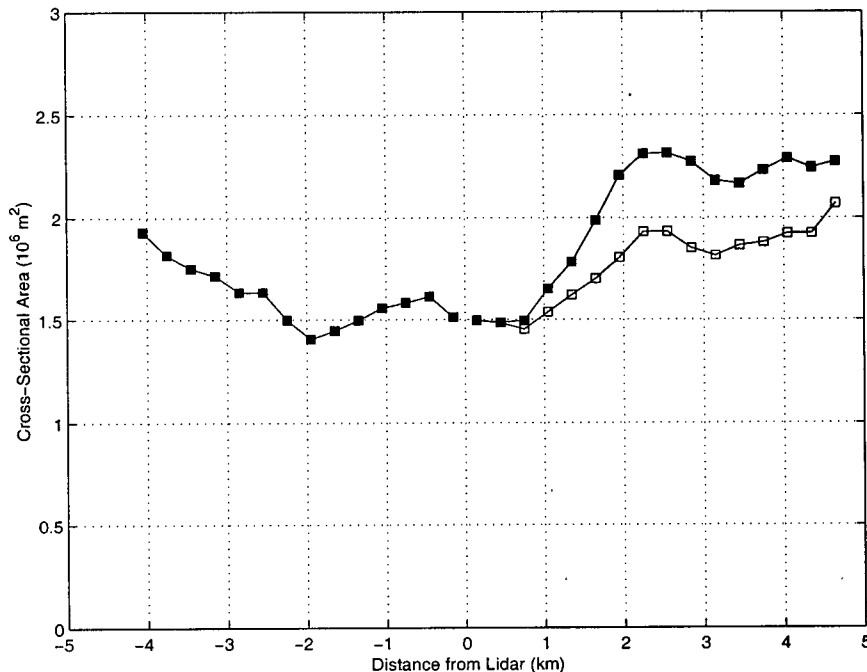


Figure 4.4: Cross-sectional area as a function of along-valley distance for a 800 m deep valley flow layer (solid squares). The open squares represent the cross-sectional areas for modified cross-sections.

(used for 17 October). It clearly shows the constriction in the Wipptal along a 3 km stretch of the valley surrounding the Doppler lidar. Up-valley from this section, the cross-sectional area increases by roughly 50%. In Section 3.2.2, a VAD scan was presented which suggests that the up-valley flow may not fill entirely the widened valley segment. Hence, fictional cross-sectional areas were calculated using radial velocity patterns from VAD scans (such as Figure 3.18) for guidance. The results, however, still show an increase in the cross-sectional area up-valley from the lidar by roughly 30%.

Calculations of the weighting factor F are based on VAD10 scans for range gates which are contained within the valley atmosphere and are not affected by airflow into tributaries (RG5 to RG7). The cross-valley coverage ranges between 70-80%, and the elevation range covered by the range gates varies between 1350-1570 m ASL and 1350-1650 m ASL for the lower and upper valley segment, respectively. Lower elevation PPI scans could not be used due to insufficient cross-sectional coverage (50-60%).

Figure 4.5 shows the normalized along-valley wind data from several VAD scans as a function of normalized cross-valley position for October 11. Although no data is available near the sidewalls, the profiles appear almost flat across the valley. The data points can be fitted fairly

Date	Up-valley	Down-valley
11 Oct	0.836	0.858
14 Oct	0.874	0.873
16 Oct	0.868	0.912

Table 4.1: Values for the weighting factor F .

well to the function

$$\frac{u(y)}{u_m} = a \left(1 - \left(\frac{y}{H}\right)^2\right)^{1/2} \quad (4.3)$$

where $u(y)/u_m$ is the along-valley wind speed $u(y)$ normalized by the mean wind speed u_m at the center of each scan (averaged over a 20° slice), y/H is the cross-valley position y normalized by the valley half-width H and parameter a represents the least-square fit of the data to Equation 4.3. Integrating Equation 4.3 over the valley width and dividing by u_m , one obtains a simple analytic expression for the weighting factor $F = a\pi/4$. It should be noted that Equation 4.3 is primarily used for convenience since it reproduces the almost flat cross-sectional profile but also matches the no-slip boundary conditions at the valley sidewalls. It is, however, not the only curve that the data can be fitted to, and as such, no physical implications are intended with the use of this particular curve.

Table 4.1 lists the values of F obtained for 11, 14, and 16 October. The days 13 and 17 October are excluded from the analysis. On 13 October, the up-valley flow is just barely visible in the VAD10 down-valley from the lidar, while on 17 October only a single VAD scan was obtained. Averaged over the three days and regardless of up-/down-valley location or height, $F = 0.87$. This value is used in the volume flux analysis.

A number of different values for the weighting factor F have been used in previous volume/mass budget studies. Most of the mass budget studies were conducted for drainage flow in the Brush Creek (ASCOT experiments 1982 and 1984). Whiteman (1986) originally assumed horizontally homogeneous conditions ($F = 1.0$), although volume flux calculations from lidar data by King (1989) later showed that this assumption clearly overestimates the true volume flux. King (1989) obtained flux ratios between 0.51 and 0.69. Clements et al. (1989) obtained an empirical value of 0.7 by fitting horizontal cross-valley wind profiles (from lidar data) to parabolic curves. For daytime valley flows in the Inntal, Freytag (1987) used a flux ratio of 0.85. These values are in agreement with experimental results for flow in pipes whereby the ratio is typically 0.5 for laminar flow, and $\approx 0.8 - 0.9$ for turbulent flow (with the ratio being proportional to the Reynolds number) (White, 1986). Generally speaking, the cross-valley velocity distribution for turbulent flow tends to be flat in the center with a sharp drop-off near the sidewalls while for laminar flow, the distribution is more parabolic in shape.

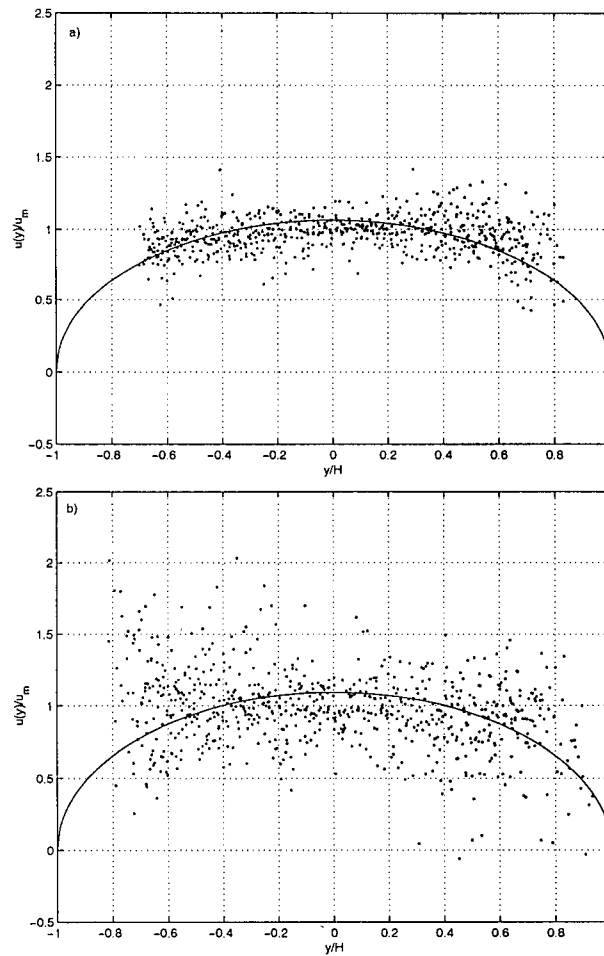


Figure 4.5: Normalized along-valley wind data as a function of normalized cross-valley position in the a) up-valley and b) down-valley direction. Data is taken from VAD scans between 1004 and 1107 UTC on 11 October. H is the valley half-width at the height of the profile. u_m represents the mean wind speed at the center of each scan (320° in the down-valley direction and 178° in the up-valley direction), averaged over a 20° slice. The solid line is the least-squares fit of the data to the function $\frac{u}{u_m} = a(1 - (\frac{y}{H})^2)^{1/2}$.

4.1.2 Results

The following discussion focuses on the volume budget analysis for 13 and 17 October since on these two days the valley flow is well confined by sidewalls. Due to uncertainties in the depth of the flow and/or lack of well-defined valley cross-sections, quantitative results for the remaining days are presented to a lesser extent. The along-valley volume fluxes are based on Prandtl-type profile extrapolations and a flux ratio of 0.87. A dynamic definition is used to determine the vertical extent of the valley flow layer. On 11 and 13 October, the depth of the valley flow layer

is marked by the reversal in the flow direction, while on 17 October the vertical extent of the valley flow is defined by the height of the wind speed minimum which occurs at roughly 800 m AGL.

To account for the effects of the assumptions made in this analysis, volume fluxes were also calculated by varying the flux ratio (F) between 0.82 and 0.92, and using straight line extrapolations for wind-profiles down-valley from the lidar (see Figure 4.2b) and modified cross-sections for range gates up-valley from the lidar (see Figure 4.4). In addition, volume fluxes on 17 October down-valley from the lidar were calculated for a 200 m deeper flow layer. The error estimates in subsequent figures represent the maximum/minimum values that can be obtained with the factors listed above.

Figures 4.6 and 4.7 show the along-valley volume flux for 13 and 17 October, respectively. The first four RHI measurements on 13 October are excluded from the analysis as surface measurements suggest down-valley flows near the surface during the times of those scans. The along-valley volume flux on 17 October is considerably larger than that on 13 October. On both days, the volume flux below the lidar is roughly constant but increases through the narrow section of the valley. Up-valley from the lidar, the along-valley volume flux on 13 October decreases slightly but on 17 October continues to increase, albeit not monotonically. The small dip in volume flux roughly 3 km up-valley from the lidar appears to be partly due to the decrease in cross-sectional area calculated for that valley segment.

By dividing the volume flux at each range gate by the corresponding cross-sectional area, one obtains the volume flux density which can be interpreted as the average wind speed of the whole valley flow layer at that range gate. In contrast to regular wind speed, however, the effect of changing valley cross-sections is removed in the volume flux density; that is, changes in the along-valley volume flux are not caused by lateral constrictions of the valley sidewalls.

Figures 4.8 and 4.8 depict the along-valley volume flux densities for 13 and 17 October. Generally speaking, on both days the volume flux density increases through the narrow section of the valley. On 13 October, however, the rate of increase in the flux density is more gradual and appears to level off or even decrease in the upper valley segment between 1216 and 1244 UTC which coincides with the decrease in solar radiation due to thickening cirro stratus clouds. On 17 October, the volume flux density increases along the entire length of the valley section under study, albeit under varying rates. The largest increase in volume flux density occurs near the lidar site; that is, in the narrow and deep portion of the valley. Interestingly, the volume flux density continues to increase, but to a lesser degree, further up-valley where the valley widens again.

The mean vertical motion required to balance the along-valley volume flux divergence / convergence for a valley segment can be calculated by dividing the difference in volume flux between the outflow and inflow boundaries by the total area at the top of the valley segment. Such calculations were performed for a valley segment bounded by range gates RG5DV and

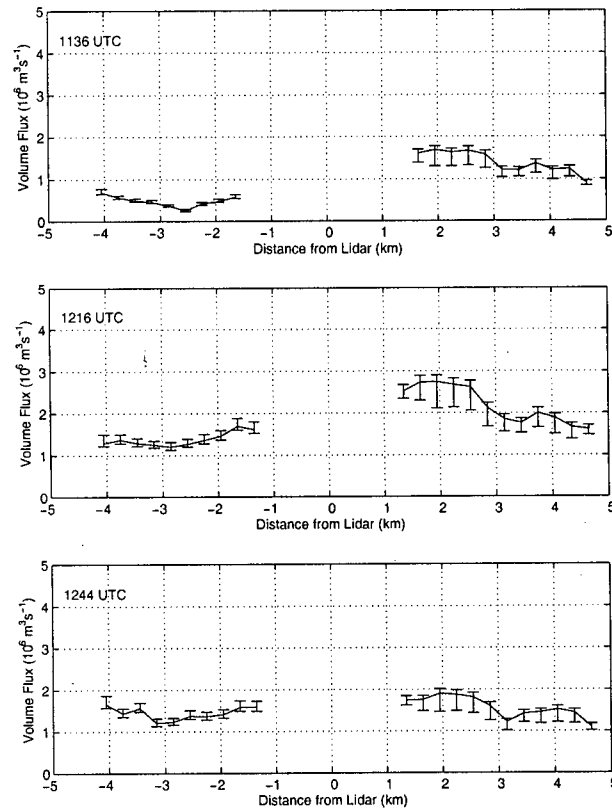


Figure 4.6: Along-valley volume flux as a function of along-valley distance for 13 October at 1136 UTC, 1216 UTC and 1244 UTC.

Date	Time (UTC)	Mean Vertical Velocity ($cm s^{-1}$)
13 Oct	1136	-12 [-10, -13]
	1216	-10 [-7, -14]
	1244	-2 [1, -4]
17 Oct	1353	-46 [-29, -53]
	1425	-39 [-32, -46]

Table 4.2: Mean vertical velocities [$cm s^{-1}$] over the valley segment bounded by range gates RG5DV and RG5UV. Upward motion is positive while downward motion (subsidence) is negative. Error estimates are given in square brackets.

RG5UV¹ (see Figure 4.3). The results are shown in Table 4.2.

Table 4.2 indicates that generally subsidence motion occurs in the narrow valley segment. The mean subsidence velocity on October 13 is approximately $10 cm s^{-1}$ and nearly four times

¹In some cases, RG6 was used instead of RG5. The total area at the top of the valley segment was calculated accordingly.

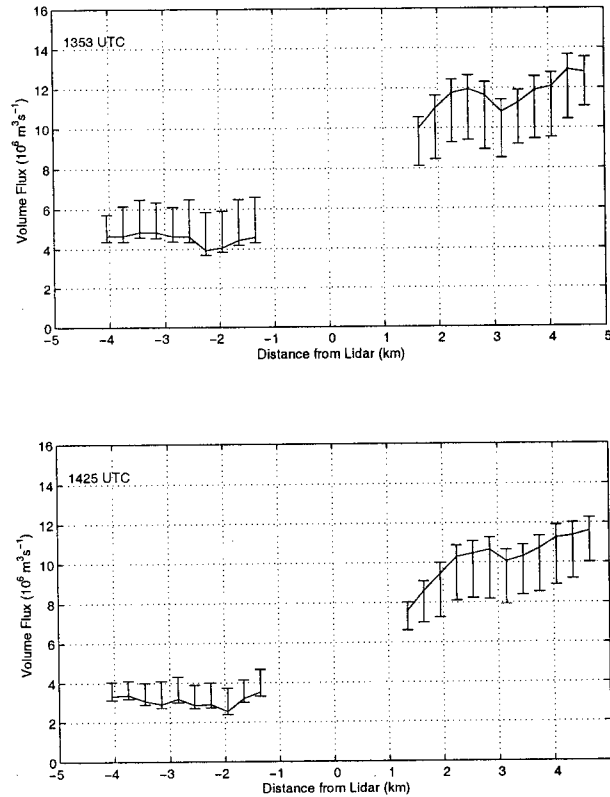


Figure 4.7: Along-valley volume flux as a function of along-valley distance for 17 October at 1353 UTC and 1425 UTC.

that rate on 17 October. It should be emphasized that these subsidence rates are based on the vertical influx of air required to compensate the along-valley volume flux divergence alone. Additional divergence due to slope flows and tributary flows, which have not been taken into account in this analysis, would increase the subsidence rates.

The along-valley volume fluxes for the remaining days (11, 14 and 16 October) are presented next. On these days, the valley flow either reached higher than the surrounding ridgelines and thus was not clearly confined by valley sidewalls (11 and 16 October), or the vertical extent of the flow was not clearly identifiable (14 and 16 October). Because of these uncertainties, flux calculations for 11, 14 and 16 October are not performed in the same detail as for 13 and 17 October, but nevertheless it is important to include volume flux estimates for these days (mean vertical velocity estimates, however, are not attempted). For 11 October, vertical wind profiles were constructed from VAD or PPI scans since no RHI scans were available for those days (see Appendix F for details).

Table 4.3 shows, for all study days, the along-valley volume flux and volume flux density at two range gates, one down-valley from the lidar (RG7DV), the other up-valley from the

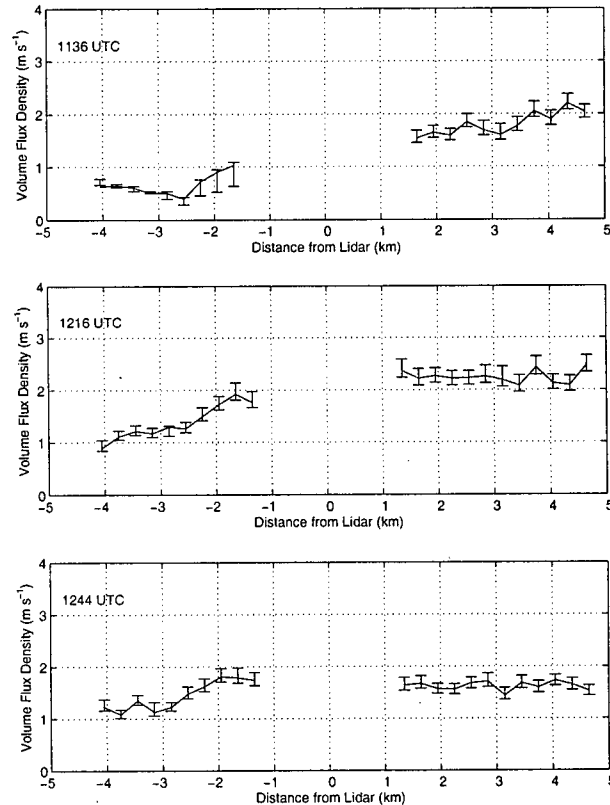


Figure 4.8: Along-valley volume flux density as a function of along-valley distance for 13 October at 1136 UTC, 1216 UTC and 1244 UTC.

lidar (RG7UV). Estimates are shown for both a 800 m deep layer as well as the whole valley flow layer (when clearly defined). On all days, the volume flux and volume flux density are larger up-valley from the lidar than down-valley from the lidar. A comparison of the volume fluxes or flux densities for different days - say, to establish a correlation between magnitude of volume flux (or volume flux density) to surface heating or ambient winds - is of relatively little use since the depth of the flow used in the calculations significantly changes the results. Two important conclusions, however, can be drawn from these results. One, the along-valley increase in wind speed is not caused by lateral constrictions of the valley sidewalls, but rather the flow is accelerating along the valley's axis. Two, the results for 11 October strongly indicate that the increase in along-valley volume flux or volume flux density is not due to interactions with upper level flows (i.e. down-mixing of momentum from aloft) since on this day the flow above the valley wind is weak and in the down-valley direction.

Koßmann and Sturman (2003) recently suggested a conceptual model whereby changes in wind speed and direction could occur along the axis of a bent valley due to pressure-driven channeling when adjacent valley segments have different orientation. Table 4.4 shows the wind

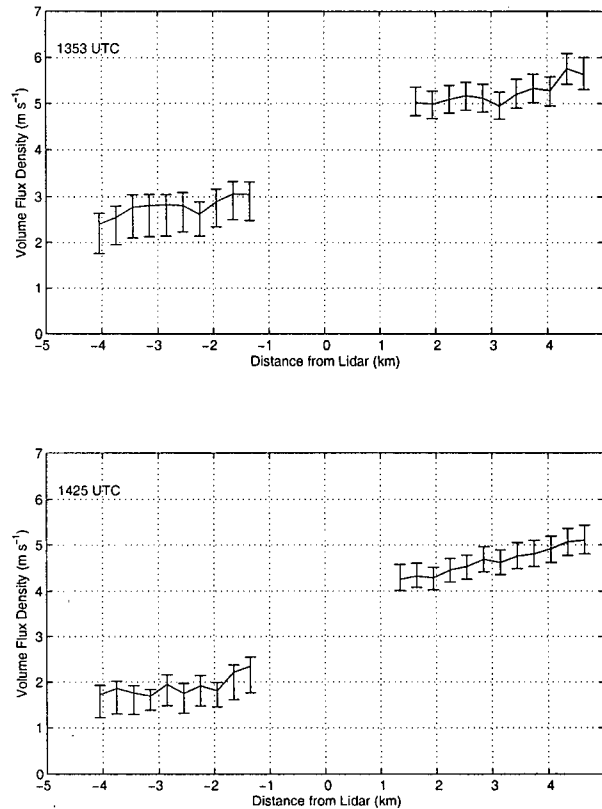


Figure 4.9: *Along-valley volume flux density as a function of along-valley distance for 17 October at 1325 UTC and 1425 UTC.*

speed and direction averaged for a 200 m layer above the mountain tops (2800-3000 m ASL). These values were obtained from radiosonde soundings at the Innsbruck Airport. It should be noted that for 11 and 13 October, these values do *not* represent the winds immediately above the valley flow layer. Kossman's concept does apply here as the upper level along-valley flow component is larger in the down-valley section than in the up-valley segment, while the valley flow increases in the up-valley direction.

In summary, the volume flux analysis leads to the following conclusions:

- The along-valley volume flux increases with distance in the up-valley direction. This is particularly true in a 3 km long segment of the valley where the lidar was located. There is significant subsidence motion in this part of the valley.
- On 17 October, the along-valley volume flux and flux density increases in the widened valley segment up-valley from the lidar.
- The increase in the along-valley flow component with distance in the up-valley direction is not caused by lateral constrictions of the valley sidewalls.

Date	Time (UTC)	Total up-valley flow				Up-valley flow up to 800 m AGL			
		RG7DV		RG7UV		RG7DV		RG7UV	
		Volume Flux ($10^6 m^3 s^{-1}$)	Flux Density (ms^{-1})	Volume Flux ($10^6 m^3 s^{-1}$)	Flux Density (ms^{-1})	Volume Flux ($10^6 m^3 s^{-1}$)	Flux Density (ms^{-1})	Volume Flux ($10^6 m^3 s^{-1}$)	Flux Density (ms^{-1})
11 Oct	1217	11.2	2.15	25.0	3.8	4.2	2.9	13.7	6.1
13 Oct	1136	0.4	0.7	1.6	1.6	-	-	-	-
	1216	1.4	1.7	2.7	1.7	-	-	-	-
	1244	1.4	1.8	1.9	1.6	-	-	-	-
14 Oct	1145	-	-	-	-	2.7	1.9	6.4	2.9
	1253	-	-	-	-	3.6	2.6	11.0	5.0
	1322	-	-	-	-	3.9	2.8	10.0	4.6
	1359	-	-	-	-	3.1	2.2	9.8	4.5
16 Oct	1059	-	-	-	-	1.2	0.8	7.4	3.3
	1133	-	-	-	-	3.3	2.3	8.3	3.8
	1204	-	-	-	-	2.6	1.8	10.1	4.6
	1225	-	-	-	-	3.4	2.4	9.3	4.5
	1302	-	-	-	-	3.3	2.3	11.1	5.0
	1405	-	-	-	-	3.4	2.4	12.0	5.4
	1450	-	-	-	-	3.4	2.4	11.5	5.2
1516	-	-	-	-	4.3	3.1	11.4	5.1	
17 Oct	1353	4.1	2.9	11.0	5.0	4.1	2.9	11.0	5.0
	1425	2.5	1.8	9.4	4.3	2.5	1.8	9.4	4.3

Table 4.3: Volume flux and volume flux density at two range gates (one down-valley from the lidar (RG7DV), the other up-valley from the lidar (RG7UV) for all study days.

Date	Time (UTC)	u_g (ms^{-1})	dir	u_{320} (ms^{-1})	u_{178} (ms^{-1})
11 Oct	00	4.2	298	3.9	1.9
12 Oct	00	6.5	289	5.6	2.1
13 Oct	00	4.1	277	3.0	0.5
14 Oct	00	7.1	307	7.0	4.3
15 Oct	00	8.9	366	8.6	8.2
16 Oct	00	2.4	360	1.8	2.4
17 Oct	12	6.5	292	5.7	2.4
17 Oct	18	9.4	298	8.7	4.4

Table 4.4: Wind speed and direction between 2800 and 3000 m ASL (mountain top height) at Innsbruck Airport, and corresponding components along the 320° and 178° azimuths.

- The increase in the along-valley flow component with distance in the up-valley direction cannot be attributed to interactions with the upper level flow.

4.2 The Role of Topography as Seen Through TAF

As was shown in the previous section, the along-valley divergence of the flow cannot be explained using arguments of mass conservation or external factors. Another explanation is that the flow reacts to changes in the intra-valley pressure gradient which in turn are induced by the geometrical configuration of the Wipptal. In this section, a geometric analysis of the valley

topography based on the TAF concept is presented and put into context with the observed flow features.

McKee and O'Neal (1989) showed that the intra-valley pressure gradient is proportional to the along-valley gradient of the valley geometric ratio; that is,

$$\frac{\partial P}{\partial x} \propto -\frac{\partial \tau}{\partial x}. \quad (4.4)$$

The valley geometric ratio τ can be written as $\frac{A}{V}$ or $\frac{W}{A}$ (see section 1.1) depending on if a whole valley segment or a vertical cross-section is being considered. It should be emphasized that Equation 4.4 does not account for advection processes or changes in surface characteristics. Also, the TAF² concept rests on the very simplified notion of a lid, which restricts the vertical exchange of heat between the valley atmosphere and the ambient air aloft.

For the TAF analysis, the Wipptal was divided into 12 segments (Figure 4.10). The geometric ratio was then calculated for each segment to a height of 1600 m ASL using Geographical Information System software (ARCGIS and ARCMAP).

Figure 4.11 shows the geometric ratio as a function of N-S distance³. The 26-km mark corresponds with the Doppler lidar site and the up-valley direction is to the right. From this figure, it appears that the strongest gradients in the geometric ratio occur just down-valley from the Doppler lidar site, and further up-valley near the Brenner Pass. According to Equation 4.4, the strongest pressure gradients should also occur in those regions. The observed increase in wind speed in the vicinity of the lidar may therefore be related to the change in the valley geometry. On the other hand, however, the volume flux density on 17 October continues to increase in an almost linear fashion in the widened valley section while the geometric ratio remains almost constant through that section. A direct link between flow kinematics and geometric ratios is difficult to establish since along-valley flow acceleration occurs not only with a change in the pressure gradient but also as flow adjusts to a constant pressure gradient.

In conclusion, it appears that the geometric ratio along the Wipptal can be used to predict some but not all of the observed flow features. The usefulness of TAF as a conceptual framework to evaluate or determine kinematic flow structures, however, should not be based on a single valley configuration. Instead, the TAF concept should be tested against all varieties of valley configurations.

²Strictly speaking, the acronym TAF refers to the ratio of the valley geometric ratio to the plain geometric ratio. In this study, the term *TAF analysis* is used to refer to the analysis of valley geometric ratios.

³The bottom axis of this figure corresponds with distance markers in the numerical modeling domain. Figure 5.6, for example, shows the topography in relation to the N-S distance.

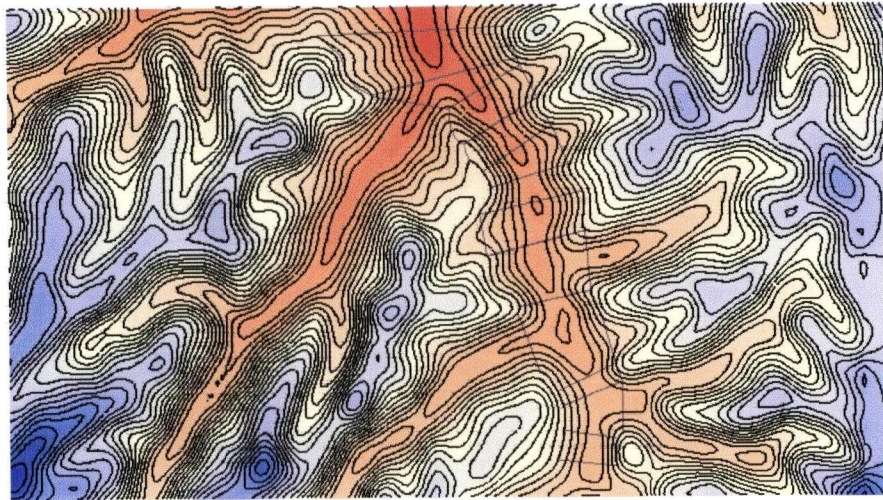


Figure 4.10: *Topographic map of the Wipptal catchment area showing valley segments (grey lines) used in TAF analysis.*

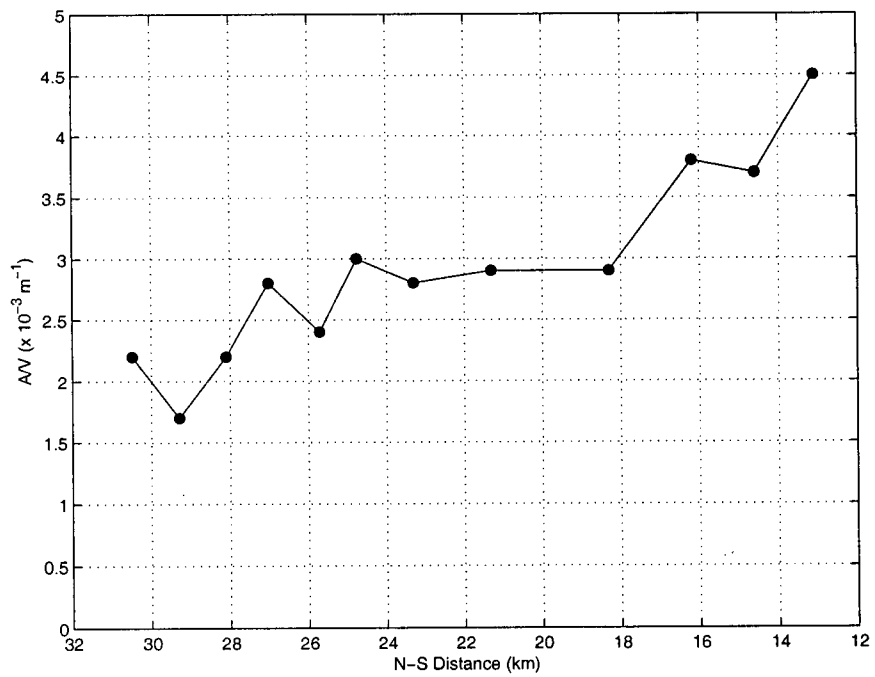


Figure 4.11: Geometric ratios as a function of N-S distance for valley segments shown in Figure 4.10. The 26-km mark corresponds with the Doppler lidar site. Up-valley is to the right of the figure.

Chapter 5

Numerical Study of Valley Flow in the Wipptal

In this chapter, results from numerical simulations of daytime valley flows are presented in order to gain a better understanding of the flow dynamics in the Wipptal. The approach taken for the numerical modeling carries elements of both idealism and realism. The simulations are idealized in the sense that initial and boundary conditions are greatly simplified, but realistic in the sense that the real topography of the Wipptal is used. Thus, the intention of the numerical simulations is not to investigate individual days (i.e. a case study approach), but to shed light on the general processes that lead to the observed flow features in the Wipptal. In this regard, the use of realistic topography allows the modeling results to be discussed in relation to the Doppler lidar observations. A second goal of this numerical study is to explore the role of topography on the flow structure and dynamics. To this end, simulations with different terrain configurations are presented.

5.1 Description of Numerical Model

The model used in this study is the Regional Atmospheric Modeling System (RAMS, version 4.3) (Pielke et al., 1992; Cotton et al., 2003). RAMS is a primitive equation, non-hydrostatic mesoscale model with physical parameterizations for boundary-layer turbulence, radiation, cloud microphysics and land surface interactions. Sub-grid scale turbulence is parameterized using a level 2.5 closure scheme with a prognostic equation for turbulent kinetic energy as proposed by Mellor and Yamada (1982) and modified for the case of growing turbulence (Hefland and Labraga, 1988). Radiative heating and cooling is determined using short- and long-wave radiation schemes by Chen and Cotton (1983). These schemes consider the effects of clouds but do not include the effects of aerosols on radiation. Shading effects due to the orientation and inclination of terrain are accounted for in the shortwave parameterization scheme following Kondratyev (1969). Topographical shading, however, is not included. The subgrid cumulus and cloud microphysics parameterizations are not activated for this study, but resolved clouds are allowed to form in areas of supersaturation based on a diagnostic scheme. Turbulent sensible and latent heat fluxes, and momentum fluxes in the surface layer are evaluated using similarity theory (Louis, 1979). Fluxes are computed separately for soil and vegetation, and are then

averaged to provide grid-area averaged fluxes. Soil and vegetation effects are modeled by the Land Ecosystem Atmosphere Feedback model, version2 (LEAF-2) (Walko et al., 2000), which computes the storage and vertical exchange of heat and moisture at the atmosphere-terrestrial interface. A version of the hydrological model TOPMODEL (Band, 1993) is incorporated into LEAF-2 to take into account horizontal water flow.

RAMS employs a terrain-following sigma-coordinate system which allows the topography to be represented independent of the number of vertical grid levels. One major drawback of this coordinate system - which is not just limited to RAMS but also affects other mesoscale models such as MM5, MC2, ARPS - is that horizontal diffusion is computed along terrain-following surfaces. This can cause spurious temperature and moisture tendencies over mountainous terrain, particularly for atmospheres with strong vertical gradients. Zängl (2002) recently addressed this problem by implementing a set of numerical modifications in the MM5 model to reduce the non-physical impact of horizontal diffusion with a terrain-following sigma-coordinate system. Simulations of local winds in the Inntal using the modified diffusion scheme showed great improvements in comparison to simulations based on the original code. In the present simulations, noisy patterns can also be seen in vertical cross sections of potential temperature. However, in contrast to the findings by Zängl (2002), the present simulated wind fields compare favourably with observations, and hence it appears that even with this flaw, the model is capable of capturing the dominant processes. As much as it would be desirable to correct this numerical deficiency, it lies outside the scope of this work.

5.2 Numerical Set-up and Experimental Design

Although RAMS allows the use of unlimited nested grids, all simulations in this study are performed on a single grid configuration. The decision to use a single grid is based on two factors. First, observations presented in the previous chapters strongly suggest that synoptic scale processes/variability do not explain the along-valley acceleration of the flow. Instead, it appears that this flow phenomenon may be linked to the local terrain. Hence, as long as the local topography is 'sufficiently' represented and boundary effects are minimized, nested gridding should not be required. Second, an important aim of the numerical study is to test different terrain configurations. This is more easily accomplished with a single grid set-up than with nested gridding.

The computational domain of the single grid covers the entire catchment area of the Wipptal. Terrain heights were derived from a 100 m resolution digital terrain dataset. To minimize boundary effects, a border of eight grid points was added to the domain and an iterative smoothing filter was applied to terrain outside the Wipptal catchment area. Inside the catchment, the terrain was smoothed with a Barnes filter to remove smaller scale features but to preserve the main topographical characteristics of the valley. Because of the single grid set-up (which would

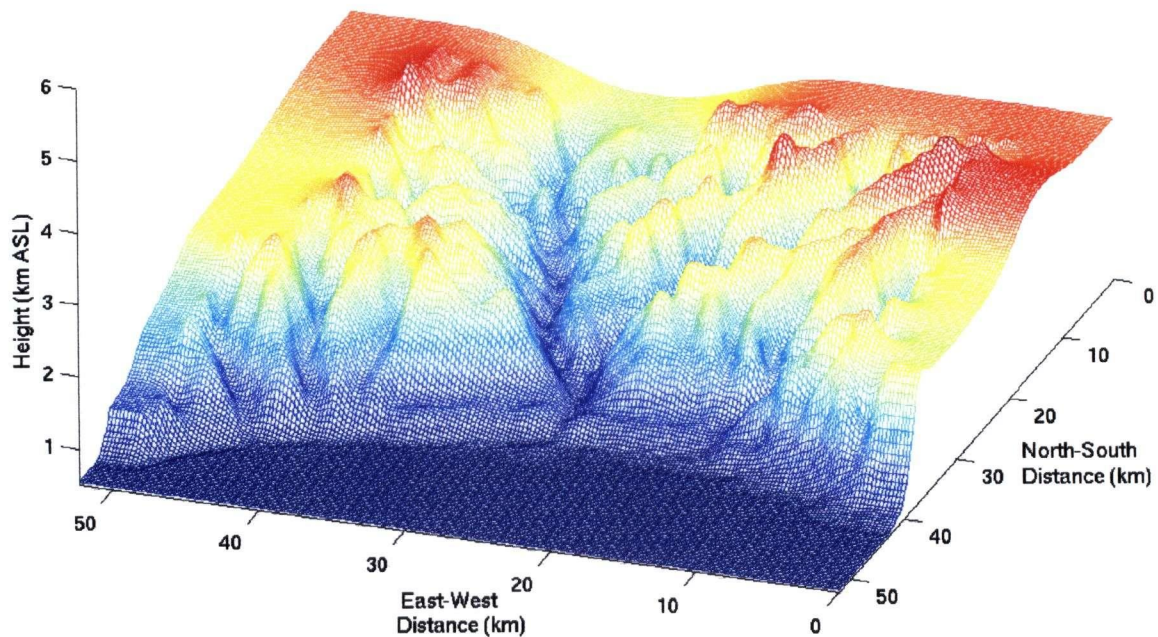


Figure 5.1: *Prospective view (from the north-northwest) of topography in the computational domain (after adding the border and smoothing).*

have captured only a small portion of the Inntal), the terrain of the Inntal was removed so that the Wipptal in the simulations opens up to a plain. Doppler lidar observations show no evidence of winds in the Inntal being channelled into the Wipptal, and thus it is assumed that the winds in the Inntal have no significant influence on the flow in the Wipptal. It is possible, however, that with this terrain modification the pressure gradient at the entrance of the Wipptal may be overestimated since air over the plain would experience less heating than air in the Inntal (volume effect). It is assumed that this plays a minor role on the flow dynamics further up in the Wipptal. The topography of the computational domain is shown in Figure 5.1.

The vertical grid spacing increases from 70 m near the surface to 1000 m near the top of domain at an elevation of 16.5 km ASL. Due to the staggered coordinate system, the lowest grid level is located 32 m AGL. With this grid, ten points out of a total of 37 are positioned within 1000 m of the ground.

A horizontal grid spacing of 250 m is used in order to resolve the geometry of the Wipptal.

Although previous numerical studies of flows over complex terrain have demonstrated that small grid spacing like this can successfully reproduce observed flow characteristics (Fast, 1995; Poulos and Bossert, 1995; Fast et al., 1996; De Wekker, 2002), the use of sub 1-km grid spacing in RANS (Reynolds-averaged Navier-Stokes) based models is still a contentious issue. The argument generally is that with sub 1-km grid spacing, the model begins to resolve turbulent components of the flow which are meant to be parameterized. In this study, it is assumed that convective motions are not resolved and that they need to be parameterized.

All simulations are initialized at 0000 UTC assuming horizontally homogeneous conditions. A 20-h simulation is then made using radiation lateral boundary conditions and a time step of 3 seconds. Simulations of the 209x209x37 computational domain were run on the Linux cluster in the Department of Physics and on the Monster Linux cluster at the Geophysical Disaster Computational Fluid Dynamics Centre, both at the University of British Columbia. Based on 20 processors, simulations took 25 hrs to complete on the Physics cluster, and 19 hrs on Monster.

The simulations are summarized in Table 5.1. Large-scale pressure gradients are neglected in the simulations, since observations clearly show similar flow features under varying external conditions. The initial soil temperature profile is set so that the temperature 1 m below the surface is 3°C colder than the surface. The initial vegetation temperature is set equal to the atmospheric temperature at the lowest model grid point. For the simulations, the atmosphere is assumed to be dry, and hence an initial, constant relative humidity profile of 20% is used. Valley atmospheres (particularly in the Alps) are typically more moist (70-90%), but it is the difference in moisture content between the atmosphere and the soil/vegetation which determines the partitioning of the available energy into sensible and latent heat flux. The soil moisture is used as a tuning parameter to adjust the sensible heat flux to reasonable magnitudes. All simulations are carried out for 11 October (the date affects the amount of solar radiation).

Numerical experiment REF represents the reference simulation. The initial potential temperature profile is based on the rawinsonde sounding at Innsbruck Airport at 0000 UTC on 11 October 1999 (see Figure 5.2). The potential temperature gradient is 0.0082 K m^{-1} below 2200 m ASL and 0.0043 K m^{-1} between 2200 and 5200 m ASL. Surface conditions are uniform for the entire domain. The soil type is specified as silty loam and the vegetation type is short grass. The soil moisture is set to 70% of its saturation value. Although there is no information available on soil moisture values in the Wipptal, observations and modeling of soil moisture for the Riviera Valley (during the MAP-SOP) suggest typical volumetric soil moisture (ratio of volume of water in a soil sample to the volume of total soil sample) values of around 0.31 (De Wekker, 2002) which corresponds to 76% of the soil's saturation value.

In addition to the reference simulation, several numerical experiments - T1 through T4 - were conducted to investigate the influence of different terrain configurations on the flow dynamics in the Wipptal. The terrain configurations for these simulations are described in Section 5.4.

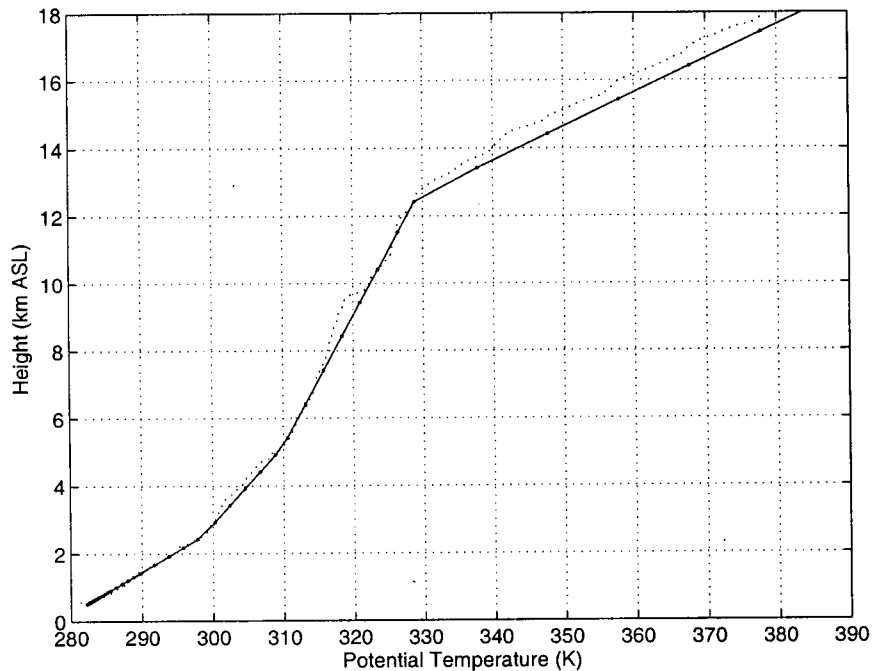


Figure 5.2: Initial potential temperature profile for reference simulation REF (solid line) and rawinsonde sounding for 11 October 1999 (dotted line).

Name	Topography	Initial wind and temperature profiles	Surface characteristics
REF	Real	Pot. temperature profile based on 0000 UTC 11 October 1999 sounding at Innsbruck Airport; calm winds (0.1 ms^{-1})	Uniform vegetation type - short grass; uniform soil type - silty loam; uniform soil moisture (70% of saturation)
T1	Widened valley	As in REF	As in REF
T2	No basin	As in REF	As in REF
T3	Modified valley entrance	As in REF	As in REF
T4	Flat valley bottom	As in REF	As in REF

Table 5.1: Summary of numerical experiments.

5.3 Numerical Experiment REF: Reference Simulation

5.3.1 General Results

The valley flow circulation is driven by sensible heating of the valley atmosphere, and hence it is fitting to examine first the modeled surface energy budget. Figure 5.3 shows the simulated diurnal variation of net radiation and sensible heat flux for a point which corresponds to the radiation site (RS in Figure 2.3) and a point over the plain. The differences in magnitude of the fluxes as well as the temporal shift in the maxima are primarily due to differences in the orientation and inclination of the terrain at the two grid points. Overall, the modeled fluxes

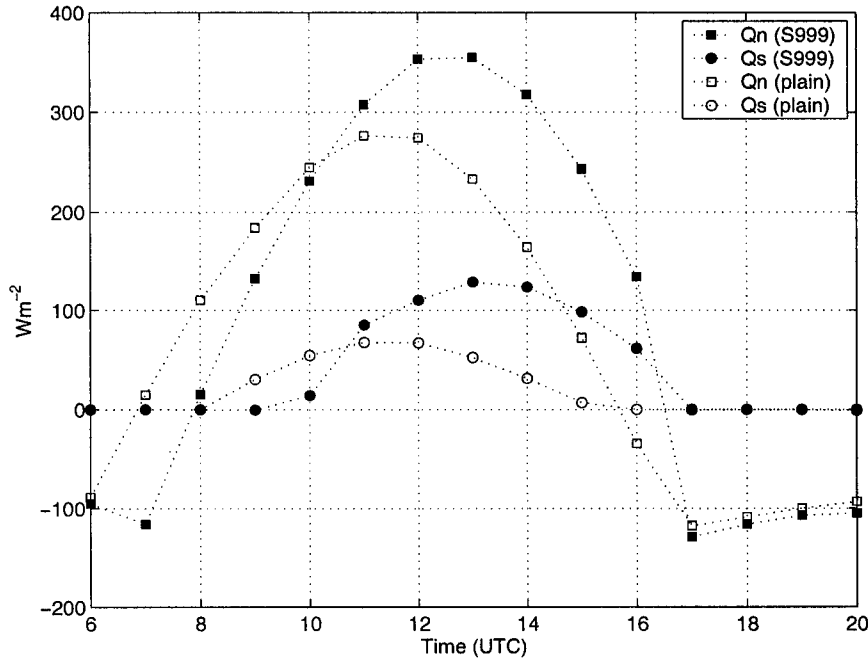


Figure 5.3: Modeled net radiation (Q_n) and surface sensible heat flux (Q_s) corresponding to the radiation measurement site (RS in Figure 2.3) and a point over the plain. Results are for simulation REF.

are of the same magnitude as those obtained from observations (see Appendix A). The spatial variation of the surface sensible heat flux at 1200 UTC is shown in Figure 5.4 which highlights the effect of slope orientation and inclination on the sensible heat flux.

Modeled near-surface (at 32 m AGL) wind fields (Figure 5.5) show that the model clearly simulates daytime up-valley flows. At 0800 UTC, the up-valley wind in the Wipptal is still weak although somewhat stronger flows occur in the upper segments of some of the tributaries. The near-surface flow increases in intensity during the morning hours and reaches maximum values in the Wipptal around 1200-1300 UTC. The near surface wind varies in strength along the Wipptal. The strongest winds can be seen just up-valley from the Doppler lidar site. At 1600 UTC, the near surface flow has weakened, although stronger flows still persist in the vicinity of the Doppler lidar as well as in some of the tributaries. The valley flow finally ceases in those areas around 1800 UTC.

To examine the spatial structure of the flow, the horizontal along-valley wind component is extracted from model output along the path shown in Figure 5.6. This path closely approximates the location of the RHI scans, and hence facilitates comparison between model results and Doppler lidar observations presented in Chapter 3. As with the observations, the along-valley wind component is positive in the up-valley direction.

The vertical structure of the simulated along-valley wind component along the center of the

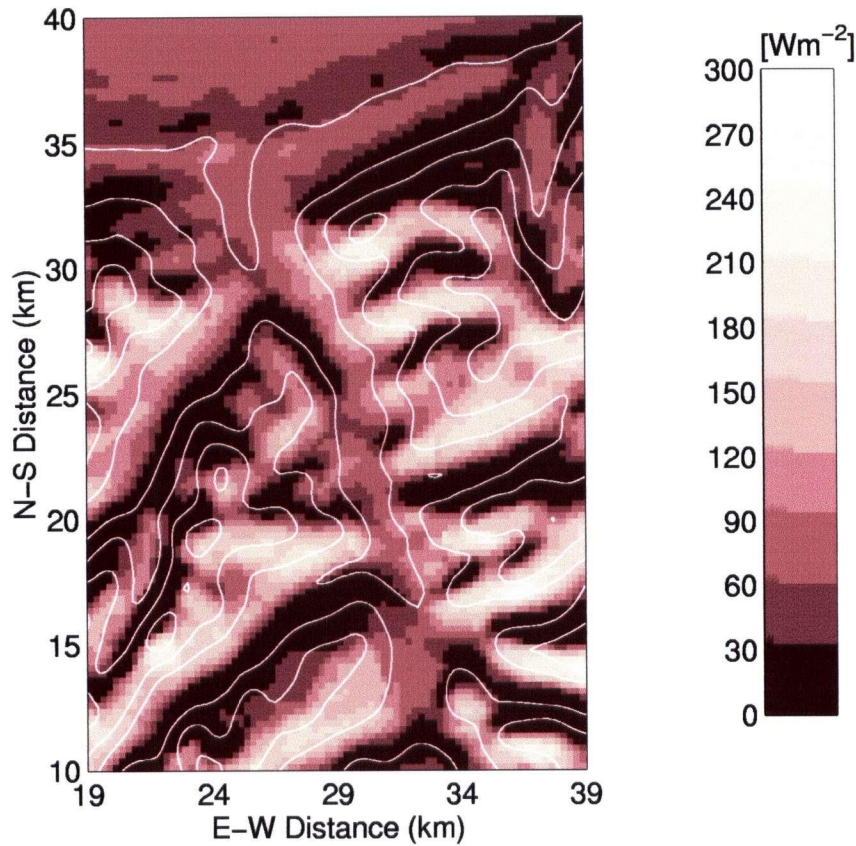


Figure 5.4: *Spatial variation of the modeled surface sensible heat flux for simulation REF at 1200 UTC. Topography is shown with a contour interval of 400 m.*

valley is shown at 2-hr intervals in Figure 5.7. At 0800 UTC, a layer of weak up-valley flow extends to a height of 1600 m ASL. As the morning progresses, the intensity of the along-valley flow increases considerably, with wind speeds reaching $9 - 10 \text{ m s}^{-1}$ up-valley from the lidar at 1200 UTC. Of particular interest is that the modeled flow intensity is not constant along this segment of the Wipptal but that it increases with up-valley distance. This can also be seen in the vertical profiles of the along-valley wind component (Figure 5.8) which were extracted from model output at two locations roughly 2.8 km up- and down-valley from the lidar site (these locations correspond to range gate 10).

Figure 5.9 shows the simulated potential temperature structure and wind vectors for the same along-valley cross-section in Figure 5.7. Several points are of interest. At 0800 UTC, heating occurs in a shallow layer of the atmosphere (between 1000 and 1200 m ASL) in the narrow section of the valley surrounding the lidar site. In subsequent cross-sections, a down-sloping of the isentropes can be seen in the same region where the flow intensity increases. Throughout the day, most of the valley's atmosphere remains stably stratified. A shallow mixed layer roughly

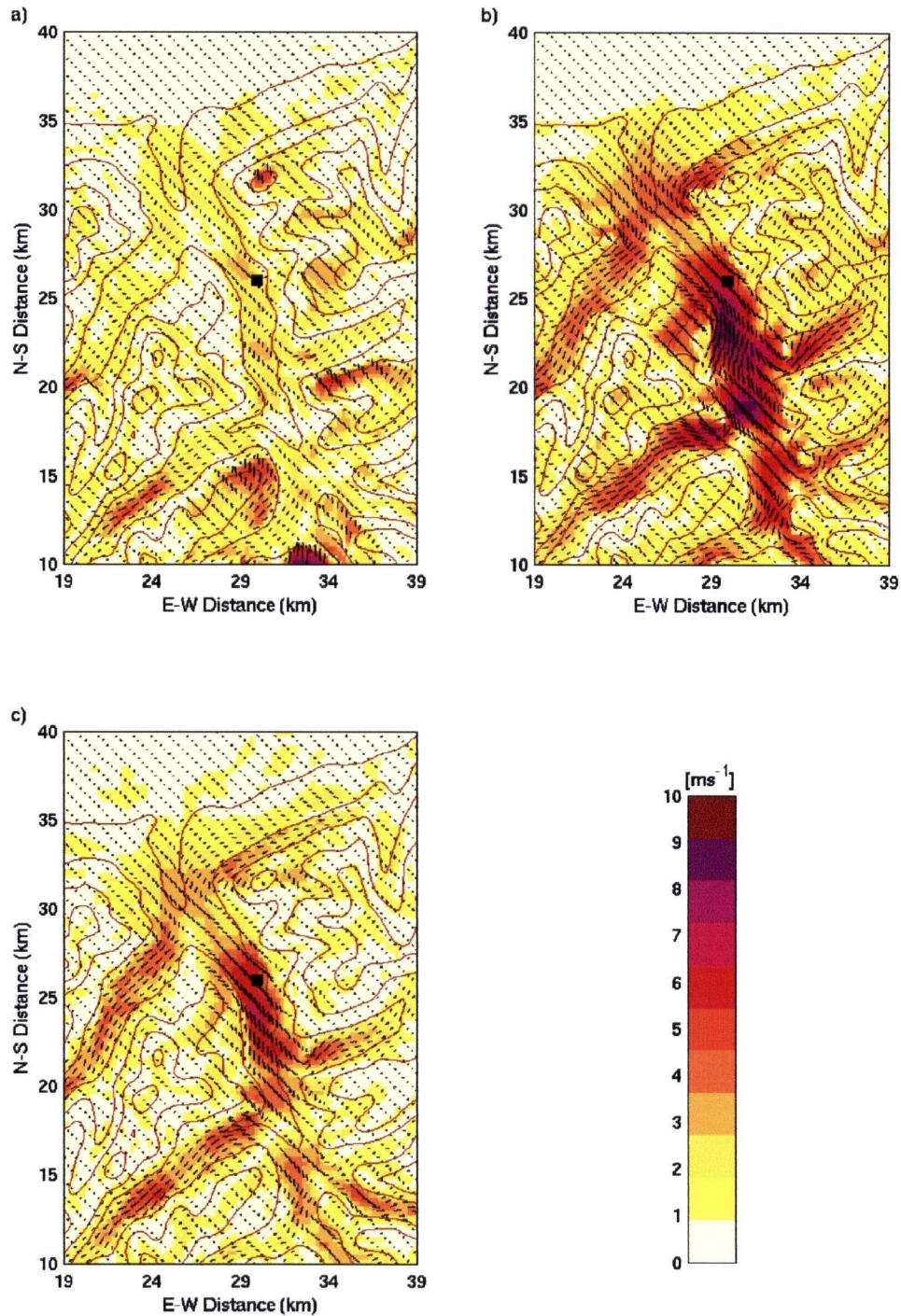


Figure 5.5: *Simulated near-surface winds (32 m AGL) in the Wipptal at a) 0800, b) 1200 and c) 1600 UTC for numerical experiment REF. The shading corresponds to the strength of the modeled wind speed. Wind vectors are shown at every fourth grid point to avoid clutter. For reference, the Doppler lidar site is marked with a solid square. Topography is shown with a contour interval of 400 m.*

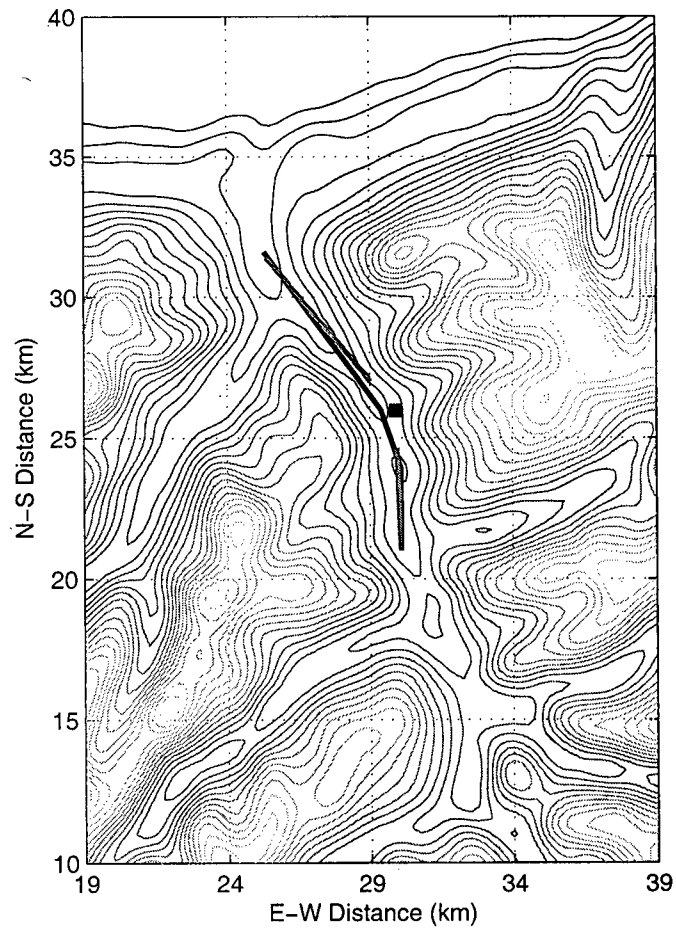


Figure 5.6: Topographical map of the Wipptal, with the location of the Doppler lidar RHI scans (gray line), and the line for which modeled along-valley wind speeds were extracted (black line). The Doppler lidar site is shown with a solid square.

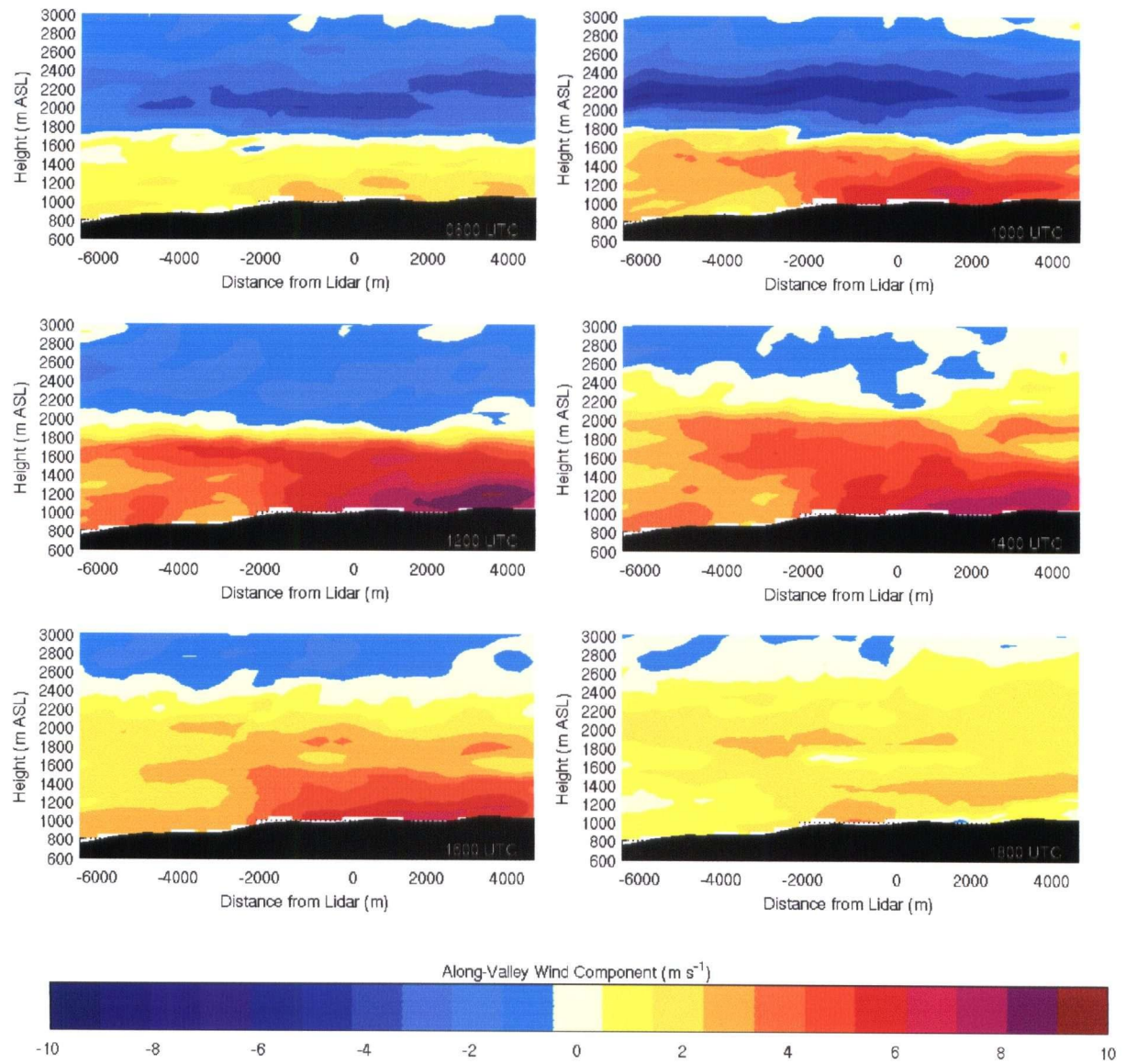


Figure 5.7: Modeled RHI cross-sections of the along-valley wind component along the path shown in Figure 5.6 for REF. The solid black area marks the valley floor. Sections are at 2-hr intervals starting at 0800 UTC.

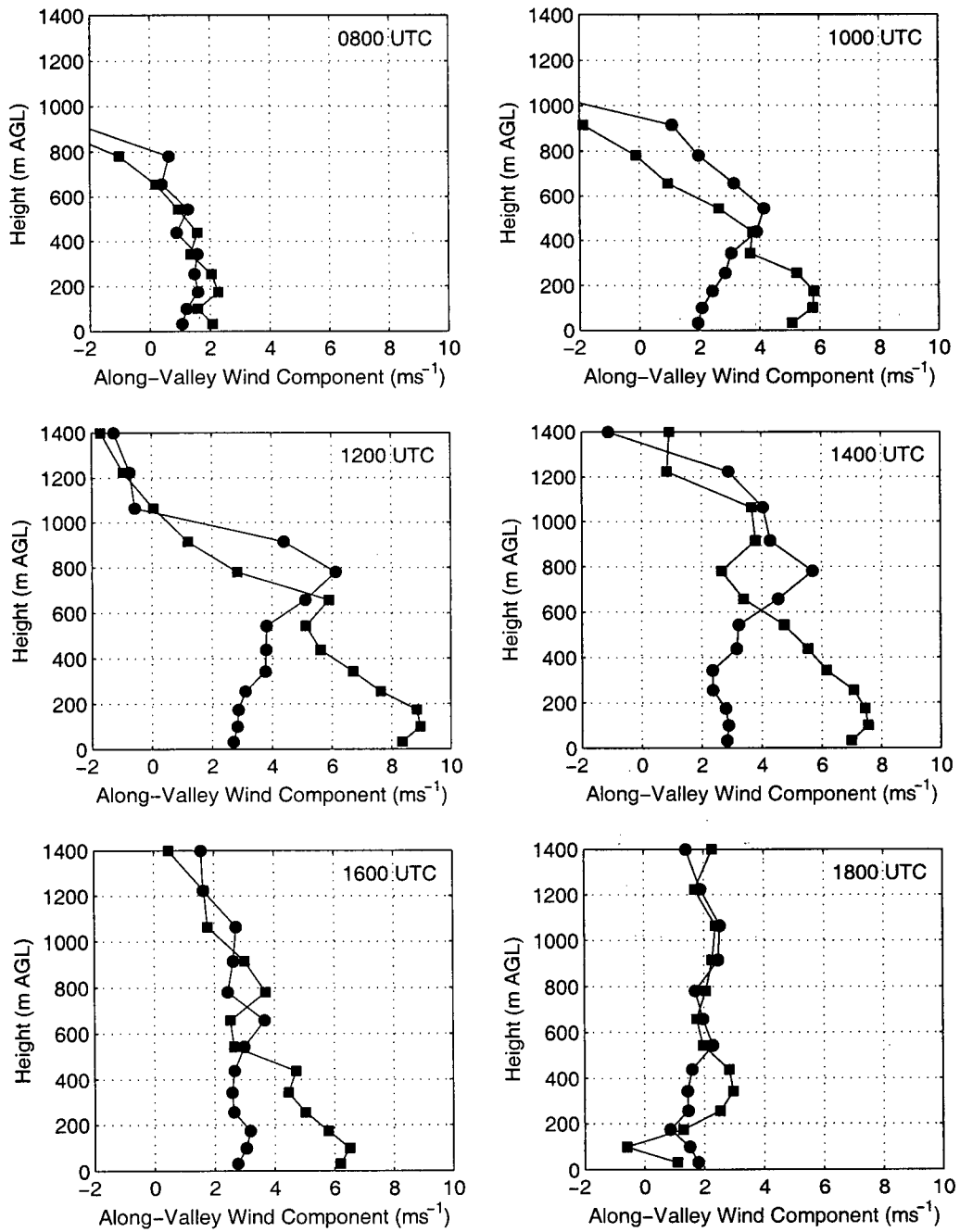


Figure 5.8: Vertical profiles of the modeled along-valley wind component (*REF*) at two locations, roughly 2.8 km down-valley (solid circles) and up-valley (solid squares) from the Doppler lidar site. Profiles are at 2-hr intervals starting at 0800 UTC.

300 m deep develops during the day, but is visible primarily down-valley from the lidar site.

The down-sloping of the isentropes appears to be associated with strong subsidence motion in this part of the valley. However, wave-like features can be seen in the flow which also occur further up the valley (not shown). Although the height of the valley bottom does not increase monotonically with distance in the up-valley direction, it appears that the valley bottom is not responsible for the wave-like motions in the flow. Instead subsidence motion appears to be associated with regions of horizontal flow divergence which would agree with the volume flux analysis presented in the previous chapter. Of interest is also that the model results do not show subsidence motion over the main valley in areas where tributaries branch from the Wipptal. Several studies have suggested that subsidence motion over the main valley, which compensates flow into tributaries, contributes to the heating of the main valley (Steinacker, 1984; Brehm, 1986; Freytag, 1988; Egger, 1990a). The present modeling results, however, do not support this concept.

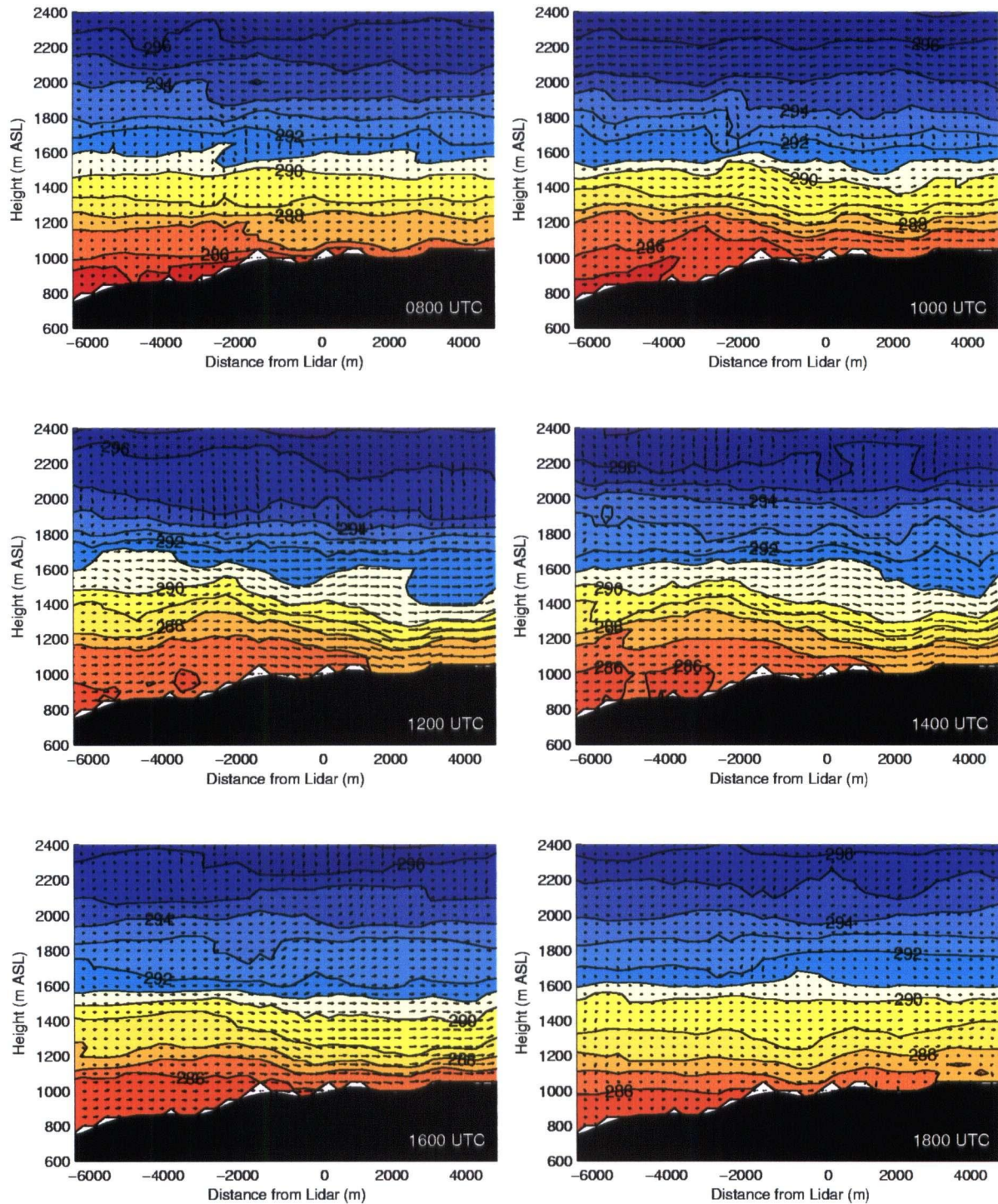


Figure 5.9: Cross-sections of potential temperature contours and wind vectors for simulation REF along the path shown in Figure 5.6. The solid black area marks the valley floor. Contour interval is 1 K. Sections are at 2-hr intervals starting at 0800 UTC.

5.3.2 Comparison to Observations

Comparison of model results to observations is often problematic, particularly in complex terrain. Observations from *in-situ* instrumentation represent the atmosphere at one particular point while model data represent conditions for a grid volume. Differences between the real terrain and the smoothed topography used in simulations as well as differences in the height between model output and observations can cause difficulty in comparing the two. In addition, observations may be influenced by local surface and terrain effects which are not captured by the model. Comparison of model results to Doppler lidar observations, however, avoids some of these difficulties since it is not limited to the surface or to one point in space. Instead, the spatial coverage of Doppler lidar data allows one to conduct a more general analysis to see if the model is capturing the flow features of interest.

Figure 5.10 shows the modeled RHI cross-section at 1300 UTC and observed RHI images around that time for 11, 16, and 17 October. In addition, modeled and observed vertical profiles of the along-valley wind component at 1400 UTC are shown in Figure 5.11. From these images, it can be seen that the model captures the observed flow divergence remarkably well. The along-valley change in the vertical structure - from a flat profile to a well defined Prandtl-like profile - is also reproduced. The maximum in the modeled wind profiles up-valley from the lidar occurs slightly closer to the ground than in the observed profiles. This difference can be accounted for by the fact that the valley bottom height in the computational terrain has not been corrected as it has for the observations. Up-valley from the lidar the modeled and observed wind maxima ($\approx 9 \text{ ms}^{-1}$) are in good agreement, while down-valley from the lidar the model simulates stronger winds (particularly at higher elevations) than were typically observed. The increase in wind speed with height which occurs in the modeled wind profiles down-valley from the lidar, however, can also be seen in some of the observations, although its nature or origin is still unclear.

In terms of the vertical extent of the flow, the modeled valley flow layer grows to 2200 m ASL in the afternoon. The initialization of the simulation resembles most closely the conditions on 11 October. On this day, however, the up-valley flow reaches heights of 2200-2400 m ASL as early as 1100 UTC. The lower valley flow depths simulated by the model may be due to the large soil moisture content at higher elevations which reduces the sensible heat input at those elevations. Generally, rocky upper slopes are much drier than valley bottoms and hence more net radiation should be converted into sensible heat at higher elevations than on the valley floor (e.g. Vergeiner and Dreiseitl, 1987; De Wekker, 2002).

General disagreement between observations and modeled output are largest for the morning transition period. Since the initialization time is not sufficient for down-valley flows to form, the simulated morning transition of the flow looks fundamentally different than what is observed on 11 or 16 October. Particularly, the large along-valley differences in valley flow depth, seen in the observations, are not simulated. Also, the model does not reproduce downsloping isolines

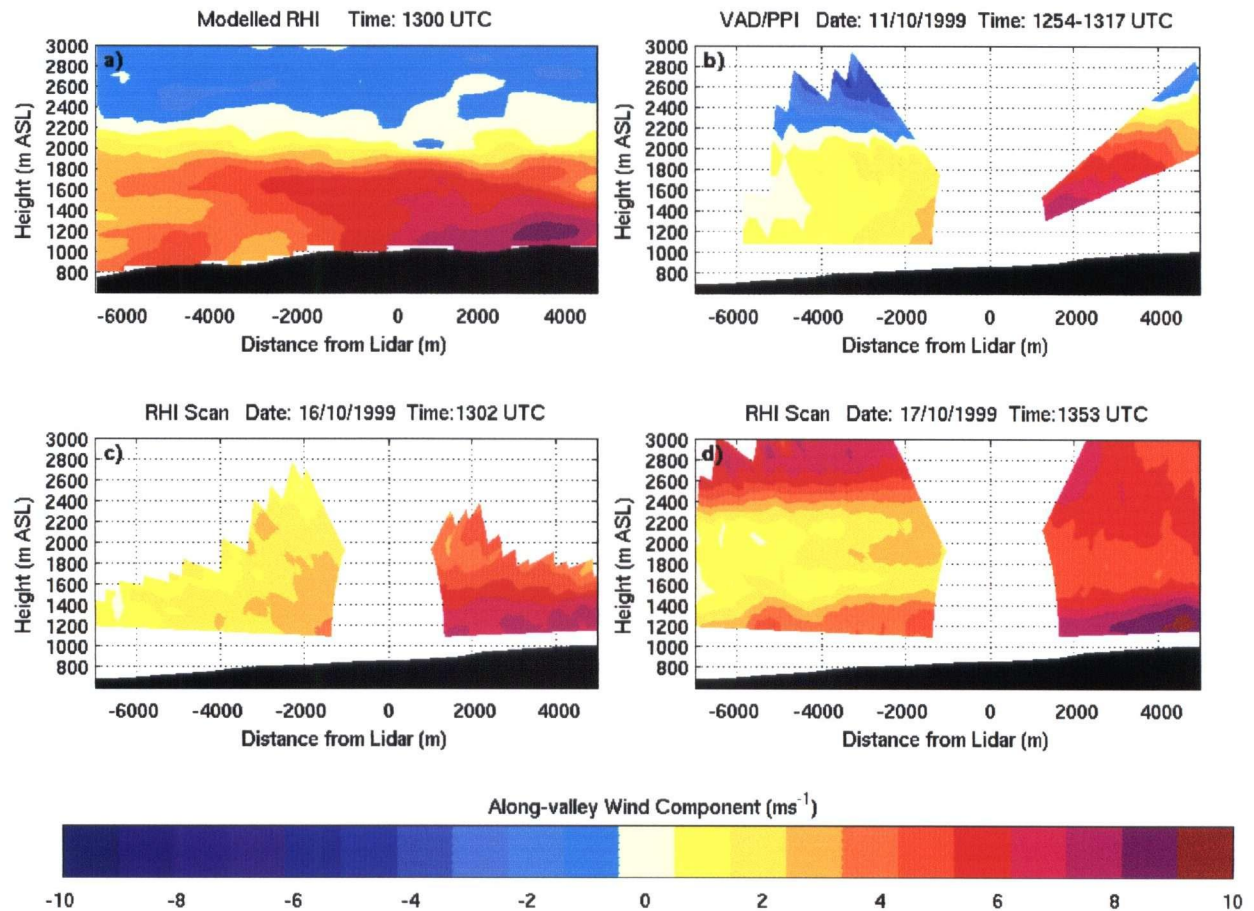


Figure 5.10: Modeled and observed RHI cross-sections of the along-valley wind component. Model output (a) is for 13 UTC and observations are for a) 11 October (1254-1317 UTC), b) 16 October (1302 UTC) and c) 17 October (1353 UTC). The solid black area marks the valley floor.

that are clearly visible on 16 October.

Unfortunately, vertical temperature profiles in the Wipptal are not available for this study period and hence the simulated temperature structure cannot be confirmed. Analysis of the backscatter intensity structure presented in Chapter 3 does suggest the existence of a well mixed aerosol layer in the valley, but this does not necessarily imply the existence of a convective boundary layer. It is of interest to note that numerical simulations by Zängl et al. (2001) of valley flows in the Kali Gandaki Valley (shown in Figure 6.3; it also has a lateral constriction, followed by a widening of the valley) also predict a stably stratified atmosphere (Figure 6.4). Observations of the temperature structure in the same valley (Egger et al., 2002), however, show the valley atmosphere to be neutrally stratified. Egger et al. (2002) speculate that the turbulence parameterization in the mesoscale model may underestimate the generation of

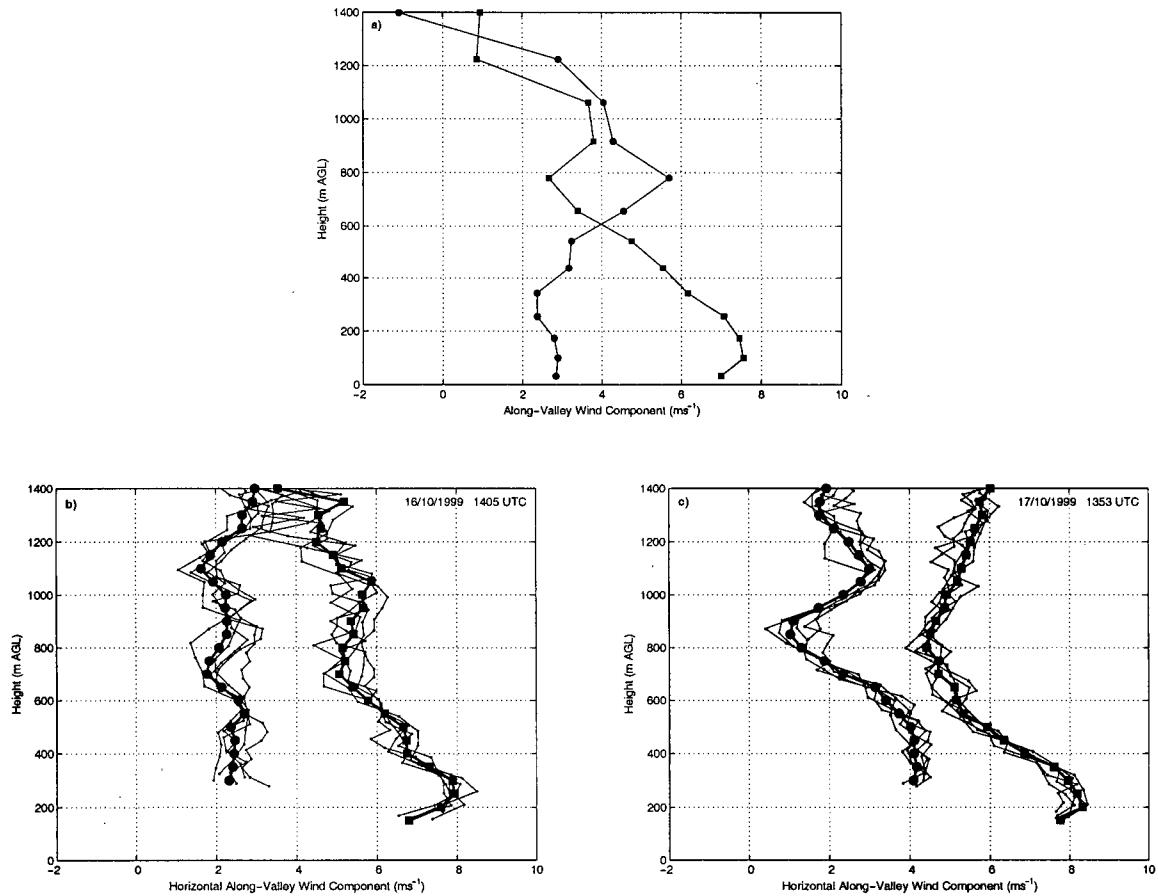


Figure 5.11: Modeled and observed profiles of the horizontal along-valley wind component at two locations, roughly 2.8 km down-valley (solid circles) and up-valley (solid squares) from the Doppler lidar site. a) Modeled profiles for simulation REF at 1400 UTC. b) Observed profiles for 16 October at 1405 UTC and c) 17 October at 1353 UTC.

turbulence in strong flow.

5.3.3 Analysis of the Momentum and Heat Budgets

As shown in the previous section, the modeled wind fields capture the essential elements of the phenomenon being investigated. In this section, the modeled momentum and heat budgets along the valley's axis are examined to provide insight into the dynamical processes of the valley flow in the Wipptal. An underlying assumption for this analysis is that since the model captures the flow kinematics, it also captures the relevant dynamical processes of the valley flow.

For the analysis, momentum and heat budget terms are extracted for a 5-grid point wide swath along the length of the valley (see Figure 5.12). The individual terms are then integrated

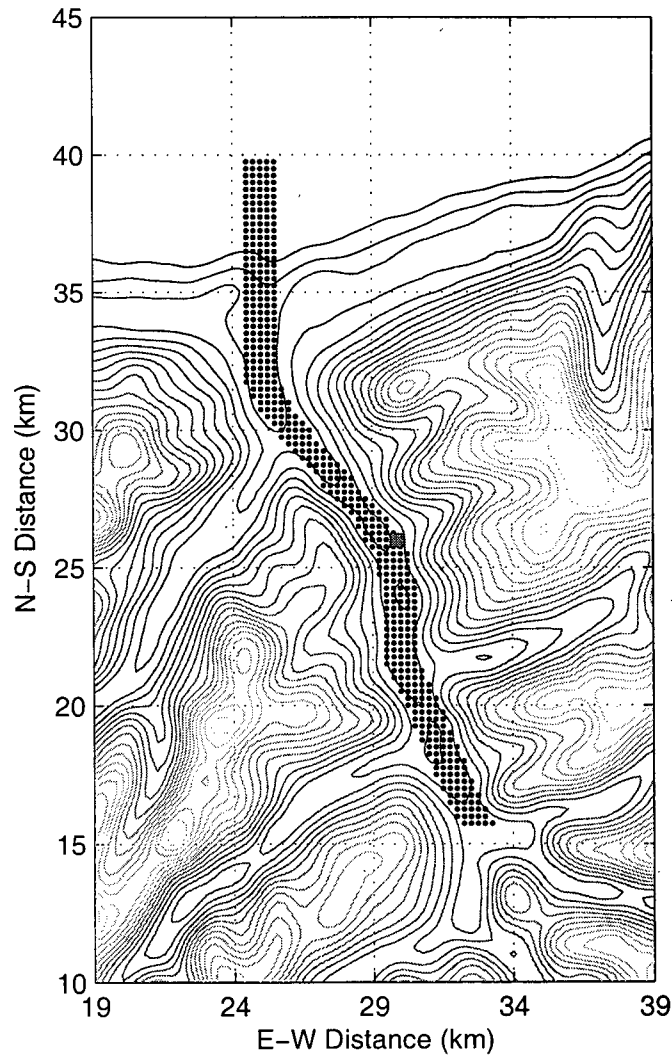


Figure 5.12: Topographical map of the Wipptal showing the location of grid points used in the momentum and heat budget analysis. For reference, the Doppler lidar site is marked with a solid square.

in the x-direction over the five grid points and vertically over the lowest 600 m.

The volume-averaged momentum budget for the horizontal wind components, u_1 and u_2 , is

$$\begin{aligned}
 \underbrace{\frac{1}{V} \iiint_V \frac{\partial u_i}{\partial t} dV}_I &= - \underbrace{\frac{1}{V} \iiint_V u_j \frac{\partial u_i}{\partial x_j} dV}_{II} - \underbrace{\frac{1}{V} \iiint_V \frac{1}{\rho_0} \frac{\partial P}{\partial x_i} dV}_{III} \\
 &\quad - \underbrace{\frac{1}{V} \iiint_V 2\varepsilon_{ijk} \Omega_j u_k dV}_{IV} + \underbrace{\frac{1}{V} \iiint_V \frac{\partial}{\partial x_i} K_M \frac{\partial u_j}{\partial x_i} dV}_V
 \end{aligned} \tag{5.1}$$

which states that the volume-averaged local rate of change of the momentum (I) is due to momentum advection (II), pressure gradient force (III), Coriolis force (IV) and turbulent diffusion (V). Momentum tendency terms are presented for the along-valley wind component which is calculated using

$$\mathcal{U} = u_1 \sin \theta - u_2 \cos \theta$$

where \mathcal{U} is the horizontal along-valley wind component, θ specifies the local orientation of the valley, and u_1 and u_2 represent the east-west and north-south horizontal wind component, respectively. Thus, for example, the total tendency for the along-valley wind component is given by

$$\frac{1}{V} \iiint_V \frac{\partial \mathcal{U}}{\partial t} dV = \frac{1}{V} \iiint_V \sin \theta \frac{\partial u_1}{\partial t} dV - \frac{1}{V} \iiint_V \cos \theta \frac{\partial u_2}{\partial t} dV.$$

Again, for consistency, the along-valley wind component \mathcal{U} is positive in the up-valley direction.

The equivalent equation for the heat budget is

$$\underbrace{\frac{1}{V} \iiint_V \frac{\partial \theta}{\partial t} dV}_I = - \underbrace{\frac{1}{V} \iiint_V u_j \frac{\partial \theta}{\partial x_j} dV}_{II} + \underbrace{\frac{1}{V} \iiint_V \frac{\partial}{\partial x_i} K_H \frac{\partial \theta}{\partial x_i} dV}_{III} + \underbrace{\frac{1}{V} \iiint_V S_\theta dV}_{IV} \quad (5.2)$$

which specifies that the volume-averaged rate of change of potential temperature (I) is due to horizontal and vertical temperature advection (II), turbulent diffusion (III) and radiative flux divergence (IV).

Figures 5.13, 5.14, 5.15 and 5.16 show the volume-averaged tendency terms of the momentum and heat budget along the length of the Wipptal between 0900-1000, 1100-1200, 1300-1400 and 1500-1600 UTC, respectively. The corresponding volume-averaged along-valley wind speed and potential temperature are shown in Figure 5.17. Although these figures show large variations in the tendency terms of the momentum and heat budgets along the valley, the following generalized statements can be made:

- The dominant terms for the momentum budget are the pressure-gradient force (PGF) and advection. These two terms alternate in causing the flow to accelerate or decelerate. Generally speaking, the PGF causes acceleration of the valley flow except in sections with tributaries where the flow is carried by inertia. Turbulent mixing slows the flow while the Coriolis force contributes to the acceleration, but overall these two terms are much smaller than PGF or advection.

- The dominant terms for the heat budget are turbulent diffusion and advection, while radiative flux divergence is negligible. Turbulent diffusion heats the air while the net effect of advection depends on the relative contributions of vertical and horizontal advection. Typically, horizontal advection is that of colder air and therefore has a cooling contribution while vertical advection (typically subsidence) heats the volume.
- Heating due to turbulent diffusion generally increases in the up-valley direction, with peak values occurring in the segment surrounding the Doppler lidar site (at the 26-km mark) and further up-valley around the 20-km and 16-km mark. At these locations, the valley is generally narrow and hence these high values of turbulent heating may be attributed to the volume (i.e. TAF) effect. Large and positive (i.e. accelerating) values of the PGF can also be found at these locations.
- Total tendencies for heat and momentum vary in both space and time.

So while the increase in intensity of the valley flow around the Doppler lidar site appears to be linked to an increase in the PGF (and greater turbulent heating), advection processes also play a significant role. Between 0900 and 1000 UTC, for example, the valley atmosphere at the entrance of the narrow section (between the 27 and 29-km mark) experiences cooling while further up the valley the air continues to warm. The cooling appears to be associated with the onset of cold air advection. Vertical advection (subsidence) contributes to the warming of the atmosphere, but is not sufficient to offset the cooling brought about by horizontal cold air advection. Further along the narrow valley section, there is less horizontal cold air advection. Together with warming through subsidence motion (and turbulent heating), the atmosphere in this part of the valley continues to warm. Warming also takes place in the widened valley section, which is partially due to the advection of warmer air. This pattern, albeit shifted up-valley, is also observed an hour later. Between 1100 and 1200 UTC, cooling occurs along the entire narrow valley section, but to a lesser degree (or even warming) in the widened valley segment. As a result, a positive PGF forms in the widened valley segment, and hence increases the flow intensity in that region.

This analysis suggests that in addition to topographical features which determine the turbulent heating and for the most part pressure gradients, advection processes also play a large role in the flow dynamics. One question that remains is: Do similar flow features occur in other valley geometries? This is addressed in the following section.

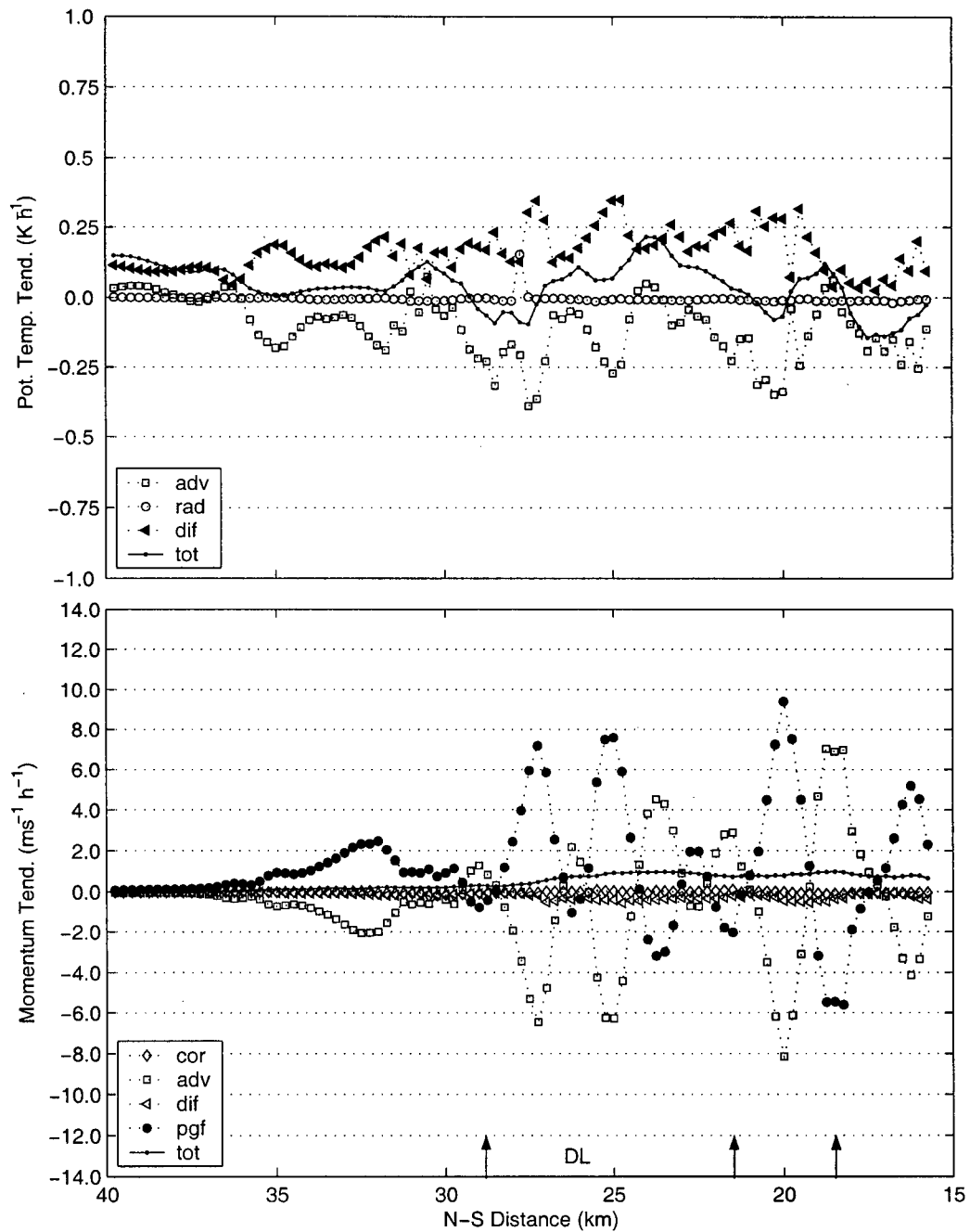


Figure 5.13: Heat and momentum budgets for 0900-1000 UTC as a function of along-valley distance for simulation REF. Arrows mark the approximate locations of tributaries and 'DL' marks the position of the Doppler lidar. Note that up-valley is to the right of the figure.

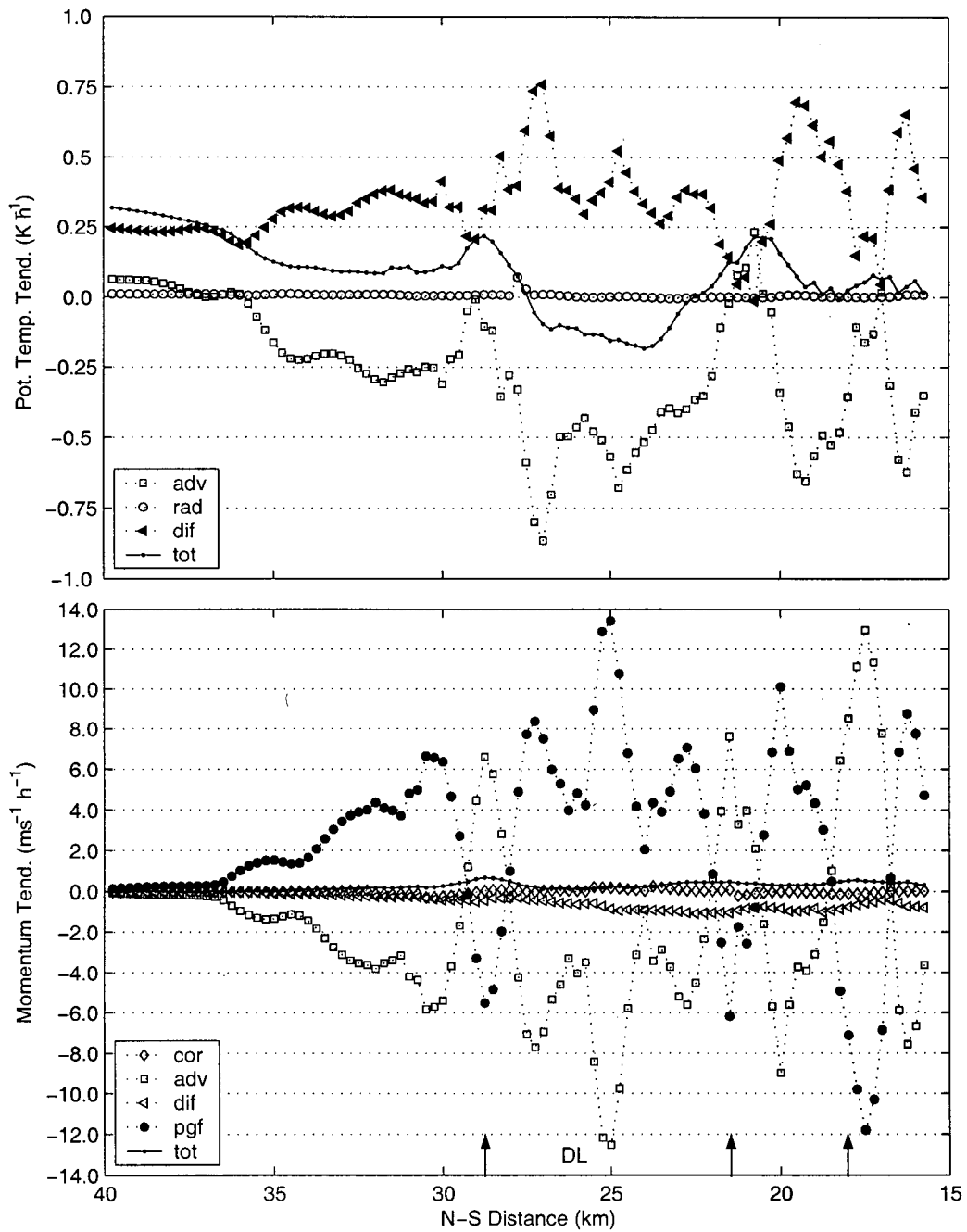


Figure 5.14: Heat and momentum budgets for 1100-1200 UTC as a function of along-valley distance for simulation REF. Arrows mark the approximate locations of tributaries and 'DL' marks the position of the Doppler lidar. Note that up-valley is to the right of the figure.

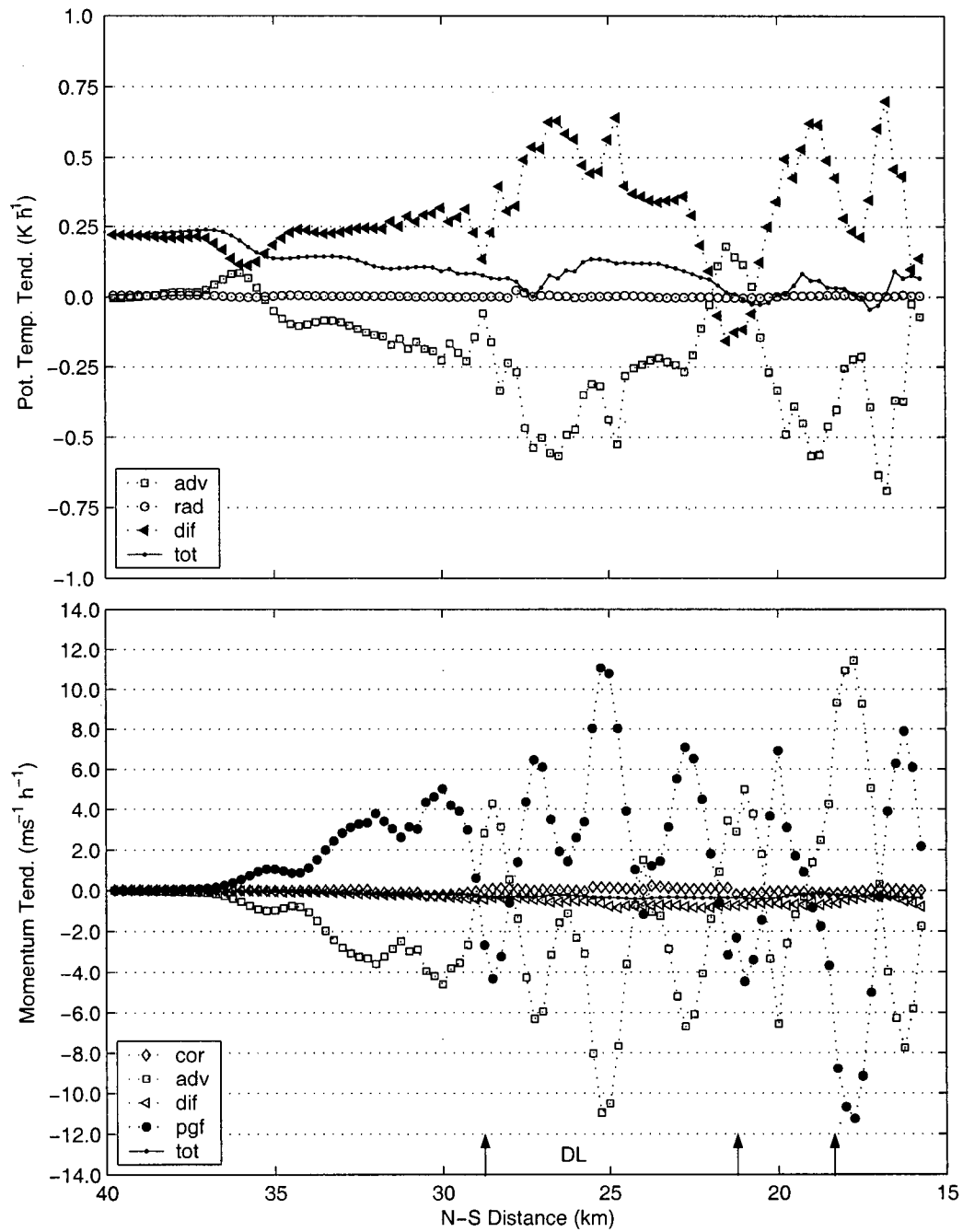


Figure 5.15: Heat and momentum budgets for 1300-1400 UTC as a function of along-valley distance for simulation REF. Arrows mark the approximate locations of tributaries and 'DL' marks the position of the Doppler lidar. Note that up-valley is to the right of the figure.

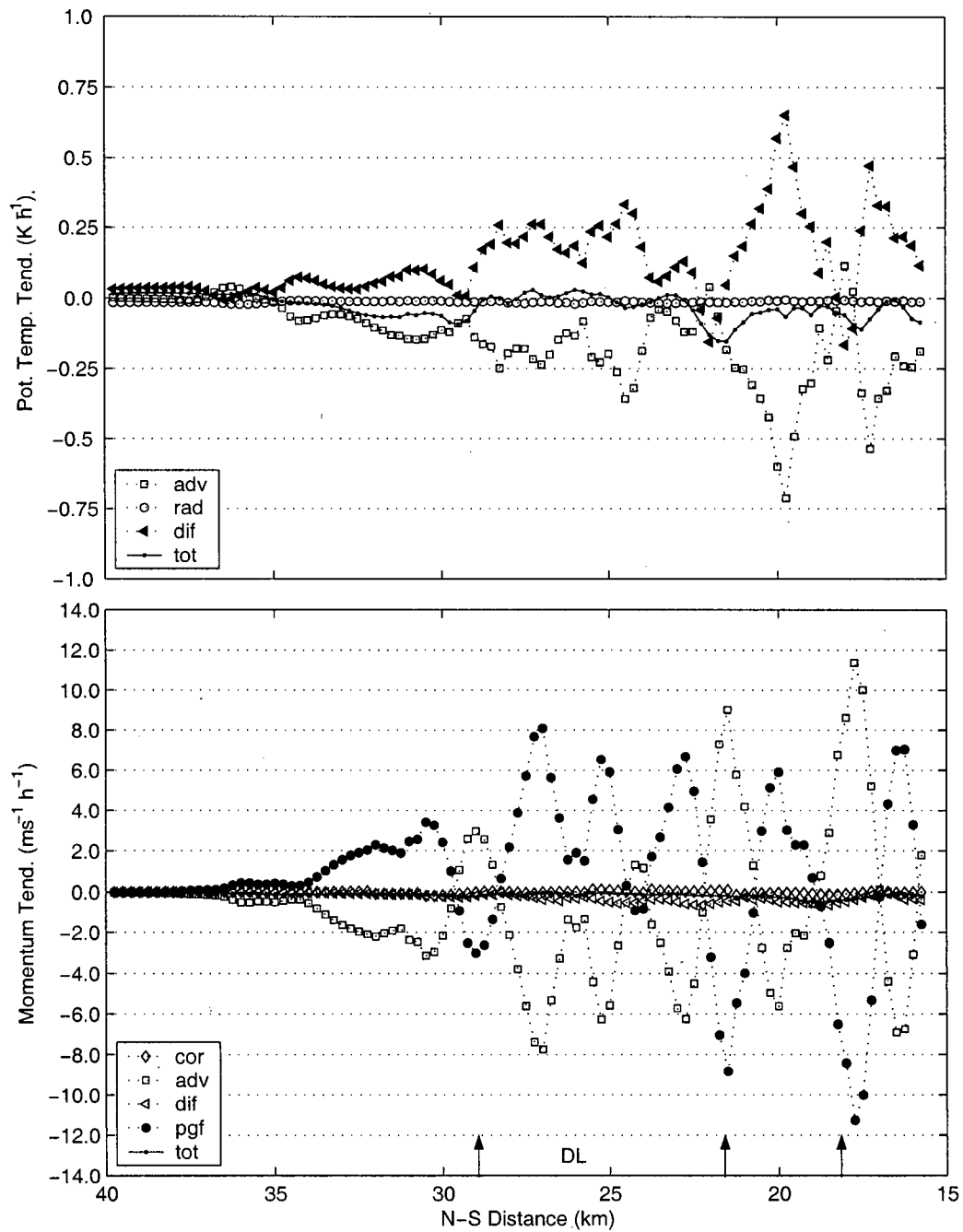


Figure 5.16: Heat and momentum budgets for 1500-1600 UTC as a function of along-valley distance for simulation REF. Arrows mark the approximate locations of tributaries and 'DL' marks the position of the Doppler lidar. Note that up-valley is to the right of the figure.

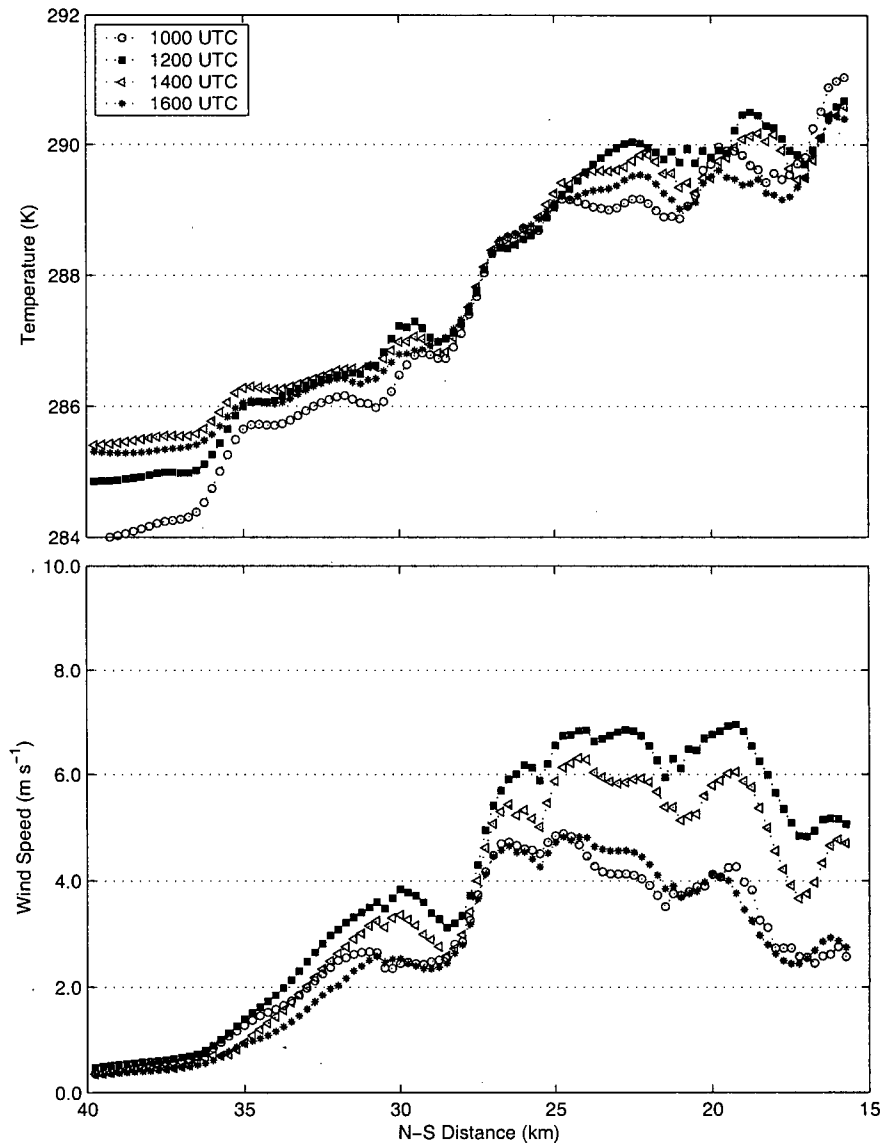


Figure 5.17: Volume-averaged along-valley potential temperature and wind speed as a function of along-valley distance for simulation REF. Note that up-valley is to the right of the figure.

5.4 Numerical Experiments T1 through T4: Sensitivity to Terrain

In this section, the sensitivity of the flow structure to terrain features is examined through modifications of the real topography. A large advantage of this method is that it allows specific changes in topography to be investigated and thus retains a connection to the reference simulation. This connection is lost with idealized topographies because changes in the flow can no longer be attributed to one particular change in the topography. This method, however, also has several drawbacks. While the sky is the limit in what terrain configurations to test, some modifications are easier to implement than others. Second, the terrain modifications are not scientifically predetermined, but are based on the author's imagined rendering of specific terrain configurations. So, for example, the effects of the modifications on the geometric ratio are only known after the fact. Third, the modified terrain configurations remain complex and hence are not conducive to generalizations.

Four modified terrain configurations are tested. These, along with the topography used in REF, are shown in Figure 5.18. What follows is a brief description of each terrain configuration and its purpose. Numerical simulations using terrain configurations T1 and T3 examine if similar flow features can be obtained without the distinct change in valley geometry that occurs between the entrance of the Wipptal and, say, the Doppler lidar site. Different modifications are applied to eliminate this change in valley geometry. For T1, the valley section between the 17 and 28-km mark in the N-S direction is widened to roughly the width of the valley near its mouth. The valley volume still decreases with up-valley distance, but at a much more moderate rate. For T3, a section of the valley near the entrance (between 29 and 35-km in the N-S direction) is modified to eliminate the along-valley change in the width of the valley. T2 examines the effect of the basin-like valley section between the 20 and 25-km mark in the N-S direction whereby the widened section is replaced with a narrower valley configuration. A similar issue was addressed by Zängl et al. (2001) whose idealized simulations of flow in the Kali Gandaki Valley suggested that wind speeds in the valley without a widening of the valley were lower than wind speeds in a valley with a widening of the valley. Lastly, for T4 all terrain elevations below 1100 m ASL are raised to 1100 m ASL, effectively eliminating the sloped valley bottom for most of the valley's length. Results from simulation REF suggest that cold air advection plays a large role in the dynamics of the flow. However, cold air advection is more pronounced with a sloping valley bottom. Thus, by eliminating the sloped valley bottom, cold air advection should be reduced as well.

Simulated near-surface winds as well as RHI cross-sections at 1200 UTC are shown for all terrain configurations in Figures 5.19 and 5.20, respectively. What is apparent from these figures is that changes in topography do have significant effects on the along-valley flow structure.

In case of the wide valley configuration (T1), the along-valley wind speeds in the segment

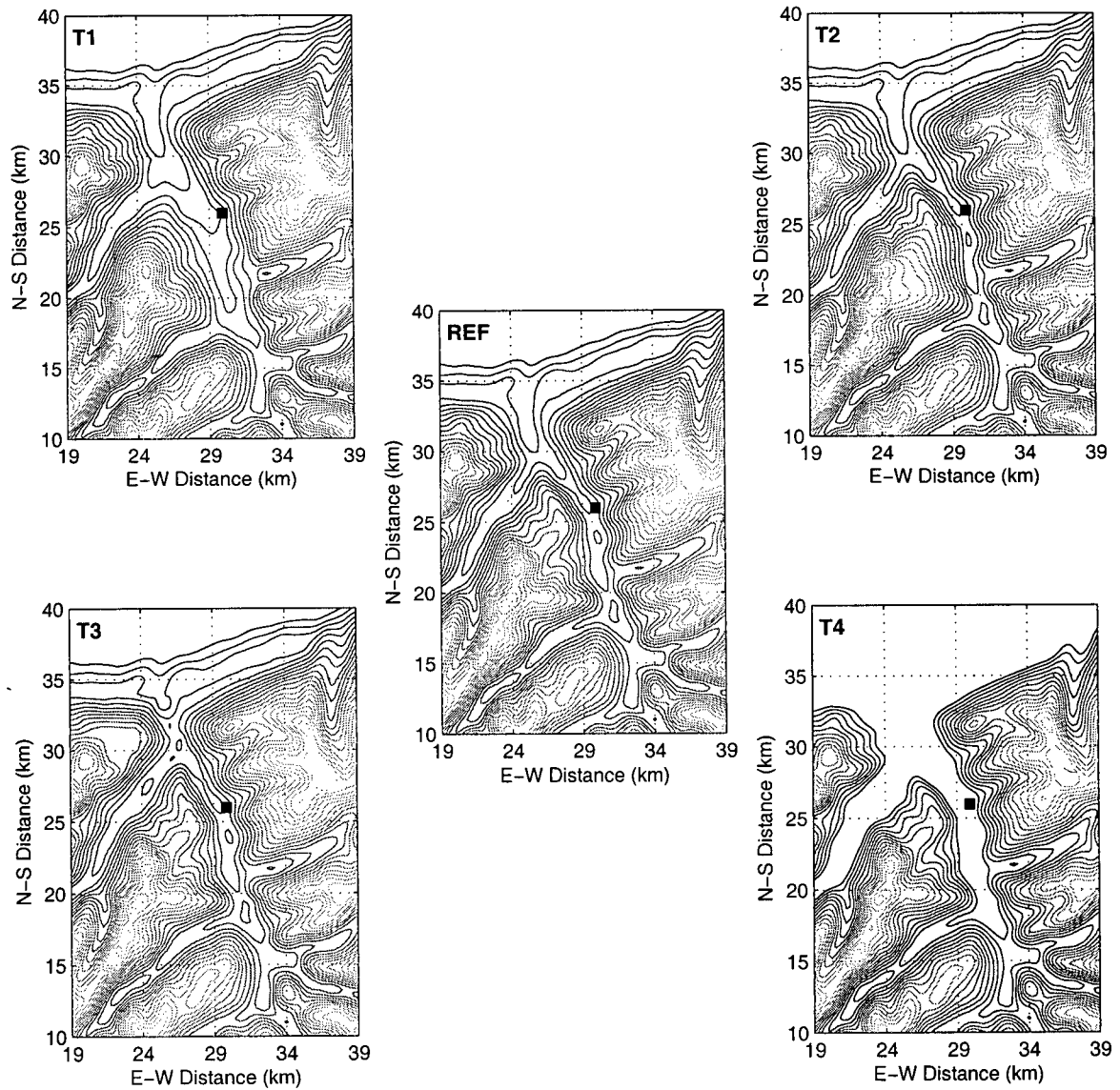


Figure 5.18: Modified topographies for simulations T1, T2, T3 and T4. The topography for REF is shown for reference. The solid square marks the Doppler lidar site. Contour interval is 100 m.

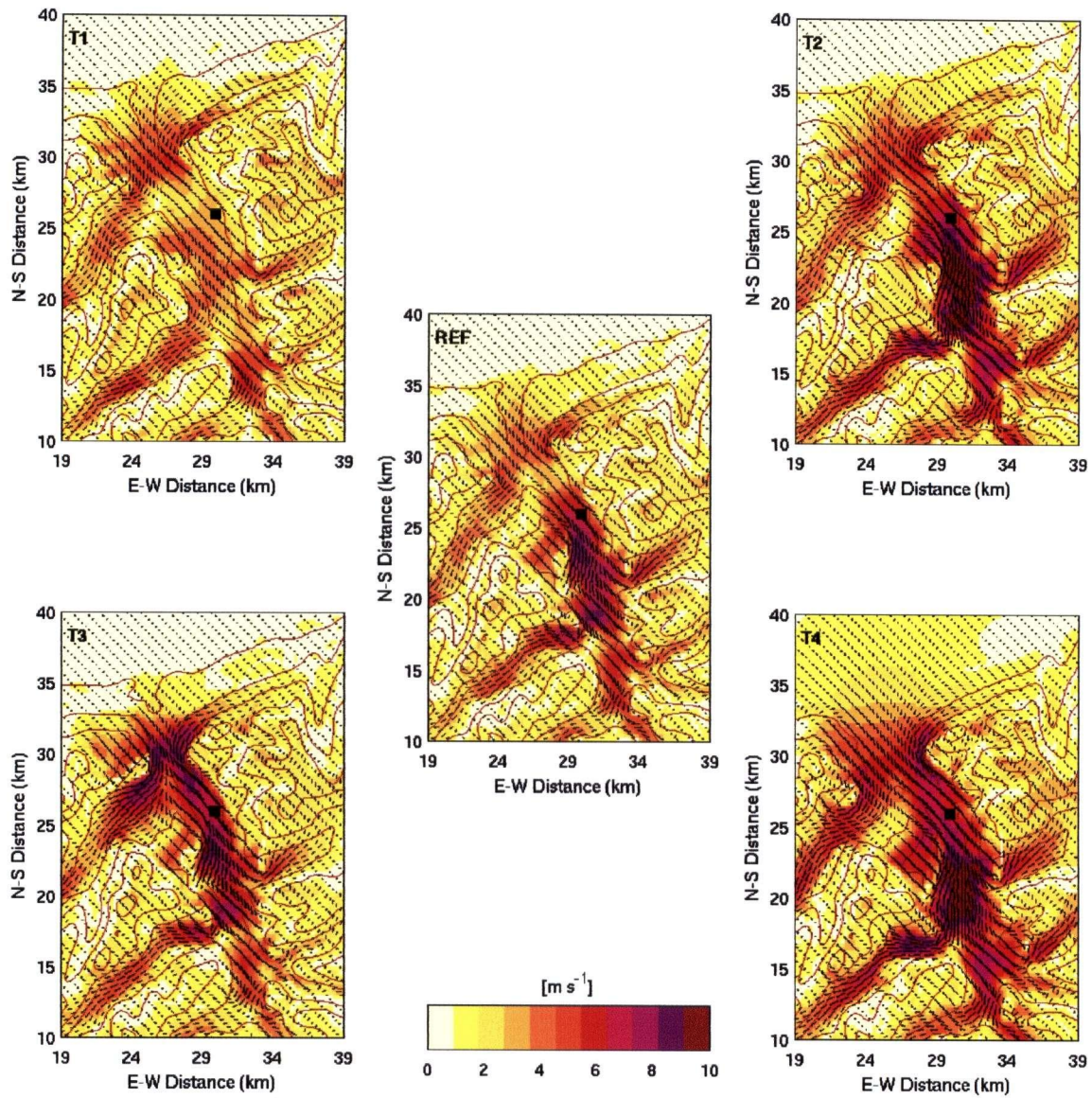


Figure 5.19: Modeled near-surface winds (32 m AGL) at 1200 UTC for simulations REF, T1, T2, T3 and T4. The solid square marks the Doppler lidar site. Topography is shown with a contour interval of 400 m.

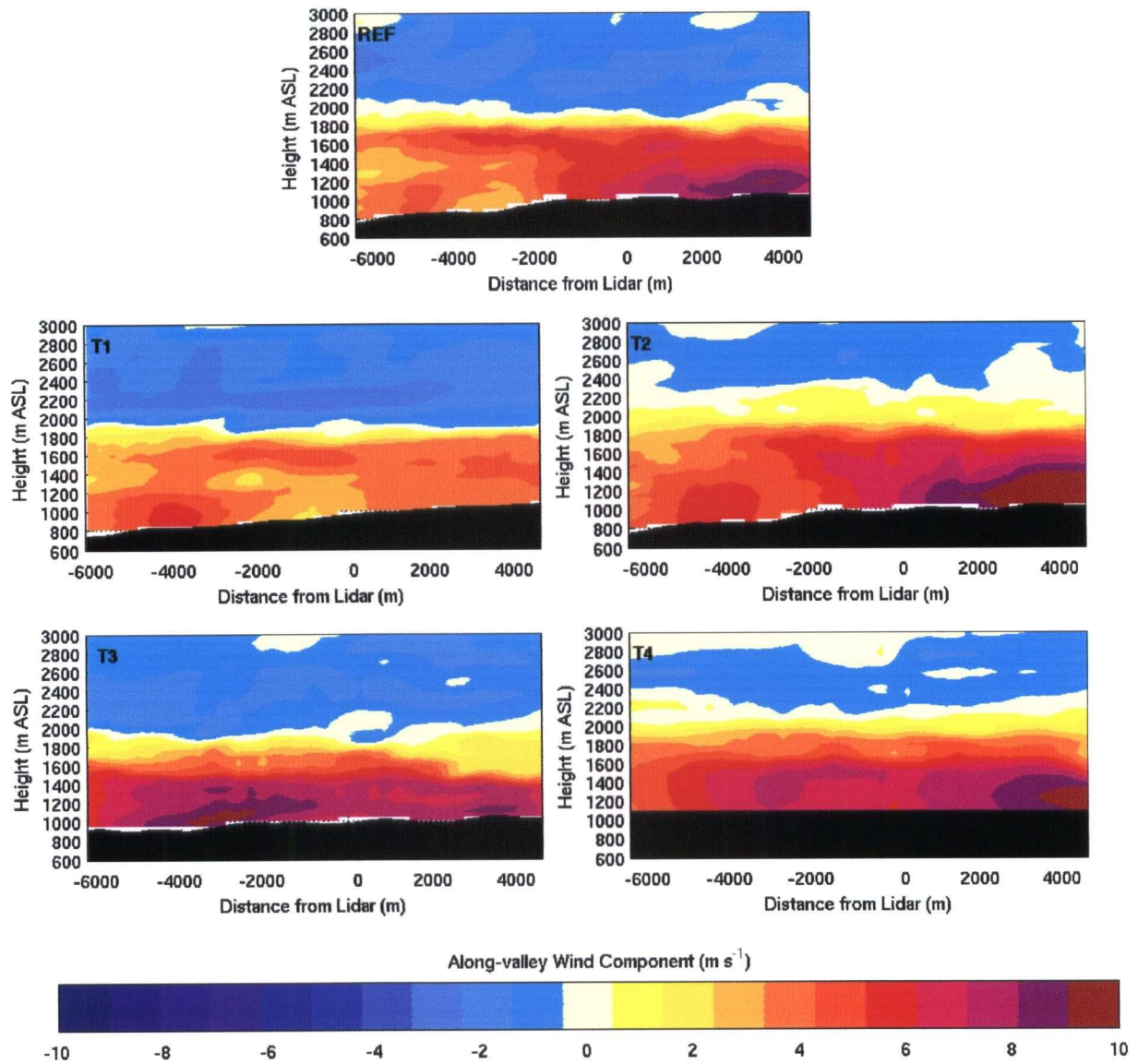


Figure 5.20: Modeled RHI images of the along-valley wind component at 1200 UTC for simulations REF, T1, T2, T3 and T4. The solid black area marks the valley floor.

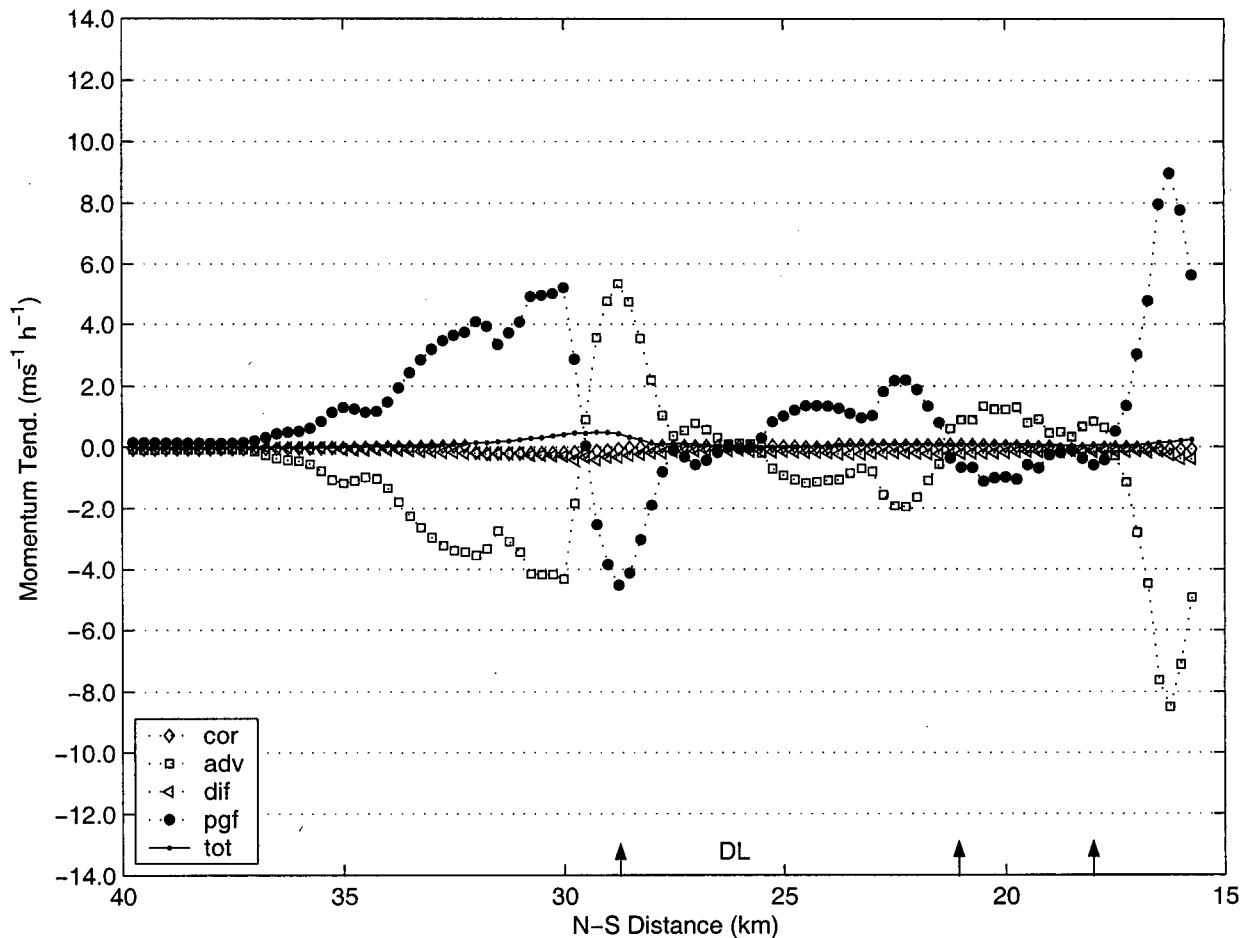


Figure 5.21: Along-valley momentum budget for 1100-1200 UTC as a function of along-valley distance for simulation T1.

surrounding the Doppler lidar are much weaker than in REF, and particularly the increase in wind speed up-valley from the lidar is no longer present. Figure 5.21 shows that the primary force terms (PGF and advection) near the mouth and head of the valley are similar in magnitude to those in REF, but are much smaller in the main portion of the valley. Vertical motions are also much smaller than in REF. The downsloping of isentropes, as was observed in REF, does not occur in this simulation.

The terrain modification in T2 has quite the opposite effect. Replacement of the basin-like section with a narrower valley geometry increases the PGF (Figure 5.22) in that segment and hence increases the along-valley acceleration of the flow. This result differs from that by Zängl et al. (2001), who obtained smaller wind speed *without* the widened valley segment than with it. It is questionable, however, if a direct comparison can be made between the two studies.

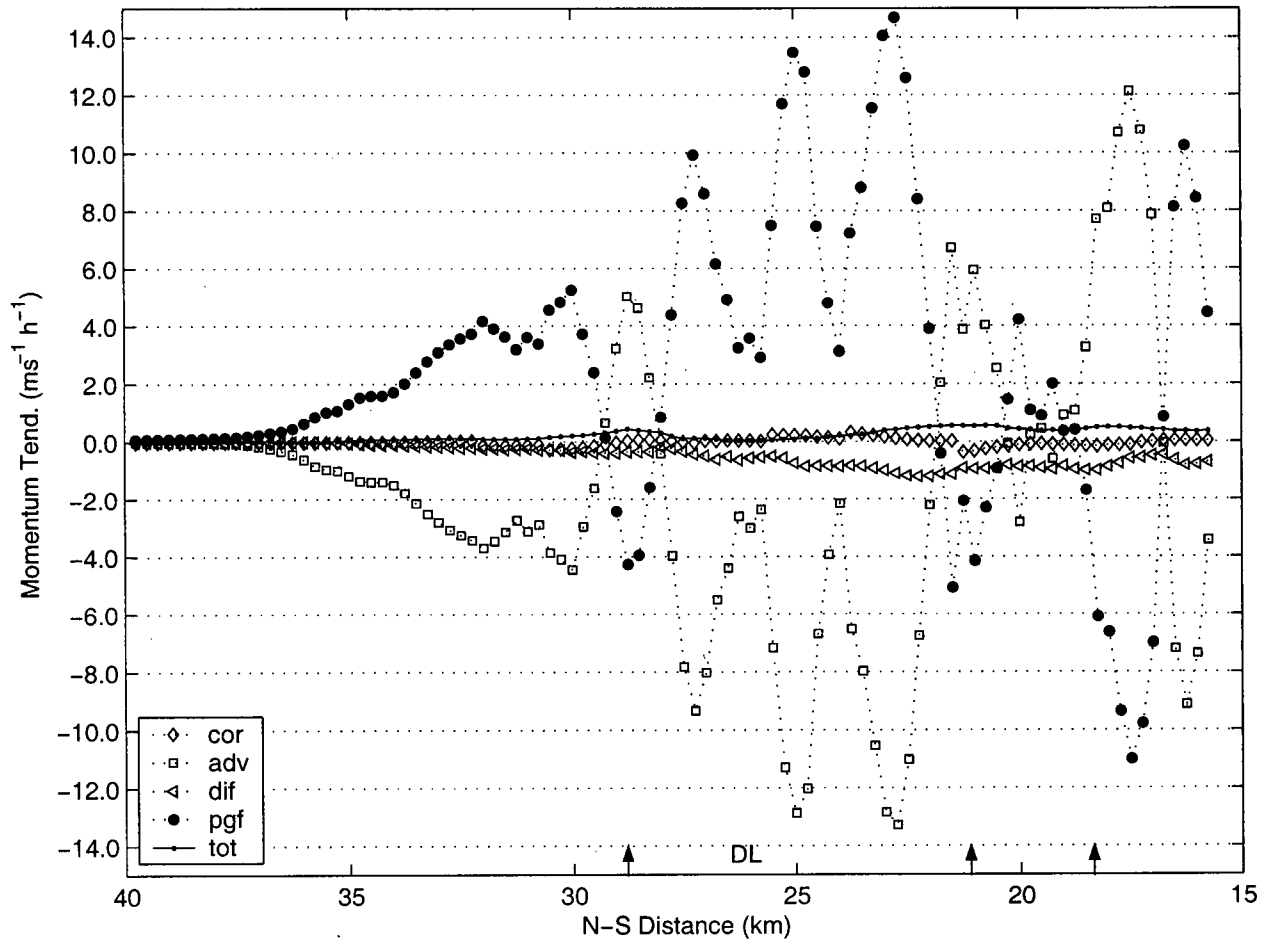


Figure 5.22: Along-valley momentum budget for 1100-1200 UTC as a function of along-valley distance for simulation T2.

As will be shown later, the terrain modification resulted in an increase of the geometric ratio in comparison to the geometric ratio of the 'original' narrow valley section while there is no increase in the geometric ratio in the idealized terrain by Zängl et al. (2001).

It is of interest to note that slightly stronger wind speeds near the entrance of the valley are simulated in T2 than in REF, even though the terrain in that region is identical. This highlights the sensitivity of the whole valley flow structure to local terrain characteristics.

In simulation T3, the narrowing of the entrance of the valley has the effect of greatly increasing the PGF at the mouth of the valley (Figure 5.23) and hence much greater wind speeds are observed at the mouth of the valley. In contrast to REF where the PGF acts to accelerate the flow between the Stubaital and the Doppler lidar site (between the 29- and 26-km mark), the acceleration of the flow in T3 for this section is due to advection of faster moving flow.

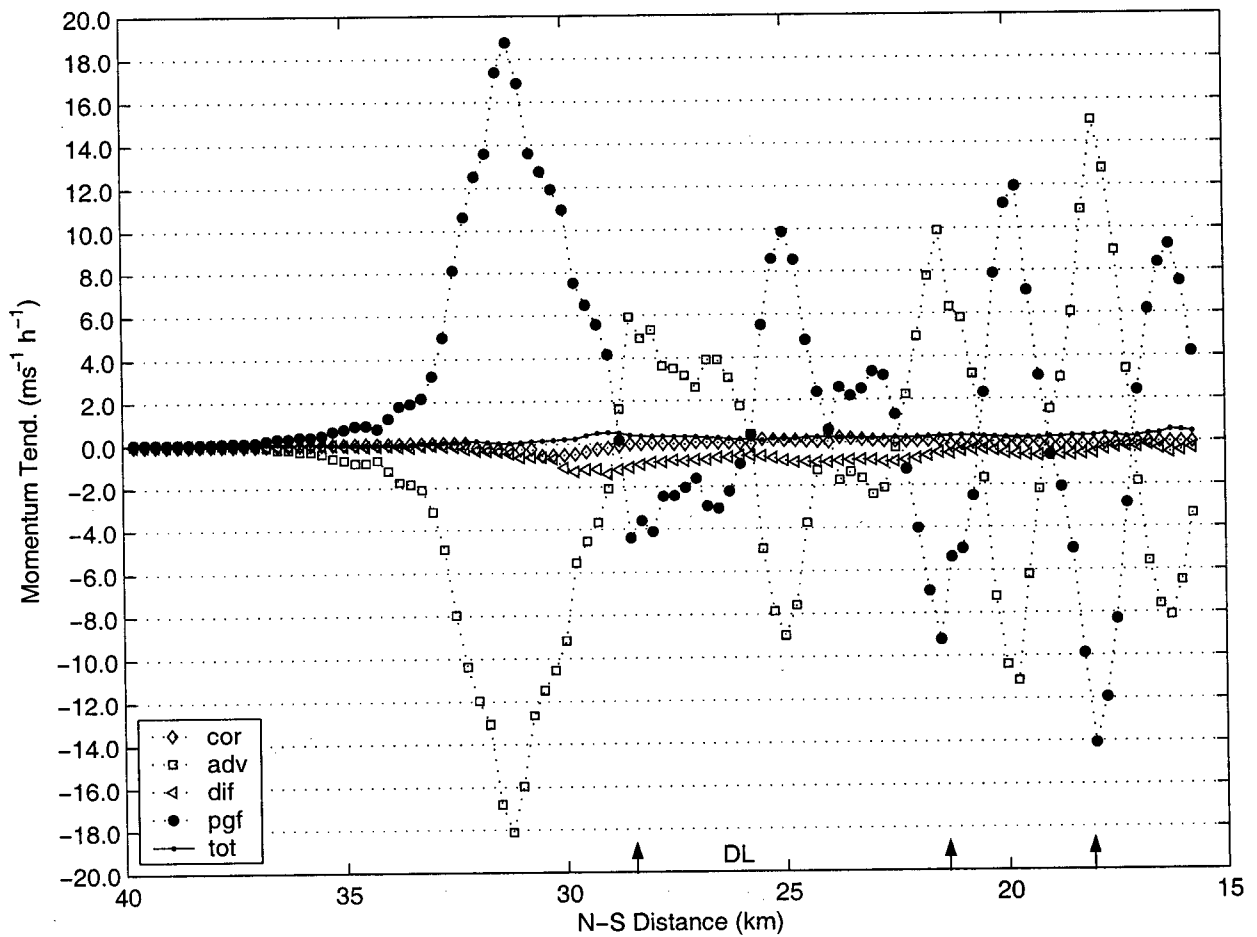


Figure 5.23: Along-valley momentum budget for 1100-1200 UTC as a function of along-valley distance for simulation T3.

For simulation T4, the flow intensity is stronger throughout the whole valley than it is in REF. An increase in flow intensity can still be seen along the valley's length although the change is more gradual. Thus, it appears that the level valley bottom reduces the role of cold air advection in setting up an intra-valley pressure gradient surrounding the Doppler lidar site (Figure 5.24).

The availability of different terrain configurations offers the opportunity to further evaluate the TAF concept as a tool to predict along-valley kinematic flow structures. Figure 5.25 shows the geometric ratio (τ or A/V) as a function of N-S distance for all terrain configurations. The segments used for this analysis are identical to those shown in Figure 4.8. The modifications in T1 have the effect of decreasing $\frac{d\tau}{dx}$ which, according to Equation 4.4, should result in a weaker along-valley pressure gradient, and hence weaker flow. In T2, the terrain modifications increase

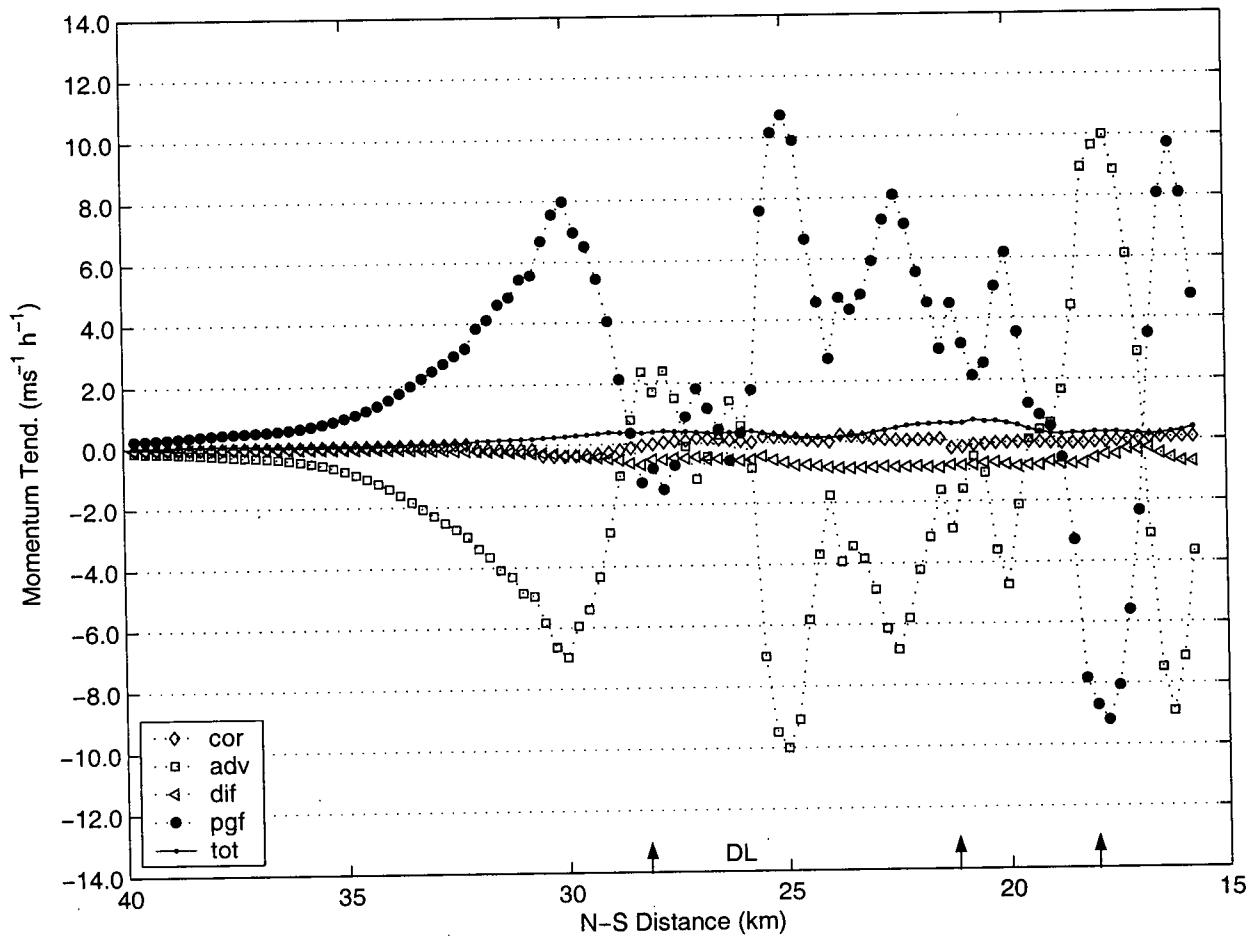


Figure 5.24: Along-valley momentum budget for 1100-1200 UTC as a function of along-valley distance for simulation T4.

$\frac{dr}{dx}$ around the 26-km mark and hence a stronger pressure gradient should occur in that region. In T3, the valley geometric ratio is enhanced near the entrance of the valley which implies a stronger $\frac{dr}{dx}$ at the valley's mouth. For T4, $\frac{dr}{dx}$ increases near the entrance of the valley, but remains roughly the same for the rest of the valley. Intercomparison of the different valley flows in Figures 5.19 and 5.20 suggest that changes in the along-valley flow structure correspond at least qualitatively to changes in the geometric ratio. However, the TAF analysis does not capture effects of advective processes, particularly when it is advection of faster or warmer air. Hence, the TAF analysis appears useful in identifying regions where a distinct change in the geometric ratio may induce an increase in the flow intensity, but it is less clear how to relate the flow intensity/structure to the geometric ratios up-valley from this distinct change in geometry.

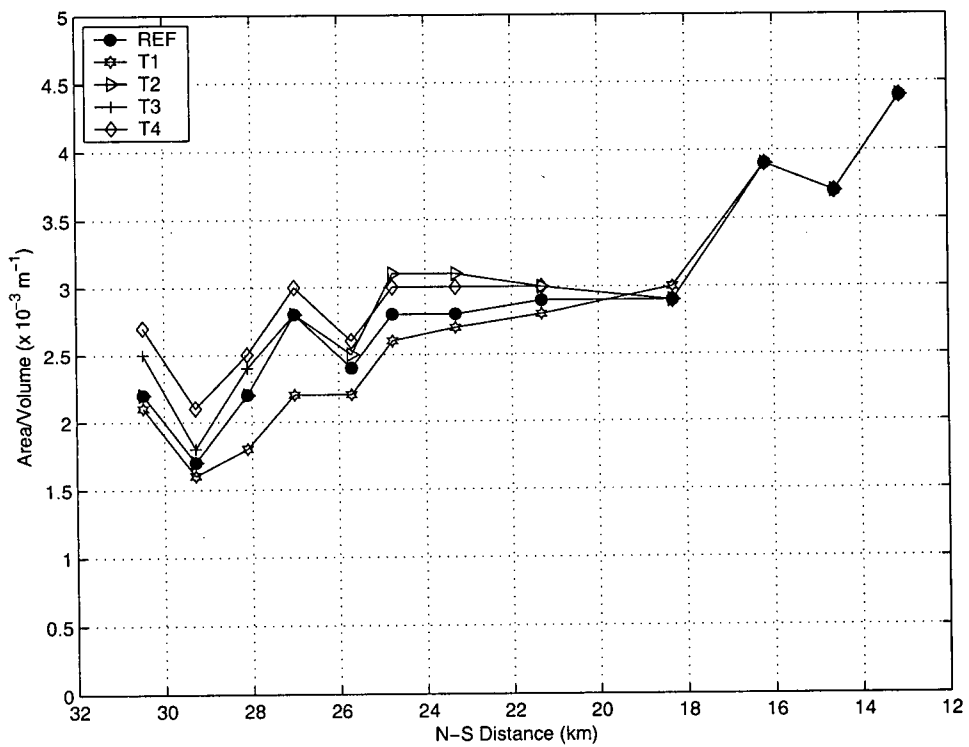


Figure 5.25: Valley geometric ratio A/V as a function of along-valley distance for topographies used in numerical experiments.

5.5 Summary

In summary, the simulation using 'real' topography reproduces the along-valley flow structure in the Wipptal remarkably well. Analyses of the momentum and heat budgets indicate that the pressure-gradient force and advection terms dominate the momentum budget, while turbulent diffusion and advection are the most important terms in the heat budget. The pressure-gradient force shows significant along-valley variability, and even reverses signs (i.e. acts to decelerate) in sections with tributaries. The analysis suggests that the increase in wind speed with up-valley distance near the Doppler lidar site is due to an enhanced pressure gradient force which in turn can be linked to increased turbulent heating in the narrow valley section. Advective processes, however, also play a significant role in the observed flow structure. The along-valley heating rate (and therefore the along-valley pressure-gradient force) are strongly influenced by horizontal cold air advection as well as warming through subsiding motion.

Regarding the influence of tributaries on flow in the main valley, the model results do not support the concept that heating in tributaries is transferred to the main valley via subsidence motion. Instead, the model results suggest that as air in the main valley is advected past the entrance of a tributary, the temperature difference of the air between the main valley and the tributary (the tributary is warmer due to its smaller volume) results in a temporary reversal of the along-valley pressure gradient.

Numerical simulations with differently modified terrain configurations were conducted as well. In the case of the widened valley (T1), the simulated valley flow is much weaker and does not diverge up-valley from the Doppler lidar site. In the case of the narrow valley entrance (T2), the flow intensity near the mouth of the valley is significantly increased. The faster-moving air is advected along the valley so that again a flow divergence in the vicinity of the lidar cannot be observed. Replacing the widened valley section with a narrower valley configuration (T3) increases the flow intensity up-valley from the lidar. Lastly, without the sloping valley bottom (T4), flow divergence still occurs along the valley, although the distinct increase in wind speed around the Doppler lidar site does not occur.

Although it is difficult to generalize from these simulations, they suggest that topography as well as flow dynamics play significant roles in the kinematic structure of the valley flow.

Chapter 6

Comparison to Other Studies

“Testing of our basic knowledge of physical processes causing complex terrain circulations, as well as the TAF concept, would be facilitated by extending experiments into valleys, basins, and tributaries of different size, shape, length, width, and other topographic characteristics.”

Whiteman (1990)

While this quote by Whiteman (1990) points the way for future research, observations and theories from two other valleys with *similar* terrain characteristics are discussed here in hope of establishing some commonalities or differences with observations and modeling results presented for the Wipptal.

The two valleys which are considered here are the Inntal in Austria and the Kali Gandaki Valley in Nepal. The Inntal is a major Alpine valley with large tributaries and subsidiary mountain ranges (see Figure 2.1). It is approximately 300 km long, 800-1500 m deep and 10 km wide at crest height. The Kali Gandaki Valley connects the Indian plains with the Tibetan plateau (see Figure 6.3). It is roughly 90 km long and 5000 m deep between Lete and Marpha. A steep rise in the valley bottom occurs near the valley mouth. Although there are large topographical differences between these two valleys and the Wipptal, there are also similarities: all three valleys appear to have lateral terrain constrictions. For the Inntal, a narrowing of the valley occurs between Radfeld and Schwaz, while for the Kali Gandaki Valley, a constriction occurs between Lete and Marpha. It should be mentioned that the along-valley flow characteristics with respect to the volume flux budget have been documented for two end-valleys, the Dischmatal (Hennemuth, 1987) and the Mesolcina Valley (Prévôt et al., 1998). These studies, however, are not included here due to the lack of spatial resolution in the observations.

Observations and theories are presented first for the Inntal. During the MERKUR experiment in March 1982, aerological measurements were obtained at several locations in the Inntal. The observations quite clearly showed an increase in wind speed and mass flux with distance in the up-valley direction between Nieder-Breitenbach and Schwaz (see Figure 2.1) where the valley narrows (Freytag, 1987, 1988). Vertical temperature profiles over the plain and at Nieder-Breitenbach and Radfeld showed the existence of a horizontal temperature/pressure gradient between the plain and the valley stations, but a *change* in the temperature/pressure gradient between Nieder-Breitenbach/Radfeld and Radfeld/Schwaz could not be established due to lack of temperature observations at Schwaz.

Freytag (1987, 1988) postulated that the increase in mass flux in the Inntal was due to

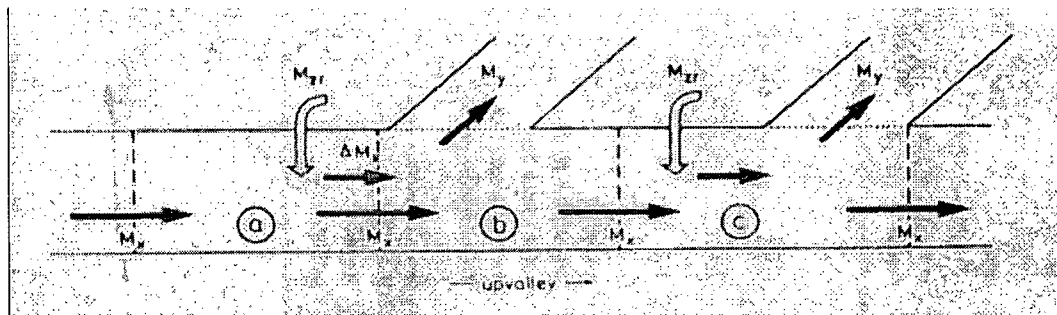


Figure 6.1: Schematic representation of the effects of side valleys on the mass budget of segments of the main valley. Taken from Freytag (1987).

subsidence over the main valley in order to quasi-locally compensate for flow into the sidevalley. This is based on observations which suggest that the reduction of volume in a valley by itself cannot explain the high heating and cooling rates of valley atmospheres (e.g. Steinacker, 1984) and that sidevalleys and high lying alpine areas have to be considered as well. Freytag reasoned that the only mechanism by which the energy could be transferred from sidevalleys to the main valley was through subsidence. While Freytag's postulate suggests that quasi-localized subsidence could induce a change in pressure gradient which causes the flow to accelerate, Freytag instead attributed the mass flux divergence purely to the location of measurement sites in relation to the sidevalleys. He envisioned three cases (Figure 6.1). In Case 1, the side valley joins the main valley just up-valley of the segment being considered. The flux into the side valley in segment (b) equals the subsidence in segment (a), and a loss of mass (mass flux divergence) of the same size will occur in segment (a). In Case 2, the side valley is situated at the down-valley edge of the segment. Most of the subsidence, compensating for the mass flux into the sidevalley, takes place outside (down-valley) the segment, so that a gain of mass (mass flux convergence) occurs in the valley segment. Finally, in Case 3, the sidevalley is situated at the up-valley edge of the segment. The flux into the sidevalley and the compensating subsidence take place in the segment itself and the mass flux stays constant. Thus, Freytag suggested that the observations in the Inntal correspond to Case 2. A link between measurements and the 'real' topography, however, was not made by Freytag.

Perusal of other studies conducted in the Inntal, however, do support the idea of a changing pressure gradient in the Inntal around Schwaz. The first such indication comes from measurements obtained during a car transverse in 1980 between Innsbruck and Nieder-Breitenbach (Vergeiner, 1983; Vergeiner and Dreiseitl, 1987) (shown in Figure 6.2), whereby a change in the surface pressure gradient is observed around Schwaz. Vergeiner and Dreiseitl (1987) explain the variable pressure gradient as follows:

"... the main valley has quite a variable cross section, with narrow valley sections

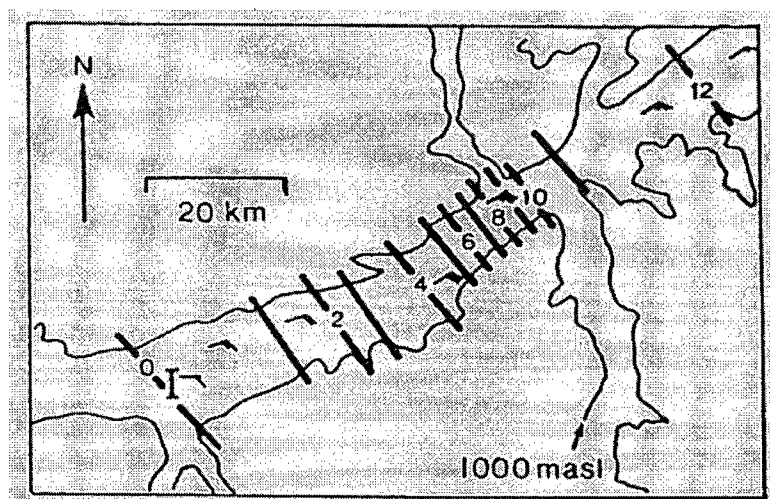


Figure 6.2: Car traverse, October 2, 1980, along the Inntal east of Innsbruck (I, 579m), 1230-1700 CET; dark line segments: height of pressure surface (gpm) relative to Innsbruck. One wind flag = 1 m/s (surface wind). Innsbruck is 2°C warmer than the eastern part of the traverse. Taken from Vergeiner and Dreiseitl (1987).

connecting basin-like wider parts. By mass continuity, the valley wind speeds up where the valley is narrow. Also, friction will, in reality, increase more than in linear proportion to the wind speed, possibly quadratically in a drag-law fashion. Therefore, the horizontal pressure gradient should be enhanced strongly across narrow valley sections, slackening where the valley gets broader.”

The concept of Venturi-type flow as suggested by Vergeiner and Dreiseitl (1987) does not seem appropriate for this situation as observations from the MERKUR experiment clearly show that the along-valley mass flux is not conserved but increases in the valley segment of interest. Furthermore, this type of argument reverses the cause and effect relationship between pressure gradient and valley flow by supposing that the pressure gradient is a result of the flow, and not the other way around.

Another indication that supports the idea of a variable intra-valley pressure gradient can be found in the paper by Vergeiner and Dreiseitl (1987) which lists the ratio of daily ranges of valley mean temperature between the plain and six valley stations (see Table 2 of that paper) averaged over a six-day fair weather period in September 1982. The rate of change of the ratio between Rattenberg (just west of Radfeld) and Schwaz is 2.5 times larger than for other segments either down- or up-valley from this valley section. One may conclude from these studies that the change in pressure gradient and the along-valley acceleration of the flow are permanent features of the valley flow in this section of the Inntal, and hence is linked to the valley topography.

The Kali Gandaki Valley (see Figure 6.3) in the Himalayas was recently studied by Egger

et al. (2000), Zängl et al. (2001) and Egger et al. (2002). The valley exhibits certain flow characteristics, such as extreme daytime up-valley flow ($\approx 20 \text{ m s}^{-1}$) and a strong asymmetry of the valley flow between day and night (Egger et al., 2000), which are not observed in 'typical' alpine valleys. Egger et al. (2000) and Zängl et al. (2001) attribute these distinct flow features to the terrain configuration whereby the Kali Gandaki Valley is simply a tube opening to the Mustang basin at the north end and (due to the steeply rising valley bottom) the free atmosphere to the south of Ghasa at the other end. Diurnal heating of the Mustang basin then generates a pressure difference which in turn drives the extreme up-valley flows.

The observations, however, also show a strong along-valley acceleration of the flow in the narrow section of the valley between Lete and Marpha *and* in the widened section further up-valley. Numerical modeling results of flow in the Kali Gandaki Valley were reminiscent of hydraulic model studies of flow through lateral contractions (Zängl et al., 2001), and it was hypothesized that a hydraulic jump took place. Subsequent field measurements (Egger et al., 2002), however, showed that a capping temperature inversion - a necessary requirement for hydraulic theory - is not present at all times, and hence the theory was dismissed. The observations, however, suggest that subsidence motion between Tukuche and Jomsom plays an important role in the flow dynamics.

So what conclusions can be drawn from these valley flow studies in relation to flow in the Wipptal? First of all, by considering *all* the observational evidence for the Inntal, it may be concluded that the along-valley mass divergence and subsequent subsiding motion in the Inntal is caused by a change in the pressure gradient which in turn is induced by changes in the valley geometry (i.e. the narrowing of the valley). Since aerological measurements are not available up-valley from Schwaz, it is not known if the flow intensity continues to increase past the narrow section of the valley.

Observations and model results for the Wipptal and the Kali Gandaki Valley show many similar features, such as significant subsidence motion towards the exit region of the valley constriction, a down-sloping of the isentropes and maximum wind speeds in the widened valley segment. It is unclear, however, if these flow features are caused by similar dynamic processes since the pressure gradients that drive the flow in the Wipptal and the Kali Gandaki Valley appear to be of different origin. In the Wipptal, it is assumed that the pressure gradient results from a change in the valley geometry (i.e. the narrow segment), while for the Kali Gandaki Valley, the pressure gradient is assumed to form between the Mustang Basin and the free atmosphere, with the actual geometry of the valley playing little role.

In conclusion, it may be said that the apparent similarities in flow features between the Inntal, Wipptal and the Kali Gandaki Valley provides some confidence in the underlying premise of this work, namely that similar topographical relief forms have similar effects on valley flows. It would be inappropriate, however, at this point to put forward a unified theory for all three valley flows. This will require a more detailed investigation.

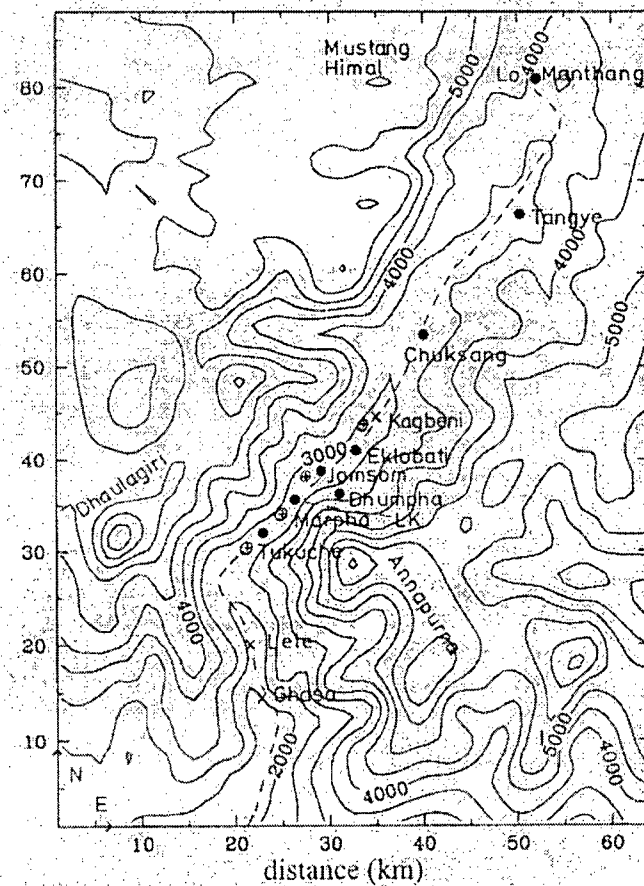


Figure 6.3: *Map of the Kali Gandaki Valley. Observation sites are indicated by dots. Taken from Egger et al. (2000).*

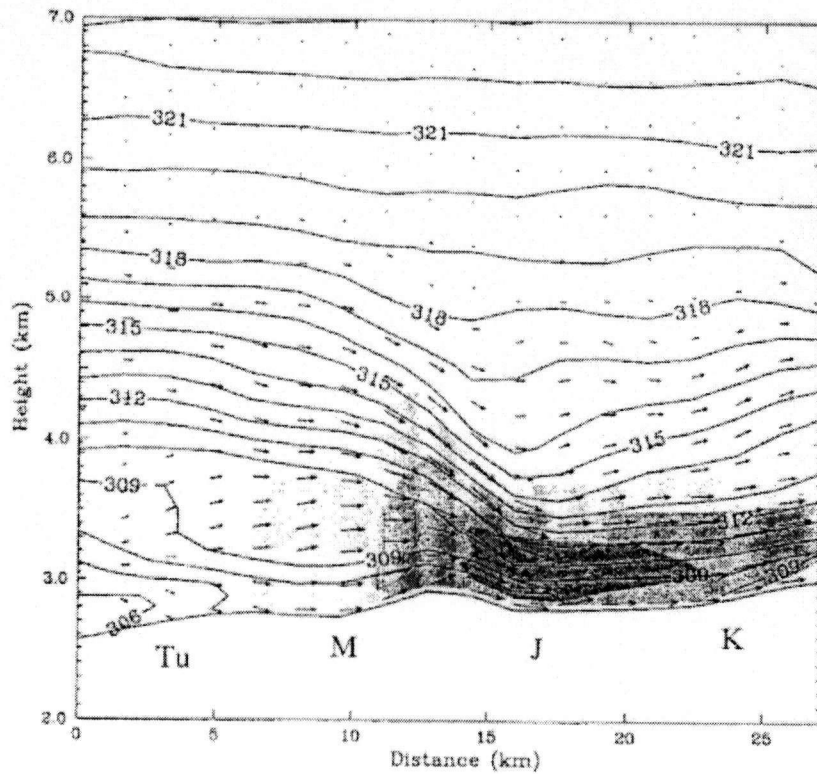


Figure 6.4: *Isentropes (contour interval, 1K; solid) and wind (vectors) in a section along the Kali Gandaki Valley as obtained in the reference run REF by Zängl et al. (2001) in the afternoon ($t = 15$ h). Shading: light, wind speeds $10 - 15\text{ms}^{-1}$; medium, $15 - 20\text{ms}^{-1}$; dar, $> 20\text{ms}^{-1}$. The letters mark the locations of Tukuhe, Marpha, Jomsom, and Kagbeni. Height is above MSL. The narrowest point of the valley is located near Marpha. Taken from Zängl et al. (2001).*

Chapter 7

Summary and Recommendations for Future Research

7.1 Summary

In this study, high spatially-resolved observations and numerical simulations of day-time thermally-driven flows in an alpine valley are used to examine the spatial structure of valley winds and how they relate to topographical relief features. The results can be summarized as follows.

The observations show that, *regardless* of external conditions,

- The along-valley wind speed increases with distance in the up-valley direction.
- The vertical wind profile is fairly uniform down-valley from the lidar and Prandtl-shaped up-valley from the lidar.
- The morning transition period from down-valley to up-valley flow occurs more rapidly up-valley from the lidar than down-valley from the lidar.

Analysis of backscatter intensity profiles shows the existence of several aerosol layer structures. Generally, the lowest layer can be associated with the valley flow, while the upper layer often coincides with the mountain top height. Although the interpretation of the backscatter analysis is hampered by the lack of vertical temperature profiles, the results do provide support for the flow analysis.

Calculations of the along-valley volume flux show that the sharp increase in wind speed with up-valley distance cannot be explained with a 'conservation of mass' argument, but that the along-valley volume flux indeed increases with up-valley distance. On days with strong thermal forcing, subsidence on the order of several 10's of $cm\ s^{-1}$ is required in order to balance the along-valley volume flux divergence.

Numerical modeling of the flow in the Wipptal reproduces the observed flow features remarkably well. A force term analysis along the length of the valley shows that the pressure-gradient force and advection are the dominant terms for the momentum budget, and turbulent diffusion and advection are the dominant terms in the heat budget. The pressure-gradient force is found to be quite variable along the valley, but large values of the pressure-gradient force are typically found in the narrow portions of the valley. In sections of the Wipptal with tributaries, the

pressure-gradient force is found to decelerate the flow. This redirection of the pressure-gradient force is attributed to the greater warming of atmospheres in the tributaries. The concept that heating in tributaries is distributed in the Wipptal through subsidence motion is not supported by the model results.

The numerical modeling suggests that, in addition to sensible heating and the volume effect, horizontal cold air advection and subsidence motion play a large role in the flow dynamics. In particular, the model suggests that for the Wipptal, horizontal cold air advection at the entrance region of the narrow section and subsidence motion towards the exit region of the narrow section produces a horizontal temperature/pressure gradient that accentuates the along-valley acceleration in this region of the valley.

Additional simulations with differently modified terrain configurations highlight the sensitivity of the valley flow structure and dynamics to topography. The results show that the narrow valley segment as well as the sloping valley bottom are important topographical features in reproducing the observed flow structure. Without the narrow valley section, the valley flow is much weaker and no significant flow divergence occurs. Without the sloping valley bottom, the flow intensity increases with up-valley distance but at a more gradual rate.

Analysis of the real topography as well as the terrain configurations used in the numerical simulations suggest that the TAF concept can be used to qualitatively predict the kinematic behaviour of the flow as long as advection processes do not play an important role.

Studies in other valleys with terrain constrictions - particularly the Inntal and the Kali Gandaki Valley - show similar flow features. This suggests that similar processes may be at play.

These findings have several implications: One, it suggests that subsidence motion can occur over a valley segment as a result of along-valley flow divergence which in turn is linked to intra-valley pressure gradients. This has the implication that air in a valley may not be entirely from the plain and statements about air pollution transport from the plain into the mountains have to be treated with care. Second, it also calls into question the concept that heating in an entire catchment area is relayed back to the main valley through subsidence at the mouth of a tributary (i.e. Steinacker's TAF concept). These findings suggest that changes in the heating are dealt with at a much more local scale.

7.2 Suggestions for Future Research

- While this study points to similarities in flow characteristics between valleys with similar terrain features (in this case, lateral constrictions), more field studies are required in valleys of varying shapes and sizes. A scanning Doppler lidar would be ideally suited for this type of study since it provides excellent data coverage along the valley's axis. In addition, however, information on the temperature structure should be obtained as well.

- The effects of tributaries of various sizes on the wind and temperature structure in the main valley have to be investigated in more detail. Again, a Doppler lidar (albeit one with a smaller minimum range) would be well suited to this type of study.
- The modeling work presented in this thesis focussed on the effects of terrain configurations. The modeling could be extended to examine the effects of ambient stability and land surface characteristics on the flow intensity and structure.
- Although the 'sensitivity' simulations presented in study highlight the importance of topography, it is virtually impossible to design realistic terrain configurations based on some predetermined characteristic (such as TAF). In the next stage of simulations, it would be useful to switch to fully idealized topography to investigate the sensitivity of the flow to different terrain configurations.

7.3 Thoughts on Scanning Strategies

Many factors, such as the type of flow, the size of the scan volume and the desired spatial resolution, must be taken into account when designing a scanning strategy. Generally speaking, however, high spatially-resolved coverage of lidar scans comes at the expense of temporal resolution. This poses somewhat of a problem when quantitative measures are to be extracted. Especially for non-stationary flows in complex terrain, it would be desirable to average over a long enough time period as to make the average statistically stable, but not so long as to degrade the essential underlying diurnal variability. To obtain such temporal coverage, however, would most likely mean a reduction in the spatial coverage.

While it would be ideal to scan the entire volume of a valley as has been done in previous studies (e.g. Post and Neff, 1986), it may not be possible to repeat such scans quickly enough to average several scans together and still capture the temporal evolution of the flow (as well as have time remaining for other scans of interest). In the present study, high spatially-resolved RHI (vertical) scans were performed only for the center of the valley. However, these scans were obtained in pairs, thus providing some confidence in the temporal representativeness of the data. Information on the cross-valley flow structure was extracted from PPI (horizontal) scans. These scans, however, were not repeated. The scanning strategy used in this study could be improved by performing consecutive RHI *and* PPI scans over a period of 10-15 minutes.

Bibliography

- Atkinson, B. W., 1981: *Meso-scale Atmospheric Circulations*. Academic Press, London, 279 pp.
- Atkinson, B. W. and A. N. Shahub, 1994: Orographic and stability effects on day-time, valley-side slope flows. *Boundary Layer Meteorology*, **68**, 275–300.
- Bader, D. C. and T. B. McKee, 1985: Effects of shear, stability and valley characteristics on the destruction of temperature inversions. *J. Climate and Applied Met.*, **24**, 822–832.
- Band, L. E., 1993: Effect of land surface representation on forest water and carbon budgets. *J. Hydrol.*, **150**, 749–772.
- Banta, R. M., 1984: Daytime boundary-layer evolution over mountainous terrain. Part I: Observations of the dry circulations. *Monthly Weather Review*, **112**(2), 340–356.
- Banta, R. M., L. S. Darby, P. Kaufmann, D. H. Levinson and C. J. Zhu, 1999: Wind-flow patterns in the Grand Canyon as revealed by Doppler lidar. *J. Applied Met.*, **38**, 1069–1083.
- Banta, R. M., L. D. Olivier, E. T. Holloway, R. A. Kropfli, B. W. Bartram, R. E. Cupp and M. J. Post, 1992: Smoke-column observations from two forest fires using Doppler lidar and Doppler radar. *J. Applied Met.*, **31**, 1328–1349.
- Banta, R. M., L. D. Olivier and D. H. Levinson, 1993: Evolution of the Monterey Bay sea breeze layer as observed by pulsed Doppler lidar. *J. Atmos. Sciences*, **50**(24), 3959–3982.
- Banta, R. M., L. D. Olivier, W. D. Neff, D. H. Levinson and D. Ruffieux, 1995: Influence of canyon-induced flows on flow and dispersion over adjacent plains. *Theor. Appl. Climatol.*, **52**, 27–42.
- Banta, R. M., P. B. Shepson, J. W. Bottenheim, K. G. Anlauf, H. A. Wieber, A. Gallant, T. Biesenthal, L. D. Olivier, C.-J. Zhu, I. G. McKendry and D. G. Steyn, 1997: Nocturnal cleansing flows in a tributary valley. *Atmos. Env.*, **31**, 2147–2162.
- Barry, R. G., 1992: *Mountain Weather and Climate*. Routledge, 2nd edition.
- Blumen, W., 1990: *Atmospheric Processes Over Complex Terrain*. volume 23 of *Meteorological Monographs*, chapter Mountain Meteorology, pp. 1–4. American Meteorological Society.
- Bougeault, P., P. Binder, A. Buzzi, R. Dirks, R. Houze, J. Kuettner, R. B. Smith, R. Steinacker and H. Volkert, 2001: The MAP Special Observing Period. *Bull. Amer. Met. Soc.*, **82**, 433–462.
- Brehm, M., 1986: *Experimentelle und numerische Untersuchungen der Hangwindsschicht und ihre Rolle bei der Erwärmung von Tälern*. Ph.D. thesis, Ludwig Maximilians Universität München, Munich, 150 pp.

- Brehm, M. and C. Freytag, 1982: Erosion of the night-time thermal circulation in an alpine valley. *Arch. Met. Geoph. Biol., Ser.B*, **31**, 331–352.
- Browning, K. and R. Wexler, 1968: The determination of kinematic properties of a wind field using Doppler radar. *J. Applied Met.*, **7**, 105–113.
- Buettner, K. J. K. and N. Thyer, 1966: Valley winds in the Mount Ranier area. *Arch. Met. Geoph. Biol., Ser.B*, **14**(2), 125–147.
- Carnuth, W. and T. Trickl, 2000: Transport studies with the IFU three-wavelength aerosol lidar during the VOTALP Mesolcina experiment. *Atmos. Env.*, **34**, 1425–1434.
- Carswell, A., 1983: Lidar measurements of the atmosphere. *Can. J. Phys.*, **61**, 378–395.
- Chen, C. and W. R. Cotton, 1983: A one-dimensional simulation of the stratocumulus-capped mixed layer. *Boundary Layer Meteorology*, **25**, 289–321.
- Clark, T. L., W. D. Hall and R. M. Banta, 1989: Two- and three- dimensional simulations of the 9 January 1989 severe Boulder windstorm: Comparison with observations. *J. Atmos. Sciences*, **51**(16), 2317–2343.
- Clements, C. B., 1999: Mountain and valley winds of Lee Vining Canyon, Sierra Nevada, California, U.S.A. *Arctic, Antarctic, and Alpine Research*, **31**(3), 293–302.
- Clements, W. E., J. A. Archuleta and D. E. Hoard, 1989: Mean structure of the nocturnal drainage flow in a deep valley. *J. Applied Met.*, **28**, 457–462.
- Colette, A. G. and R. L. Street, 2002: Inversion-layer breakup in steep valleys and the effects of topographic shading. in *Proceedings to the 10th AMS Conference on Mountain Meteorology*, pp. 101–104, Park City, Utah.
- Cotton, W. R., R. A. P. Sr., R. L. Walko, G. E. Liston, C. J. Tremback, H. Jiang, R. L. McAnelly, J. Y. Harrington, M. E. Nicholls, G. G. Carrio and J. P. McFadden, 2003: RAMS 2001: Current status and future directions. *Meteorol. Atmos. Phys.*, **82**, 5–29.
- Coulter, R. L., M. Orgill and W. Porch, 1989: Tributary fluxes into Brush Creek Valley. *J. Applied Met.*, **28**, 555–568.
- Darby, L. S., A. Gohm, L. B. Nance, S. Gabersek, R. M. Banta and S. Sandberg, 2000: Föhn flow in the Austrian Alps interrupted by a cold front passage: Part I. in *Proceedings to the Ninth AMS Conference on Mountain Meteorology*, pp. 79–82, Aspen, Colorado.
- De Rooy, W. C. and A. A. M. Holtslag, 1999: Estimation of surface radiation and energy flux densities from single-level weather data. *J. Applied Met.*, **38**, 526–540.
- De Wekker, S. F. J., 2002: *Structure and morphology of the convective boundary layer in mountainous terrain*. Ph.D. thesis, The University of British Columbia, Vancouver, BC.
- Defant, F., 1949: Zur Theorie der Hangwind, nebst Bemerkungen zur Theorie der Berg- und Talwinde. [A theory of slope winds, along with remarks on the theory of mountain winds and valley winds.]. *Arch. Meteor. Geophys. Bioklim.*, **A1**, 421–450, English translation: C.D.

- Whiteman and E. Dreiseitl, 1984: Alpine meteorology: Translations of classic contributions by A. Wagner, E. Ekhart and F. Defant. Pacific Northwest Laboratory, Richland, Washington, 121 pp. [PNL-5141/ASCOT-84-3].
- Dreiseitl, E., H. Feichter, H. Pichler, R. Steinacker and I. Vergeiner, 1980: Windregimes an der Gabelung zweier Alpentälern. *Arch. Met. Geoph. Biol., Ser.B*, **28**(3), 257–275.
- Durran, D. R., T. Maric, R. M. Banta, L. S. Darby and R. M. Hardesty, 2002: A comparison of ground-based Doppler lidar and airborne in situ wind observations above complex terrain. *submitted to Q. J. R. Meteorol. Soc.*
- Egger, J., 1987a: Simple models of the valley-plain circulation. Part I: Minimum resolution model. *Meteorol. Atmos. Phys.*, **36**, 231–242.
- Egger, J., 1987b: Simple models of the valley-plain circulation. Part II: Flow resolving model. *Meteorol. Atmos. Phys.*, **36**, 243–254.
- Egger, J., 1990a: *Atmospheric Processes Over Complex Terrain*. volume 23 of *Meteorological Monographs*, chapter Thermally Forced Flows: Theory, pp. 43–58. American Meteorological Society.
- Egger, J., 1990b: Thermally induced flow in valleys with tributaries. Part I: Response to heating. *Meteorol. Atmos. Phys.*, **42**, 113–125.
- Egger, J., S. Bajrachaya, U. Egger, R. Heinrich, J. Reuder, P. Shayka, H. Wendt and V. Wirth, 2000: Diurnal winds in the Himalayan Kali Gandaki Valley. Part I: Observations. *Monthly Weather Review*, **128**, 1106–1122.
- Egger, J., S. Bajrachaya, R. Heinrich, P. Kolb, S. Lämmlein, M. Mech, J. Reuder, W. Schaäper, P. Shakya, J. Schween and H. Wendt, 2002: Diurnal winds in the Himalayan Kali Gandaki Valley. Part III: Remotely piloted aircraft soundings. *Monthly Weather Review*, **130**, 2042–2058.
- Ekhart, E., 1944: Beiträge zur alpinen Meteorologie [Contributions to alpine meteorology]. *Meteorologische Zeitschrift*, **61**(7), 217–231, English translation: C.D. Whiteman and E. Dreiseitl, 1984: Alpine meteorology: Translations of classic contributions by A. Wagner, E. Ekhart and F. Defant. Pacific Northwest Laboratory, Richland, Washington, 121 pp. [PNL-5141/ASCOT-84-3].
- Ekhart, E., 1948: De la Structure Thermique de l'Atmosphere dans la Montagne [On the thermal structure of the mountain atmosphere]. *La Meteorologie*, **4**(9), 3–26, English translation: C.D. Whiteman and E. Dreiseitl, 1984: Alpine meteorology: Translations of classic contributions by A. Wagner, E. Ekhart and F. Defant. Pacific Northwest Laboratory, Richland, Washington, 121 pp. [PNL-5141/ASCOT-84-3].
- Fast, J. D., 1995: Mesoscale modeling in areas of highly complex terrain. *J. Applied Met.*, **34**, 2762–2782.
- Fast, J. D., S. Zhong and C. D. Whiteman, 1996: Boundary layer evolution within a canyonland basin. part II: Numerical simulations of nocturnal flows and heat budgets. *J. Applied Met.*, **35**(12), 2162–2178.

- Freytag, C., 1983: MERKUR: Mesokaliges Experiment in Raum Kufstein-Rosenheim. Wiss. mitt. nr. 48, Meteorologisches Institut, Universität München, 132 pp.
- Freytag, C., 1985: MERKUR results: Aspects of the temperature field and the energy budget in a large alpine valley during mountain and valley wind. *Beitr. Phys. Atmosph.*, **58**(4), 458-475.
- Freytag, C., 1987: Results from the MERKUR Experiment: Mass budget and vertical motions in a large valley during mountain and valley wind. *Meteorol. Atmos. Phys.*, **37**, 129-140.
- Freytag, C., 1988: Atmosphärische Grenzschicht in einem Gebirgstal bei Berg- und Talwind. Wiss. mitt. nr. 60, Meteorologisches Institut, Universität München, 197 pp.
- Freytag, C. and B. Hennemuth, 1981: DISKUS, Gebirgswindexperiment im Dischmatal - Datensammlung Teil 1: Sondierungen. Wiss. mitt. nr. 43, Meteorologisches Institut, Universität München, 250 pp.
- Furger, M., J. Dommen, W. K. Graber, L. Poggio, A. S. H. Prévôt, S. Emeis, G. Grell, T. Trickl, B. Gomiscek, B. Neiningner and G. Wotawa, 2000: The VOTALP Mesolcina Valley Campaign 1996 - Concept, background and some highlights. *Atmos. Env.*, **34**, 1395-1412.
- Hägeli, P., D. G. Steyn and K. B. Strawbridge, 2000: Spatial and temporal variability of mixed-layer depth and entrainment zone thickness. *Boundary Layer Meteorology*, **17**(24), 1-25.
- Hawkes, H. B., 1947: *Mountain and winds with special reference to the diurnal mountain winds of the Great Salt Lake Region*. Ph.D. thesis, Ohio State University, 312 pp.
- Hayden, K. L., K. G. Anlauf, R. M. Hoff, J. W. Strapp, J. W. Bottenheim, H. A. Wiebe, F. A. Froude and J. B. Martin, 1997: The vertical chemical and meteorological structure of the boundary layer in the Lower Fraser Valley during Pacific '93. *Atmos. Env.*, **31**(14), 2089-2105.
- Hefland, H. M. and J. C. Labraga, 1988: Design of a non-singular level 2.5 second-order closure model for the prediction of atmospheric turbulence. *J. Atmos. Sciences*, **45**, 113-132.
- Hennemuth, B., 1987: Heating of a small alpine valley. *Meteorol. Atmos. Phys.*, **36**, 287-296.
- Hennemuth, B. and H. Schmidt, 1985: Wind phenomena in the Dischma Valley during DISKUS. *Arch. Met. Geoph. Biol., Ser.B*, **35**, 361-387.
- Hoff, R. M., M. Harwood, A. Sheppard, F. Froude and J. B. Martin, 1997: Use of airborne lidar to determine aerosol sources and movement in the Lower Fraser Valley (LFV, BC). *Atmos. Env.*, **31**(14), 2123-2134.
- Kavaya, M. J. and R. T. Menzies, 1985: Lidar aerosol backscatter measurements: systematic, modeling, and calibration error considerations. *AO*, **24**(21), 3444-3453.
- King, C. W., 1989: Representative of single vertical wind profiles for determining volume flux in valleys. *J. Applied Met.*, **28**(6), 463-366.

- King, C. W., 1997: A climatology of thermally forced circulations in oppositely oriented airsheds along the continental divide in Colorado. NOAA Technical Memorandum ETL-283, NOAA/ETL.
- Kondratyev, K. J., 1969: *Radiation in the Atmosphere*. Academic Press, 912 pp.
- Koßmann, M. and A. P. Sturman, 2003: Pressure-driven channeling effects in bent valleys. *J. Applied Met.*, **42**, 151–158.
- Kuwagata, T. and F. Kimura, 1995: Daytime boundary layer evolution in a deep valley. Part I: Observations in a Ina Valley. *J. Applied Met.*, **34**, 1082–1091.
- Li, J.-G. and B. W. Atkinson, 1999: Transition regimes in valley airflows. *Boundary Layer Meteorology*, **91**, 385–411.
- Louis, J.-F., 1979: A parametric model of vertical eddy fluxes in the atmosphere. *Boundary Layer Meteorology*, **17**, 187–202.
- Marsik, F. J., K. W. Fischer, T. D. McDonald and P. J. Samson, 1995: Comparison of methods for estimating mixing height used during the 1992 Atlanta Field Intensive. *J. Applied Met.*, **34**, 1802–1814.
- Mayr, G. J., L. Armi, S. Arnold, R. B. Banta, L. S. Darby, D. D. Durran, C. Flamant, S. Gabersek, A. Gohm, R. Mayr, S. Mobbs, I. Vergeiner, J. Vergeiner, L. B. Nance and C. D. Whiteman, 2003: Gap flow measurements during the Mesoscale Alpine Programme. *Meteorol. Atmos. Phys.*, accepted.
- Mayr, R., 2000: Temperature profiles along mountain slopes and their relationship to vertical profiles in the mid-valley atmosphere. Research report.
- McElroy, J. L. and T. B. Smith, 1991: Lidar descriptions of mixing-layer thickness characteristics in a complex terrain/coastal environment. *J. Applied Met.*, **30**, 585–597.
- McKee, T. B. and R. D. O'Neal, 1989: The role of valley geometry and energy budget in the formation of nocturnal valley winds. *J. Applied Met.*, **28**, 445–456.
- McKendry, I. G. and J. Lundgren, 2000: Tropospheric layering of ozone in regions of urbanized complex and/or coastal terrain - A review. *Progress in Physical Geography*, **24**(3), 329–354.
- McKendry, I. G., D. G. Steyn, J. Lundgren, R. M. Hoff, W. Strapp, K. Anlauf, F. Froude, J. B. Martin, R. M. Banta and L. D. Olivier, 1997: Elevated ozone layers and vertical down-mixing over the Lower Fraser Valley, BC. *Atmos. Env.*, **31**, 2135–2146.
- Mellor, G. L. and T. Yamada, 1982: Development of a turbulent closure model for geophysical fluid problems. *Rev. Geophys. Space Phys.*, **20**, 851–875.
- Müller, H. and C. D. Whiteman, 1988: Breakup of a nocturnal inversion in the Dischma Valley during DISKUS. *J. Applied Met.*, **27**(188-194).
- Neff, W. D., 1990: *Atmospheric Processes Over Complex Terrain*. volume 23 of *Meteorological Monographs*, chapter Remote Sensing of Atmospheric Processes over Complex Terrain, pp. 173–228. American Meteorological Society.

- Neff, W. D., 1995: Advances in measurement systems, ASCOT (1979-1995). in *Seventh Conference on Mountain Meteorology*, pp. 297-303, Breckenridge, CO. American Meteorological Society.
- Nickus, U. and I. Vergeiner, 1984: The thermal structure of the Inn Valley atmosphere. *Arch. Met. Geoph. Biol., Ser. A*, **33**, 199-215.
- Nyeki, S., M. Kalberer, I. Colbeck, S. F. J. De Wekker, M. Furger, H. W. Gäggeler, M. Kößmann, M. Lugauer, D. Steyn, E. Weingartner, M. Wirth and U. Baltensperger, 2000: Convective boundary layer evolution to 4 km asl over high-alpine terrain. *Geophys. Res. Lett.*, **27**, 689-692.
- Pielke, R. A., W. R. Cotton, R. L. Walko, C. J. Tremback, W. A. Lyons, L. D. Grasso, M. E. Nicholls, M. D. Moran, D. A. Wesley, T. J. Lee and J. H. Copeland, 1992: A comprehensive meteorological modeling system - RAMS. *Meteorol. Atmos. Phys.*, **49**, 69-91.
- Porch, W. M., R. B. Fritz, R. L. Coulter and P. H. Gudiksen, 1989: Tributary, valley and sidewall air flow interactions in a deep valley. *J. Applied Met.*, **28**, 578-589.
- Post, M. J. and R. E. Cupp, 1990: Optimizing a pulsed Doppler lidar. *Appl. Optics*, **29**, 4145-4158.
- Post, M. J. and W. D. Neff, 1986: Doppler lidar measurements of winds in a narrow mountain valley. *BAMS*, **67**, 274-281.
- Pottier, J. L., S. C. Pryor and R. M. Banta, 1997: Synoptic variability related to boundary layer and surface features observed during Pacific '93. *Atmos. Env.*, **31**(14), 2163-2173.
- Poulos, G. S. and J. E. Bossert, 1995: An observational and prognostic numerical investigation of complex terrain dispersion. *J. Applied Met.*, **34**, 650-669.
- Prévôt, A. S. H., M. Furger, B. Neininger, L. Poggio, J. Dommen and W. Graber, 1998: Mesolcina Valley = Highly efficient air pump for vertical transport. in *Proceedings to the Eighth AMS Conference on Mountain Meteorology*, pp. 401-403, Flagstaff, Arizona.
- Ramanathan, N. and K. Srinivasan, 1998: Simulation of airflow in Kashmir Valley for a summer day. *J. Applied Met.*, **37**, 497-508.
- Rao, P. K., 1968: *An investigation of the valley-plain wind circulation in the valleys of Vermont*. Ph.D. thesis, New York University.
- Reiter, R., H. Müller, R. Sladkovic and K. Munzert, 1983: Aerologische Untersuchungen der tagesperiodischen Gebirgswinde unter besonderer Berücksichtigung des Windfeldes im Talquerschnitt. *Meteorol. Rdsch.*, **36**, 225-242.
- Reiter, R., H. Müller, R. Sladkovic and K. Munzert, 1984: Aerologische Untersuchungen des tagesperiodischen Windsystems im Inntal während MERKUR. *Meteorol. Rdsch.*, **37**, 176-190.
- Rotach, M., 2000: MAP Riviera Project. in *Proceedings to the 9th AMS Conference on Mountain Meteorology*, pp. 232-234, Aspen, Colorado.

- Ruffieux, D., W. D. Neff and R. M. Banta, 1992: Visualization of flows channelled in canyons using Doppler lidar data. in *Proceedings to the Sixth AMS Conference on Mountain Meteorology*, pp. 111-113.
- Savov, P. B., T. S. Skakalova, I. N. Kolev and F. L. Ludwig, 2002: Lidar investigation of the temporal and spatial distribution of atmospheric aerosols in mountain valleys. *J. Applied Met.*, **41**, 528-541.
- Somieski, F., 1987: *Numerische Simulation der thermisch angeregten Zirkulation zwischen Gebirge und Vorland*. Ph.D. thesis, Ludwig-Maximilians Universität München, Munich, 186.
- Steinacker, R., 1984: Area-height distribution of a valley and its relation to the valley wind. *Beitr. Phys. Atmosph.*, **57**(1), 64-71.
- Stephens, G. L., 1993: *Remote Sensing of the Lower Atmosphere: An Introduction*. Oxford University Press.
- Steyn, D. G., M. Baldi and R. Hoff, 1999: The detection of mixed layer depth from lidar backscatter profiles. *J. Atmos. Oceanic Techn.*, **16**(7), 953-959.
- Sturman, A. P., 1987: Thermal influences on airflow in mountainous terrain. *Prog. Phys. Geog.*, **11**, 183-206.
- Ulrich, W., 1987: *Simulation von thermisch induzierten Winden und Überströmungssituationen*. Ph.D. thesis, Wiss. Mitt. Meteor. Inst. München, 192.
- Urfer-Henneberger, C., 1970: Neuere Beobachtungen über die Entwicklung des Schönwetterwindsystems in einem V-förmigen Alpentäl (Dischmatal bei Davos). *Arch. Met. Geoph. Biol., Ser. B*, **18**, 21-42.
- Vergeiner, I., 1983: Dynamik Alpiner Windsysteme. Forschungsprojekt No 3556 des Fonds zur Förderung der wissenschaftlichen Forschung, Institut für Meteorologie und Geophysik, Innsbruck, p129.
- Vergeiner, I. and E. Dreiseitl, 1987: Valley winds and slope winds - Observations and elementary thoughts. *Meteorol. Atmos. Phys.*, **36**, 264-286.
- Wagner, A., 1932a: Der tägliche Luftdruck- und Temperaturgang in der freien Atmosphäre und in Gebirgstälern. *Gerlands Beitr. Geophys.*, **37**, 315-344.
- Wagner, A., 1932b: Hangwind - Ausgleichsströmung - Berg- und Talwind. *Meteorol. Zeitschrift*, **49**(6), 209-217.
- Wagner, A., 1932c: Neue Theorie des Berg- und Talwindes. *Meteorol. Zeitschrift*, **49**, 329-341.
- Wagner, A., 1938: Theorie und Beobachtung der periodischen Gebirgswinde [Theory and observation of periodic mountain winds]. *Gerlands Beitr. Geophys.*, **52**, 408-449, English translation: C.D. Whiteman and E. Dreiseitl, 1984: Alpine meteorology: Translations of classic contributions by A. Wagner, E. Ekhardt and F. Defant. Pacific Northwest Laboratory, Richland, Washington, 121 pp. [PNL-5141/ASCOT-84-3].

- Walko, R. L., L. E. Band, J. Baron, T. G. F. Kittel, R. Lammers, T. J. L. and D. Ojima, R. A. Pielke, C. Taylor, C. Tague, C. J. Tremback and P. L. Vidale, 2000: Coupled atmosphere-biophysics-hydrology models for environmental modeling. *J. Applied Met.*, **39**, 931-944.
- White, F. M., 1986: *Fluid Mechanics*. McGraw-Hill Book Company, second edition.
- Whiteman, C. D., 1982: Breakup of temperature inversions in deep mountain valleys: Part I. Observations. *J. Applied Met.*, **21**, 270-271.
- Whiteman, C. D., 1986: Atmospheric mass transport by along-valley wind systems in a deep Colorado valley. *J. Applied Met.*, **25**, 1205-1212.
- Whiteman, C. D., 1990: *Atmospheric Processes Over Complex Terrain*. volume 23 of *Meteorological Monographs*, chapter Observations of Thermally Developed Wind Systems in Mountainous Terrain, pp. 5-42. American Meteorological Society.
- Whiteman, C. D., 1995: Conceptual advances, (ASCOT 1979-1995). in *Seventh Conference on Mountain Meteorology*, pp. 289-292, Breckenridge, CO. American Meteorological Society.
- Whiteman, C. D., 2000: *Mountain Meteorology: Fundamentals and Applications*. Oxford University Press, 355 pp.
- Whiteman, C. D. and J. C. Doran, 1993: The relationship between overlying synoptic-scale flows and winds within a valley. *J. Applied Met.*, **32**, 1669-1682.
- Whiteman, C. D., J. M. Hubbe and W. J. Shaw, 2000: Evaluation of an inexpensive temperature datalogger for meteorological applications. *J. Atmos. Oceanic Techn.*, **17**(1), 77-81.
- Wotawa, G. and H. Gromp-Kolb, 2000: The research project VOTALP - general objectives and main results. *Atmos. Env.*, **34**, 1319-1322.
- Zängl, G., 2002: An improved method for computing horizontal diffusion in a sigma-coordinate model and its application to simulations over mountainous topography. *Monthly Weather Review*, **130**, 1423-1432.
- Zängl, G., J. Egger and V. Wirth, 2001: Diurnal winds in the Himalayan Kali Gandaki Valley. Part II: Modeling. *Monthly Weather Review*, **129**, 1062-1080.

Appendix A

Determination of Surface Energy Fluxes

Calculations of surface energy fluxes are based on a scheme proposed by De Rooy and Holtslag (1999) which allows surface fluxes to be determined from routine single-level weather data. The scheme was tested with data over a fairly homogeneous site at Cabouw, the Netherlands. The effects of a complex site are unknown, but it is assumed that the scheme allows relative trends in the sensible heat flux to be assessed for the study period.

The scheme was modified slightly to make use of the observed net radiation. In addition, the surface temperature was determined using

$$L^{\uparrow} = \epsilon_s \sigma T_0^4 + (1 - \epsilon_s) L^{\downarrow} \quad (\text{A.1})$$

where L^{\uparrow} is the outgoing longwave radiation, L^{\downarrow} the incoming longwave radiation, σ the Stefan-Boltzmann constant, and ϵ_s the surface emissivity. Site-specific parameters used in the calculations are listed in Table A.1.

Figure A.1 shows the observed net radiation as well as the calculated sensible, latent and soil heat fluxes. The 1-hourly averaged net radiation fluxes agree well with the author's personal field observations during the study period. Differences in net radiation fluxes during the morning hours between 11 and 13 October, and 14, 16 and 17 October are due to valley fog which was present in the Wipptal during morning hours in the latter part of the study period. On 13 October, the net radiation was reduced during midday by thickening cirrus clouds. Solar noon occurs at 1100 UTC which is reflected in the net radiation values.

The magnitudes and apportionment of the calculated surface fluxes correspond well with observations made in other moist valley environments (e.g. Whiteman, 1990; Vergeiner, 1983). The Bowen ratio (at 1100 UTC) is approximately 0.4. From Figure A.1d, it can be seen that

Parameter	Value
Emissivity, ϵ_s	0.92
Roughness length for heat, z_{0H}	0.003 m
Roughness length for momentum, z_{0M}	0.03 m (local) 0.07 m (effective)
Soil heat transfer coefficient, A_G	$5.0 \text{ W m}^{-2} \text{ K}^{-1}$
b (used to calculate surface resistance)	$10 \text{ s kg m}^{-1} \text{ g}^{-1}$

Table A.1: *Site-specific surface parameters used in radiation scheme.*

the (peak) latent heat flux decreases over the study period as the soil dries. Overall, the largest sensible heat flux is obtained for 17 October. It should be remembered that the surface energy budget is strongly dependent on the orientation, inclination and surface characteristics of a individual measurement site. Much larger Bowen ratios, for example, could be expected for sites in alpine areas.

The diurnal pattern of the calculated fluxes appears reasonable. However, the soil heat flux shows a slight delay in its peak. Observations show that the soil heat flux typically peaks 2-3 hours before solar noon. The delay in the peak of the soil heat flux is due to the parameterization of the soil heat flux in this scheme which is based on $G = -A_G(T_r - T_0)$. Symbol A_G is the soil heat transfer coefficient, T_r is the temperature at 2 m AGL averaged over the past 24 hours and T_0 is the surface temperature. This parameterization is meant to reflect the time history of the atmosphere acting on the soil at this site, but it does not capture the correct time of the peak.

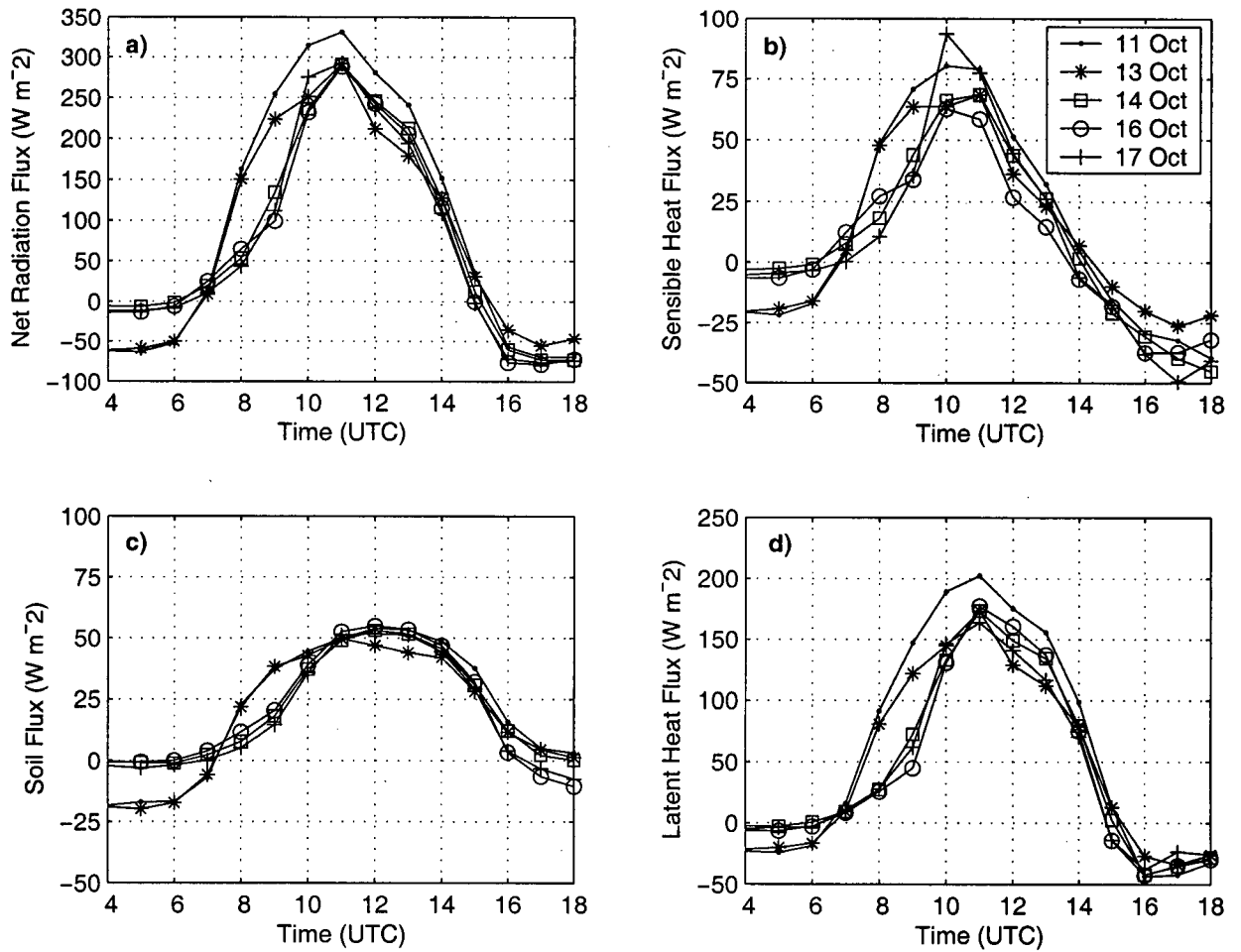


Figure A.1: a) Measured net radiation and calculated b) sensible, c) soil and d) latent heat flux for 11, 13, 14, 16 and 17 October.

Appendix B

Calibration of Tethered Balloon Data

The tether sonde model TS-3A-SPH measures pressure, wind speed, wind direction, temperature, relative humidity and ozone. The ozone sensor was disabled for this study.

The heights as determined by the tether sonde software were adjusted so that the starting and finishing heights of each flight were equivalent. Any pressure/height drifts that occurred during a flight were linearly distributed over the whole flight (according to time). To ensure consistency between the two tether sonde packages which were used in the field, the cup anemometer and thermistor of each tether sonde package were calibrated.

The cup anemometer calibration was performed in the 'Green' wind tunnel (cross sectional area of 27" by 36.125") of the Civil/Mechanical Engineering Department at the University of British Columbia. The wind speeds were increased incrementally from 0 – 12 $m s^{-1}$. At each setting, some time was allowed to pass to ensure that steady state conditions were reached. Data at each setting was obtained for a one minute period.

Wind tunnel velocities are calculated using Bernoulli's Equation

$$P_1 + \frac{1}{2}\rho V_1^2 = P_2 + \frac{1}{2}\rho V_2^2 \quad (B.1)$$

and the Continuity Equation

$$V_1 A_1 = V_2 A_2. \quad (B.2)$$

where V is the velocity, P the pressure, ρ the density, and A the cross-sectional area. Subscript 1 refers to the upstream section while subscript 2 refers to the test section. Combining Equations B.1 and B.2 yields the following equation for V_2 :

$$V_2 = \sqrt{\frac{P_1 - P_2}{\frac{1}{2}\rho \left(1 - \left(\frac{A_2}{A_1}\right)^2\right)}} \quad (B.3)$$

For this wind tunnel, the ratio of the cross-sectional areas, $\frac{A_2}{A_1}$, was 0.1532. The pressure difference, $P_1 - P_2$, is related to the height of the water column in the manometer via

$$P_1 - P_2 = \frac{\rho g h}{1000} \quad (B.4)$$

Sonde	m	b	sigm	sigb	q
2	1.147	- 0.461	0.022	0.165	1.0
5	1.159	- 0.314	0.022	0.17	1.0

Table B.1: Regression Coefficients for tethersondes 2 and 5.

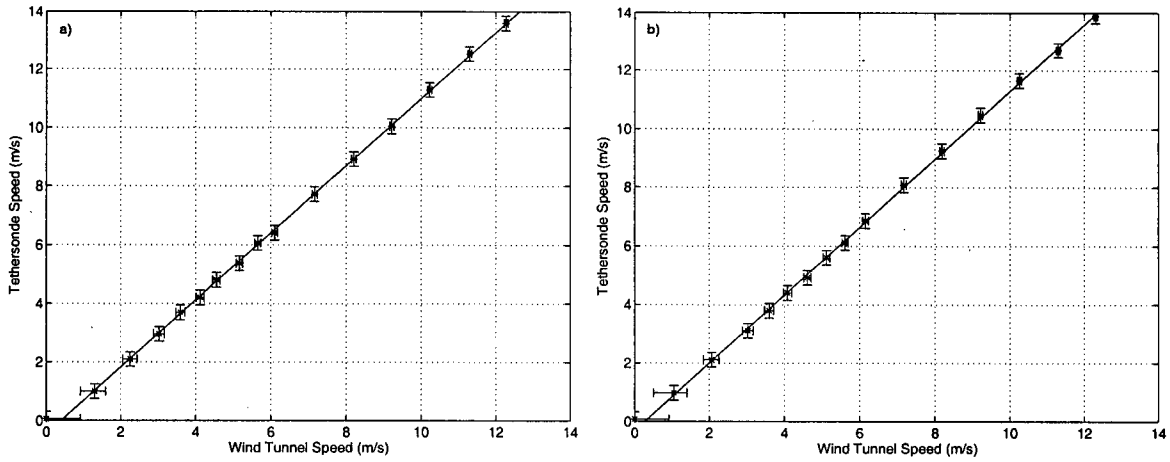


Figure B.1: Linear regression plots with error bars for tethersondes a) 2 and b) 5. Actual data points are indicated by stars.

where ρ is the density of water in the manometer (998 kg m^{-3}), g the gravitational acceleration (9.81 m s^{-2}) and h the manometer reading in mm .

Substituting Equation B.4 and the Equation of State into Equation B.3, the following equation is obtained:

$$V_2 = \sqrt{\frac{\rho g h R T_{atm}}{500 P_{atm} \left(1 - \frac{A_2^2}{A_1^2}\right)}} \quad (\text{B.5})$$

or

$$V_2 = 75.860 \sqrt{\frac{h T_{atm}}{P_{atm}}} \quad (\text{B.6})$$

For the linear regression analysis, errors in both variables (V_2 and V_{teth}) were assumed. For V_{teth} , an accuracy of 0.25 m s^{-1} (as specified by the manufacturer) was assumed, while for the calculation of the wind tunnel speeds, the following errors were used: $\delta h = 0.05 \text{ mm}$, $\delta T_{atm} = 0.5^\circ \text{C}$ and $\delta P_{atm} = 0.05 \text{ KPa}$.

Figure B.1 shows the linear regressions for tethersondes 2 and 5. Table B.1 lists the regression coefficients and fit.

The regression analysis shows threshold velocities (minimum speed required for cup anemometer to start moving) of 0.4 m s^{-1} and 0.27 m s^{-1} for tethersondes 2 and 5, respectively.

The thermocouples were calibrated by applying adjustments of 0.24 K and 3.17 K to tethersonde 2 and 5, respectively. These adjustments were determined through calibration studies following the field experiment, and were also verified by psychrometer measurements taken at the start of every tethersonde flight. The offsets were assumed to be temperature independent.

Appendix C

Hobo Temperature Measurements

During the MAP-SOP, Hobo temperature loggers were positioned along the sidewalls of the Wipptal and Inntal in order to obtain temporally highly-resolved information on the stratification of the valley atmosphere. Mayr (2000) compared pseudo-vertical temperature profiles obtained from the Hobo data loggers at Patscherkofel with radiosonde soundings at Gedeir (Doppler lidar site) during pre-foehn and foehn conditions. His findings show that slope and free-air temperatures agree well on days with strong winds, but that under conditions of weak winds and strong radiation, the slope temperatures are dominated by the local microclimates of individual Hobo sites.

Analyses of Hobo measurements for this study period show similar results. One interesting finding, however, is that during conditions of valley fog (i.e. the morning hours of 14, 16 and 17 October), the pseudo-vertical temperature profiles obtained at different locations almost collapse onto each other (Figure C.1). This suggests that there is no horizontal temperature gradient along the valley. The profiles remain this way until the cloud and fog cover begins to dissipate at which point effects of the local microclimates can be seen again.

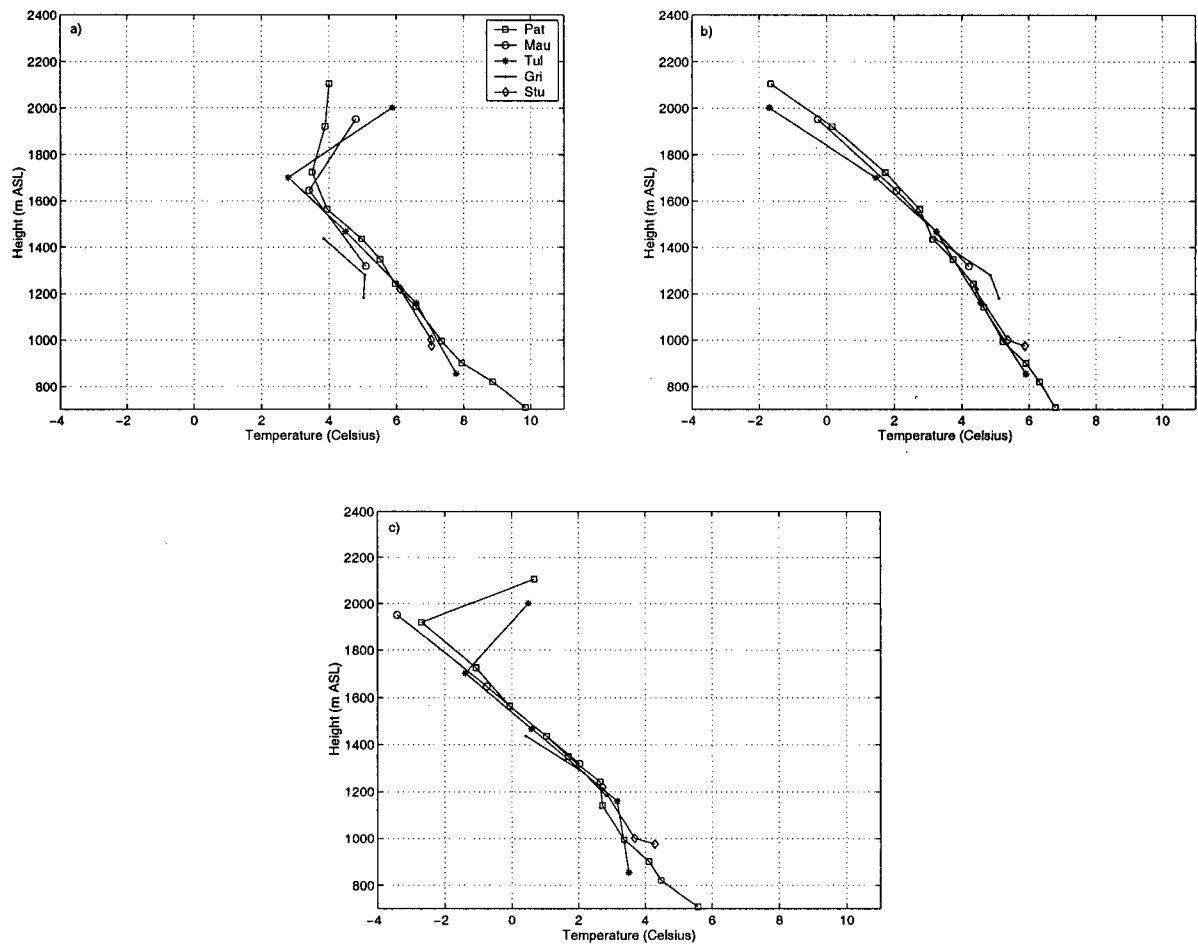


Figure C.1: Pseudo-vertical temperature profiles obtained by Hobo data-loggers on a) 14 October, b) 16 October and c) 17 October. All profiles are averaged for the period 0400-0415 UTC.

Appendix D

Terrain Removal Algorithm

A Doppler lidar is well suited for atmospheric studies in complex terrain. Its narrow beam width ($90 \mu\text{rad}$) and absence of sidelobe radiation allow the lidar to scan very close to the surface. To eliminate any terrain signals in the post-analysis of lidar data, range gates contaminated or masked by terrain have to be accurately removed. The work presented in this dissertation focuses on flow characteristics near the ground, and hence terrain removal forms an important component of the post-processing of lidar data.

As discussed by Neff (1990), terrain removal from lidar data can be accomplished in two ways. One method is to derive terrain elevation and location from topographic maps and then transpose this information onto lidar data. However, small errors in the position coordinates of the lidar and systematic variations in the positioning of the lidar beam make it practically impossible to match lidar measurements with topographic data with the accuracy needed to remove terrain affected range gates. Another method is to detect and flag terrain masked range gates and therefore map the terrain as observed by the lidar. This method was pioneered by Post and Neff (1986) and later applied by Ruffieux et al. (1992) in the visualisation of drainage flows in narrow canyons. Unfortunately, the terrain detection scheme used by Post and Neff (1986) and Ruffieux et al. (1992) is not well documented, and hence a new algorithm was independently developed for this study.

Terrain masking in lidar data is most easily identified in the backscatter intensity signal. Along a normal beam, that is, one that does not intersect a solid object, the backscatter intensity decays with distance due to attenuation by the atmosphere (Figure D.1a). As the backscatter intensity approaches background (or noise) levels, the radial velocity begins to fluctuate, giving erroneous estimates of the radial velocity. When the beam hits a solid target, such as the side of a mountain slope, the intensity signal rises sharply (hard target, hard return) and then quickly drops off to noise level, whereby the radial velocity signal again begins to fluctuate (Figure D.1b). This spike in the intensity signal can be used as a marker for terrain hits in lidar data.

Both magnitude and shape of the terrain-induced spike in the backscatter intensity signal can vary from scan to scan. The magnitude of the spike generally depends on the power output of the lidar system during that particular scan. The shape of the backscatter terrain spike is determined by the location of the range gates in relation to the terrain and can give some indication as to how close the last valid range gate is to the actual terrain. Figure D.2

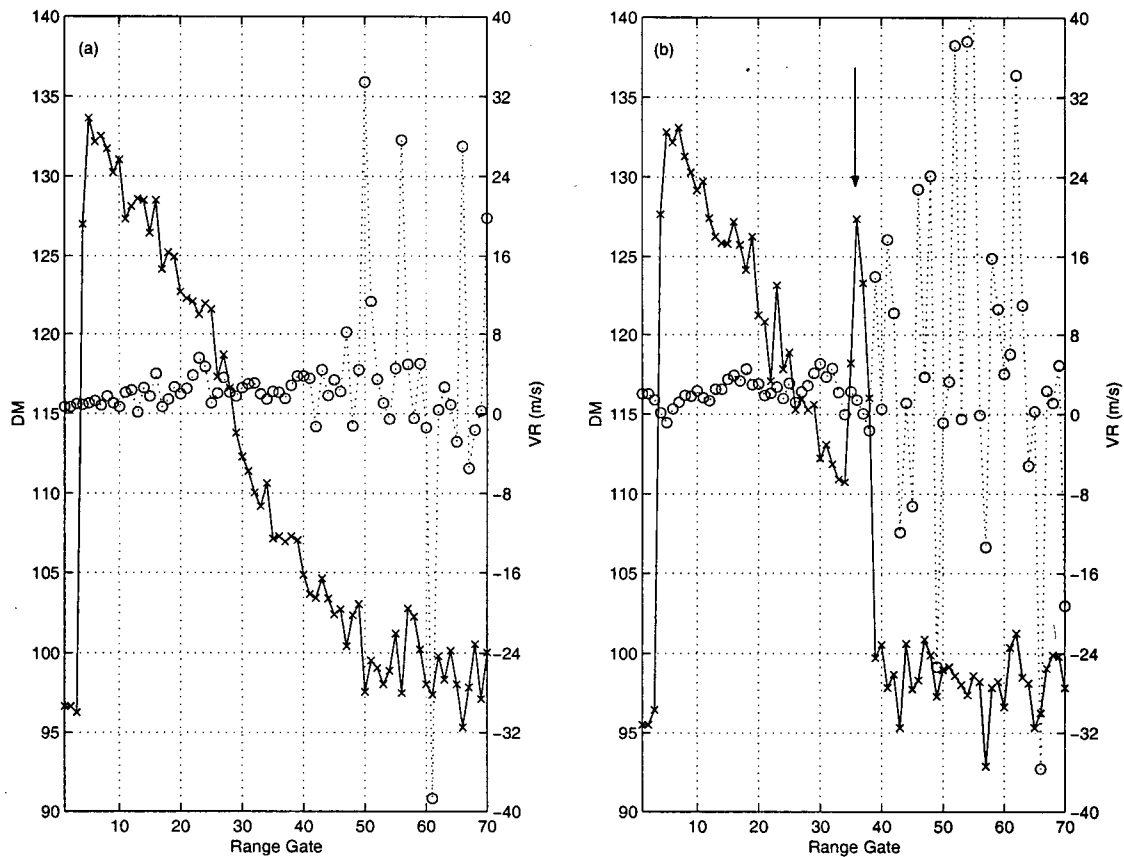


Figure D.1: Two individual Doppler lidar beams showing backscatter intensity (labelled 'DM') in arbitrary units (stars) and radial velocity in m s^{-1} (open circles) for a) no terrain hit and b) with terrain hit (indicated by arrow). Beams are taken from Pacific '93 data set.

schematically presents some possible backscatter intensity spike configurations.

In Figure D.2a, the beam intersects the terrain immediately after range gate 2. The drop in backscatter intensity between range gates 1 and 2 is due to atmospheric attenuation, while the large jump in backscatter value between range gates 2 and 3 correlates with the terrain hit. The intensity peaks at range gate 3. Assuming a range resolution of 300 m (typical for the NOAA/ETL TEACO2 Doppler lidar), the center of the last valid range gate is approximately 150 m from the terrain surface. In Figure D.2b, a small portion of the beam volume at range gate 2 is contaminated by terrain, and hence the intensity for this range gate increases slightly. The intensity maximum still occurs at range gate 3 which is completely masked by terrain. In this case, the center of the last valid range gate (1) is 300 to 450 m from the terrain. In the last case (Figure D.2c), most of range gate 2 is contaminated by the terrain, and therefore a larger jump in the backscatter occurs than in case b). The distance between the last valid range gate and the terrain ranges between 150 and 300 m.

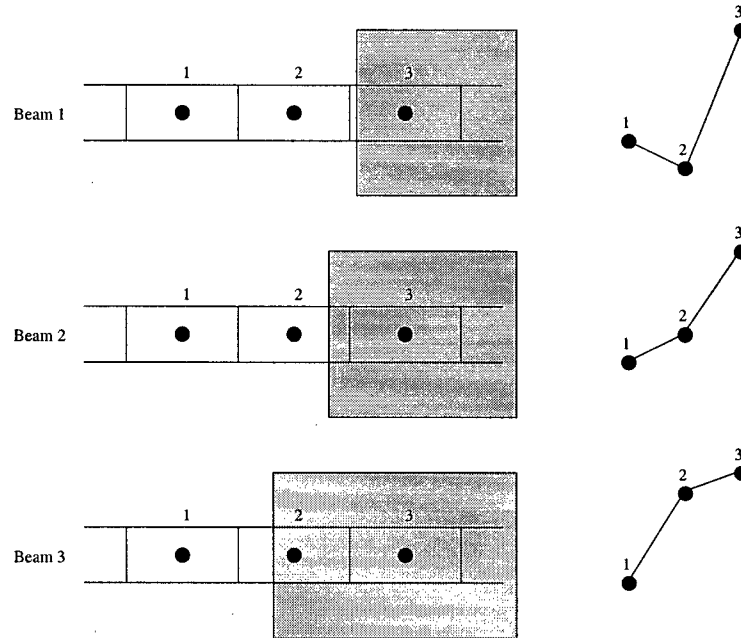


Figure D.2: Schematic of backscatter intensity return signal for different terrain hits. The solid circles represent the centre of the range gates (i.e. the centre of the volume over which the backscatter intensity is averaged). The shaded area indicates the terrain. The corresponding backscatter intensity signals are shown to the right.

For the removal of terrain-contaminated range gates, outlier-removal methods based on backscatter intensity thresholding are generally not accurate enough or may remove valid range gates. In addition, the NOAA Doppler lidar uses a pulse which contains a tail with different frequency properties than that of the primary pulse. When this trailing part of the transmitted pulse is scattered from a solid object, it can generate a frequency shift and power return signal in range gates further from the lidar which are similar to returns from the actual atmosphere. Thresholding of the backscatter intensity signal is therefore not a good solution to differentiate contaminated range gates from non-masked range gates. A better method is one which identifies the terrain-induced intensity peak. Such an algorithm is presented next.

The terrain detection algorithm requires two parameters. DM_{spike} specifies a minimum value for the terrain-induced spike in the backscatter intensity signal. This parameter allows the scheme to differentiate between small fluctuations in the backscatter intensity signal and the larger fluctuation that typically occurs with a terrain hit. The second parameter $DM_{threshold}$ provides a cut-off value for the intensity signal (i.e. the noise level). As the lidar power output

can vary from day-to-day, or even scan-to-scan, these parameters have to be determined from data through trial and error. For the MAP data set, an additional parameter, the signal to noise ratio (SNR), is available. SNR is defined as the peak signal power at the output of the receiver (before detection) divided by the average noise power at the same point. SNR responds similarly to hard target hits as the backscatter intensity signal does.

The scheme can be summarized as follows:

1. Calculate the change in backscatter intensity between two consecutive range gates for the whole beam length ($\Delta DM_i = \Delta DM_{i+1} - \Delta DM_i$), and tag all range gates for which this change is positive ($\Delta DM_i > 0$).
2. Discard $\Delta DM_i > 0$ if it occurs within the first four range gates.
3. Add all positive ΔDM_i of consecutive range gates to obtain the total increase in backscatter intensity of consecutive tagged range gates.
4. Determine the first range gate for each backscatter spike.
5. Find all spikes for which the total increase in intensity exceeds DM_{spike} . If none are found, then there is no terrain hit.
6. For each spike
 - (a) If the intensity for the first range gate of the spike is below $DM_{threshold}$, then set terrain hit equal to the first range gate. (This step was introduced since it was found that once the backscatter signal dropped below the threshold value, the signal became too unreliable for the detection scheme).
 - (b) Otherwise find the DM value averaged over 5 range gates immediately following the intensity spike.
 - i. If this average value is less than $DM_{threshold}$, then a terrain hit has been found. For the Pacific '93 data set, the last valid range gate is set to the first range gate in the intensity spike. In case of the MAP data set, the first terrain-contaminated range gate is correlated with the range gate within the spike which has the largest increase in SNR.
 - ii. Otherwise return to 6 and try next spike.
7. If none of the spikes are followed by a drop-off in the intensity level, then there is no terrain hit.

This detection scheme has been tested on two separate data sets: Pacific '93 and MAP. Figure D.3 shows an example of the terrain detection algorithm applied to a lidar scan from the Pacific '93 data set.

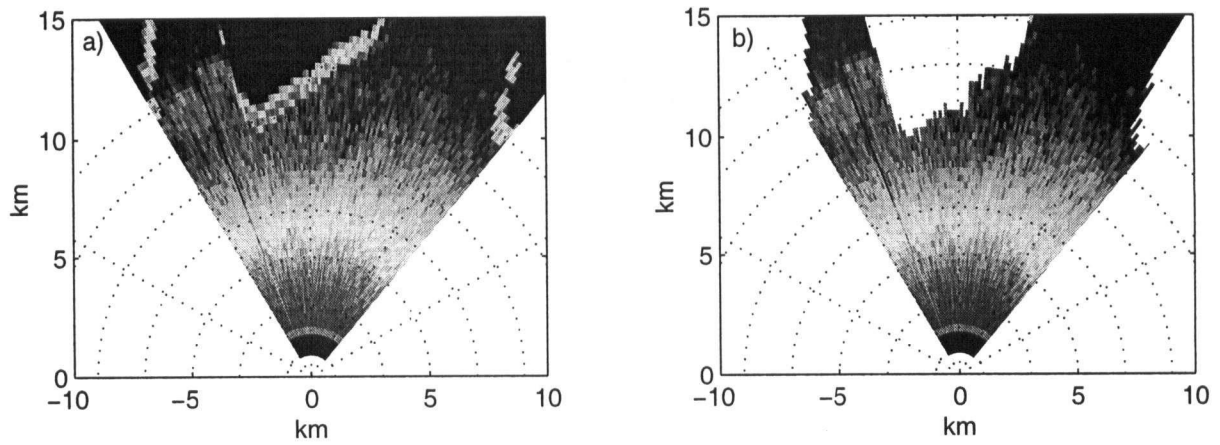


Figure D.3: Lidar scan showing backscatter intensity a) before and b) after terrain removal. The bright bands in a) indicate terrain. Scan was taken from the Pacific '93 data set.

Appendix E

Pre-processing of RHI Scans

RHI scans pointing up- and down-valley from the lidar at 178 and 320 degrees, respectively, were completed on four out of the five days. Each scan was performed twice. The RHI scans were post-processed with the following goals in mind

- Remove erroneous data.
- Combine consecutive RHI scans to form an averaged scan.
- Integrate RHI178 and RHI320 scans to form a picture of the flow along the valley.

For the purpose of averaging over consecutive RHI, the RHI profiles were first interpolated onto predetermined elevation angles, with a resolution of 1 degree (it was found that the recorded elevation angles could differ slightly between consecutive scans). The radial velocities and backscattered intensity were then averaged for each elevation angle and range gate. Using this method, the vertical resolution for each range gate remains the same as the original recorded data. The vertical spacing increases with range gate distance, and varies from 24 m at a range of 1.35 km to 102 m at a range of 5.85 km (based on an effective scanning rate of 1 beam/degree). In addition, as the elevation angle increases, the pulse volume covers more vertical than horizontal distance. For example, at an elevation angle of 5 degrees, the vertical distance covered by a range gate of 300 m is 26 m while at an elevation angle of 45 degrees, the vertical distance covered is 212 m.

To remove faulty data points, radial velocity estimates were discarded for range gates for which the backscatter intensity value dropped below some threshold value. The threshold value was determined for each day separately. Furthermore, any data with elevation angles greater than 45 degrees was discarded (this affected only range gates closest to the lidar). Finally, a Gaussian filter with a sigma value of 50 m was applied to smooth the horizontal radial velocity profiles. Backscattered intensity profiles were not smoothed.

Appendix F

Composite Wind Profiles for 11 October

Although high resolution vertical profiles of the along-valley wind speed are not available for 11 October, it is of interest - for comparison purposes - to approximate the volume flux for this day. Due to the limited elevation angles used in the VAD or PPI scans and the depth of the valley flow on this day, no complete vertical wind profile could be obtained with a single range gate. Therefore, composite profiles were created using Doppler lidar data from several range gates. A Prandtl-type formulation was used to fill in the profile near the surface. For the profile up-valley from the lidar, the flow maximum was assumed to be 300 m AGL.

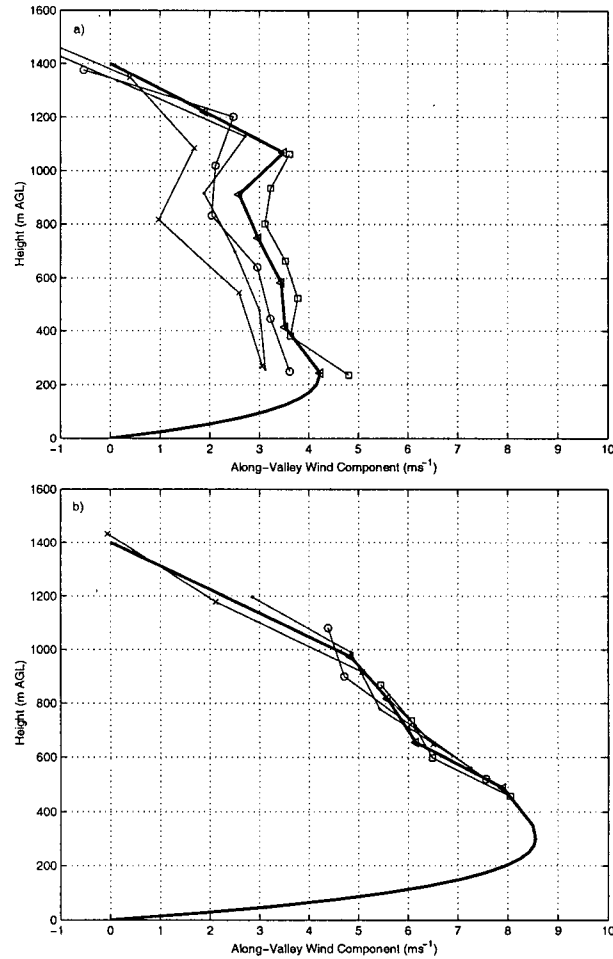


Figure F.1: Vertical profiles of the along-valley wind component a) below the lidar and b) above the lidar on 11 October between 1217 and 1233 UTC. Profiles below the lidar are from PPI scans while profiles above the lidar are obtained from VAD scans. The thin lines with symbols show profiles at various range gates: RG6 (squares), RG7 (triangles), RG8 (circles), RG9 (dots) and RG10 (crosses). The heavy line in each graph represents the approximated profile at range gate 7.

Appendix G

VAD Analysis

In order to extract information of the flow above the valley atmosphere, vertical wind profiles were derived from Doppler lidar VAD25 scans using the linear VAD technique by Browning and Wexler (1968). This technique assumes that the wind field varies linearly across the scan volume. Kinematic properties of the wind (centered around the Doppler lidar) are then determined by approximating the velocity components with a first order Taylor series expansion and comparing the terms to a second harmonic Fourier expansion of the radial velocity. The Fourier expansion coefficients are calculated from the measured radial velocities.

The results from the linear VAD analysis for the various study days are shown in Figures G.1, G.2, G.3, G.4 and G.5. For comparison purposes, wind profiles from tethered sonde soundings are included where available. The tethered balloon was located roughly 1.5 km NE from the lidar in a small tributary valley. Hence, the lowest 200-400 m of the tethered sonde soundings typically show local flow characteristics with either flow up the local slope or along the tributary valley from which the tethered balloon was operated. At higher elevations, the VAD and tethered sonde profiles generally show good agreement despite the very different nature of the two instruments.

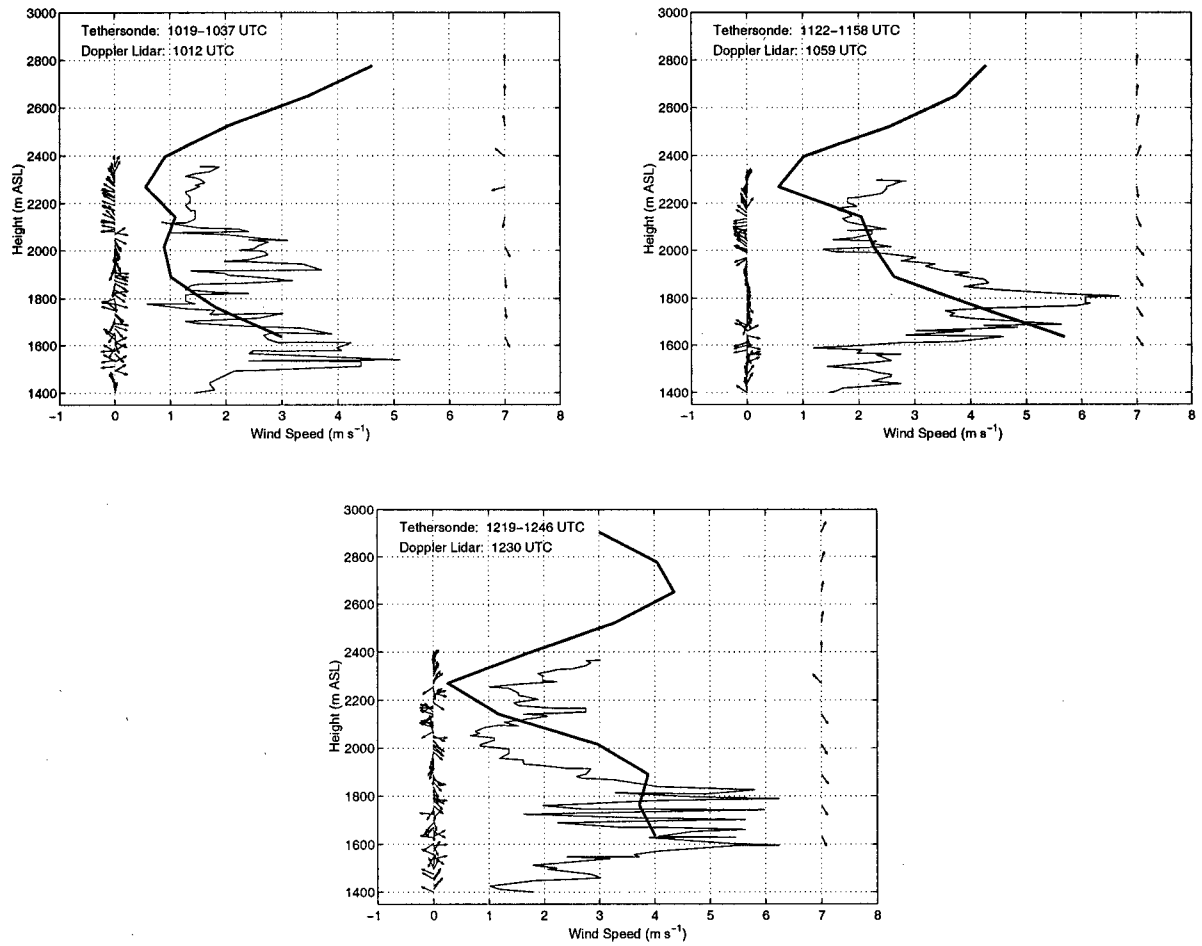


Figure G.1: Wind speed and direction for 11 October. The heavy line and wind vectors to the right hand side are for the VAD analysis. The thin line and wind vectors to the left hand side are from tethersonde soundings.

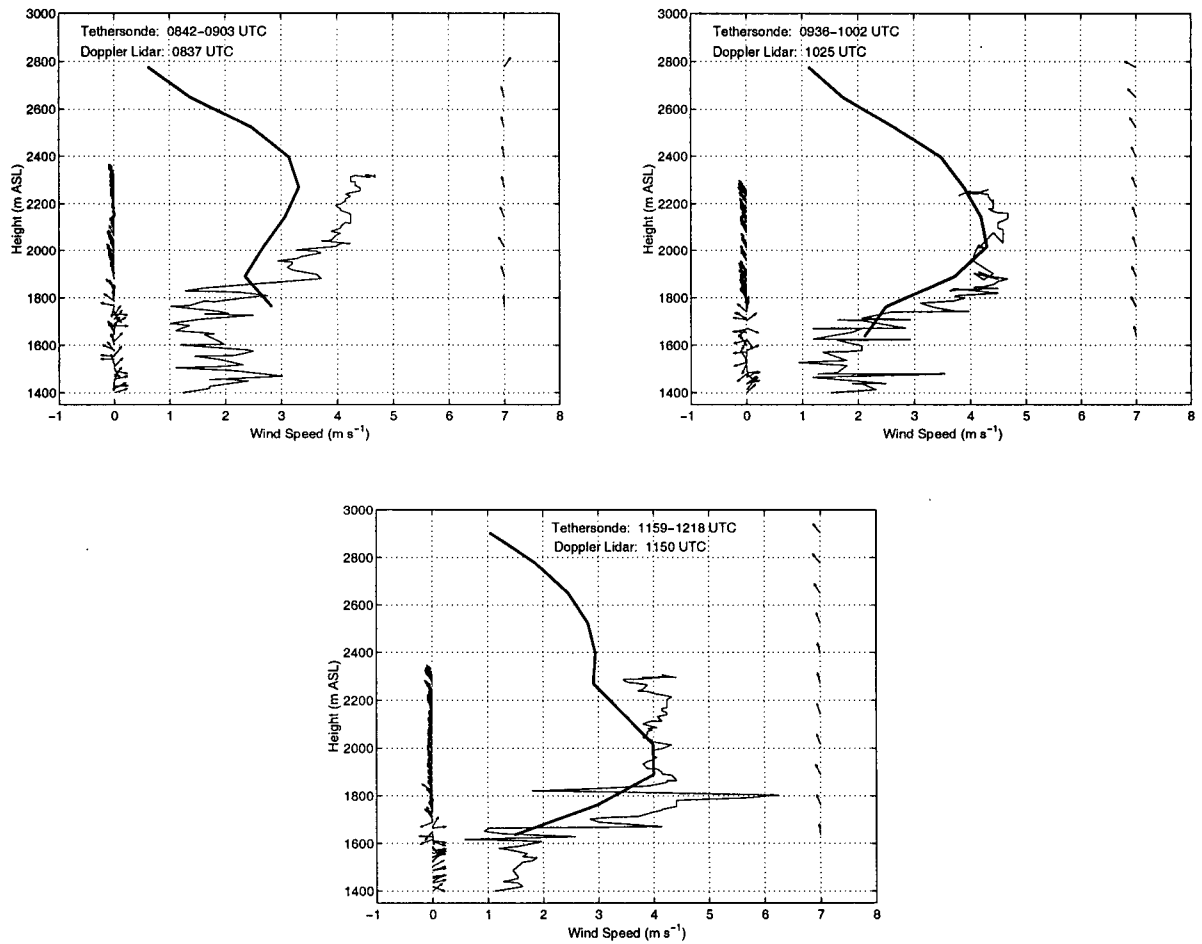


Figure G.2: Wind speed and direction for 13 October. The heavy line and wind vectors to the right hand side are for the VAD analysis. The thin line and wind vectors to the left hand side are from tethersonde soundings.

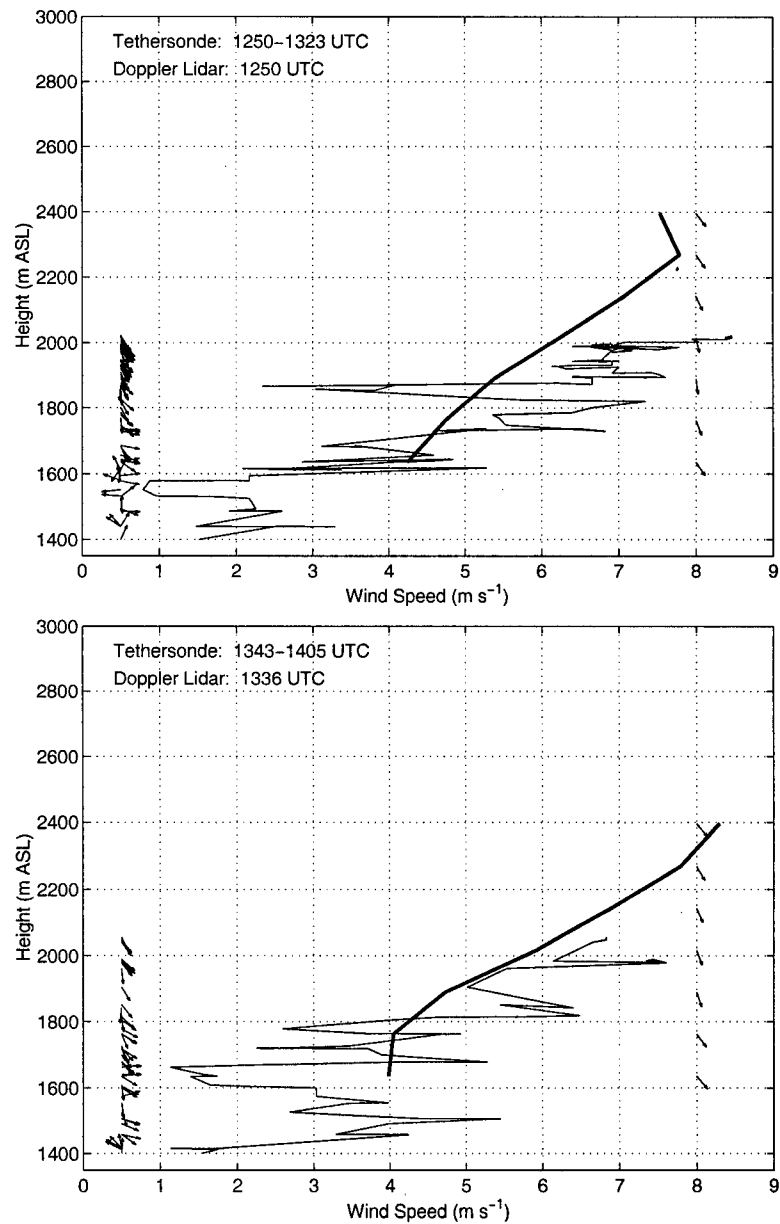


Figure G.3: Wind speed and direction for 14 October. The heavy line and wind vectors to the right hand side are for the VAD analysis. The thin line and wind vectors to the left hand side are from tethersonde soundings.

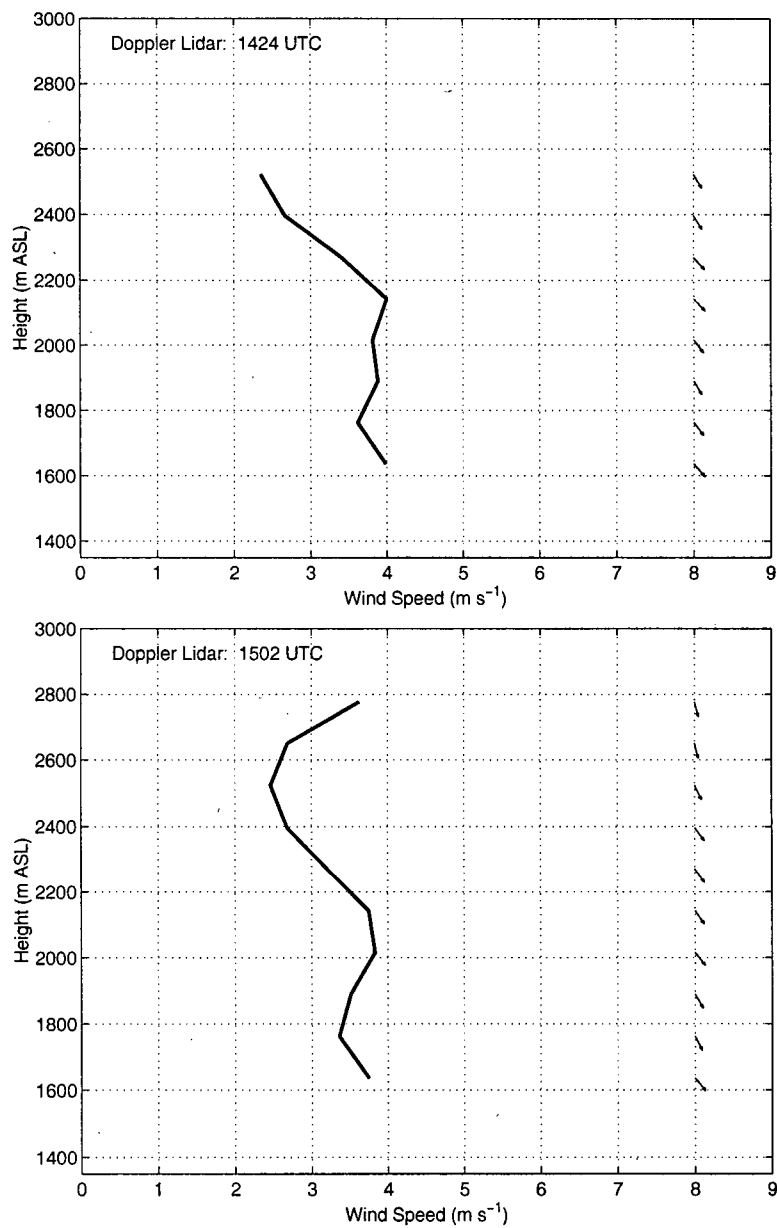


Figure G.4: Wind speed and direction for 16 October from VAD analysis.

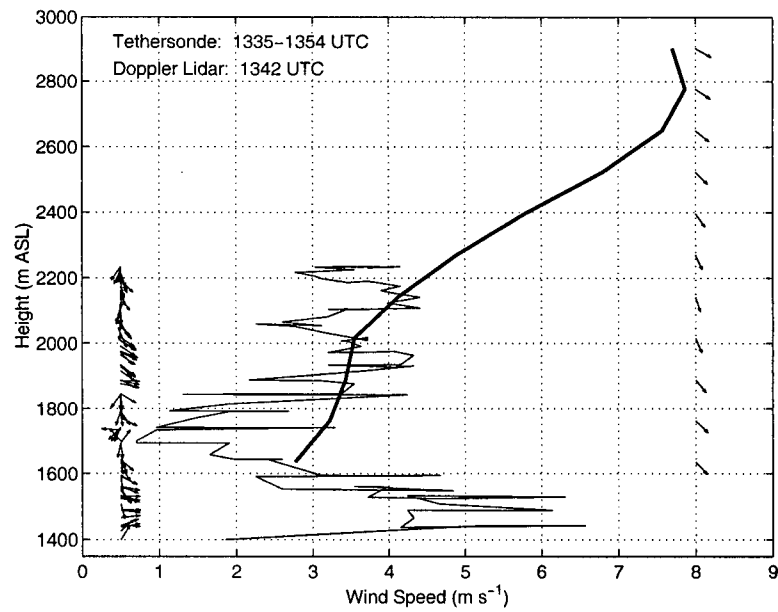


Figure G.5: Wind speed and direction for 17 October. The heavy line and wind vectors to the right hand side are for the VAD analysis. The thin line and wind vectors to the left hand side are from tethersonde soundings.

Appendix H

On Analysing Backscatter Intensity Fields

The backscatter intensity at a given range is described by the lidar equation

$$P(R) = \frac{K}{R^2} \beta(R) e^{-2 \int_0^R \alpha(r) dr} \quad (\text{H.1})$$

where $P(R)$ is the range received power [W], $\beta(R)$ is the range-dependent volumetric backscatter coefficient of the atmosphere [$km^{-1} sr^{-1}$], $\alpha(R)$ is the range-dependent extinction coefficient [km^{-1}], R is the range [km] and K is the lidar constant which includes transmitted power, receiver cross-section and other instrument factors. Equation H.1 assumes that a single scattering event takes place to scatter part of the energy pulse back to the receiver. This assumption is reasonable for clear conditions (Carswell, 1983), but not valid for high turbidity situations (such as fog or clouds) where multiple scattering becomes important. The two unknown parameters $\beta(R)$ and $\alpha(R)$ are complex functions of a number of aerosol attributes such as concentration, composition and particle size, but they are typically interpreted to represent aerosol content (e.g. McKendry et al., 1997; Banta et al., 1997; Pottier et al., 1997).

Equation H.1 is indeterminate but can be solved for β or α as functions of range if a functional relationship between the backscatter and extinction coefficient is assumed. The backscatter information (usually depicted as the aerosol backscatter ratio, e.g. Hoff et al. (1997)) is then mapped in three-dimensional space, providing valuable visualization of boundary layer structures and processes.

The aforementioned extraction of the backscatter (or extinction) coefficient as a function of space is typical for data from aerosol lidars which operate in the near-infrared or visible light spectrum, but is generally not possible for backscatter information obtained from CO_2 lidars which operate in the infrared spectrum. The problem is that the attenuation of an infrared transmitted energy pulse is mainly molecular (water vapour and CO_2), while scattering is primarily due to aerosol particles (Kavaya and Menzies, 1985). As a result, an analytical relationship between attenuation and scattering is not possible, and the lidar equation cannot be closed. Consequentially, the range dependency in Equation H.1 cannot be removed and 3-D mapping of aerosol content is not possible.

Backscatter information from CO_2 lidars, however, is not entirely for naught. The problem of range dependency can be partially circumvented by considering backscatter intensity data

at constant range gates. With the additional assumption that changes in the integrated attenuation are negligible in comparison to changes in the backscatter coefficient, relative changes in backscatter intensity can then be interpreted as changes in aerosol content/properties (e.g. Pottier et al., 1997; Banta et al., 1997, 1999). Banta et al. (1992) were able to show plan view mappings of backscatter data by correcting for range and water vapour attenuation (water vapour corrections were based on radiosonde soundings and the assumption of horizontal homogeneity).